

The ratio of the proton and neutron structure functions in
490 GeV/c deep inelastic muon scattering

by

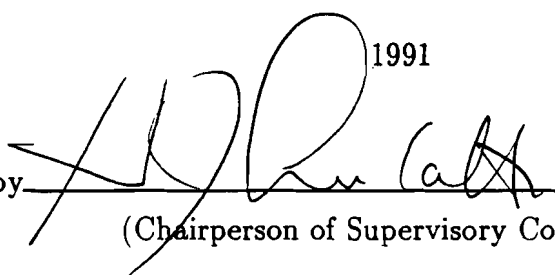
Anwar Ahmad Bhatti

A dissertation submitted in partial fulfillment
of the requirements for the degree of

Doctor of Philosophy

University of Washington

Approved by

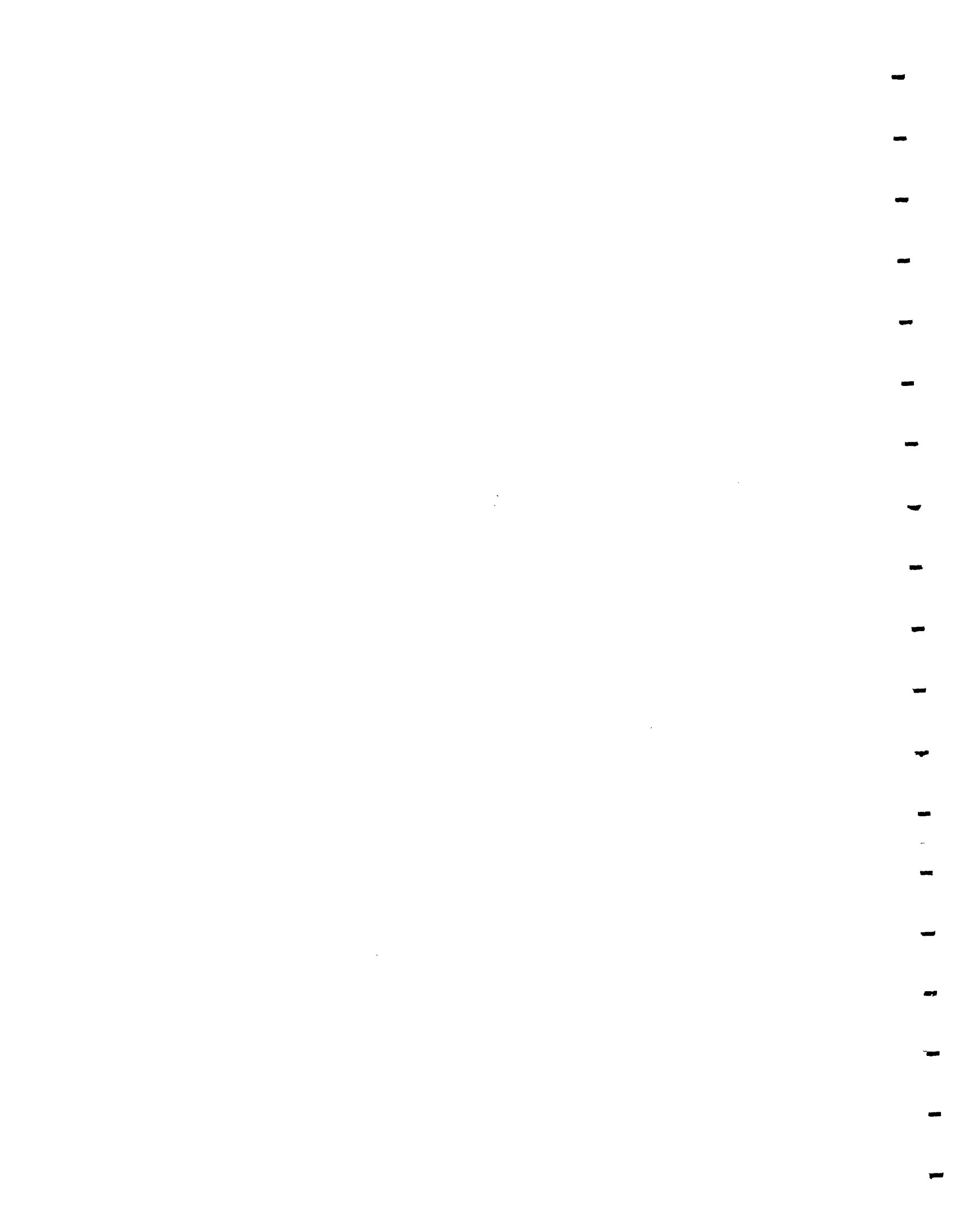

(Chairperson of Supervisory Committee)

1991

Program Authorized
to Offer Degree

Date

ANR/609



In presenting this dissertation in partial fulfillment of the requirements for the Doctoral degree at the University of Washington, I agree that the Library shall make its copies freely available for inspection. I further agree that extensive copying of this dissertation is allowable only for scholarly purposes, consistent with "fair use" as prescribed in the U.S. Copyright Law. Requests for copying or reproduction of this dissertation may be referred to University Microfilms, 300 North Zeeb Road, Ann Arbor, Michigan 48106, to whom the author has granted "the right to reproduce and sell (a) copies of the manuscript in microform and/or (b) printed copies of the manuscript made from microform."

Signature_____

Date_____



University of Washington

Abstract

The ratio of the proton and neutron structure functions in 490
GeV/c deep inelastic muon scattering

by Anwar Ahmad Bhatti

Chairperson of Supervisory Committee: *Professor Henry J. Lubatti*
Department of Physics

The ratio of the proton and neutron structure functions in 490 GeV/c deep inelastic muon scattering experiment is measured. Using the measured F_2^n/F_2^p ratio and a Morfin-Tung parameterization of parton distributions, the Gottfried Sum rule is evaluated in a restricted x_{bj} range. The measure F_2^n/F_2^p ratio in the x_{bj} range 0.001-0.125 at low Q^2 is found to be consistent with unity. The contribution to the Gottfried sum from the x_{bj} range 0.001-0.125 is -0.044 ± 0.123 .

The experiment E665 extends the range of ratio of the structure functions measurement from $x_{bj}=0.004$ to 0.001. The measured ratio is higher but consistent with measurement done by previous experiments in the region where the data overlaps.



TABLE OF CONTENTS

List of Figures	vii
List of Tables	x
Chapter 1 Structure of Nucleons	1
1.1 Definition of the Variables	2
1.2 Scattering of Two Dirac Particles	4
1.3 Elastic Muon-Proton Scattering	7
1.4 Inelastic Muon-Proton Scattering	8
1.4.1 F_1 and F_2 for Point Particles	11
1.5 Naive Quark Parton Model	12
1.5.1 Role of the Infinite Momentum Frame	13
1.6 Parton Distributions and F_2	14
1.7 The Sum Rules	16
1.7.1 The Gottfried Sum Rule	17
1.7.2 Adler Sum Rule	18
1.7.3 Gross-Llewellyn Smith Sum Rule	19
1.8 Theoretical Expectations for F_2	20
1.8.1 Regge model and Counting Rules	21
1.8.2 Proton Structure and QCD	22
1.9 Nuclear Environment and F_2	27
1.10 Physics Motivation to Measure the Structure Functions	29
1.11 Physics Processes where Structure Functions can be Measured	30
1.11.1 Muon and Neutrino Scattering Comparison	32
1.12 Present Experimental Status of F_2	32
1.12.1 Experimental Value of Gottfried Sum	33
1.13 Experimental Issues	35

1.13.1	Role of R in Extraction of F_2^n/F_2^p	35
1.13.2	Fermi Smearing	36
1.13.3	Nuclear Effects in Deuterium	37
1.13.4	Target Mass Corrections	38
1.13.5	Radiative Corrections	39
Chapter 2 Data Acquisition Hardware		43
2.1	Muon Beam	43
2.2	1987-88 Targets	47
2.3	Beam Tagging system	49
2.3.1	SBT Hodoscopes	49
2.3.2	PBT Chambers	49
2.3.3	Halo Veto System	50
2.4	Vertex Detector	50
2.4.1	PCV chambers	50
2.4.2	PTA Chambers	51
2.4.3	Streamer Chambers	51
2.5	Forward Tracking	52
2.5.1	PCN chambers	52
2.5.2	PCF chambers	53
2.5.3	DC chambers	53
2.5.4	PSA chambers	54
2.6	Muon Detection	54
2.6.1	SPM and SMS	54
2.6.2	PTM chambers	55
2.7	Particle ID and Calorimeter	55
2.8	Triggers	55
2.8.1	Large Angle Trigger	56
2.8.2	Small Angle Trigger	57
2.8.3	Random Beam trigger for LAT (RBEAM)	58
2.8.4	Random Beam for SAT (RSAT)	59
2.8.5	FCAL trigger	59

2.8.6	Halo Trigger	59
2.9	Data Acquisition System	59
2.9.1	Monitoring and Calibration	60
2.10	Data Set 1987-1988 run	61
Chapter 3 Data Analysis Software		64
3.1	Alignment	64
3.1.1	Coordinate System	65
3.1.2	Alignment Procedure	66
3.1.3	Analysis and Results	68
3.2	Pattern Recognition	72
3.2.1	Beam Spectrometer	72
3.2.2	Muon Projections	73
3.2.3	Forward Spectrometer	74
3.3	Track Fitting	79
3.3.1	Beam Track	80
3.3.2	Forward Spectrometer Tracks	80
3.3.3	Rescue Procedure	82
3.3.4	PCV Hunt Procedure	82
3.3.5	The Resolutions and Performance	82
3.4	Muon Match	86
3.4.1	Multiple Scattering Match	87
3.4.2	Intersection Match	87
3.4.3	Muon Match Performance	88
3.5	Vertex Program	89
3.5.1	Fitting Procedure	89
3.5.2	Muon-Muon Phase	93
3.5.3	Hadron Phase	94
3.5.4	Secondary Vertices	94
3.5.5	Vertex Output	94
3.5.6	Selection of Scattered Muon	94
3.5.7	Vertex Parameters	95

3.6	Detector Simulation	96
3.6.1	Monte Carlo Stage I	96
3.6.2	Monte Carlo Stage II	104
Chapter 4	Data Processing and Performance	106
4.1	Data Processing	106
4.1.1	The SPLIT Program	106
4.1.2	The LAT Filter Program	106
4.1.3	The SAT Filter Program	108
4.1.4	The PTMV Program	110
4.1.5	The Data Reduction Program	111
4.2	Beam Normalization	113
4.2.1	LAT Normalization	114
4.2.2	SAT Normalization	118
4.2.3	Estimate of Errors in Normalization	120
4.3	Momentum Calibration	122
4.4	Geometrical Acceptance of the Trigger	123
4.4.1	LAT Acceptance	126
4.4.2	SAT Acceptance	129
4.5	Trigger Efficiency	131
4.5.1	LAT Trigger Efficiency	131
4.5.2	SAT Trigger Efficiency	134
4.6	Detector Hardware Efficiency	137
4.7	Radiative Corrections	138
Chapter 5	Results and Conclusions	148
5.1	The Kinematic Region of E665 SAT Data	148
5.1.1	Muon-Electron Scattering background	150
5.1.2	Resolution	153
5.2	Empty Target Corrections	153
5.2.1	Empty target correction for SAT data	153
5.3	The μ Proton and μ Deuteron Scattering Cross Sections	154

5.4	Ratio of Neutron and Proton Structure Functions	157
5.4.1	Estimate of systematic errors for F_2^n/F_2^p	163
5.4.2	Comparison of F_2^n/F_2^p with other Experiments	165
5.5	Comparison of Event Yield with Previous Experiments	166
5.6	Evaluation of $F_2^p(x) - F_2^n(x)$ and Gottfried Sum	168
5.7	Conclusion	170
Bibliography		172
Appendix A PCF Chambers		178
A.1	Principle of Operation	178
A.1.1	Gas Mixture	179
A.2	Need for the PCF Chambers	180
A.3	Acceptance	180
A.4	Physical Construction	181
A.4.1	Location of Chambers	182
A.4.2	Gas System	182
A.5	Readout Electronics	182
A.6	Initial Tests and Efficiency	184
A.7	Computer Interface and Readout System	185
A.7.1	Online Monitoring	187
A.8	Performance During the 1987-88 Run	187
Appendix B Technical Detail of analysis		193



LIST OF FIGURES

1.1	One Photon exchange Feynman diagram for scattering of muon from a point particle	3
1.2	Deep Inelastic Scattering Diagram	8
1.3	QCD Leading Order Diagrams to DIS scattering	24
1.4	First Order QCD corrections Virtual diagrams	25
1.5	The ratio of nuclear structure function to the deuterium structure function	28
1.6	The Feynman diagrams for direct photon productions	31
1.7	The value of $R(x, Q^2)$ for a fit to world data	36
1.8	Q^2 variation of the F_2^n/F_2^p ratio	37
1.9	Leading and higher order electroweak radiative processes contributing to the observed deep inelastic cross section	42
2.1	E665 forward spectrometer 1987-88	44
2.2	Muon Beam Line at Fermilab	46
2.3	The track parameters of the LAT beam at the target	48
3.1	Residual plots for PBT Chambers Alignment	70
3.2	The $P(\chi^2)$ probability of the fitted tracks Monte Carlo	83
3.3	The difference between the generated and reconstructed track parameters of scattered muon tracks (SAT Monte Carlo)	84
3.4	The difference between the generated and reconstructed momenta for beam and scattered muon (SAT Monte Carlo)	85
3.5	The mismatch between Forward track and PTM projections	90
3.6	χ^2 of the match between PTM projection and forward tracks	91
3.7	The difference between the generated and reconstructed kinematics of the SAT Monte Carlo events	97

3.8	The mean difference between the generated and reconstructed kinematics as function of kinematic variable	98
3.9	The fractional resolution in x_{bj} , y_{bj} and Q^2 as function of x_{bj} , y_{bj} and Q^2	99
3.10	The difference in position of primary and $\mu\mu$ vertices	100
3.11	The quality of the vertex parameter for $\mu\mu$ and the primary vertex	101
3.12	The difference in event variables between Primary vertex and $\mu\mu$ vertex	102
4.1	Comparison between End-Of-Spill scalers and EVEnt Scalers . .	115
4.2	Pre Scale Factor for RBEAM data	116
4.3	Pre Scale Factor for RSAT data before correction	119
4.4	The comparison of RBEAM momenta as measured by Beam and Forward spectrometer	124
4.5	LAT acceptance as function of vertex position, θ and ϕ	127
4.6	LAT acceptance as function of x_{bj} and Q^2	128
4.7	SAT acceptance as function of vertex position, θ and ϕ	130
4.8	SAT acceptance as function of x_{bj} and Q^2	132
4.9	ϕ distribution of LAT events sample	133
4.10	Geometric properties of SAT Deep Inelastic Sample	136
4.11	The number of planes contributing to incident beam and scattered muon track	139
4.12	The reconstruction efficiency for SAT deuterium and hydrogen data	140
4.13	Radiative Corrections for different choice of Structure Functions .	143
4.14	Radiative Corrections to the D/H ratio	144
4.15	Different Contributions of Radiative Corrections	145
5.1	Kinematic distribution of the SAT deuterium events	149
5.2	The x_{bj} distribution of SAT events after DR selection	150
5.3	The ratio of muon-electron scattering events from deuterium and hydrogen data sets	151
5.4	Comparison of empty target data with SAT hydrogen data . . .	155

5.5	The double differential cross section ($\Delta\sigma/\Delta x\Delta Q^2$) for SAT deuterium data as a function of x_{bj}	158
5.6	The double differential cross section ($\Delta\sigma/\Delta x\Delta Q^2$) for SAT hydrogen data as a function of x_{bj}	159
5.7	The Q_2 distributions of SAT deuterium data for each x_{bj} bin	160
5.8	The Q_2 distributions of SAT hydrogen data for each x_{bj} bin	161
5.9	The ratio of neutron and proton structure functions for SAT data	162
5.10	Comparison of F_2^2/F_2^p from E665 with the results from other experiments	167
A.1	Efficiency as function of high voltage and trigger delay time	186
A.2	The wire spacing alignment: The residue as a function of distance perpendicular to the wire	189
A.3	The α alignment of PCF Chambers	190
A.4	PCF Efficiency during 1987-88 Deuterium Run	191

LIST OF TABLES

1.1	Leading order QCD splitting Functions	26
1.2	The experimental values for Gottfried sum	34
2.1	Raw Statistics per Spill for hydrogen	56
2.2	Raw Trigger Statistics for Deuterium (all)	62
2.3	Deuterium Raw Trigger Statistics (post Dec 1987)	62
2.4	Hydrogen Raw Trigger Statistics	63
3.1	The trigger and magnet setting for alignment	69
3.2	The difference in alignment constant from surveyed values	69
3.3	Reasons for Muon Match Failure in PTMV D LAT	88
3.4	Reasons for failure of the vertex fitting program for deuterium LAT data	96
4.1	The LAT Filter Program cuts.	107
4.2	The LAT Filter Statistics for deuterium.	108
4.3	The LAT Filter Statistics for hydrogen	109
4.4	The SAT Filter Statistics for deuterium	109
4.5	The SAT Filter Statistics for hydrogen	109
4.6	Data Reduction statistics for the LAT deuterium sample.	112
4.7	Data Reduction statistics for the SAT Hydrogen sample.	112
4.8	The event sample after the Data Reduction Program	113
4.9	The number of live muons deuterium for LAT sample	118
4.10	Fraction of RBEAM events LAT sample	118
4.11	The number of live muons deuterium	120
4.12	The number of live muons hydrogen	121
4.13	LAT trigger efficiency deuterium	134
4.14	LAT trigger efficiency hydrogen	134

4.15	SAT trigger efficiency deuterium	135
4.16	SAT trigger efficiency hydrogen	137
4.17	The magnitude of radiative corrections using Bardin code	146
4.18	The magnitude of radiative corrections using Mo-Tsai	147
5.1	The kinematic and geometrical requirements used for SAT data sample	152
5.2	The uncorrected beam flux used in 1987-88 running period	153
5.3	Kinematic cuts for the x_{bj} bins for SAT analysis	154
5.4	Raw Event Yield for SAT Deuterium data set	156
5.5	Raw Event Yield for SAT Hydrogen data set	156
5.6	Comparison of event yield from E665 SAT deuterium data with predictions calculated using different structure functions	168
5.7	Comparison of event yield from E665 SAT hydrogen data with predictions calculated using different structure functions	168
5.8	The difference in the proton and neutron structure functions and Gottfried sum	171
A.1	The PCF Efficiency for deuterium using SAT data	188
A.2	The PCF Efficiency for hydrogen using SAT data	192

ACKNOWLEDGMENTS

This dissertation would not have been possible without support and help of many individuals. The encouragement and guidance and confidence shown by Prof. H. J. Lubatti played a great role in my development as an experimentalist.

This experiment and analysis was a joint effort by all the individuals in the E665 collaboration and would not have been possible otherwise. I would like to thanks all of them and in particular Clive Halliwell, Hugh Montgomery, Tom Kirk, Don Geesaman Richard Nickerson, Steve Wolbers, Harry Melanson, Shuichi Kunori for their guidance and help.

During the years I spent in Muonlab building the detector and writing software, I had the company of Michael Schmitt, Silhacene Aid, Doug Jansen, Alex Salvarani, Uwe Ecker, John Ryan, Erik Ramberg, Steve Magill, Janet Conrad, Mark Baker and many other fellow students. Their company was both enjoyable and fruitful and I learned from all of them.

During my stay in this country I made a few friends. Without their help and support, life would have been quite different and very difficult. I would like to specially thank Jose Mustre de Leon, Doug Jansen, Janet Conrad and Sandra Campbell (I met them in that order). Sandra Campbell was one of the few sources of happiness during the difficult period of writing the dissertation.

And most important of all, I am grateful to my mother, who made me realize the importance of knowledge and hard work. I also appreciate the patience and courage she showed in raising me and the family.



Chapter 1

STRUCTURE OF NUCLEONS

Scattering experiments have been used as a tool to investigate the structure of the particles. At the beginning of this century the Rutherford experiment lead to the discovery of the nucleus in the atom. Later scattering experiments were used to measure the properties of the nucleons and nuclei. The nucleons, proton and neutron, were measured to have finite charge radii indicating that they are not truly elementary particles. In 1968, the classic SLAC-MIT experiment [1] showed that nucleons are made of point-like particles. These point particles were named partons by Feynman. Since then the deep inelastic scattering, scattering of high energy leptons from the constituents of the nucleons, has been used to measure the internal structure of nucleons. The internal structure is characterize in terms of structure functions which are related to the momentum distribution of partons in the nucleon.

In the SLAC-MIT experiment it was found that the structure functions (SF) were approximately independent of the momentum transferred in the interaction (scaling). The scaling behaviour had been predicted by Bjorken in the high energy limit [2]. He argued that at very high energies, masses of the particles involved in the interaction become irrelevant and therefore the structure of proton can depend on dimensionless variables only. The results of the SLAC-MIT experiment were explained by Feynman in terms of parton model. In this model it is assumed that the proton is made of point particles which are almost free during interaction. Later on it was found that the scaling is not exact and the structure functions vary logarithmically as a function of Q^2 , the square of momentum transferred in the interaction. The Q^2 dependence can be explained by the gauge theory of strong interactions, quantum chromodynamics (QCD).

In this chapter the basic formulation of deep inelastic scattering and quark parton model are described. The behaviour of the SF's as a function of x_b and Q^2 is discussed. The relations between different structure functions and the sum

rules are also described. In the last section the issues relating the extraction of SF's from the experimental data are discussed.

Even though the aim of this analysis is to measure the ratio of the neutron to proton structure function as a function of x_{bj} , some general aspects of the deep inelastic scattering, present experimental status of the absolute structure functions and the effect of nuclear environment on the parton distribution are also discussed.

After defining the variables in section 1.1, the electromagnetic scattering cross section of two point particles is evaluated in section 1.2. The high energy limit of the cross section is expressed in terms of Mandelstam variables. Using this limiting expression, it is easy to relate the lepton kinematics to the parton distributions in nucleon.

The elastic form factors for the proton are discussed in section 1.3. The structure functions F_1 and F_2 are defined in section 1.4 and their functional form in the quark parton model is given in section 1.5.

The sum rules are derived within the scope of quark-parton model in section (1.7). The evolution of the structure functions and the corrections to sum rules due to QCD are also discussed.

In last section the QED radiative corrections, the target mass effect and the nuclear binding effects on the deuteron are discussed.

1.1 Definition of the variables

The lowest order electromagnetic interaction between a muon and a spin-1/2 point particle can be represented by Feynman diagram shown in Fig. 1.1. A virtual photon of 4 momentum q is exchanged between the incoming muon (k) and the target (p). The 4-momenta of the target (p), incident muon (k), outgoing muon (k'), photon exchanged (q) and the final hadronic system (p') can be written as :

$$\left. \begin{array}{l} p = (E_p, \mathbf{p}) \\ k = (E, \mathbf{k}) \\ k' = (E', \mathbf{k}') \\ q = k - k' \\ p' = p + q \end{array} \right\} \quad (1.1)$$

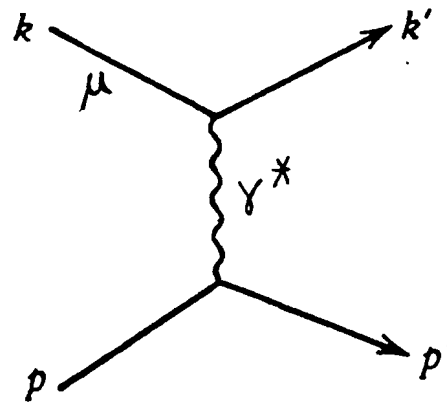


Figure 1.1: One Photon exchange Feynman diagram for scattering of muon from a point particle

In the rest frame of the target, the laboratory frame, its 4-momentum is $(M, \mathbf{0})$ and $q = (\nu, \mathbf{q})$ where

$$\nu = E - E' \quad \mathbf{q} = \mathbf{k} - \mathbf{k}' \quad (1.2)$$

If we neglect the mass of the muon, the momentum transferred square in the laboratory frame is given by

$$q^2 = -4EE' \sin^2 \frac{\theta}{2} \quad (1.3)$$

where θ is the scattering angle in the laboratory frame.

In deep inelastic scattering, q^2 , the mass square of the virtual photon is space-like (negative) and it is common to define a positive definite variable Q^2 equal to $-q^2$. We define two dimensionless Lorentz scalars x_{bj} and y_{bj} :

$$x_{bj} = \frac{Q^2}{2 p \cdot q} = \frac{Q^2}{2M\nu} \quad (1.4)$$

$$y_{bj} = \frac{p \cdot q}{p \cdot k} = \frac{\nu}{E} \quad (1.5)$$

In the extreme relativistic regime, the masses of particles involved in the scattering can be neglected except, perhaps, at very small Q^2 . In this limit the Mandelstam

variables are

$$\left. \begin{aligned} s &\equiv (p+k)^2 \simeq 2k \cdot p \simeq 2k' \cdot p' = 2ME \\ u &\equiv (k'-p)^2 \simeq -2k' \cdot p \simeq -2k \cdot p' = -2ME' \\ t &\equiv (k-k')^2 \simeq -2k \cdot k' \simeq -2p \cdot p' = 4EE' \sin^2 \frac{\theta}{2} \end{aligned} \right\} \quad (1.6)$$

where $p^2 = p'^2 = M^2 = 0$ and $k^2 = k'^2 = m^2 = 0$ have been used. The last column gives the values in the laboratory frame. The phase space factor $d^3 k' / 2E'$ is

$$\frac{d^3 k'}{2E'} = \frac{1}{2} E' dE' d\Omega \quad (1.7)$$

$$= \frac{\pi}{2s} du dt. \quad (1.8)$$

The variable ν expressed in Mandelstam variables is

$$\nu \equiv \frac{p \cdot q}{M} = \frac{2p \cdot k - 2p \cdot k'}{2M} = \frac{s+u}{2M}. \quad (1.9)$$

1.2 Scattering of two Dirac particles

The scattering cross section of two particles can be written as [4]

$$d\sigma = \left[\frac{1}{4((k \cdot p)^2 - m^2 M^2)^{\frac{1}{2}}} \right] \frac{|\mathcal{M}|^2}{4\pi^2} \left\{ \frac{d^3 k'}{2E} \frac{d^3 p'}{2p'_0} \delta^{(4)}(p+k-p'-k') \right\} \quad (1.10)$$

where the first term is the flux factor and the last one is the phase space factor. The physics of the interaction is described by $|\mathcal{M}|^2$, the matrix element square. Using the identity

$$\int \frac{d^3 p'}{2p'_0} \delta^{(4)}(p+q-p') = \delta(2p \cdot q + q^2) \quad (1.11)$$

we get

$$d\sigma = \frac{1}{4((k \cdot p)^2 - m^2 M^2)^{\frac{1}{2}}} \frac{|\mathcal{M}|^2}{4\pi^2} \frac{d^3 k'}{2E'} \delta(2p \cdot q + q^2) \quad (1.12)$$

$$= \frac{1}{4((k \cdot p)^2 - m^2 M^2)^{\frac{1}{2}}} \frac{|\mathcal{M}|^2}{4\pi^2} \frac{\pi}{4s} du dt \delta(2p \cdot q + q^2) \quad (1.13)$$

$$= \frac{1}{(2E)(2M)} \frac{|\mathcal{M}|^2}{4\pi^2} \frac{1}{2} E' dE' d\Omega \delta(2M\nu + q^2). \quad (1.14)$$

The double differential cross section for the scattering of two point particles in the laboratory frame is

$$\frac{d\sigma}{dE'd\Omega} = \frac{1}{4ME} \frac{|\mathcal{M}|^2}{4\pi^2} \frac{E'}{2} \delta(2M\nu + q^2) \quad (1.15)$$

where $|\mathcal{M}|^2$ is the invariant amplitude squared where initial spin states have been average and final spin states have been summed. The lowest order matrix element \mathcal{M} for interaction of two Dirac particles via quantum electrodynamics is

$$\mathcal{M} = -e^2 \bar{u}(k') \gamma^\mu u(k) \frac{1}{q^2} \bar{u}(p') \gamma_\mu u(p) \quad (1.16)$$

where $u(k)$ and $u(p)$ are the Dirac spinors for two point particles. Let us consider the two point particle to be the muon and point-proton. The point-proton is an idealized particle with no spacial extension but has the same quantum numbers and the mass as the physical proton. The invariant amplitude squared can be written as :

$$|\mathcal{M}|^2 = \frac{e^4}{q^4} L^{\mu\nu} L_{\mu\nu}^p \quad (1.17)$$

where

$$L^{\mu\nu} = \frac{1}{2} \sum_{\mu \text{ spin}} [\bar{u}(k') \gamma^\mu u(k)] [\bar{u}(k) \gamma^\nu u(k')]^* \quad (1.18)$$

is the spin-averaged lepton tensor. A similar expression describes $L_{\mu\nu}^p$. The $L^{\mu\nu}$ can be evaluated using the trace theorems and the result is

$$L^{\mu\nu} = \frac{1}{2} \sum_{s'} \bar{u}_\alpha^{(s')}(k') \gamma^\mu_{\alpha\beta} \sum_s u_\beta^{(s)}(k) \bar{u}_\gamma^{(s)}(k) \gamma^\nu_{\gamma\delta} u_\delta^{(s')}(k') \quad (1.19)$$

$$= 2 \left\{ k'^\mu k^\nu + k'^\nu k^\mu - (k \cdot k' - m^2) g^{\mu\nu} \right\} \quad (1.20)$$

where m is the muon mass. Similarly the $L_{\mu\nu}^p$ is given by

$$L_{\mu\nu}^p = 2 \left\{ p'_\mu p_\nu + p'_\nu p_\mu - (p' \cdot p - M^2) g_{\mu\nu} \right\} \quad (1.21)$$

where M is the mass of the proton. From the above equation the exact spin-averaged $\mu p \rightarrow \mu p$ amplitude is

$$|\mathcal{M}|^2 = \frac{8e^4}{q^4} \left\{ (k' \cdot p')(k \cdot p) + (k' \cdot p)(k \cdot p') - m^2 p' \cdot p - M^2 k' \cdot k + 2m^2 M^2 \right\}. \quad (1.22)$$

In the extreme relativistic limit, the mass of the muon and proton can be neglected and the amplitude squared reduces to

$$\overline{|\mathcal{M}|^2} = \frac{8e^4}{q^4} \{(k' \cdot p')(k \cdot p) + (k' \cdot p)(k \cdot p')\}. \quad (1.23)$$

The $\overline{|\mathcal{M}|^2}$ expressed in terms of the variables defined in equation (1.6) is

$$2e^4 \frac{s^2 + u^2}{t^2} \quad (1.24)$$

and the cross section (equation 1.12) is reduced to

$$\left[\frac{d\sigma}{dt du} \right] = \frac{2\pi\alpha^2}{t^2} \left(\frac{s^2 + u^2}{s^2} \right) \delta(t + s + u). \quad (1.25)$$

The equation (1.25) will be used in section 1.5 to relate the muon vertex kinematics with the properties of the partons in the nucleon.

Let us calculate the cross section in the laboratory frame. The laboratory cross section will be useful in comparing the hadronic structure function with point particle structure functions in section 1.4.1. If we only neglect the mass of muon, the amplitude squared (1.22) can be written as

$$\overline{|\mathcal{M}|^2} = \frac{8e^4}{q^4} \left\{ -\frac{1}{2}q^2(k \cdot p - k' \cdot p) + 2(k' \cdot p)(k \cdot p) + \frac{1}{2}M^2q^2 \right\}. \quad (1.26)$$

where $k'^2 = k^2 \simeq 0$ and $q^2 = -2k' \cdot k$ have been used. In the laboratory frame where the proton is at rest the above equation reduces to

$$\overline{|\mathcal{M}|^2} = \frac{8e^4}{q^4} 2M^2 E E' \left[\cos^2 \frac{\theta}{2} - \frac{q^2}{2M^2} \sin^2 \frac{\theta}{2} \right]. \quad (1.27)$$

Using equations (1.15) and (1.27) one can write the differential cross section as

$$\frac{d^2\sigma}{dE' d\Omega} = \frac{(2\alpha E')^2}{q^4} \left[\cos^2 \frac{\theta}{2} - \frac{q^2}{2M^2} \sin^2 \frac{\theta}{2} \right] \delta \left(\nu + \frac{q^2}{2M} \right) \quad (1.28)$$

and integrating over the δ function, the angular distribution of scattered muon is given by

$$\frac{d\sigma}{d\Omega} = \left[\frac{\alpha^2}{4E^2 \sin^4 \frac{\theta}{2}} \right] \frac{E'}{E} \left[\cos^2 \frac{\theta}{2} - \frac{q^2}{2M^2} \sin^2 \frac{\theta}{2} \right]. \quad (1.29)$$

1.3 . Elastic Muon-Proton Scattering

For equation (1.29) the proton was assumed to be a point particle whereas the physical proton has a non-zero size in space and, therefore, the electromagnetic current of a real proton can not be described by Dirac spinors. The current should describe the spacial extension of the proton. The most general vector current J^μ which conserves parity is

$$J^\mu = \left[F_1(q^2) \gamma^\mu + \frac{\kappa}{2M} F_2(q^2) i\sigma^{\mu\nu} q_\nu \right] \quad (1.30)$$

where F_1 and F_2 are functions of the Lorentz scalar q^2 only. The constant κ , the anomalous magnetic moment, is to be determined by experiment.

Using the expression for J^μ the muon-proton elastic scattering cross section in the laboratory frame is

$$\frac{d\sigma}{d\Omega} = \left[\frac{\alpha^2}{4E^2 \sin^4 \frac{\theta}{2}} \right] \frac{E'}{E} \left\{ \left(F_1^2 - \frac{\kappa^2 q^2}{4M^2} F_2^2 \right) \cos^2 \frac{\theta}{2} - \frac{q^2}{2M^2} (F_1 + \kappa F_2)^2 \sin^2 \frac{\theta}{2} \right\}. \quad (1.31)$$

Linear combinations of F_1 and F_2 can be defined as:

$$G_E \equiv F_1 + \frac{\kappa q^2}{4M^2} F_2 \quad G_M \equiv F_1 + \kappa F_2 \quad (1.32)$$

Then the cross section takes the form

$$\frac{d\sigma}{d\Omega} = \left[\frac{\alpha^2}{4E^2 \sin^4 \frac{\theta}{2}} \right] \frac{E'}{E} \left(\frac{G_E^2 + \tau G_M^2}{1 + \tau} \cos^2 \frac{\theta}{2} + 2\tau G_M^2 \sin^2 \frac{\theta}{2} \right) \quad (1.33)$$

where $\tau \equiv -q^2/2M^2$. The G_E and G_M are called the electric and magnetic form factors of the proton. These form factors can be related to the electric charge and magnetic moment of the proton in a frame where $\mathbf{p} = -\mathbf{p}'$. The angular distribution of lepton-proton elastic scattering events can be used to separate the two form factors. The experimental data suggests that

$$G_E(q^2) \approx \left(1 - \frac{q^2 (\text{GeV}^2)}{0.71} \right)^{-2}. \quad (1.34)$$

which correspond to a mean square charge radius for the proton of $(0.81 \times 10^{-13} \text{cm})^2$ or 6.56 millibarn. $G_M(q^2)$ also has the same functional dependence. This functional form is measured to be valid at least up to Q^2 of 25 GeV 2 .

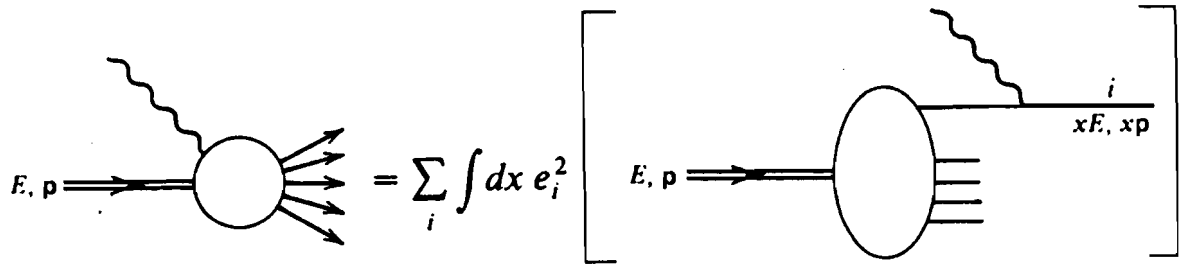


Figure 1.2: Deep Inelastic Scattering Diagram

1.4 Inelastic Muon-Proton Scattering

If the energy transferred during muon proton scattering is large enough, the proton breaks up and the final state is a complex system consisting of many particles. In analogy with equation (1.17) the expression for the invariant amplitude squared is

$$|\mathcal{M}^2| \sim L^{\mu\nu} W_{\mu\nu} \quad (1.35)$$

where $L^{\mu\nu}$ describes the leptonic tensor and is given by (1.20). The exact form of hadronic tensor $W_{\mu\nu}$ is unknown but we can construct it from available 4-vectors and tensors based on general principles. The available elements are the metric tensor $g_{\mu\nu}$ and two independent vectors p_μ and q_μ . The vector γ_μ is not included as $W_{\mu\nu}$ is already summed and averaged over the spins. The parity even hadronic tensor is

$$W_{\mu\nu} = -W_1 g_{\mu\nu} + \frac{W_2}{M^2} p_\mu p_\nu + \frac{W_4}{M^2} q_\mu q_\nu + \frac{W_5}{M^2} (p_\mu q_\nu + q_\mu p_\nu). \quad (1.36)$$

The antisymmetric combination $(p_\mu q_\nu - q_\mu p_\nu)$ is not included here because it does not contribute when contracted with the symmetric leptonic tensor. The functions

W_i depend only on the Lorentz scalars which can be constructed from the Lorentz vectors at the hadronic vertex (p_μ, q_μ) . The factor of M in the denominator is added so that all the W_i 's have the same dimensions [mass]. There are, in general, only two independent variables in the deep inelastic scattering. A common choice of variables is

$$q^2 \quad \text{and} \quad \nu \equiv \frac{p \cdot q}{M}. \quad (1.37)$$

Current conservation at the hadronic vertex requires that

$$q^\mu W_{\mu\nu} = q^\nu W_{\mu\nu} = 0. \quad (1.38)$$

Using (1.38) two of the structure functions can be eliminated and the hadronic tensor can be expressed as

$$W_{\mu\nu} = W_1 \left(-g_{\mu\nu} + \frac{q_\mu q_\nu}{q^2} \right) + \frac{W_2}{M^2} \left(p_\mu - \frac{p \cdot q}{q^2} q_\mu \right) \left(p_\nu - \frac{p \cdot q}{q^2} q_\nu \right). \quad (1.39)$$

Contracting hadronic and leptonic tensors we get

$$L^{\mu\nu} W_{\mu\nu} = 4W_1(k \cdot k') + \frac{2W_2}{M^2} [2(p \cdot k)(p \cdot k') - M^2 k \cdot k'] \quad (1.40)$$

Defining ¹ $F_1 = MW_1$ and $F_2 = \nu W_2$ equation 1.40 can be written as

$$L^{\mu\nu} W_{\mu\nu} = 4 \frac{F_1}{M} (k \cdot k') + \frac{2F_2}{\nu M^2} [2(p \cdot k)(p \cdot k') - M^2 k \cdot k'] \quad (1.41)$$

If we neglect the mass of proton and use Mandelstam variables, equation (1.41) can be written as :

$$L^{\mu\nu} W_{\mu\nu} = -\frac{2t}{M} F_1 - \frac{su}{\nu M^2} F_2 \quad (1.42)$$

Using

$$-\frac{t}{s+u} = \frac{Q^2}{2M\nu} = x \quad (1.43)$$

$$-t = x(s+u) \quad (1.44)$$

¹ In the literature this association is made only in the Bjorken limit i.e. when $\nu \rightarrow \infty$, $Q^2 \rightarrow \infty$ but $\frac{Q^2}{2M\nu}$ is finite

and equation (1.9) we can write

$$L^{\mu\nu}W_{\mu\nu} = 2x(s+u)\frac{F_1}{M} - us\frac{2F_2}{M(s+u)} \quad (1.45)$$

$$= \frac{2}{M(s+u)} [(s+u)^2 x F_1 - us F_2] \quad (1.46)$$

The cross section is given by

$$d\sigma = \frac{1}{4((k.p)^2 - m^2 M^2)^{\frac{1}{2}}} \left[\frac{e^4}{q^4} L^{\mu\nu} W_{\mu\nu} \right] \frac{d^3 k'}{2E'(2\pi)^3} \quad (1.47)$$

can be written as

$$\left(\frac{d\sigma}{dtdu} \right) = \frac{4\pi\alpha^2}{t^2 s^2} \frac{1}{s+u} \left\{ (s+u)^2 x F_1 - us F_2 \right\}. \quad (1.48)$$

In the laboratory frame $L^{\mu\nu}W_{\mu\nu}$ can be written as

$$4EE' \left[\cos^2 \frac{\theta}{2} \frac{F_2(\nu, q^2)}{\nu} + \sin^2 \frac{\theta}{2} 2 \frac{F_1(\nu, q^2)}{M} \right] \quad (1.49)$$

and the cross section in the laboratory frame is equal to

$$\frac{d\sigma}{dE'd\Omega} = \frac{\alpha^2}{4E^2 \sin^4 \frac{\theta}{2}} \left[\frac{F_2(\nu, q^2)}{\nu} \cos^2 \frac{\theta}{2} + 2 \frac{F_1(\nu, q^2)}{M} \sin^2 \frac{\theta}{2} \right]. \quad (1.50)$$

As the QED vertex is well understood theoretically, deep inelastic scattering is sometimes described in terms of virtual photon-proton scattering. The scattering of the photon can be decomposed in terms of different polarization components of the photon. Each helicity of the photon couples to a definite helicity state of the target. As opposed to a real photon, the virtual photon has both longitudinal and transverse polarizations.

It is customary to define a variable $F_L(x, Q^2)$ as the linear combination of the $F_1(x, Q^2)$ and $F_2(x, Q^2)$ which couples to a longitudinally polarized photon. The longitudinal structure function $F_L(x, Q^2)$ is given by

$$F_L(x, Q^2) = \left\{ \left(1 + \frac{4M^2 x^2}{Q^2} \right) F_2(x, Q^2) - 2x F_1(x, Q^2) \right\}. \quad (1.51)$$

The ratio of the longitudinal and transverse structure functions, $R(x, Q^2)$, is

$$R(x, Q^2) = F_L(x, Q^2)/2xF_1(x, Q^2) \quad (1.52)$$

which approaches zero at very large momentum transfer Q^2 if the Callan-Gross relation is satisfied.

The naive parton model predicts $R = 0$ as long as the transverse mass of the parton can be neglected. If partons have intrinsic transverse momenta k_t , R is given by [3]

$$R = \frac{4(\langle k_t^2 \rangle + m_q^2)}{Q^2} \quad (1.53)$$

where m_q is the mass of the parton. Experimentally intrinsic k_t is inferred to be ~ 0.4 GeV on average. The value of R may not be negligible at very low Q^2 .

1.4.1 F_1 and F_2 for point particles

Comparing equation (1.50) and (1.28) we can write

$$2F_1^{point} = \frac{Q^2}{2M\nu} \delta\left(1 - \frac{Q^2}{2M\nu}\right) \quad \text{and} \quad F_2^{point} = \delta\left(1 - \frac{Q^2}{2M\nu}\right). \quad (1.54)$$

1.5 Naive Quark Parton Model

In naive quark parton model (QPM), the proton is considered to be a collection of many Dirac point particles. The basic assumption in this model is that these particles interact with the virtual photon independently of each other in deep inelastic scattering. Then the total cross section is an incoherent sum of the individual parton contributions.

Let parton i with charge e_i have 4-momentum p_i and let p be the 4-momentum of the proton. Then momentum fraction x , carried by i th parton, is

$$x = \frac{p_i}{p} \quad (1.55)$$

Let $f_i(x)$ be the probability density of finding parton i with momentum fraction x . In the naive parton model this probability depends only on x as there are no

other variables in the problem. In the QPM the cross section $\mu p \rightarrow \mu X$ can be written as

$$(\text{cross section})_{\text{proton}} = \sum_i \int dx f_i(x) (\text{cross section})_i \quad (1.56)$$

where the sum i is over all types of partons.

The cross section for a muon scattering from a parton is the same as that of a muon scattering of a point-proton provided charge, mass and all the kinematic factors are replaced by appropriate values. It is assumed here that all the charged partons in a proton are spin-1/2 point particles. Let e_i be the charge of the parton i in units of proton charge (e). The Mandelstam variables at the parton level are given by

$$\left. \begin{array}{lcl} \hat{s} &= (k + xp)^2 &= 2xk \cdot p &= xs \\ \hat{u} &= (k' - xp)^2 &= -2xk' \cdot p &= xu \\ \hat{t} &= (k - k')^2 &= -2k \cdot k' &= t \end{array} \right\} \quad (1.57)$$

Using (1.57) in equation (1.25), the contribution to the $\mu p \rightarrow \mu X$ cross section from the muon-parton scattering is

$$\begin{aligned} (\text{cross section})_i &= \left(\frac{d\sigma}{dt du} \right)_{\mu q \rightarrow \mu q} = x \frac{d\sigma}{d\hat{t} d\hat{u}} \\ &= x \frac{2\pi\alpha^2 e_i^2}{t^2} \left(\frac{s^2 + u^2}{s^2} \right) \delta(t + x(s + u)). \end{aligned} \quad (1.58)$$

The total muon-proton cross section is

$$\left(\frac{d\sigma}{dt du} \right)_{\mu p \rightarrow \mu X} = \sum_i \int dx f_i(x) x \frac{2\pi\alpha^2 e_i^2}{t^2} \left(\frac{s^2 + u^2}{s^2} \right) \delta(t + x(s + u)). \quad (1.59)$$

Comparing (1.59) and (1.48) we get

$$2x F_1(x) = F_2(x) = x \sum_i e_i^2 f_i(x) \quad (1.60)$$

We see that $F_1(x)$ and $F_2(x)$ are functions of only the momentum fraction x which is fixed by delta function in equation (1.59) :

$$x = \frac{-t}{s + u} = \frac{Q^2}{2(p \cdot k - p \cdot k')} = \frac{Q^2}{2p \cdot q} = \frac{Q^2}{2M\nu} \quad (1.61)$$

This implies that in the quark-parton model the momentum fraction carried by partons is completely defined in terms of the lepton variables. Therefore the momentum fraction distribution of the partons can be measured in the deep inelastic lepton-nucleon scattering.

1.5.1 Role of infinite momentum frame

The relation $p_i = xP$ is a strange equation [4]. It is a 4 momentum relation where x varies between 0 and 1 but clearly the mass of a particle is not variable. The equality is exact only if $m = M = 0$. This condition is realized by boosting the whole system to the infinite momentum frame (IMF) where the proton is moving very fast. In such a frame all the masses and the transverse momenta associated with the particles involved in the interaction can be neglected. In the IMF, the interaction time between different partons is dilated and the partons in a nucleon appear to be non interacting during scattering [3]. This implies that a parton interacts with the external probe independently of the other partons around it and hence the assumption that the total cross section is an incoherent sum of all the contributions from individual partons is valid.

The struck and the spectator partons change into observable hadrons with unit probability. The hadronization is also assumed to be independent of the initial collision. In the laboratory frame, the time of interaction between the muon and parton is $\sim 1/\nu$ whereas the time of hadronization is $\sim 1/M$ where M is the mass of the proton [5]. The hadronization time scale is much larger than the interaction time.

This QPM picture is valid when both the mass Q of the virtual photon and the invariant mass W of the final-state hadronic system are large. Large Q^2 ensures that the resolving power of the incoming photon is small enough to see individual partons in the proton. Large W or energy transfer ν means that the final state hadronization is on a time scale much larger than the interaction time [6]. The interaction time is not a Lorentz invariant concept but it gives us a good classical intuitive picture of deep inelastic scattering.

The above explanation of the deep inelastic scattering depends on the reference frame use. It is easier to understand certain phenomena in a particular frame of reference because the wave function in that frame is simple. The formulation is

Lorentz invariant and therefore is true in any frame but the interpretation is frame dependent.

The success of the quark-parton model in explaining the experimental data justify the assumptions of the quark parton model. These assumptions arise naturally in asymptotically free theories like QCD.

1.6 Parton distributions and F_2

The charged partons in the nucleon can be identified with quarks of the static quark model with a few differences. In the static quark model, the proton is made up of uud and the neutron is made of udd quarks. The static quark model is very successful in explaining the various quantum numbers, spin-parity assignment, magnetic moment, multiplet structure and the mass splitting of hadrons. The quarks in the static quark model, called constituent quarks, have finite masses whereas their masses in the QPM are explicitly assumed to be zero. The quarks in the QPM are called current quarks. On the length scale of the nucleon, the constituent quarks can be considered as current quarks along with the energy stored in the gluon field around them [7] but this relationship is not very well defined. The nucleons are made of fixed number of quarks in static quark model but the number of quarks is variable in QPM. The quarks in the QPM which correspond to those in the static quark model are called valence quarks. The additional $q\bar{q}$ pairs in the QPM are called sea quarks.

Identifying the charged partons with quarks, the electromagnetic structure functions $F^{\mu p}$ and $F^{\mu n}$ is given by :

$$\frac{1}{x} F_2^{\mu p}(x) = e_u^2 [u^p(x) + \bar{u}^p(x)] + e_d^2 [d^p(x) + \bar{d}^p(x)] + e_s^2 [s^p(x) + \bar{s}^p(x)] \quad (1.62)$$

$$\frac{1}{x} F_2^{\mu n}(x) = e_u^2 [u^n(x) + \bar{u}^n(x)] + e_d^2 [d^n(x) + \bar{d}^n(x)] + e_s^2 [s^n(x) + \bar{s}^n(x)] \quad (1.63)$$

Here the contributions from heavy flavor quarks to structure functions of the nucleons have been ignored. The e_u , e_d , e_s are the electric charge of up (u), down (d) and strange (s) quark respectively. Using isospin invariance and assuming the

strange quark component in the proton and neutron is the same i.e.

$$\left. \begin{aligned} u^p(x) &= d^n(x) \equiv u(x) \\ d^p(x) &= u^n(x) \equiv d(x) \\ s^p(x) &= s^n(x) \equiv s(x) \end{aligned} \right\} \quad (1.64)$$

the structure functions can be written as

$$\frac{1}{x} F_2^{\mu p}(x) = \frac{4}{9} [u(x) + \bar{u}(x)] + \frac{1}{9} [d(x) + \bar{d}(x)] + \frac{1}{9} [s(x) + \bar{s}(x)] \quad (1.65)$$

$$\frac{1}{x} F_2^{\mu n}(x) = \frac{4}{9} [d(x) + \bar{d}(x)] + \frac{1}{9} [u(x) + \bar{u}(x)] + \frac{1}{9} [s(x) + \bar{s}(x)] \quad (1.66)$$

Under these assumptions the ratio $F^{\mu n}(x)/F^{\mu p}(x)$ is given by

$$\frac{[u(x) + \bar{u}(x)] + 4 [d(x) + \bar{d}(x)] + [s(x) + \bar{s}(x)]}{4 [u(x) + \bar{u}(x)] + [d(x) + \bar{d}(x)] + [s(x) + \bar{s}(x)]} \quad (1.67)$$

which has a lower (upper) limit of 1/4 (4) if only u (d) quark are present in the proton. The relationship (1.67) is true at all x_{bj} . In particular it is also true at $x_{bj} \sim 1$ where the up quark is expected to have a dominant contribution to the proton structure function. Hence as $x_{bj} \rightarrow 1$, the ratio should approach 0.25.

As described above the proton consists of three valence quarks (uud) in the static quark model. Let $u_s(x)$ and $d_s(x)$ be the up and down quark density distributions arising from the sea, then valence quark distributions by definition are given by

$$\left. \begin{aligned} u_v(x) &\equiv u(x) - u_s(x) \\ d_v(x) &\equiv d(x) - d_s(x) \end{aligned} \right\} \quad (1.68)$$

Let us define the total contribution to the proton $F_2(x, Q^2)$ from the sea quarks be $xS^p(x)$

$$xS^p(x) = x \sum_i e_i^2 S_i^p(x) \quad (1.69)$$

where $S_i^p(x)$ is the sea quark distribution of flavour i with charge e_i . The structure functions for the proton and neutron take the simple form

$$\frac{1}{x} F_2^{\mu p}(x) = \frac{1}{9} [4u_v(x) + d_v(x)] + S^p(x) \quad (1.70)$$

$$\frac{1}{x} F_2^{\mu n}(x) = \frac{1}{9} [u_v(x) + 4d_v(x)] + S^n(x) \quad (1.71)$$

where $S^n(x)$ is defined for neutrons in the same manner as (1.69). Thus the ratio $F_2^{en}(x)/F_2^{ep}(x)$ is given by

$$\frac{u_v(x) + 4d_v(x) + S^p(x)}{4u_v(x) + d_v(x) + S^n(x)}. \quad (1.72)$$

At low x_{bj} , most of the contribution to structure functions comes from the sea quarks. If the sea quarks contribute to the proton by the same amount as they do to the neutron, above ratio is expected to become unity as $x_{bj} \rightarrow 0$.

The d_v/u_v ratio is measured in a neutrino experiment [8]. The ratio varies from 0.306 ± 0.107 to 0.169 ± 0.018 over the x_{bj} range of 0.1 to 0.7 indicating that the up-valence quarks dominate at high x_{bj} .

1.7 The Sum Rules

Based on isospin symmetry and general assumptions about the hadronic current structure, some relations (sum rules) between the structure functions can be derived. Originally derived on the basis of commutation relations between hadronic currents and the dispersion equation, the sum rules have a simple explanation within the frame work of the quark-parton model. There are three main sum rules, i) Gottfried, ii) Adler and iii) Llewellyn Smith, which are related to deep inelastic scattering on unpolarized targets. The Gottfried sum can be evaluated in charged lepton scattering experiments whereas the other two can be evaluated only from neutrino scattering data. The Adler and Llewellyn Smith sum rules are described here for completeness.

1.7.1 The Gottfried Sum Rule

The Gottfried Sum rule was originally stated [9] as

$$I_G = \int_0^\infty d\nu W_2(Q^2, \nu) = \int_0^1 \frac{dx}{x} F_2(x, Q^2) \quad (1.73)$$

$$= (2\pi)^3 \int d^3r e^{-i\mathbf{Q}\cdot\mathbf{r}} \langle \rho(r) \rho(0) \rangle_\infty \quad (1.74)$$

The $\langle \dots \rangle$ refers to spin-averaged quantity and the subscript ∞ denotes a frame where the proton has very large momentum (IMF).

Equation (1.74) was derived for the static quark model where it was assumed that the hadronic Hamiltonian is $SU(2)$ invariant and therefore unchanged under a permutation of any pair of $S=0$ quarks. The integral is evaluated at fixed Q^2 . The charge density (ρ) correlation is given by

$$\langle \rho(x)\rho(0) \rangle = \sum_i e_i^2 \langle \sigma(r_i - x)\sigma(r_i) \rangle + \sum_{i \neq j} e_i e_j \langle \sigma(r_i - x)\sigma(r_j) \rangle \quad (1.75)$$

where $\sigma(r_i)$ is the probability density of i th finding quark at point r_i . The invariance of the hamiltonian under exchange of quarks leads to

$$\langle \sigma(r_1 - x)\sigma(r_1) \rangle = \langle \sigma(r_2 - x)\sigma(r_2) \rangle. \quad (1.76)$$

The two point correlation function is given by

$$\langle \sigma(r_i - x)\sigma(r_j) \rangle = \langle \sigma(r_1 - x)\sigma(r_2) \rangle \quad (1.77)$$

Using the explicit charge assignment of quarks in static quark model the sum rules for the proton and neutron are

$$I_G^p = 1 \quad (1.78)$$

$$I_G^n = \frac{2}{3}(2\pi)^{-3} \{ \langle \sigma(r_1 - x)\sigma(r_1) \rangle - \langle \sigma(r_1 - x)\sigma(r_2) \rangle \} \quad (1.79)$$

If quarks distributions are totally uncorrelated, the spin averaged two point correlation function (1.77) is zero. Then the difference in the Gottfried sum of the proton and the neutron is

$$I_G^{p-n} = 1/3 \quad (1.80)$$

In the frame work of quark-parton model, built on the assumption that all the quarks contribute *incoherently* to the cross section, the Gottfried sum rule has a simpler derivation. The I_G^{p-n} can be written as

$$I_G^{p-n} = \int_0^1 \frac{dx}{x} \{ F_2^p(x, Q^2) - F_2^n(x, Q^2) \} \quad (1.81)$$

$$= \int_0^1 dx \left\{ [e_u^2 u_v^p(x) + e_d^2 d_v^p(x) + \sum_i e_i^2 S_i^p(x)] - [e_u^2 u_v^n(x) + e_d^2 d_v^n(x) + \sum_i e_i^2 S_i^n(x)] \right\} \quad (1.82)$$

Assuming the contribution from the sea quarks is the same for proton and neutron, we get I_G^{p-n} equal to 1/3. Dynamic effects do not modify this sum rule as long as the effects are the same for the proton and neutron. The Gottfried sum rule is a statement about the net flavour and charge assignment of quarks in nucleons.

Another way to state the Gottfried sum rule is [10]

$$I_G^{p-n}(x) = \frac{1}{3} \int_x^1 \{u_v(x') - d_v(x')\} dx' + \frac{2}{3} \int_x^1 \{\bar{u}(x') - \bar{d}(x')\} dx' \quad (1.83)$$

This follows from the naive quark parton model under the assumption that the density of $\bar{u}(x)$ in the proton is equal to $\bar{d}(x)$ in the neutron and vice versa. The strange quark contribution for the neutron and proton is also assumed to be equal. If the sea quark contribution in the proton (neutron) is isospin invariant i.e.

$$\bar{u}(x) = \bar{d}(x)$$

then the second term in equation (1.83) vanishes and the integral $I_G^{n-p}(0)$ is equal to 1/3.

1.7.2 Adler Sum Rule

The Adler sum rule [11] is defined as:

$$I_A = \int_0^1 dx \frac{1}{2x} \{F_2^{\bar{\nu}p}(x, Q^2) - F_2^{\nu p}(x, Q^2)\} = 1 \quad (1.84)$$

This sum rule can be tested in neutrino and anti neutrino scattering only. The neutrino structure functions in naive QPM with 4 flavours are given by

$$\left. \begin{aligned} F_2^{\nu p}(x, Q^2) &= 2x\{d(x) + s(x) + \bar{u}(x) + \bar{c}(x)\} \\ F_2^{\bar{\nu}p}(x, Q^2) &= 2x\{u(x) + c(x) + \bar{d}(x) + \bar{s}(x)\} \end{aligned} \right\} \quad (1.85)$$

where all the threshold effects associated with the quark masses have been neglected. The equation (1.85) is a statement that neutrinos interact with down and anti-up quarks whereas the antineutrinos interact with up and anti-down quarks. Their coupling strength is equal.

In this model the Adler sum can be evaluated as

$$I_A = \int_0^1 dx \{u(x) + c(x) + \bar{d}(x) + \bar{s}(x)\} - \{d(x) + s(x) + \bar{u}(x) + \bar{c}(x)\}$$

$$\begin{aligned}
&= \int_0^1 dx \{u(x) - \bar{u}(x)\} - \{d(x) - \bar{d}(x)\} - \{s(x) - \bar{s}(x)\} + \{c(x) - \bar{c}(x)\} \\
&= 1
\end{aligned} \tag{1.86}$$

The difference in ν and $\bar{\nu}$ cross section on the same target is equal to the difference in quarks and antiquarks contributions therefore I_A depends on valence quarks in nucleons only. Since the QCD effects produce the quark and antiquark always in pairs, I_A is independent of Q^2 . The Adler sum rule, stated as [12]

$$I_A = \int_0^1 \frac{dx}{2x} \{F_2^{\nu p} - F_2^{\bar{\nu} n}\} = 1, \tag{1.87}$$

does not depend on QCD corrections as long as the corrections are the same for the neutron and proton.

In the QPM model $F_2^{\bar{\nu} n}$ can be obtained from $F_2^{\nu p}$ by the replacement $d(x) \leftrightarrow u(x)$ and $\bar{d}(x) \leftrightarrow \bar{u}(x)$ and so on, if isospin symmetry is assumed. The $F_2^{\bar{\nu} p}$ is obtained from $F_2^{\nu p}$ by replacing $q(x) \leftrightarrow \bar{q}(x)$. From which it follows that the two statements (1.84) and (1.87) of the Adler sum rule are equivalent. The measured Adler sum, $1.01 \pm 0.08(\text{stat.}) \pm 0.18(\text{syst.})$, is consistent with expected value of 1.0 [13].

1.7.3 Gross-Llewellyn Smith Sum rule

The Gross-Llewellyn Smith Sum (I_{GLS}) is defined as

$$\int_0^1 dx \frac{1}{2x} \{xF_3^{\bar{\nu} p}(x, Q^2) + xF_3^{\nu p}(x, Q^2)\} \tag{1.88}$$

In the naive quark-parton model, $F_3(x, Q^2)$ is given by

$$F_3^{(\nu, \bar{\nu})} = 2 \sum_j f_j(x) \lambda_V^j \lambda_A^j \tag{1.89}$$

where the interaction between the neutrinos and partons is described by the $\gamma_\mu(\lambda_V - \lambda_A \gamma_5)$ coupling and $f_i(x)$ is the probability density of parton i . The λ_V and λ_A are constants to be determined from experiment. In pure (V-A) theory, $\lambda_V = \lambda_A = 1$

Explicitly the F_3 is given by

$$F_3^{\nu p} = 2x \{d(x) + s(x) - \bar{u}(x) - \bar{c}(x)\} \tag{1.90}$$

$$F_3^{\bar{\nu} p} = 2x \{u(x) + c(x) - \bar{d}(x) - \bar{s}(x)\} \tag{1.91}$$

The GLS integral is given by

$$\begin{aligned} I_{GLS} &= \int_0^1 dx \{ [u(x) - \bar{u}(x)] + [d(x) - \bar{d}(x)] + [s(x) - \bar{s}(x)] + [c(x) - \bar{c}(x)] \} \\ &= 3 \end{aligned} \quad (1.92)$$

The commutation relations used to derive the GLS sum rule in the Bjorken limit are not exact at finite Q^2 and ν [15, 14]. If one includes the leading order QCD corrections, the I_{GLS} is given by [12]

$$I_{GLS} = \int_0^1 dx \frac{1}{2x} \{ F_3^{\bar{\nu}p}(x, Q^2) + F_3^{\nu p}(x, Q^2) \} = 3 \left(1 - \frac{\alpha_s(Q^2)}{\pi} \right) \quad (1.93)$$

The predicted value of the I_{GLS} is $2.66 \pm .06$ at $Q^2 = 3.0$. Its measured value [16] is $2.66 \pm 0.029(stat) \pm 0.075(syst.)$ which in very good agreement with the prediction.

1.8 Theoretical Expectations for F_2

In general the nucleon structure functions (SF) depend on the two variables, x_{bj} and Q^2 . The x_{bj} dependence of the SF is not theoretically established. The x_{bj} behaviour of the SF at high and very low x_{bj} is given by counting rules and Regge behaviour.

The Q^2 evolution of the SF is described by the Quantum Chromodynamics (QCD), a field theory based on non-abelian group $SU(3)_c$, where c denotes the color quantum number. The QCD is a well established theory of strong interactions. The Q^2 evolution of the SF is one of the more convincing arguments for such a color force.

At very small x_{bj} , in large Q^2 limit, the $F_2(x, Q^2)$ can also be calculated in the QCD [17].

1.8.1 Regge model and Counting rules

The asymptotic properties of deep inelastic structure functions at large ν and fixed Q^2 are conjectured to be governed by Regge behaviour [6, 18, 19]. In this limit the leading behaviour of the structure functions W_1 and W_2 is given by

$$W_1(\nu, Q^2) \rightarrow \nu^\alpha g_\alpha^1(Q^2) + \dots \quad (1.94)$$

$$W_2(\nu, Q^2) \rightarrow \nu^{\alpha-2} g_\alpha^2(Q^2) + \dots \quad (1.95)$$

where α is the intercept of the appropriate Regge trajectory. In the limits $Q^2 \rightarrow \infty$ only the leading contribution survives.

If the same expression (1.95) is valid at very large Q^2 , it should exhibit Bjorken scaling as $Q^2 \rightarrow \infty$. Therefor the functions g should have the functional form

$$\left. \begin{array}{l} g_\alpha^1(Q^2) \rightarrow (Q^2)^{-\alpha} \\ g_\alpha^2(Q^2) \rightarrow (Q^2)^{1-\alpha} \end{array} \right\} \quad (1.96)$$

Using Equation (1.95), the equation (1.96) can be written as

$$\left. \begin{array}{l} W_1 \rightarrow (\frac{\nu}{Q^2})^\alpha + \dots \\ W_2 \rightarrow (\frac{\nu}{Q^2})^{\alpha-2} + \dots \end{array} \right\} \quad (1.97)$$

Keeping only the leading order terms, the structure functions can be written as

$$\left. \begin{array}{l} F_1 \rightarrow x^{-\alpha} \\ F_2 \rightarrow x^{1-\alpha} \end{array} \right\} \quad (1.98)$$

Note that Bjorken limit has been only used to fix the functional form of g 's. The equation (1.98) is valid only in very small x_{bj} region i.e. ($\nu \rightarrow \infty$ and finite Q^2). For the Pomeron exchange (when no quantum numbers are exchanged) α is equal to 1 and α is 1/2 for vector meson exchange.

The (1.98) suggest that $F_2(x)$ tends to a constant value for $\alpha = 1$ as x tends to zero which agrees with experimental measurement. For $F_2(x)$ to be constant, the parton number density should approach infinity as $x \rightarrow 0$ such that

$$x f(x) \rightarrow \text{constant}$$

Large number of partons can only be excited out of vacuum. The partons from the vacuum must be generated in pairs only to conserve all the quantum numbers. In other words, Regge behaviour predicts the existence of quark-antiquark pairs or sea quarks at small x_{bj} .

The experimental value of F_2 is finite as $x \rightarrow 0$ but the slope of $F_2(x)$ not precisely measured. Moreover the precise value of x_{bj} where the Regge behaviour sets in is also not determined accurately due to lack of data in the low x_{bj} region.

The behaviour of the quark distribution in the high x_{bj} range is described by the counting rules [21, 20]. The number density distribution is given by [22]

$$f(x, Q_0^2) \approx (1 - x)^{2n-1} \quad \text{as } x \rightarrow 1 \quad (1.99)$$

where n is the minimum number of spectator quarks involved in the reaction. The structure functions should clearly vanish as $x \rightarrow 1$ because it would imply that all the momentum is carried by single parton. Equation (1.99) is valid in the Q^2 range where the naive quark parton model is valid i.e. $Q_0^2 \approx 2.5 \text{ GeV}^2$. The number density for different types of partons is given by

$$u_v, d_v \approx (1 - x)^{(2*2-1)} = (1 - x)^3 \quad (1.100)$$

$$G(x) \approx (1 - x)^{(2*3-1)} = (1 - x)^5 \quad (1.101)$$

$$S(x) \approx (1 - x)^{(2*4-1)} = (1 - x)^7 \quad (1.102)$$

where u_v , d_v , G and S are the distributions for up, down, gluon and sea quark respectively.

1.8.2 Proton Structure and QCD

The naive quark-parton model is successful in explaining scaling behaviour observed in the deep inelastic data. The structure function F_2 in QPM can be written as

$$\frac{1}{x} F_2 \sim \int \frac{dy}{y} f_0(y) \sigma_{\text{point}}(yP + q) + O(1/Q^2). \quad (1.103)$$

where f_0 is the parton distribution function. The sum over the quark and anti-quark flavours is implied. The description of any physical process at hadronic level factorizes into two parts 1) the process at the partonic level and 2) the probability of finding partons in a nucleon. The total cross section at hadronic level is the convolution of partonic cross section with partonic probability distribution as given in equation (1.103).

For such a description to be true, two requirements must be met. First the transverse momenta involved in the target wave function must be small enough to be neglected and second, one should be able to represent the the underlying

process in terms of interaction between point particles. The naive quark-parton model satisfies both these requirements and the structure function is given by

$$\frac{1}{x} F_2(x) \sim \int \frac{dy}{y} f_0(y) e^2 \delta\left(\frac{x}{y} - 1\right) = e^2 f_0(x). \quad (1.104)$$

Even when we include the effects of QCD interaction between partons the factorization still holds if we make the same assumption about target wave function i.e. the transverse component of the wave function is small enough to be neglected. However the parton level cross sections are no longer pointlike and receive contribution from the higher order QCD processes and equation (1.104) is modified to

$$\frac{1}{x} F_2(x, Q^2) \sim \int \frac{dy}{y} f_0(y) \left[e^2 \left(\frac{x}{y} - 1 \right) + \sigma_\alpha \left(\frac{x}{y}, Q^2 \right) + \dots \right] \quad (1.105)$$

where $\sigma_\alpha(z, Q^2)$ is the contribution from leading order QCD processes.

In QCD, the interaction is mediated by vector bosons, called gluons, which carry only color force. In contrast to the photon, the carrier of electromagnetic force, the gluons couple with each other. This self-coupling leads to the confinement of the quarks inside hadrons provided the total number of flavours is less than 17. Both the gluons and quarks are assumed to be massless. The strength of QCD interaction is described by strong coupling constant α_s given by

$$\alpha_s(Q^2) = \frac{12\pi}{(33 - 2n_f) \log(Q^2/\Lambda^2)} \quad (1.106)$$

where n_f is the number of active light flavours. Λ is called QCD scale parameter which is calculated from physically measured quantity, α_s . The coupling strength decreased with Q^2 and thus at very high Q^2 the quarks are almost free but still confined in the nucleons.

The first experimental hint for the existence of gluons was furnished by deep inelastic scattering data. The total momentum fraction carried by all the charged partons in a nucleon was measured to be approximately 50%. The natural explanation for the missing momentum is the existence of the particles which do not have electroweak coupling and hence can not be detected by electroweak probes like photon or W^\pm in deep inelastic scattering. The existence of the color field

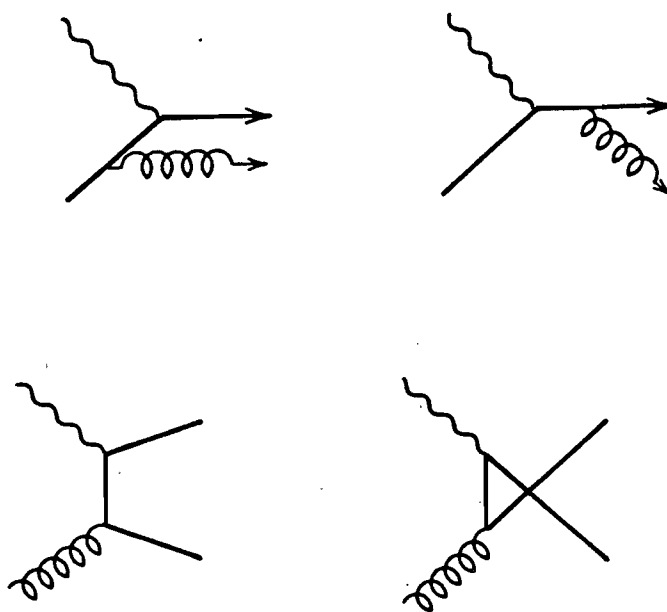


Figure 1.3: QCD Leading Order Diagrams to DIS scattering

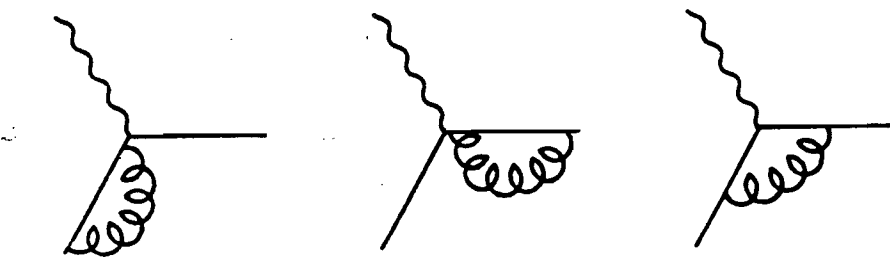


Figure 1.4: First Order QCD corrections Virtual diagrams

results in interaction between quarks and gluons which modifies the momentum distribution of the charged leptons. As the strength of this interaction depends on $\alpha_s(Q^2)$ which varies as $1/\log(Q^2)$, the parton distributions and therefore structure functions evolve logarithmically with Q^2 .

The first order QCD Feynman diagrams are given in Fig. 1.3. The quarks can radiate gluons and hence the momentum fraction carried by the quarks will decrease. On the other hand a gluon can convert to a quark-antiquark pair increasing the number density and the momentum carried by quarks. Another feature of QCD is that a gluon can split into two gluons. Gluon radiation by quarks has two singularities which arise from the emission of either a gluon collinear with the parent quark or a gluon which carries zero momentum. These singularities will lead to infinite value of bare $F_2(x, Q^2)$. The soft singularity i.e. the emission of a zero momentum gluon is cancelled by the contribution from the virtual loop diagrams given in Fig. 1.4. The collinear singularity, emission of a gluon parallel to the initial quark is only possible if both the quarks and gluons are massless. This singularity is regularized by introducing an arbitrary finite mass cut off μ . After regularization, physical structure function $F_2(x, Q^2, \mu)$ are finite and depend on the cut off μ , called the factorization scale.

The evolution of the parton distributions due to QCD effects, to first order, is given by the Altarelli-Parisi equations [44] as below.

$$\frac{df_p^q(x, Q^2)}{d \log Q^2} = \frac{\alpha_s(Q^2)}{2\pi} \int_x^1 \frac{dy}{y} \left[P_{q \rightarrow q} \left(\frac{x}{y} \right) f_p^q(y, Q^2) + P_{g \rightarrow q} \left(\frac{x}{y} \right) f_p^g(y, Q^2) \right] \quad (1.107)$$

$$\frac{df_p^g(x, Q^2)}{d \log Q^2} = \frac{\alpha_s(Q^2)}{2\pi} \int_x^1 \frac{dy}{y} \left[\sum_q P_{q \rightarrow g} \left(\frac{x}{y} \right) f_p^q(y, Q^2) + P_{g \rightarrow g} \left(\frac{x}{y} \right) f_p^g(y, Q^2) \right] \quad (1.108)$$

The functions f_p^q and f_p^g are the distribution function for quarks and gluons respectively in the proton. The functions $P_{a \rightarrow b}(z)$ are called splitting functions and are given in Table 1.1.

The splitting functions have a simple physical interpretation. They are related to the probability of finding the parton a inside the parton b . Consider the function

Table 1.1: Leading order QCD splitting Functions

$$\begin{aligned}
 P_{q \rightarrow q} &= \frac{4}{3} \frac{1+z^2}{1-z} \\
 P_{q \rightarrow g} &= P_{q \rightarrow q}(1-z) \\
 P_{g \rightarrow q} &= \frac{1}{2} [z^2 + (1-z)^2] \\
 P_{g \rightarrow g} &= 6 \left(\frac{z}{1-z} + \frac{1-z}{z} + z(1-z) \right)
 \end{aligned}$$

$\Pi_{a \rightarrow b}$ [40] given below.

$$\Pi_{a \rightarrow b} = \delta_{a \rightarrow b} \delta(1-z) + \frac{\alpha_s}{2\pi} P_{a \rightarrow b}(z) \log(Q^2/\mu^2) + \dots$$

The quantity Π can be interpreted as the probability density of finding a parton b inside a parton a when parton b carries a momentum fraction z of the parent parton a . The δ function corresponds to no change in the parton momentum which correspond to naive QPM result. The second term comes from the first order QCD corrections. To first order, all the Q^2 dependence appears in $\log(Q^2/\mu^2)$ and the splitting functions $P_{a \rightarrow b}(z)$ are independent of both Q^2 , the interaction scale, and μ^2 , the factorization scale where the ultraviolet infinities of the theory are subtracted. The running coupling constant α_s , evaluated at $Q^2 = \mu^2$, is fixed in equation (1.109).

The physical quantities like cross section should not depend on the arbitrary choices like the renormalization scheme or the renormalization point μ^2 . This is true only if all the terms in the perturbation series are summed. In practice, the series is truncated at a finite order and therefore the theoretical predictions do depend on the choices made. The first order QCD amplitudes depend on μ^2 only. The magnitude of the next to leading order QCD corrections depends on the renormalization procedure adopted. Hence the next to leading order parton distributions derived from structure functions are both scale and scheme dependent. When calculating the rate of a physical process, the same renormalization scheme should be used which is used to extract the parton distributions.

The Altarelli-Parisi equations 1.108 describe the decay of the partons. At very

low x_{bj} , the number density is very large and it is expected that partons recombine together. A possible result of these creation and annihilation processes is that the number density of partons reach saturation. This would imply that QCD structure functions do not increase with x_{bj} but reach a constant value (up to powers of $\ln(\frac{Q^2}{Q_0^2})$) [41]. The set of equations describing QCD decay and recombination are non-linear.

QCD processes involve non-zero transverse momenta and therefore the longitudinal structure function $F_L(x, Q^2)$ is also modified. The leading order QCD contribution [42] to $R(x, Q^2)$ is

$$R^{\text{QCD}}(x, Q^2) = F_L(x, Q^2)/F_2(x, Q^2) \sim \alpha_s(Q^2) \sim 1/\log(Q^2) \quad (1.109)$$

where F_L is the longitudinal structure function given by

$$F_L(x, Q^2) = \frac{4\alpha_s(Q^2)}{3\pi} \int_x^1 \frac{dy}{y} \left\{ \left(\frac{x}{y}\right)^2 F_2(y, Q^2) + \left[\left(\frac{x}{y}\right)^2 - \left(\frac{x}{y}\right)^3 \right] y G(y, Q^2) \right\}. \quad (1.110)$$

The function $G(x, Q^2)$ describes the gluon distribution in proton.

1.9 Nuclear Environment and F_2

So far we have discussed the structure of a free nucleon. Naively one would expect that nucleon's structure is unchanged when it is confined to a nucleus. This expectation arises from the fact that nuclear binding energy (\sim MeV) is much smaller than interaction energy (\sim 100 GeV) available in modern high energy experiments. However it was experimentally discovered that the nucleons behave differently when they are bound in the nuclei (EMC effect). The observation of the EMC effect is an indication of existence of degrees of freedom in nuclei in addition to free nucleons. This effect was first discovered by European Muon Collaboration (EMC) in 1983, and later confirmed by SLAC electron scattering data and CERN neutrino data. It has been studied in detail by the NMC collaboration [23].

The EMC effect is described quantitatively by the ratio

$$R_{\text{EMC}} = F_2^A(x, Q^2)/F_2^D(x, Q^2)$$

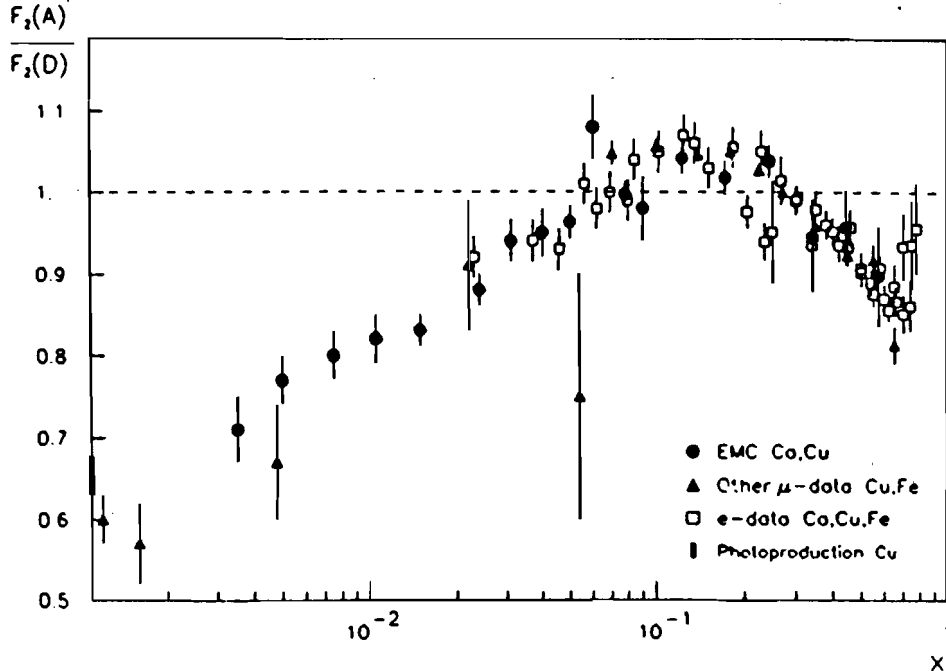


Figure 1.5: The ratio of nuclear structure function to the deuterium structure function

where $F_2^A(x, Q^2)$ is the structure function (per nucleon) for a nuclear target and $F_2^D(x, Q^2)$ the same for deuterium target.

R_{EMC} is shown in Fig. 1.5 from different experiments. The data from the different experiments is consistent within errors. The rise in the ratio at the high x_{bj} is due to the Fermi motion of the nucleons in the nucleus which is a kinematic effect. At low x_{bj} , the cross section exhibits shadowing i.e. the per nucleon cross section in nuclear environment is smaller than what is observed in deuterium. The naive quark parton model can not be used to explain shadowing as the scattering at the parton level is assumed to be incoherent i.e. independent of the surrounding partons or nucleons.

The decrease in the cross section at low x_{bj} can be explained in the recombination model [24] within the framework of QCD. In this model the partons at $x_{bj} < x_{bj}^C$ have a large enough spacial extension to overlap other nucleons. The partons from different nucleons combine such that the effective number density is reduced and thus the effective cross section is smaller than what is expected by σA where σ is the cross section for a free nucleon and A is the number of

nucleons in the nucleus. This model predicts that the magnitude of shadowing weakly depends on the Q^2 . The Q^2 dependence can be calculated using modified Altarelli-Parisi equations. The parton distributions at $x_{bj} > x_{bj}^C$ are still a property of individual nucleons. The critical x -Bjorken (x_{bj}^C) depends on the details of the model.

In reference [25] the EMC effect at low x_{bj} (shadowing) is explained in terms of the hadronic structure of virtual photons. In the space-time evolution picture of the γ^*N interaction, the virtual photon may fluctuate into a $q\bar{q}$ pair which interacts with nucleons as a hadronic state. Because of large hadronic cross section, the hadronic state interacts at the surface of the target and therefore the total cross section varies as $\sim \sigma A^{\frac{2}{3}}$ where σ is per nucleon cross section and A is the number of nucleons in nucleus. This model is similar to the generalized vector dominance model but has one major difference that the q and \bar{q} interact with nucleons independently.

1.10 Physics motivation to measure structure functions

The knowledge of the proton structure from deep inelastic scattering enable us to predict how the nature will behave if looked at through some other window like hadron-hadron collisions or Drell-Yan production. The universal nature of the quarks in nucleon (the same entities couple to photon, W^\pm , Z^0 and gluons, apart from small well understood mixing of quarks) makes these predictions possible. The disagreement between the predictions based on the measured parton densities and the experimentally measured quantities may lead us to new physics or to the refinement of already known theories.

The structure functions should satisfy certain relations based on the present understanding of the quark-parton model and QCD. These relations are called sum rules. One of them, the Gottfried sum rule is related to the difference between structure of the proton and neutron and can be tested in the charged-lepton scattering. Recently, a CERN deep inelastic scattering experiment has suggested that the measured sum is not consistent with the isospin symmetry of sea quarks in nucleons. The NMC data suggest that the distributions for the anti-up (\bar{u}) quark is different than the one for anti-down (\bar{d}). This conclusion is contrary to the expectation that sea quark distributions are SU(2) flavour symmetric. The

expectation is based on the fact that color interaction does not depend on the flavour of the quarks.

1.11 Physics processes where structure functions can be measured

The quark and gluon distributions can be measured in a variety of high energy processes. A few such processes are described below.

- **DIS $ep - \mu p$ scattering :** The $ep - \mu p$ scattering, a largely electromagnetic process at present energies, measures the quark and antiquark distributions in the nucleon. Since the electromagnetic charge appears as e_q^2 in cross section, the quarks can not be distinguished from antiquarks in this process. The gluons being electrically neutral do not couple to the photon directly. Their contribution is normally extracted from the Q^2 variation of the structure functions. Gluon distributions also enter μp scattering through the first order QCD process called photon-gluon fusion. In this process the gluon splits into $q\bar{q}$ pair and q or \bar{q} interacts with the incoming photon. The gluon distribution extracted from deep inelastic data has a large uncertainty as it is highly correlated with the value of QCD coupling constant which is usually extracted from the same data.
- **DIS Neutrino-Nucleon Scattering :** The neutrinos interact with quarks via the weak interactions only. The neutrinos interact with \bar{u} , \bar{c} , \bar{d} and \bar{s} and the antineutrinos interact with u , c , \bar{d} and \bar{s} only. Therefore combining the results of ν and $\bar{\nu}$ interactions from the same target, one can in principle separate the quark and antiquark distributions.
- **Drell-Yan :** In the lowest order Drell-Yan process (DY) the quark from one hadron combines with the antiquark from the other hadron to form a virtual photon which decays into a lepton pair. Higher order processes involve the quark or antiquark from one hadron interacting with the gluon from other. Using deep inelastic μp data to constrain the valence quark contribution the sea quark distribution can be extracted from pp scattering DY data. Present DY data and the theoretical calculations are both not very accurate as compared to the DIS data [26].

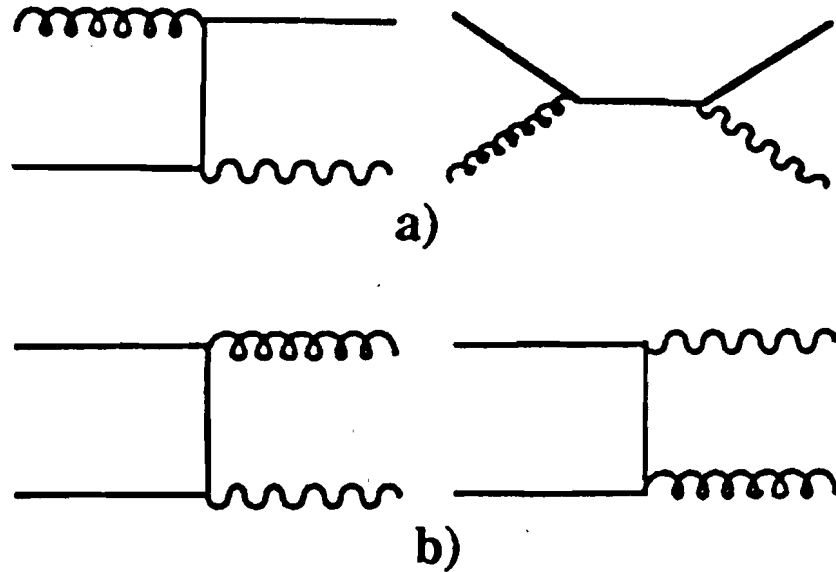


Figure 1.6: The Feynman diagrams for direct photon productions

DY is the only process which can be used to determine the structure functions of unstable hadrons like pions.

- **Proton-Antiproton collisions :** At the CDF energy (1.8 TeV) W production is dominated by the annihilation of valence quarks and sea quarks. From the asymmetry in W^- and W^+ production, the d/u ratio can be determined [27]. Given the energy of the proton/anti proton beam, this can be evaluated only at single x_{bj} point (0.05 at CDF).
- **Direct Photon Production :** The QCD compton scattering (Fig. 1.6) is directly related to the gluon distribution in the nucleons. Recently direct photon production data (WA70) in $pp \rightarrow \gamma X$ and the μp scattering data (BCDMS) have been analysed together to extract the gluon distribution function of the proton [28]. This analysis is done in two steps. The parametric dependence of gluon distribution functions is assumed as

$$x G(x) = A_g (1 - x)^{\eta_g} \quad (1.111)$$

Keeping η_g fixed, the QCD scale parameter Λ , the valence and sea quark distributions are determined from BCDMS data. These fitted parameters

are used to predict the direct photon data and its compatibility with experimental measurement is checked. The best gluon distributions are obtained which fit both the DIS and direct-photon data. The power η_g is mainly determined by direct photon data and the Λ by deep inelastic data. In other words the χ^2 contribution from the BCDMS data is not sensitive to value of η_g and the χ^2 contribution from the WA70 data are not sensitive to the value of Λ .

1.11.1 Muon and neutrino scattering comparison

The DIS muon experiment has advantage over the neutrino data because 1) the energy of the beam particle is determined more accurately and 2) the flux of incoming beam can be directly measured. The neutrino experiment have unique advantage of measuring q and \bar{q} separately because neutrino and antineutrino couple to different sets of quarks and antiquarks. Combining the different structure functions from ν and $\bar{\nu}$ events the contribution from the different flavour quarks can be separated.

1.12 Present Experimental Status of F_2

E665 is the third generation experiment to measure nucleon structure. The previous experiments include the classic SLAC-MIT experiment, the Fermilab Muon experiments (E98 and E398) [58] and the two very high statistics experiments at CERN, EMC [56, 32] and BCDMS [57, 33]. More recently the NMC Collaboration has measured the A -dependence of the structure functions. The NMC Collaboration has also measured the neutron to proton ratio with very high statistics over a wide range of kinematic variables [23]. Moreover the effect of a nuclear environment on structure functions of nucleons has been studies by EMC-NA28 [59] and E140 at SLAC.

The high statistics muon scattering data from EMC and BCDMS are in contradiction exhibiting different x_b behaviour and absolute normalization and have been subject of a lot of discussion. As the BCDMS and EMC experiment used the same beam line at CERN, the kinematic regions of the two experiment almost overlap. However, the experimental design of two experiments differs and

Table 1.2: The experimental values for Gottfried sum

Experiment	x_{bj} range	Q^2	I_G
EMC	0.020-0.8	—	$0.197 \pm 0.011 \pm 0.087$
BCDMS	0.060-0.8	20 GeV	$0.197 \pm 0.006 \pm 0.036$
NMC	0.004-0.8	4 GeV	$0.227 \pm 0.007 \pm 0.014$

thus the BCDMS kinematic region extends to higher Q^2 and higher x_{bj} . The two data sets may be in disagreement because of systematic problems in the experiments or because of different assumptions made in the extraction of $F_2(x, Q^2)$ from the measured cross sections. The original analysis of EMC data was done using $R(x, Q^2) = 0$. The radiative correction were performed using the Mo and Tsai program [29]. The BCDMS data were analysed using R_{QCD} and the radiative correction using the Bardin formalism [30]. The SLAC data overlap with the CERN experiments in the medium x_{bj} range but are disjoint in Q^2 range. Therefore they can be used to resolve the discrepancy only when extrapolated in Q^2 . This extrapolation can be done either using phenomenological fits or using the QCD evolution of structure functions.

A recent study [31] using data from three experiments, shows that the SLAC data are in agreement with both the BCDMS and EMC data after renormalization of EMC data by $+8 \pm 2\%$ and of BCDMS data by $-1 \pm 1\%$ for hydrogen and $-1 \pm 1\%$ for deuterium. After renormalization the EMC and BCDMS data are in agreement at small x_{bj} but the disagreement is enhanced at high x_{bj} . QCD inspired phenomenological fits were used to extrapolate the SLAC data.

The EMC data have been reanalysed after above study using a different radiative correction scheme and $R_{QCD}(x, Q^2)$ instead of a constant value of zero. This reanalysis has reduced the discrepancy between BCDMS and EMC data but has not completely eliminated it.

1.12.1 Experimental value of Gottfried Sum

The Gottfried sum rule has been measured by EMC [32], BCDMS [33] and NMC [34] collaborations. The x range and the sum as defined in section 1.7.1 is given in the Table 1.2 All the measurements are less than $1/3$, the expected value

if the sea quark distributions are assumed to be isospin symmetric. The NMC results are most precise and cover a wider range of kinematics. The contributions in the unmeasured region in the NMC data are estimated by extrapolating the measured data and the total Gottfried sum is

$$\int_{0.0}^{1.0} \frac{dx}{x} \{F_2^p(x, Q^2) - F_2^n(x, Q^2)\} = 0.240 \pm 0.016. \quad (1.112)$$

The difference from the expected value can be translated into the flavour symmetry breaking of the sea quarks. The NMC collaboration has reported that the difference implies that

$$\int_0^1 (\bar{u} - \bar{d}) dx = -0.14 \pm 0.024. \quad (1.113)$$

In fact the failure of the Gottfried sum was noticed Feynman [35] in earlier less precise SLAC data and he suggested that the \bar{u} quarks are suppressed in proton due to Pauli exclusion principle.

The NMC data have been analysed by Martin et. al. [10] in conjunction with BCDMS data and they find that Gottfried sum as measured by NMC is in good agreement with the expectation. Three different parton distribution functions are used. In KMRS(B_0) and KMRS(B_-) the sea quark and gluon distributions are constrained to behave as $x^0, x^{1/2}$ as $x \rightarrow 0$ at $Q_0^2 = 4.0$. In HMRS fit the sea quarks distributions are determined from data alone. The sea distributions are assumed to be SU(2) flavour symmetric. The results from all three fits are consistent with NMC data and the Gottfried sum is consistent with 1/3. This would imply that the sea quark distributions in the proton is symmetric in up and down quarks.

The difference in the conclusions by the NMC collaboration and the Martin et. al. can be traced to the contribution from the small x_{bj} region. The NMC collaboration assumed a functional form of ax^b to characterise the behaviour of $F_2^p - F_2^n$ in the unmeasured low x_{bj} region. This form is motivated by the expectation that at low x_{bj} the parton distributions are described by Regge trajectory. The total contribution from the x_{bj} region 0.0-0.004 to the Gottfried sum as evaluated by NMC is 0.011 ± 0.003 whereas the same region contributes to ≈ 0.10 to the sum in analysis by Martin et. al. This difference can only be resolved by a direct measurement at low x_{bj} .

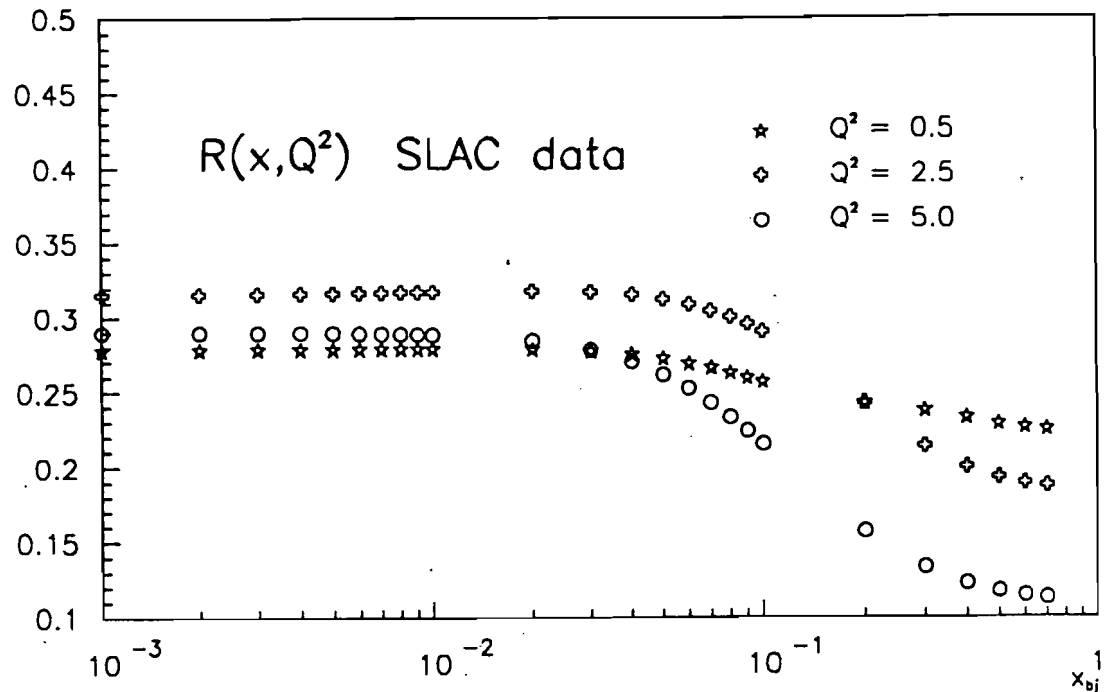


Figure 1.7: The value of $R(x, Q^2)$ for a fit to world data

1.13 Experimental Issues

In this analysis the ratio of the x_{bj} dependence of the structure functions of proton and neutron is determined from the muon scattering data from the hydrogen and deuteron targets from E665. In this section, some of the issues relating to the extraction of this ratio from the data are discussed.

For experimental analysis it is useful to write the double differential cross section as

$$\frac{d\sigma}{dxdQ^2} = \frac{4\pi\alpha^2}{Q^4x} \left\{ 1 - y - \frac{Mxy}{2E} - \frac{y^2(1 + 4M^2x^2/Q^2)}{2(1 + R(x, Q^2))} \right\} F_2(x, Q^2). \quad (1.114)$$

In this equation all the quantities except $F_2(x, Q^2)$ and $R(x, Q^2)$ are experimentally measured. Given the fact that E665 data were taken at one beam energy, E , only one of the structure functions can be extracted.

1.13.1 Role of R in extraction of F_2^n/F_2^p

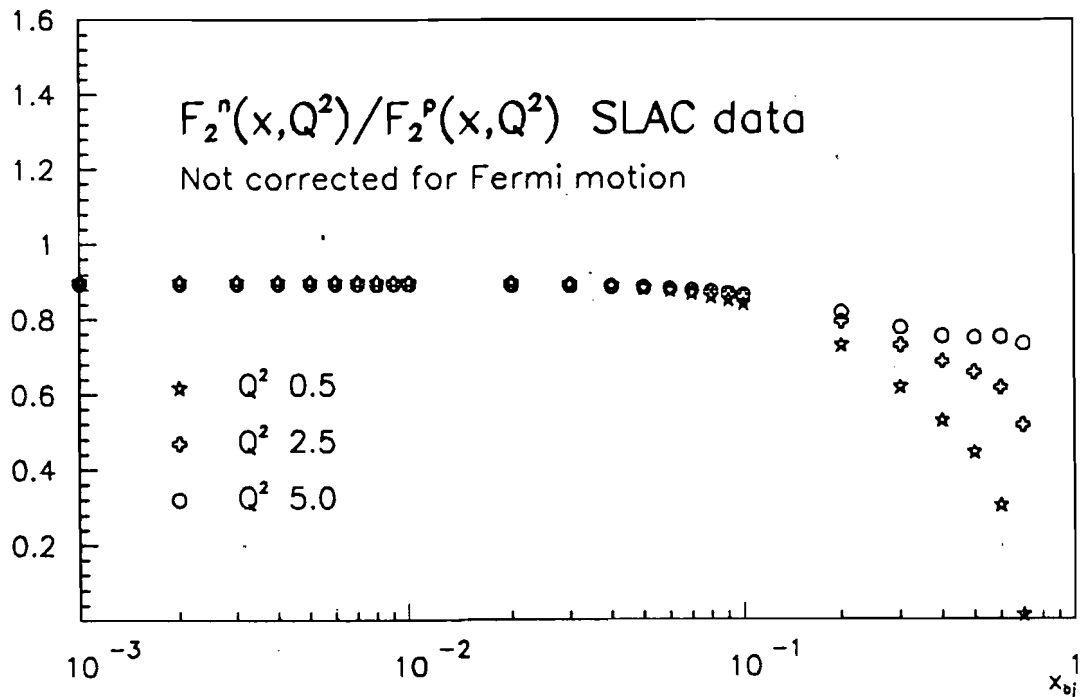


Figure 1.8: Q^2 variation of the F_2^n/F_2^p ratio

The ratio F_2^n/F_2^p is equal to the ratio of the cross sections as long as the $R(x, Q^2)$ is same for the proton and deuteron. Previous experiments have shown that the value of R is small and is independent of the target used. In particular the SLAC data on proton and deuteron [36] show that the $R^d = R^p$ with total experimental error of ± 0.013 . This is true at all Q^2 measured so far.

Theoretically the non-zero value of R arises from the finite transverse momentum (k_t) of the partons in nucleon and QCD effects. Both of these effects are same for the proton and neutron and hence the value of R is expected to be same for both targets as is experimentally found [36].

To determine the structure functions R and F_2 simultaneously, one needs data sets at least two different energies. The data set from E665 1987-88 run is limited to single beam energy and therefore one can not determine R . The value of $R(x, Q^2)$ was taken from [36]. The functional form used is a phenomenological fit to the data from SLAC, BCDMS, EMC and CDHSW. The parameterization is motivated by QCD and is shown in Fig. 1.7. The $R(x, Q^2)$ is shown for two different values of Q^2 .

It is found experimentally that the ratio F_2^n/F_2^p depend on the Q^2 weakly.

The Gottfried sum rule (I_G) as described in section 1.7.1 is evaluated at fixed Q^2 . In a given experiment, the mean Q^2 increases with increasing x_{bj} . Therefore extrapolation must be used to evaluate the F_2^n/F_2^p ratio at fixed Q^2 from which the I_G can be calculated. The Q^2 variation of the ratio is shown in Fig. 1.8. At low Q^2 the variation is small and therefore is ignored in this analysis. Note that the distributions used have not been corrected for Fermi motion (see 1.13.2) and the strong Q^2 dependence at high x_{bj} is reflection of that effect. The Fermi motion corrections are important only at high x_{bj} and low x_{bj} results are not effected.

1.13.2 Fermi Smearing

The deuteron is a weakly bound composite object and hence the proton and neutron in it are neither on mass shell nor at rest. The kinematics of the interaction depend on the Fermi motion of the nucleons in deuteron. The change in kinematics is called Fermi smearing. Knowing the deuteron wave function, the smearing effects can be calculated. Fermi smearing is expected to be large only at very large x_{bj} where the struck quark carries a large fraction of the nucleon momentum. The procedure to extract the free neutron structure function from μd scattering data are described in [37, 38]. These models give insignificant corrections in the kinematic region of this analysis [36]. No corrections have been made for this effect. Stated in another way, the ratio of structure functions presented in this analysis is the ratio of smeared structure functions.

1.13.3 Nuclear Effect in Deuterium

The decrease of the cross section at low x_{bj} (shadowing) in nuclear targets compared to the deuteron fully established experimentally but what happens to the proton and neutron structure functions when they are confined in the deuteron is not completely known. However, some estimates of such an effects have been made.

The E665 data is concentrated at low Q^2 . The virtual photon data (μN) data should smoothly cross over to real photon data. For a real photon ($Q^2=0$) the ratio of the γd to γp cross sections varies from 0.915 to 0.812 when photon energy is changed from 50 GeV to 400 GeV [55].

The shadowing of the hadronic component, if any, of the virtual photon is

related to the shadowing of pion scattering. The ratio of the πd to πp cross section varies from 0.991 to 0.963 for pion beam energy from 50 GeV to 400 GeV [55].

An estimate of the shadowing in deuteron can be made using the ν and $\bar{\nu}$ data as is done by Bodek et. al. [48]. They estimated the up and down quark distributions in the proton assuming that only valence quarks contribute to the cross section. Using isospin symmetry between proton and neutron, the structure functions for deuteron are completely determined. They find that the shadowing in the deuteron is consisted with zero within large errors ($\pm 5\%$). In other words no EMC effect (shadowing) is observed in deuteron. The assumption that only valence quarks contribute to the scattering is valid only at relatively large x_{bj} . No such conclusion can be made at very small x_{bj} where shadowing is relevant.

1.13.4 Target Mass Corrections

In the definition of the momentum fraction carried by a struck parton, x_{bj} the mass of the parton was completely neglected. At very low Q^2 this approximation may lead to large difference between the x_{bj} and the actual momentum carried by the parton. Various modifications to the x_{bj} have been suggested to take into account the so called target mass effects. Georgi and Politzer [45] predict that the structure functions should scale in variable ξ defined as

$$\xi = \frac{2x}{1 + (1 + Q^2/\nu^2)^{\frac{1}{2}}}.$$

At small Q^2 and large ν , the denominator can be expanded and the variable ξ is

$$\xi = \frac{x}{1 + Q^2/4\nu^2}. \quad (1.115)$$

At Q^2 equal to 1.0 and ν equal to 100, ξ differs from x by less than 1% which is a negligible effect and will be ignore. Note that the mean Q^2 in the lowest x_{bj} bin in the E665 data used in the analysis is 1.5 GeV².

This variable is called the Nachtmann variable ξ and commonly written as

$$\xi = \frac{2x}{1 + (1 + 4M^2x^2/Q^2)^{\frac{1}{2}}}. \quad (1.116)$$

The power corrections $\mathcal{O}(1/Q^{2n})$ to the quark-parton model also arise from QCD effects [47]. These QCD corrections contribute to order (Λ^2/Q^2) , where Λ is related to the QCD coupling constant α_s . The QCD $\mathcal{O}(1/Q^2)$ corrections may not be negligible in the Q^2 range of the E665 data. These corrections are ignored in this analysis.

1.13.5 Radiative Corrections

The cross section measured in the laboratory includes not only the first term in the QED perturbation expansion (Born term) but also all the higher order terms. It may also include the various other background processes which are very difficult to separate in an inclusive measurement. To compare the experimental result with theoretical predictions, it is a common practice to reduce the measured cross section to the single-photon exchange cross section (Born term). These extra contributions to the Born term are called radiative corrections.

Fig. 1.9 shows the various Feynman diagrams which contribute to the measured cross section.

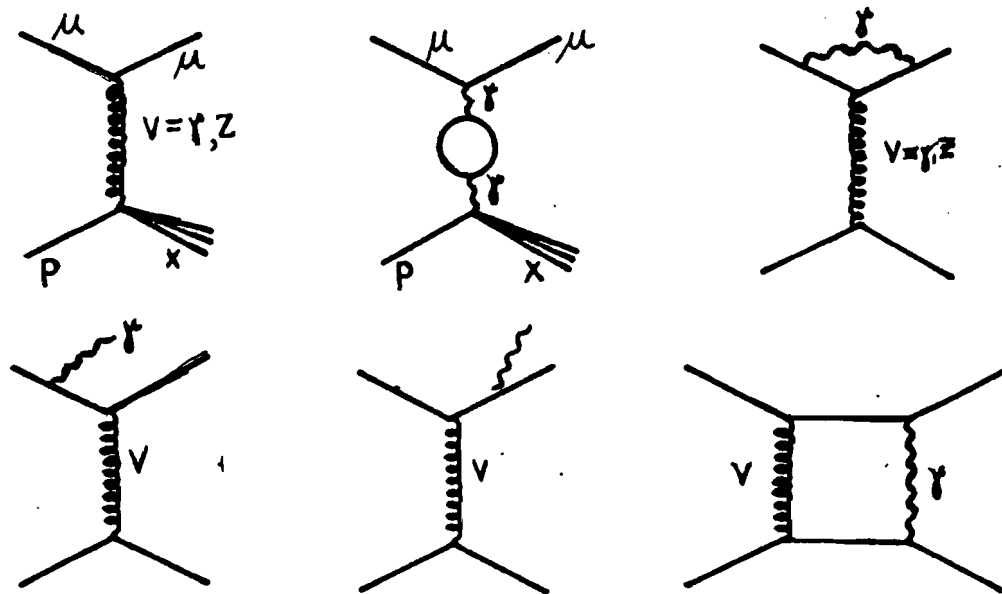


Figure 1.9: Leading and higher order electroweak radiative processes contributing to the observed deep inelastic cross section

The radiative effect can be categorized into:

1. the vacuum polarization and vertex corrections
2. emission of real photons on the lepton lines
3. Z^0 exchange
4. emission of real photons on quark lines
5. two photon exchange and higher order processes
6. elastic scattering from the nucleus
7. quasi elastic scattering from the protons and neutrons

It is well known that to get rid of unphysical infinities in the QED predictions, extra terms should be added to the QED lagrangian (Renormalization). These extra terms not only subtract out the unwanted infinities but leave a finite part which modifies the physical predictions. To get the single photon interaction cross section given by Fig. (1.9 a), the contributions from the vacuum polarization (1.9 b) and vertex correction (1.9 c) diagrams should be subtracted even to lowest order. The procedure for the subtraction is well understood and can be easily implemented at muon-quark level.

The vertex correction at the lepton vertex is independent of the quark vertex. The vacuum polarization correction depends only on the fermion mass (primarily the lightest fermion, electron) in the internal loop and does not depend on the flavour of lepton or quark. Therefore these corrections are the same for both neutrons and protons.

The Fig. (1.9 d,e) show the emission of a real photon from the lepton. These photons are real and can be observed in the detector if they have enough energy. The lower limit of the energy of these photons is zero leading to infra-red singularity. Fortunately the singularity in the real photon emission amplitude is cancelled by the virtual photons diagram (1.9 b,c).

The hadronic radiative corrections (corrections associated with the hadronic vertex) are model dependent as the exact form of the hadronic current is not known. These corrections can be calculated in the framework of the naive quark parton model. In this calculation quarks are assumed to have a finite mass. The electroweak contribution to the cross section from Z^0 exchange is small within the E665 kinematic range.

The second order QED contribution is represented by two photon exchange diagram (1.9 f). The contribution of two photon exchange term has the opposite sign for $l^+ p$ and $l^- p$ scattering and therefore its magnitude can be estimated

experimentally. The contribution was found to be less than 2% [50]. These corrections are called internal Bremsstrahlung corrections.

Experimentally, it is difficult to separate μp , μn or μA elastic events from the deep inelastic events over all kinematic regions. Fortunately, the elastic form factors (G_E , G_M) of the proton and neutron are known. The (quasi)elastic scattering from the proton or neutron can be calculated and therefore subtracted.

The emission of the real photons when the lepton passes through the target is called external Bremsstrahlung. For electrons this correction is the same order of magnitude as the internal Bremsstrahlung contribution discussed above [94]. For muons the correction is smaller by a factor of $(m_e/m_\mu)^2 \simeq 1/40,000$ and be safely neglected as is done in previous muon DIS experiments. This effect is called straggling.

The calculation of the radiative corrections used in this analysis are described in Chapter 4.

Chapter 2

DATA ACQUISITION HARDWARE

The E665 spectrometer[62] is a general purpose detector based on two superconducting dipole magnets arranged in focussing geometry. The incoming muon is detected by the beam tagging system. The beam interacts with the target located inside the CVM, a dipole magnet. The scattered muon and the produced charged particles are detected by the forward spectrometer built around a dipole magnet CCM. The muon is identified by a set of scintillator and proportional tubes planes behind a hadron absorber. In this chapter the E665 spectrometer, the muon beam, targets used in 1987-88 run and the data acquisition system are described. The main components of the forward spectrometer are shown in Fig. 2.1.

The E665 coordinate system is a right handed system (x,y,z) with +x axis oriented along the beam line and +z axis pointing up. The Z(Y) chambers measure z(y) coordinate and hence the wires are horizontal(vertical). The vector +u lie in (+y,+z) quadrant and +v in (-y,+z). The units used in the plots are meters, radians and GeV for distance, angle and momentum respectively.

2.1 Muon Beam

The NM beam line in the Neutrino area at Fermilab transports the world highest energy muon beam[66]. The 800 GeV proton beam extracted from the Tevatron is incident on a 48.5 cm long beryllium target. The hadronic interaction between protons and Beryllium produces pions, kaons and other particles. The primary protons are separated by magnetic deflection from the secondary hadrons and are dumped into an absorber. The secondary hadrons are momentum selected and are transported through 1097 m using a focussing-defocussing arrangement of quadrupole magnets (π -K FODO). During this distance about 5% of the pions decay into muons. At the end of π -K FODO, there is a 11 m long beryllium ab-

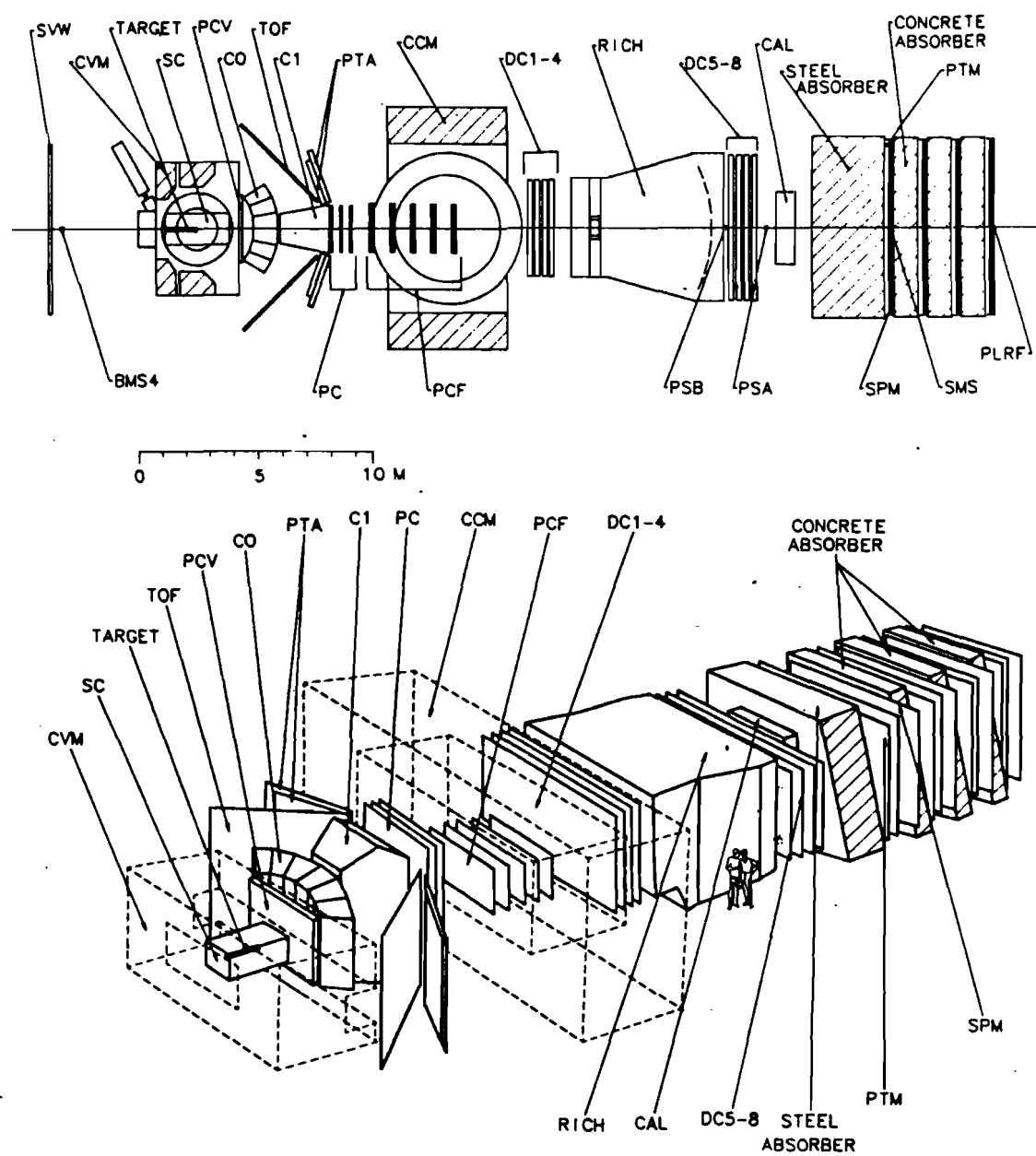


Figure 2.1: E665 forward spectrometer 1987-88

sorber. Almost all the charged particles except muon are stopped by this absorber. The muons are transported by a ~ 360 m long μ FODO to the experimental hall.

The decay muons are spread over wide area, some of them even outside the beam pipe. The muons outside the useful beam¹ are defined to be *halo*. A special feature of Fermilab muon beam is the use of the Mupipe. Mupipe is a toroid magnet with the beam pipe going through the magnet. The toroidal field spreads out the muons outside the beam pipe radially, thus decreasing the halo around the beam. The number of halo muons was about 20-30% of the useful beam during 1987-88 running period. About 50% of halo was within 20 cm radius of useful beam region.

The muon yield per proton, μ/p ratio, depends on the definition of useful beam and on the beam tune. For standard beam tune and beam definition during 1987-88 run the muon yield per proton was $\sim 0.55 \times 10^{-5}$. The muons coming from decay of pion are naturally polarized. The polarization factor depends on the momentum of the muon. The mean helicity of muon beam used in 1987-88 was calculated to be -0.83 ± 0.13 [67].

The Muon beam purity was checked during a special run. During this run the interaction rate was measured as the function of the length of the Beryllium absorber located at the end of π -K FODO in the beam line. The hadron contaminations of beam was determined to be 0.879×10^{-6} [68]. The hadrons in the beam do not effect the final event rate as an identified muon is required in the reconstructed event. The hadron contamination has a negligible effect of the incident muon beam flux.

The nominal Tevatron beam cycle time was 57 second. The beam spill was 22 second long. A 1024 Hertz clock was used to record the "real time" of the event. The elapsed time between the first and the last event in the same spill was measured to be 21.714 seconds with a spread of 0.156 seconds. The time between first events of two consecutive spills was 56.338 with a spread of 0.031 seconds. The most probable time elapsed between two consecutive events was 5 milliseconds. The minimum time between events, dictated by readout electronics, was 3 milliseconds. The spill gate defined by E665 electronics was set to 23 seconds and measured to be 22.996 seconds. The length of spill was calculated from the

¹ for definition of "useful" see section 2.8.1

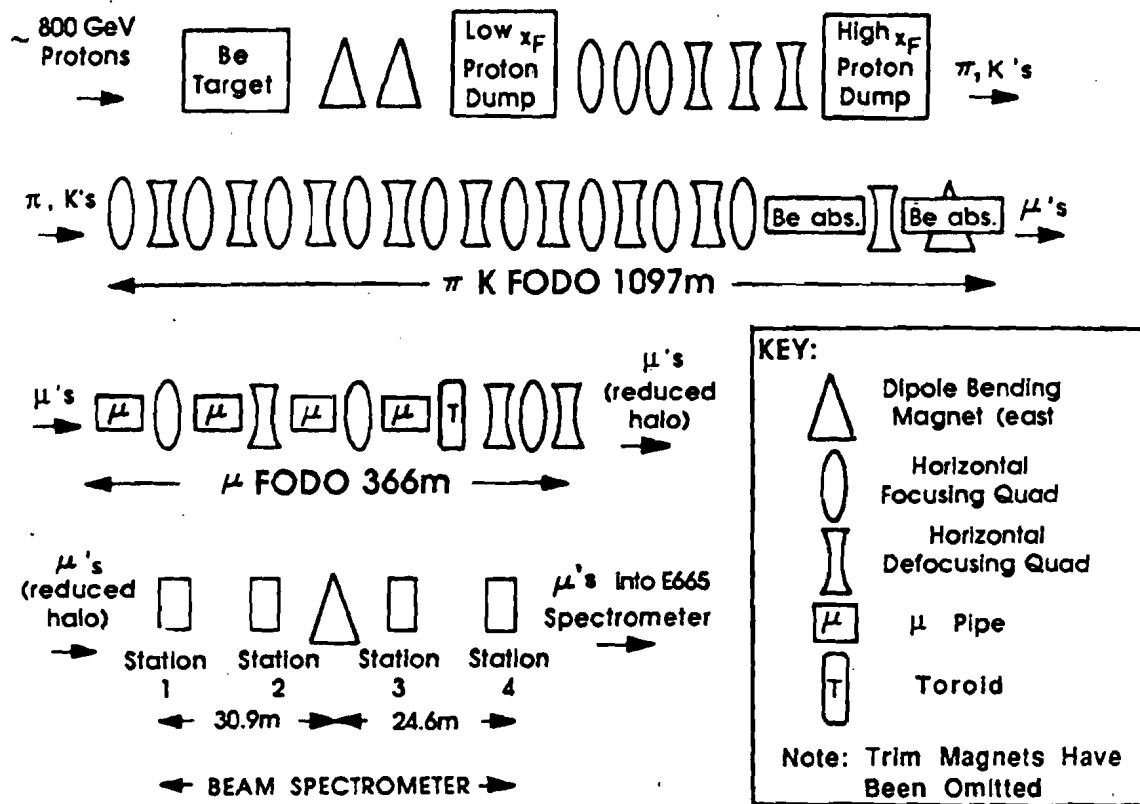


Figure 2.2: Muon Beam Line at Fermilab

number of ungated RF pulses scaled during the spill.

The proton beam at the Tevatron is bunched in buckets which are 18.8 ns apart (53.1047 Mhz). The muon beam preserves the proton beam time structure. A signal (PLRF) is produced by phase-locking the distributed accelerator RF to the time of arrival of muons in the experiment hall. The PLRF is used as a common time strobe for the data acquisition throughout the experiment. The muon signal is generated by the coincidence of four scintillators located behind the last muon detector plane.

The position of the beam (y, z) at the middle of the target is shown in Fig. 2.3. All of the beam is well inside the target volume except for the xenon target. The mean momentum of muon beam is 490 ± 60 GeV. The mean divergence of the beam at the target is less than 0.04 mr in both directions.

During the run the proton flux varied between 5×10^{11} to 4×10^{12} . Using a μ/p ratio of 0.55×10^{-5} , the mean number of muons per RF bucket was 0.0207 at maximum intensity. At this rate only 1.05% of the occupied RF buckets had more than one muon in it.

2.2 1987-88 Targets

During 1987-88 run data were collected with deuterium, hydrogen and xenon targets. The deuterium target was 1.15 meter long with a diameter of 9 cm. The walls of the target vessel were made of 0.025 cm thick mylar foil; wrapped by 20 layers of 0.006 mm mylar and surrounded by 2.1 cm of Rohacell foam. This assembly was contained in a 0.013 cm thick mylar vacuum cylinder. This assembly insulated the target vessel both thermally and electrically. The total thickness of the target vessel along the beam direction is about 1 mm (mylar/Kapton) equivalent to 1% of the thickness in grams of a deuterium filling.

The liquid deuterium temperature was held at 23.8 K°. The density of the deuterium, calculated from the vapor pressure, was 0.1602 g/cm³. The same target vessel was used for hydrogen. The liquid hydrogen temperature was held at 20.4 K° and the density was 0.0707 g/cm³.

The xenon target was 1.13 meter long and 7.07 cm is diameter. The xenon gas was held under 14 atmosphere of pressure. The xenon gas density was 0.085 g/cm³. The details of the calculation of density of the liquid targets and estimated

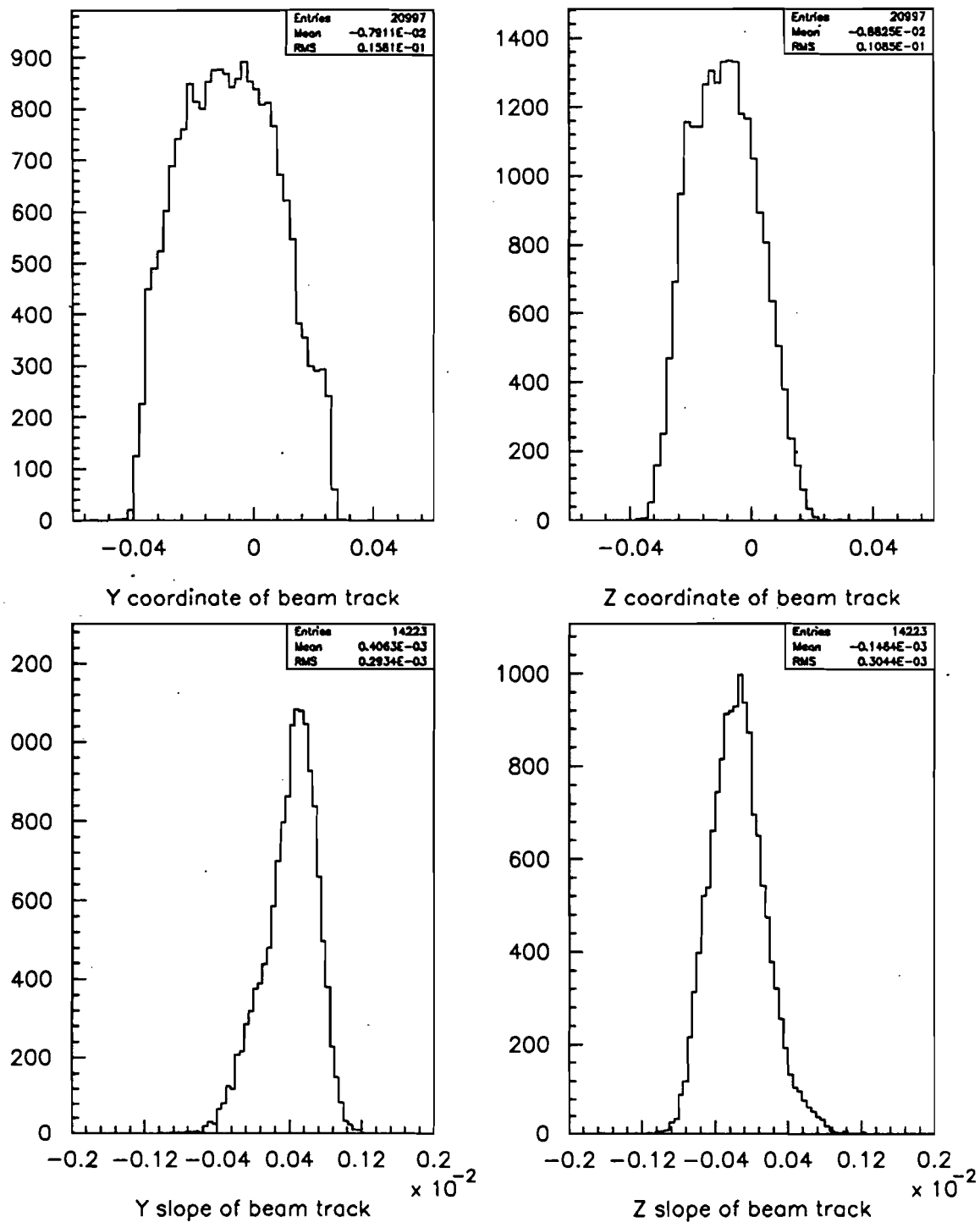


Figure 2.3: The track parameters of LAT beam at target
 The units for coordinates are in meters and for slopes are in radians

errors are described in [69].

2.3 Beam Tagging

The incoming beam trajectories are measured by the beam tagging system. The beam tagging system consists of four stations. There are two stations upstream of the dipole magnet (NMRE) and other two downstream. Each station consists of scintillator planes (SBT), wire chambers (PBT) and veto counters.

2.3.1 SBT Hodoscopes

The fast, precise timing information for the beam track is obtained by a set of scintillator planes (SBT). A SBT plane consists of 13, 1/2-inch thick, varied width, fingers with total area of 0.18 by 0.14 m². The beam station 1, 3 and 4 have two scintillator planes, one each in the Y and Z view. Station 2 has only one plane which measures the z coordinate. The output of the photo tubes is discriminated, shaped and latched. The width of the output signal is set to \sim 40 ns. The signals from the SBT fingers in a plane are ORed and are used in the hardware trigger for LAT. The amplitude of the analog signal from each SBT finger is digitized using a Lecroy ADC LRS2249. For hodoscope plane SBT4Y, the time of arrival of signal is also recorded using a TDC module.

2.3.2 PBT Chambers

The precise space position of beam tracks is recorded using 24 wire chambers planes (PBT). Each station has 6 wire planes measuring the U,Y,Z,V,Y',Z' views. These chambers have 12.8 \times 12.8 cm² physical area with 1 mm wire spacing. The Y'(Z') plane is offset by 0.5 mm from Y(Z) plane. The PBT chambers are operated at -3.1 keV high voltage. The gas used is 50-50 argon-ethane mixture. The readout is based on Lecroy PCOS system with Nanometric pre-amplifiers used to amplify the signal. The electronic gate used to record the signals on the wires was 200 ns wide. Assuming that all the chambers have same gate width and perfect hardware and software efficiency, it was calculated that 10% of the RBEAM events should have more than 1 beam tracks for a beam intensity of 1×10^6 per second.

Given the wire spacing of the chambers, and the lever arm between PBT stations, the angular resolution is approximately $10 \mu\text{r}$ for a reconstructed beam track. The fractional momentum resolution ($\Delta p/p$) is approximately 0.5%.

2.3.3 Halo Veto System

The triggers generated by muons outside the tagged beam present a serious problem in muon experiments because they add to the dead time during data acquisition and to the cpu time during analysis. In E665, a set of veto scintillators is used to detect the muons outside the useful beam region and inhibit any physics or normalization trigger during the RF bucket in which a halo muon is detected. This veto system consists of a veto wall (SVW) and 4 pairs of adjustable-aperture small scintillators (SVJ1-4). The veto wall has total area of $7 \times 3 \text{ m}^2$ which is segmented into 28 counters each having an area of $1.5 \times 0.55 \text{ m}^2$. These counters are mounted on 5 cm thick steel wall. There is a $25 \times 25 \text{ cm}^2$ hole in the veto wall at the beam region. The beam aperture at the veto wall can be adjusted using a pair of small scintillator veto jaws (SVJ4) mounted on the main structure of veto wall. The three pairs of veto jaws (SVJ1-3) are mounted on the last three beam stations further restrict the the beam phase space. The signals from the veto scintillators are used in the LAT trigger but are not used in the SAT trigger. These signals are also latched and digitized for further analysis.

2.4 Vertex Detector

The vertex detector, the part of the spectrometer which records the event information close to the interaction region consists of a steamer chamber(SC), 6 planes of wire chambers (PCV), and wide-angle proportional tube planes (PTA).

2.4.1 PCV chambers

The PCV chambers [70], with an active area of $2.8 \times 1.0 \text{ m}^2$ and 2 mm wire spacing, are located approximately 2 meters downstream of the center of the target, in the fringe field of CVM magnet. The six planes in PCV measure Y,U1,U2,V1,V2 and Y views of the track. The PCV chambers are important for providing good momentum resolution due to their large distance from the CCM. They also in-

crease vertex position accuracy due to their proximity to interaction point. The track density in the PCV chambers is very high because the particles are not well spread out as they pass through these chambers. This high density of tracks makes pattern recognition in PCV chambers difficult.

The cathode planes are made of graphite sprayed on 75 μm thick mylar which is glued on the Rohacell foam. The anodes are made of 20 μm gold-plated tungsten wires. The signal on the anode wires is preamplified and transmitted to a discriminator/univibrator on 66 m (450 ns) long cable. The univibrator pulse is 30 ns wide, therefore PCV chambers have virtually zero readout dead time. The output of the univibrator is latched by the Level I trigger and readout by CAMAC at the Level II trigger.

2.4.2 PTA Chambers

The wide angle proportional tube array consists of 4 (Y,Z,U,V) planes each on the east and west side of the beam line for a total of 8 planes. The proportional tubes are 2.54 cm square. Each plane, $1.90 \times 1.90 \text{ m}^2$ in area, consists of two layers, offset by half a cell, giving an effective wire spacing of 1.27 cm. The PTA planes can be read out in two different ways, as drift or proportional counters. In the drift mode the time of arrival of the signal on two offset cells is recorded. Using the drift velocity of the electrons the position of track can be calculated very accurately. In the proportional mode only the wire addresses are recorded. During the 1987-88 run the PTA were used in the proportional mode. The PTA chambers detect wide angle (low or negative x_f) hadrons and therefore are not important for cross section measurements.

2.4.3 Streamer Chambers

The only optical measurement device in the E665 spectrometer is a $200 \times 120 \times 72 \text{ cm}^3$ streamer chamber (SC) giving almost 4π coverage of in the center of mass frame of the μN system. The target vessel sits inside the streamer chamber. The streamers produced by charged particles in He-Ne-Isobutane gas mixture, are photographed by three cameras at different angles. The pictures are digitized by scanners. The digitized information from the three cameras is combined in software to give a 3 dimensional picture of the interaction. The SC has sin-

gle track space resolution of 0.85 mm and two track separation of 3 mm. The memory time of the streamer chamber depends on the gas composition and is approximately $1\mu\text{s}$. The SC is operated at rate of 1.5 pictures per second because several hundred milliseconds seconds are required to charge the Marx generator. The Marx generator is used to apply ± 350 kV high voltage on electrodes. Due to the large dead time in streamer chamber operation, a special trigger based on the track multiplicity in the PCN chambers is used. The streamer chamber is very important for studying the backward hemisphere in the center of mass frame of the interaction i.e. target remnant fragmentation. The streamer chamber does not add any information to the muon variables.

2.5 Forward Tracking

The forward tracking system which measures the medium and high momentum tracks is built around a dipole magnet, Chicago Cyclotron Magnet (CCM). Twelve planes of proportional chambers (PCN) measure the straight line section of tracks in front of the CCM. The CCM magnet, operated at 13.5 kGauss field, imparts a 2.2 GeV momentum kick to the tracks in the y direction. The straight section of the track which get through the magnet is measured by two stations of drift chambers(DC), eight planes each. The curved segment of the track is measured by the fifteen planes of wire chambers (PCF), located in the CCM magnet gap. The whole system has a design fractional momentum resolution ($\Delta p/p$) of 5.0% of momentum of the particle.

The drift chambers are deadened in the central region to withstand the high intensity beam without large dead time. The beam hole in the second station of drift chambers is almost covered by eight proportional chambers (PSA). The PSA chambers measure those muon tracks which scatter at very small angles.

2.5.1 PCN Chambers

There are 12 $2 \times 2 \text{ m}^2$ 3 mm chambers (PCN) arranged in three stations [71]. Each station in the PCN system consists of 4 wire planes with only 5 cathode foils. The wires are oriented perpendicular to the Y, Z, U, V directions where the U and V chambers make 61.92° and 118° with $-Z$ axis. The cathode is made of

a foil with graphite coated on both sides. A special feature of the PCN chambers is that they can be desensitized around the beam region. To achieve this end each cathode plane is divided in three regions, a central 60 mm diameter disc, a ring with external diameter of 120 mm and rest of the cathode. Each region is connected to the high voltage source separately. The spacing between planes is 1.2 cm and the stations are separated by 40.9 cm. The readout system is similar to PCV chambers based on a pre-amplifier, long cable delay, discriminator, a one-shot and the encoding electronics. The gas used is a mixture of argon (71.8%), isobutane (28%) and Freon (0.14%).

2.5.2 PCF Chambers

The 15 PCF, $2 \times 1 \text{ m}^2$, chambers are located in the CCM gap. They are arranged in 5 stations of 3 (U, V, Z) planes each. The wire spacing of the PCF chambers is 2 mm. A non-flammable gas mixture, Argon-CO₂, is used. The typical operating voltage is -3.8 keV . The data is readout serially using electronics built by Nanometric Inc. The University of Washington is responsible for construction, testing and maintenance of the PCF chambers. The construction, electronics and performance of the PCF chambers is described in detail in Appendix A.

2.5.3 DC Chambers

The drift chambers [72] are arranged in 2 stations of 8 physical planes each. The first station (DCA) has an active aperture equal to $4 \times 2 \text{ m}^2$. The active aperture of the second station (DCB) is $6 \times 2 \text{ m}^2$. The second station is located approximately 8.5 m downstream of the first station. Each DC plane consists of two anode wire planes. The wires in the two planes are offset by half a cell. The *time sum*, sum of the time of arrival of the signal on the offset wires, is independent of the position of the track in the cell. This information is used to reject the out-of-time hits in the DC chambers. The Z chambers are divided at the middle into two independent planes to increase the capability to detect multiple tracks. All the DC chambers have the same size drift cell, $5.08 \times 0.95 \text{ cm}^2$. The gas used is argon-ethane with a field gradient of approximately 800 volts. The drift velocity was measured using halo tracks. The typical drift velocity was $\sim 4 \text{ cm}/\mu\text{s}$. A four parameter time-to-distance relationship is used in the analysis [73] to calculate the position of

the track from the recorded time information. The typical spacial resolution (σ) for the 1987-88 run is 0.55 mm for Z chambers and 0.4 mm for U/V chambers. The preamplified, discriminated anode signals are sent to MUTES, multihit-time-encoding-system, via a long twisted-pair cable. The two track resolution is about 4 mm (100 ns), dictated by front end amplifier response time.

The drift chambers are made dead in the beam region. The location and size of the dead regions was determined from deep inelastic data[74] and the results agree with an earlier study [75] using halo tracks. The size of the dead region determined from data is a little bigger than the physical size. The extra dead region is caused by the edge effects of high voltage field shape.

2.5.4 PSA Chambers

The beam dead region in second station of drift chambers is covered by the eight PSA chambers. These chambers have the same mechanical design and electronic readout system as the beam chambers described in section 2.3.2. Four of the PSA chambers measure Z, Y, Z', Y' coordinates where Z'(Y') is offset by 0.5 mm with respect to Z(Y). The other four chambers are rotated by 45° and measure U, V, U' and V' coordinates. The planes have an active area of $12.8 \times 12.8 \text{ cm}^2$. The typical high voltage used is -3.1 kV for the PSA chambers. The gas mixture used is 50-50 argon-ethane bubbled though ethanol at 0°C.

2.6 Muon Detection

The scattered muon detection system is based on an 18 nuclear interaction (3 m) length hadron absorber made of steel and four planes of scintillators (SPM, SMS) and four planes of proportional tubes (PTM).

The scintillator planes (SPM, SMS) give fast timing information for the triggers. The PTM's give accurate space information for the reconstruction of the muon tracks. These PTM planes are separated by 90 cm thick concrete walls to minimize the effect of electromagnetic showers which accompany the muon emerging from a thick absorber.

2.6.1 SPM and SMS

Each scintillator plane consists of large counters (SPM) and a small hodoscope (SMS) in the beam region. The SPM planes are divided into two rows each containing 15 counters. Each counter is a $150 \times 50 \times 2.5 \text{ cm}^3$ sheet of Rohm GS 2030 except the central counters (top, bottom) which are made of NE110 plastic sheet, $140 \times 20 \times 2.5 \text{ cm}^3$ in area. The light produced in these counters is wave shifted by $2 \times 2.5 \text{ cm}^2$ Rohm GS1919 shifter bar and is collected by photo tubes. The maximum travel time of the light is about 6 ns. The total light integration time is approximately 20 ns. The analog threshold is set at 2–3 photons. The output of the photo tube is discriminated and shaped at the base of the tube. The shaped signals are transmitted to the electronics on twisted-pair cables. The width of the output signal is set to 40 ns, approximately two RF buckets. The hole in the SPM in the beam region is covered by the SMS hodoscope with small overlap. Each SMS station consists of 2 planes, one measuring the Y coordinate and other the Z coordinate. Each plane consists of 16 fingers. Each finger is $21.6 \times 1.27 \text{ cm}^2$ in area. The signal from each finger is latched and digitized. Moreover the signal from the SMS are made available to both the SAT and LAT trigger logic electronics. The SMS latch information is used in reconstructing the trajectory of muons which scatter at small angles.

2.6.2 PTM chambers

Each PTM station has two $6 \times 2 \text{ m}^2$ planes one each in the Y and Z views. Each PTM plane is made of two layers of 2.54 cm wide extruded Aluminium tubes offset by half a cell, giving an effective wire spacing of 1.27 cm. The active area of the PTM planes is $3.6 \times 7.2 \text{ m}^2$. The system used 50-50 argon-ethane gas mixture, operated at 2.7 keV, with a maximum drift time of 250 ns in a cell.

2.7 Particle ID and Calorimeter

In addition to the muon identification system, two threshold Cerenkov counters C0 and C1, one ring imaging Cerenkov (RICH), time of flight counters (TOF) and an electromagnetic calorimeter are used to identify the particles in the E665 spectrometer. The particle identification detectors are not used in the analysis

presented in this dissertation.

2.8 Triggers

During the 1987-88 data taking run, 8 different triggers were used for data acquisition. They included physics triggers (LAT, SAT, FCAL), normalization triggers (RBEAM, RSAT) and a calibration trigger (HALO). Two special triggers were used for the Streamer Chamber data acquisition.

Special trigger configurations were used for data taken for alignment of the detector. During a special run, the data were taken using the electron beam. These data was used to calibrate the EM calorimeter, the Cerenkov detectors and Time of Flight system. The hardware features of the triggers used are described in this section. The typical trigger rates per spill for hydrogen running period during 1987-88 run are given in table 2.1.

Table 2.1: Hydrogen Raw Statistics per Spill

Beam (7/7 SBT)	1.62×10^7
B. \bar{V} (ungated)	1.30×10^7
Beam for LAT (LATB)	1.10×10^7
Beam for SAT (SATB)	1.45×10^6
LAT triggers	280
SAT triggers	219
RBEAM triggers	22
RSAT triggers	33

2.8.1 Large Angle trigger

The large angle trigger (LAT) consisted of following requirements :

1. presence of useful beam;
2. absence of any veto signal in beam region;
3. detection of the muon behind the absorber out side the beam region;
4. absence of any muon inside the beam region behind the absorber.

An incident muon is defined to be beam if all 7 SBT planes have hits. The fingers in the SBT plane are ORed to generate the signal. The veto signal is the OR of all the scintillator counters described in section 2.3.3. The detection of the muon by all SBT planes with no signal the in veto counters defines the useful beam. Symbolically it is defined as

$$\text{LATB} = \prod_{i=1}^7 (\text{SBT})_i \cdot \overline{\sum_{j=1}^4 \text{SVJ}_j + \text{SVW}}$$

In hardware terms the detection of the muon outside the beam region means that at least 3 out of 4 SPM planes have a signal. The counters in each SPM plane are ORed together. The absence of a muon in the beam region implies that the SMS stations 1 or 4 does not have any signal.

Symbolically the large angle trigger (LAT) can be written as

$$\text{LAT} = \text{LATB} \cdot (3/4)\text{SPM} \cdot \overline{\text{SMS1} + \text{SMS4}}$$

where the LATB is defined above. For the LAT trigger, hits in different SPM planes are not required to be correlated in space. Moreover the track is not required to point back to the target. The positive muon signal in the SPM planes does not reduce the trigger rate to a low enough level. The reduction in trigger rate is achieved by using SMS veto. The SMS veto signal is an OR of four hodoscope planes (SMS 1Y,1Z,4Y,4Z) and thus is quite efficient. Remember that the veto inefficiency must be less than 1×10^{-5} to reach a reasonable ratio of useful to background triggers. This is important because the experiment is dead time limited. The expected physics trigger rate is approximately 10^{-6} per incident muon.

2.8.2 Small Angle Trigger

The small angle trigger (SAT) is based on a floating veto. The position of the veto region moves with the trajectory of incoming muon. The beam defined by the SBT fingers is projected to the SMS planes behind the absorber. If a signal is detected in SMS planes within a small window around the projected beam, the event is not triggered. The hardware of the SAT trigger is explained in detail in reference [83].

The SAT beam is defined by four SBT Z planes and two SBT Y planes (SBT3Y, SBT4Y). For the SAT veto signal only SMS1Y and SMS2Y are used.

The size of the SMS veto is variable. It depends on the hit pattern in the SBT planes. The minimum size of veto is equal to three SMS counters. The SAT beam is defined by only the central five counters in SBT planes. Thus the SAT trigger utilizes approximately 12% of total beam available.

From the beam trajectories generated by monte carlo, the possible combination of the SBT fingers were determined. These possible combinations define the useful beam for SAT trigger denoted by SATB. Given these possible combinations the y,z point at muon scintillator hodoscope was calculated assuming the muon trajectory to be a straight line. The straight line approximation is good if the spectrometer is arranged in focussing geometry. The maximum error in predicted point is approximately equal to width of 1 SMS finger (1.2 cm) in y direction for a beam tracks which passes through central SBT fingers. The central SBT fingers are 6.4 mm wide and the two SBT stations (3Y,4Y) are 20.66 m apart. The above estimate assumes that the incident beam can have a slope upto 3 mr. In reality the slope of the beam is less .1 mr in Y directions. The typical size of the veto region was 5 SMS counters.

The set of SBT fingers defining incident beam and the predicted SMS fingers defining the veto region constitute a trigger matrix. The trigger matrices are stored in an ECL based lookup table. The lookup table is downloaded using CAMAC and can be changed very easily. For each incoming beam track, the actual hit pattern is compared with the entries in this table and the appropriate signal is generated.

A few extra requirements were made to cleanup the SAT beam in the 1987-88 run. If any of the SBT planes had more than one hit, the event was rejected. Moreover it was required that there be no muon in the preceding or the following RF bucket. The veto counters in the beam tagging system described in section 2.3.3 were not used in the SAT trigger, implying that the SAT beam is not a subset of the LAT beam (LATB).

2.8.3 Random Beam trigger for LAT (RBEAM)

For measurement of the incoming beam flux, the prescaled LATB (as defined above) was used as trigger. This trigger is named RBEAM trigger. The LATB was prescaled by a by a factor of 2^{18} for the deuterium and 2^{19} for the hydrogen target. The prescaler (RAND1) randomly prescaled the RF signal by 2^{15} . The random number is generated using an electronic circuit described in Horowitz and Hill. The prescaled RF is further prescaled by a factor of four for deuterium data and six for hydrogen using a prescaler which is not random. The trigger signal is generated by a coincidence of the prescaled random RF and the LATB signal.

2.8.4 Random Beam for SAT (RSAT)

The SAT normalization trigger (RSAT) was generated by prescaling SATB, beam defined by SAT matrices, by a 2^{16} . The same random number generator module (RAND1) used for the RBEAM is used for the RSAT. This enables a the direct comparison of RBEAM and RSAT triggers on an event by event bases.

2.8.5 FCAL

The FCAL trigger is based on the total energy deposited in the electromagnetic calorimeter. The beam requirement for this trigger are same as for Large Angle Trigger except it was required that there be no muons in the preceding 15 buckets. The FCAL trigger does not require any muon behind the absorber. This is the only physics trigger which does not use veto behind the steel, hence can be used to study the effect of veto on LAT and SAT triggers. The energy in the calorimeter outside 32 cm wide vertical and horizontal stripes centered on the beam is summed. If the energy deposited is more than 60 GeV, the event is triggered.

2.8.6 Halo Trigger

The HALO trigger is based on the hits in the veto scintillators in coincidence with 3/4 SPM planes behind the absorber. These data are used to monitor the alignment and efficiency of the wire chambers. The data from the Halo trigger covers all the active area of the large chambers and hence is very useful for the calibration and the efficiency studies.

2.9 Data Acquisition System

The E665 data acquisition system is based on four frontend machines, a μ VAX and a VAX780/11. The four frontends consist of 3 PDP-11 computers and a fastbus module. The PDP-11s read the data from CAMAC and send them to the μ VAX. The calorimeter data is read by a FASTBUS module. The μ VAX concatenates the subevents received from four frontend machines and writes them to a 6250 bpi tape. The subevents are correlated using a hardware event number read by all four frontend machines. The tape writing process is asynchronous from electronic readout of individual modules. Thus the experiment's electronic dead time is determined by the CAMAC/FASTBUS readout and the memory of the frontend machines only. The local memory of the machines determines the amount of data which can be stored before being written to tape. A small fraction of events is sent to the VAX 780/11 for online monitoring. The data acquisition software is based on Fermilab Vax Online software, modified to accommodate the E665 hardware. All the operations are controlled from the μ Vax. The typical readout time of an event is \sim 3 milliseconds. At maximum throughput the apparatus dead time from readout is \sim 20%.

2.9.1 Monitoring and Calibration

One of the important functions of the data acquisition system is to ensure the integrity of the data being written to tape. In E665 data acquisition system, monitoring was done in following different ways.

- As mentioned above a sample of events was sent to the VAX780 for monitoring. These data from various detectors were decoded and the software made a rudimentary efficiency check and looked for dead channels in the wire chambers and hodoscopes. In case of gross malfunction a message was sent to the shift personnel and appropriate action was taken. Due to CPU limitations only a very small number of events could be processed by the VAX780.
- In between spills, monitoring tasks were run on PDP-11s. These tasks checked, among other things, the high and low voltages on various ph-

totubes and wire chambers and recorded ADC pedestal information for various detectors. The normalization information like the number of incoming muons, LATBs, SATBs, event yields per muon, relative contribution of various triggers and the event size from each sub detector were monitored for each spill. This was a very quick method to spot the changes in beam tune, drop in voltages on various scintillator planes or other electronic failures.

- The data integrity was checked offline for a small subset of data using a dedicated μ Vax. In Data Validation program, some elementary plots for wire chambers (wiremaps, number of hits per plane) and scintillator hodoscopes (pedestal of ADC, TDC) were made. Some basic pattern recognition was done to calculate the efficiency of wire chambers. The data validation program, though not much more sophisticated than the vaxonline program, was very useful because the cpu was available and it was easy to use.
- Various sub-detectors e.g. PCF, TOF, RICH used microcomputers to run interspill tasks to read the ADC pedestals and high and low voltages. For TOF and RICH the data was processed on the microcomputer and sent to the main data stream in between spills via the dual memory modules sitting in the CAMAC crates. For PCF system, the microcomputer was used only for controlling the high voltages and debugging the electronics, if there was a problem.

2.10 Data Set 1987-1988 run

A summary of the number of events recorded during the 1987-1988 run is given in tables 2.2 and 2.4 for deuterium and hydrogen targets. These tables were compiled using the end-of-spill scaler information (see section 4.2.1). The three tables contain the information respectively from entire deuterium sample, post Dec 1,1987 deuterium sample and hydrogen sample. The deuterium data taken before Dec 1, 1987 was not used in analysis due to unstable detector performance. The SAT trigger configuration was changed after Dec. 1, 1987. Before December 1, the veto was used in both vertical and horizontal directions whereas the veto used after December 1 was only in Y direction. The acceptance for two trigger

Table 2.2: Deuterium Raw Trigger Statistics (all)

Beam (7/7 SBT)	3.06×10^{11}
B. \bar{V} (ungated)	2.34×10^{11}
Beam for LAT (LATB)	1.83×10^{11}
Beam for SAT (SATB)	0.27×10^{11}
LAT triggers	4.28×10^6
SAT triggers	2.94×10^6
RBEAM triggers	0.72×10^6
RSAT triggers	0.53×10^6
LAT/LATB	2.34×10^{-5}
SAT/SATB	1.04×10^{-4}

configurations is different and therefore the two data sets can not be combined trivially.

The trigger rate per incident muon for deuterium and hydrogen is comparable despite the factor of two difference in target densities. This indicates that a large fraction of the triggers for both the hydrogen and deuterium data set are fake. In addition data sets were taken with modified trigger, beam and magnet configurations. These data sets were used for the calibration of detector. These data include alignment data, DC calibration data, and electron beam data.

Table 2.3: Deuterium Raw Trigger Statistics (post Dec 1987)

Beam (7/7 SBT)	0.69×10^{11}
B. \bar{V} (ungated)	0.54×10^{11}
Beam for LAT (LATB)	0.44×10^{11}
Beam for SAT (SATB)	0.53×10^{10}
LAT triggers	1.07×10^6
SAT triggers	0.88×10^6
RBEAM triggers	0.17×10^6
RSAT triggers	0.12×10^6
LAT/(LATB)	2.45×10^{-5}
SAT/SATB	1.68×10^{-4}

Table 2.4: Hydrogen Raw Trigger Statistics

Beam (7/7 SBT)	1.72×10^{11}
B. \bar{V} (ungated)	1.38×10^{11}
Beam for LAT (LATB)	1.16×10^{11}
Beam for SAT (SATB)	0.15×10^{11}
LAT triggers	2.72×10^6
SAT triggers	2.30×10^6
RBEAM triggers	0.23×10^6
RSAT triggers	0.35×10^6
LAT/LATB	2.34×10^{-5}
SAT/SATB	1.50×10^{-4}

Chapter 3

DATA ANALYSIS SOFTWARE

To extract physics information from the data written on magnetic tapes, one needs to translate the latched bits, pulse heights and wire addresses to the kinematics of the interaction and the properties of the individual particles. The process of translating data falls under the general heading of data analysis. The E665 main analysis chain is divided in four subprograms. Each subprogram is logically and structurally independent of the other subprograms except for a well define I/O format. These subprograms are structurally parallel and can be combined together easily. These subprograms, pattern recognition (PR), track fitting (TF), muon match (MM) and vertex fitting (VX) are described in this chapter. The alignment program used to align the detector is a separate program but follows the same structure. The procedure of alignment and the results are described in section (3.1). The E665 Monte Carlo program used to simulate physics processes and the detector response is also described in this chapter.

3.1 Alignment

One of the basic requirements before any pattern recognition, grouping hits into candidate tracks, can be done is the relative position of the various detectors is known accurately. The encoded wire addresses can be translated to space coordinates only if the location of a wires in space is known. The accuracy of the location of chambers in space determines how many and how well the trajectories of particles can be reconstructed. The accuracy of the track parameters, in particular the momentum, determines the precision of event kinematics (Q^2 and ν) and hence the final physics results.

The wires in the proportional chamber, in general, are coplaner, equally spaced and parallel to each other. Assuming these properties for the chambers the minimum requirement is to determine for each plane

1. the position of the wire plane along beam direction	(X_0)
2. the orientation of the wire plane around the y axis	(β)
3. the orientation of the wire plane around the z axis	(γ)
4. the position of the first wire in the wire plane	(θ_0)
5. the wire spacing	(λ)
6. the wire orientation	(α)

With this information, the addresses of the wires can be translated into space coordinates. This is nothing but the statement that to specify a vector(wire) in space one needs 6 parameters.

In E665 500 GeV muon tracks were used to do the software alignment of the chambers. Given the fact that the muons are incident on the chambers at very small angles, one cannot determine the x position of the chambers accurately using the muon beam. The maximum survey error in the x position is of the order of a few millimeter. The maximum survey error in the angles β and γ is less than a few milliradians. An error of 2 mr in β or γ will translate into an error of 2 mm in x for a track which is 1 m away from the center of chamber. The track parameters (y, z, y', z') are not sensitive to such small errors in x position. Therefore x position of the chamber, and the angles, β and γ , were not determined by software. Instead their survey values were used. The parameters θ_0 , α and λ were determined by software for every wire chamber and the hodoscope plane used for the pattern recognition.

3.1.1 Coordinate System

The first step in alignment is the choice of a coordinate system. The $Y=0$ and $Z=0$ line (X axis) is defined by the nominal muon beam line. This line passes through the center of CVM and goes 2.0 inches west of the centre of the CCM. All the elements in the E665 detector were surveyed with respect to this line. For software alignment, it was assumed that first wires in the four beam chambers (see section 2.3.2) PBT3Y1, PBT3Z1, PBT4Y2, PBT4Z2 were surveyed correctly. These four chambers define the new software X axis of the experiment. All other chambers were aligned with respect to these four chambers. In general one can define any coordinate system as long as the position of every detector and the magnetic field maps are represented in the same coordinate system. Comparing the software

alignment results (see below) with the survey constants of PCF chambers it was determined that the deviation of the software x axis from the nominal beam line is not more than few millimeter which is much smaller than the grid size (4 inches by 2 inches) used to measure and represent the magnetic field in CCM. Therefore the effect of the difference in coordinate systems on the momentum measurement is negligible and can be ignored.

3.1.2 Alignment Procedure

The alignment program is based on the tracks found by pattern recognition program. In the alignment program only those hits are used which are associated with the found tracks. The alignment program is an iterative program. The pattern recognition reconstructs candidate tracks using an approximate set of constants. These tracks are used to determine new set of constants. The procedure was repeated until the change in the constants was less than $\sim 5\%$ of the wire spacing.

- **Reference Tracks** To do the alignment one needs a vector in space (track) as a reference. The reference track parameters were determined in two different ways.
 1. **Defining the track** : Given four vectors in space, a straight line which intersects all four vectors is uniquely defined¹. The line defined by these vectors depend on the their Euler angles (α, β, γ). The wires in four different chambers form such a 4-vector set. The chambers PBT2Y1, PBT3Z1, PBT4Z2, PBT4Y2 were selected to align PBT chambers and therefore they define the reference system for the whole experiment. These chambers have good resolution, a long lever arm and are located downstream of NMRE magnet and can be used to align the forward spectrometer even when NMRE is on.
 2. **Fitting the track** : In this case a straight line fit was used to calculate the track parameters assuming the β and γ angles were zero for all the planes. This method was useful to factor out the effects of wire

¹ In the most general case it is an overconstrained system but in E665 most of the chambers are parallel to each other and the system is not overconstrained.

quantization on the track parameters. To align PCV, PCN, PCF, PSA, PTM, SMS detectors the PBT station 3 and station 4 were used as reference system for the θ alignment. At least 8 chambers (out of a maximum of 12) were required to contribute to the fit. In the case of the DC chambers, the PCF chambers served as the reference system. The PCF chambers were used to do α and λ alignment of PC, PCV, PCF and DC chambers.

- **Wire Position Alignment (θ)** The generalized coordinate perpendicular to the wire direction is called θ in E665. A wire plane measures the θ coordinate of the track. The θ is measured with respect to first wire (θ_0) in the plane. To do a θ alignment the reference track is projected to the plane to be aligned and the intercept is calculated. This intercept (y, z) is transformed to the local coordinate system giving θ of the incident track. The residue

$$R = \theta_{\text{projected}} - \theta_{\text{real}} \quad (3.1)$$

is plotted. The mean of the residue distribution was made zero by adjusting the position of θ_0 . After the wire position alignment, θ_0 (more correctly the middle wire) in the plane is known accurately with respect to E665 coordinate system.

- **Wire Orientation Alignment (α)** If the orientation of the wires in the planes is wrong, the residue, as defined above, will depend on the position of the track along the wire. It can be easily seen graphically or using algebra as shown below.

The generalized coordinate θ is given by

$$\theta = y \sin \alpha - z \cos \alpha \quad (3.2)$$

Differentiating with respect to α one gets

$$\frac{\delta \theta}{\delta \alpha} = y \cos \alpha + z \sin \alpha \quad (3.3)$$

where $y \cos \alpha + z \sin \alpha$ is the direction perpendicular to θ i.e. along the wire direction. Therefore, if α is wrong, the residue will change as we move along the wire. The mean residue was plotted as a function of distance along the wire. The slope of this plot is related to the error in α . Adjustments were made in α to make the the slope equal to zero.

- **Wire Spacing Alignment (λ)** If the wire spacing in the plane is wrong, the residue will change in the direction perpendicular to the wire. In other words the residue will increase or decrease with the wire number. This is evident from the definition

$$\theta = \theta_0 + n_{\text{wire}} \lambda \quad (3.4)$$

where θ_0 is the position of the first wire, n_{wire} the ordinal number of the wire hit and λ is the wire spacing. The mean residue was plotted as a function of distance perpendicular to the wire and the slope of the plot the wire spacing was adjusted. The corrections to the hardware nominal values were so small that the momentum measurement is not affected except at the very edges of chambers where there are only a few tracks.

3.1.3 Analysis and Results

All the detectors were aligned using 500 GeV muon tracks with magnet and trigger conditions as given in table 3.1 for the θ alignment. For α and λ alignment of PCV, PCN, PCF, DC and PTM the halo muon tracks were used because they were spread over the whole face of the chambers. There were 5 different alignment runs during 1987-88 data taking period. Five different sets of alignment constant were generated. They were organised by run block numbers.

- **θ Corrections :** All the chambers except the DC were aligned using PBT planes as reference planes. For DC chambers, PCFs were used as a reference system. The residue plots for PBT chambers are shown in figure (3.1). The typical accuracy achieved was less than 1% of the wire spacing. For PBT chambers different combination of reference planes were used to check consistency of the results and choice of reference planes. Moreover the results

Table 3.1: The trigger and magnet setting for alignment

Detector	NMRE	CVM	CCM	TRIGGER
PBT	OFF	--	--	RBEAM
PCV	ON	OFF	OFF	RBEAM
PCN	ON	OFF	OFF	RBEAM
PCF	ON	OFF	OFF	RBEAM
PSA	ON	OFF	OFF	RBEAM
DC	ON	OFF	OFF	HALO
PTM	OFF	OFF	OFF	RBEAM
SMS	ON	OFF	OFF	RBEAM

using the data taken when dipole magnet NMRE was on were compared with the results from the magnet off data. This comparison was done to study the change in alignment constants if the incident angle of the incoming track is changed. This study was done for the PBT, PCV, PCN, PCF chambers. The difference in the two sets of constants was consistent with zero within errors.

The final changes in the position of the first wire from surveyed values are given in table (3.2). The surveyed values are not available for the PCN chambers. The changes for the PCF chambers are not meaningful because the position of the wires with respect to the surveyed marker points was not known accurately. The variation between constants for different run blocks is no more than few millimeters in most cases.

Table 3.2: The difference in alignment constant from surveyed values

Detector	view	
	z	y,u,v
PBT	0-1 mm	0-1 mm
PCV	—	0-1 mm
PCF	1-2 mm	4-6 mm
PSA	1-2 mm	6-8 mm
PTM	5-6 mm	7-13 mm
DC	0-1 mm	8-9 mm

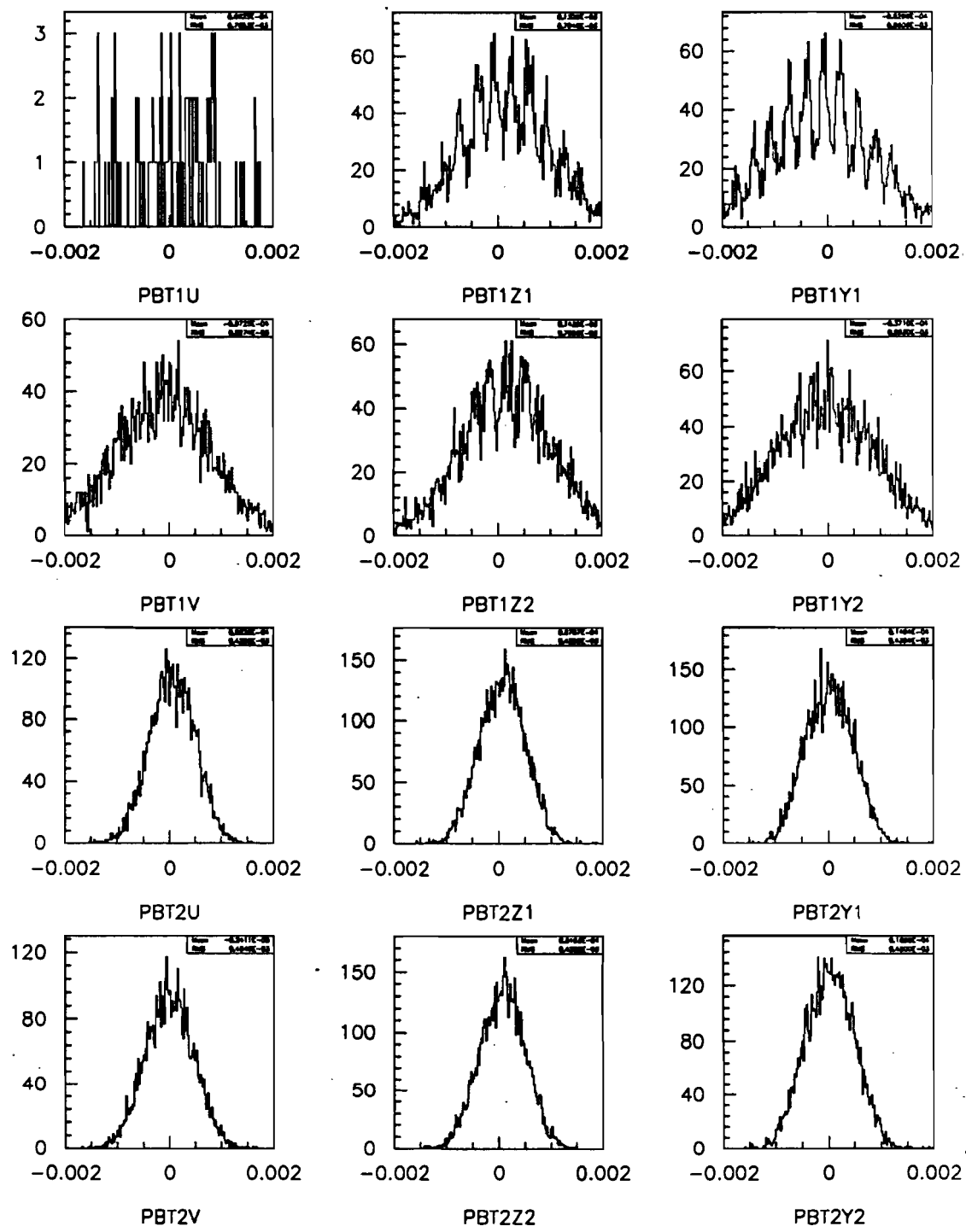


Figure 3.1: Residual plots for PBT Chambers Alignment

- λ Corrections : The wire spacing for PBT chambers was checked and found to be 1.000 mm, consistent with design value. A consistent set of wire spacings was determined using different types of reference tracks and reference planes in PCV, PCN, PCF chambers. The PCF wire spacing was changed from the nominal 2.000 mm to 1.997 mm which in better agreement with the measured value on a small test chamber. No change was made to the wire spacing of PCV and PCN chambers from the nominal values 3.000 mm and 2.000 mm, respectively. The tracks using hits from PCV, PCN and PCF chambers were used to find the wire spacing of DC chambers. The wire spacing of the Z chambers in DCA was changed from nominal of 50.800 mm to 50.702 (0.19%), and of the Z chambers in DCB to 50.068 mm (0.23%). This implies that a wire which is 1 m away from the center of the chambers is displaced by ~ 2 mm ($\sim 3\sigma$). No hardware reason for this effect could be determined and the software results were taken at their face value. For the U/V DC chambers, the nominal wire spacing was found to be correct within errors. The wire spacing in PTM and SMS did not need any change also.
- α Corrections : Corrections the angle of orientation of wires (α) were made for the PBT, PCF and DC chambers. The nominal α values for PCV, PCN and PSA were found to be correct. The the surveyed values of the orientation of wires in PTM's and SMS's planes were used. As PTM and SMS are not used in momentum measurement, the small inaccuracy in their constants has no effect on the final results.
- Miscellaneous Corrections
 - It was discovered that some of the PCF U/V chambers were split by approximately 0.3 mm in the middle. Remember that the two halves of the PCF U/V chambers were wired independently. A special set of constants were used to corrected the translated position of the wires. A similar correction was made for PCF2Z also.
 - It was found the PCV and DCA chambers move down by 0.5 mm when the CVM and CCM magnets are turned on. The constants were

changed to reflect this effect.

- It was discovered that three readout cards, one each in PBT1V,PBT3U and PBT4Z were not plugged in correctly and software correction were made in PBT decoder. A card in PC3U was also found to be misplaced and corrected accordingly.

The location of minimum y, z point of the physical aperture of the chambers were adjusted to reflect the changes in the wire position of the chambers. For the PCF chambers, even though the the position of first wire was adjusted by ~ 6 mm, the changes in the y corner and z corner were less than 2 mm. The y and z corners did not change because the orientation of the wires (α) was also changed at the same time. This suggests that the software x -axis was less than 2 mm away from survey x axis. The PCF chambers are very good for cross checking the x -axis because they are very close the center of CCM, the (0,0,0) of E665 coordinate system.

3.2 Pattern Recognition

The purpose of the pattern recognition program (PR) is to group the wire chamber hits into candidate tracks. The pattern recognition program in E665 is a multi-pass, multi-processor program. It consists of many independent subprograms , called processors, using different algorithms. The processors (except beam processor) are used twice (muon and hadron phase) using different internal requirements. In this section some aspects of the pattern recognition program are described.

3.2.1 Beam Spectrometer

As described above the beam tagging system consists of 4 stations. Each station has 6 planes (U,Y,Z,V,Y,Z) with 1 mm wire spacing. A dipole magnet (NMRE) is located between station 2 and 3 which bends the 500 GeV particles by 3 mr. The beam pattern recognition is based on the so called space point algorithm.

In the space point algorithm, the hits in three planes are combined as space point candidate if the sum

$$\Delta = \theta_1 \sin(\alpha_2 - \alpha_3) + \theta_2 \sin(\alpha_3 - \alpha_1) + \theta_3 \sin(\alpha_1 - \alpha_2) \quad (3.5)$$

is less than Δ_{max} where Δ_{max} depend on the geometry of the chambers. The preselection of space point candidates saves cpu time. Note that the above equation requires only three multiplications and two additions and hence is very fast. The trigonometric functions are evaluated only once. The good space points are selected from these candidates using a least square fit. Only the space point having good χ^2 probability are retained. For each PBT station, eight 3-plane combinations (space points) can be formed, given a hit in each plane. The fitted space points in a station are grouped together to form the super-space-points. A super-space-point has more than three planes contributing to it. Given the space points at each station a straight line fit is done in the non-bend view (Z). The space points associated with this z line form the space line which has two straight segments in the y view. These y segments are required to meet within 1.5 mm at the middle of the NMRE magnet. If due to chamber inefficiency or position of the track within a chamber, a station does not have at least one space point, the track is reconstructed using three stations with a space point each and the fourth one contributing only a y - z intersection. This allows us to reconstruct tracks going near the corners of the U/V chambers where due to mechanical construction difficulties, sense wires are not installed.

After the space track is found using wire chamber information, hodoscope information is used to determine whether the track is in time with the PLRF strobe which triggered the experiment (SB processor). The beam track is categorized *in-time* if all the 7 scintillator planes have hits within a small window around the track projected to that plane. The window is chosen a little bigger than width of the fingers in SBT hodoscope. An extra 1.5 mm is added to take into account any potential misalignment between the wire chambers and hodoscopes.

The beam pattern reconstruction efficiency was estimated to be $96.51 \pm 0.16\%$ for single in time track events. The efficiency was estimated using SAT Monte Carlo (MC) data for hydrogen time period. In MC simulation, the chamber efficiencies extracted from data were used.

3.2.2 Muon Projections

The muon identification system in E665 consists of four sets (Y,Z views) of proportional tube planes (PTM) downstream of the absorber. The wire spacing of

these planes in 12.7 mm. The dead region in the PTM planes around the beam region is covered by four sets (Y,Z views) of scintillator planes (SMS) having the same resolution. The y and z projections cannot be grouped into a three dimensional track because there were no planes which can correlate y and z coordinates. This is true for both PTMs and SMSs.

The pattern recognition in the muon identification system is done in three steps with almost identical algorithms. First the projections in the PTM planes are reconstructed. It is followed by reconstruction in SMS planes. After that the leftover hits in SMS and PTM chambers are used together to find projections in overlap region. At least three stations are required to contribute to a projection. The projections are required to point back to the target region. The target pointing requirement is quite loose, allowing many wide halo tracks to be reconstructed. This is necessary to reconstruct tracks which undergo scattering in the steel.

The projections with very low χ^2 probability are rejected. This increases the likelihood that the found projections are associated with real particles. The efficiency of reconstructing at least one muon projection is above to 99%.

3.2.3 Forward Spectrometer

The pattern recognition in forward spectrometer (FS) is done in two phases. These phases are called muon phase and hadron phase.

In muon phase, the projections in muon identification system are used to define the search window in the forward tracking chambers. If the muon projections are found in the PTMs, they are projected into DC and PC chambers to define a "search window". In case projections are reconstructed in the SMS's planes or no projections are found, no such search window is defined. In muon phase a narrow set of cuts are used to find the stiff tracks only.

In the hadron phase, the tracks are searched within full aperture of the chambers. The cuts used in this phase are much wider. This ensured that all the tracks, even very low momentum ones, are reconstructed.

The hits used in the muon phase are marked and are not used in the hadron phase.

The FS pattern recognition is divided in many different processors. There are two almost independent main chains. 1) PC-DC-MA 2) SF-SN-MD

In first chain, the tracks are reconstructed using projections method in PC and DC chambers by PC and DC processors. The found tracks are link together by MA processor.

In the second chain, the tracks are found using space points in PCF chambers by SF processor. The found tracks are projected outward into PC chambers by SN processor and into DC chambers by MD processor.

Another processor, PF, uses the PC projections to find the tracks in the PCF chambers.

PC Processor

There are three station of four chambers each (Y,U,V,Z) upstream of the CCM magnet with wire spacing of 3.000 mm. The PC processor is used to find the projections in these chambers. A projection is a track segment only in one view e.g. U view. These projections are combined to form a three dimensional space track. A projection in the PC chambers is required to have 3 hits. Only those projection which point back to the target are accepted. Only the projection having good χ^2 probability are kept. The different projections are not allowed to share more than 1 hit. A track in the PC chambers can consist of either 4 or 3 or 2 projections. The tracks segments are not allowed to share any projections. After all the tracks had been found the hits in the missing view are picked up for tracks which are reconstructed from three or two projections only. These hits are picked up only if they are located within a small window around the projected track segment. A track segment is required to have a minimum of 9 hits to be accepted as a candidate track. For 1987-88 run data the tracks consisting of only two projections are not used.

DC Processor

The two stations of drift chambers are located downstream of the CCM magnet. Each station has 8 planes (Z,Z,U,U,V,V,Z,Z). Two sets are approximately 8 meters apart. In DC pattern recognition, first Z projections are made requiring at least 4 hits. Because there are not enough chambers in either U or V view, hits in two view are combined together to find the Y coordinates of the tracks. The Y coordinates made from U/V views are used to find projections in Y view. Then

Y and Z projections are combined together to reconstruct the space tracks. The information from U/V chambers is used to correlate the Y and Z projections and thus make the track in three dimensions.

MA Processor

The tracks reconstructed by the PC and the DC processors are matched together using the "method of principle components". A set of parameters is calculated, representing all possible tracks generated in Monte Carlo data. These parameters define the road widths within which a track segment in the PC chambers can be matched to a track segment in the DC chambers. Given two matched track segments (one each in the PC and DC chambers), the position of the hits in the PCF chambers belonging to the track can be predicted to about 2 mm. If more than 7 hits are present on the predicted path in the PCF chambers, the segments are assumed to belong to the trajectory of the same particle. The PC and DC track segments and PCF hits are combined into a full track. The track segments and hits used are marked and are not used in further pattern recognition.

PF Processor

This processor was originally designed to reconstruct low and medium energy tracks which have large curvature in the CCM magnetic field and do not enter the wire chambers downstream of the CCM. In this processor the track segments found in the PC processor but not linked to the DC chamber hits are used as seed tracks. These segments are projected into the PCF chambers. Hits close to the track in the last PCF station are combined into a space point. Given these *seed* hits (a space point in the magnetic field), the seed track segment (straight line outside the magnetic field) and the field strength, the helical trajectory of the particle can be predicted. All the hits (not only the closest) along this trajectory within a window are considered to be candidate to belong to track. A helical fit is used to select the group of the best hits. Given the best helical fit, the hits in the PCF chambers which did not contribute to the track are picked up.

A further quality check is made by doing a combined fit to the PC-PCF track using the fitting routine called DHFIT3. This is least square fitting routine in which the track is modelled as a straight line outside the magnetic field and as a

parabola inside. The magnetic field is assumed to be constant within a rectangular region and zero outside. Using DHFIT3 more hits are picked up in the PC and PCF chambers, if they exist.

If, for a given PC projection, the track can not be reconstructed using the hits in the last PCF station or the last station does not have any hits, the hits in the second last PCF station are used as seed hits.

The magnetic field is approximated as a uniform field with a fixed sharp cut off in the PF processor. For the helical fit, some empirical corrections are made to take into account the inhomogeneity of the field for low momentum tracks. Moreover the approximate vertex point is used as one of the points on the track for the fit. The approximate vertex point is calculated by projecting the beam track to the middle of the target.

SN-SF Processors

After the PC-DC-MA and PF processors, SF-SN processor is used to reconstruct the remaining tracks. The SF processor is based on the space point algorithm described for beam pattern recognition (3.2.1). Given the space point (x,y,z) at the PCF stations, radii of circles are calculated for all possible combination of three space points. Circles with similar radii are combined to make a track segments with 3,4 or 5 space points. A parabolic fit is done to check the quality of the tracks. Hits in the chambers which did not contribute to the initial track are picked up if they lie on the trajectory given by the fit. After this stage all the duplicate tracks are removed. This is necessary because the 3 and/or 4 space-point circles may be fully contained in the 5 space-point circle. These track segments are projected into PCN chambers using the parameters of the parabolic fit at the edge of the field and hits are picked up in PCN chambers (SN processor). After the track is reconstructed in the PC and PCF chambers, the DHFIT3 is used to check the quality of track. Approximate vertex point is used as a point on the track in the above fitting procedure.

As an option the SF processor can reconstruct tracks with only 2 space points and the vertex point. This option is not used in 1987-88 data analysis.

CF Processor

The hits used in the PF processor are also available to the SF-SN processors. Some of tracks reconstructed by the two processors are similar. In the CF processor the tracks from the above two processors are compared on hit-by-hit bases. If any two tracks are similar, the track with larger number of hits is kept. If the two tracks have equal number of hits, the track with better χ^2 probability is kept. The $P(\chi^2)$ is calculated using the routine **DHFIT3**. The fitting routine is described in section 3.2.3.

PS Processor

The PSA chambers (Y,Z,Y,Z,U,V,U,V) are located just downstream of the second station of drift chambers to cover the beam region where the drift chambers have been made insensitive. The PSA chambers are very important for reconstructing the scattered muon tracks at very small angles. Pattern recognition in the PSA chambers is based on the space point algorithm described for beam pattern recognition (3.2.1). The output of the PS processor is the super-space-points in the PSA chambers. A super-space-point is a space point consisting of more than three planes. The minimum number of planes required to define a space point is three. The direction of the track cannot be determined from the information in the PSA chambers because the PSA planes are very close along the beam direction.

MS-MD Processors

The PCN-PCF track segments remaining after the CF processor are projected into the PSA using fitting routine **DHFIT3** and linked to space points in the PSA chambers (MS processor). The space point in the PSA chambers is required to be within 4 mm in z and 1.5 cm in y of the projected position of track. These values were determined from the Monte Carlo data [83].

In the MD processor PCN-PCF track segments are projected into the DC chambers and are linked to DC track segments found by the DC processor. In the second part of the MD processor, tracks are projected into DC stations and individual hits from different planes are picked up. A combined fit of PCN-PCF-DC track is done to check the quality of the track. All tracks are required to have

hits in both DC stations and at least two of the hits should be in the z view.

PV-MV Processors

Pattern recognition in PCV chambers, a set of 6 chambers (Y,U1,U2,V1,V2,Y) located down stream of the CVM uses the same space point algorithm as the one used for beam chambers (3.2.1). The space points are combined into super space points. At least 4 hits are required for a super space point. The PCV chambers are very close to the interaction point and therefore the track multiplicity in the PCV chambers is very high. The incident angle of the tracks vary over a large range. To take into account the different slopes of the tracks, the PCV pattern recognition is done in three passes. Each pass has different internal requirements to take into account the slope of tracks. The output of the PV processor is space points.

In the MV processor, the PCN-PCF-DC or PCN-PCF-PSA or PCN-PCF track is projected into PCV chambers. If a space point in the PCV chambers is close to the projected track, the track is extended to include that space point. The best space point is selected based on χ^2 probability.

During track fitting program (see below), the PCV hits are picked up from each plane separately. A hits from different planes are not required to be correlated whereas they are required to form a space point in the PV-MV processors. This is possible only because the projected position of the fitted track is accurate to 1.5 mm whereas the wire spacing of the PCV chambers is 2 mm.

WA-PA Processor

The WA processor is used to find the wide angle track segments in the PTA chambers, and the PA processor is used to link the found segments to PCV track segments. The WA is based on the space points method (3.2.1).

3.3 Track Fitting

The track fitting program (TF) in the E665 is used to fit the track reconstructed by the pattern recognition program (PR). The track reconstructed by PR is a list of hits from different planes. These hits are described in the generalized

coordinates (θ). The TF program determines the trajectory of the particle from these hits and calculates the track parameters (y, z, y', z') at a given x position. If the reconstructed tracks passes through the CCM magnet then momentum of the track is also calculated. The track fitted program also calculates the errors associated with the track parameters and the χ^2 probability that the track is associated with a charge particle.

3.3.1 Beam Track

The beam momentum is determined using a least square fit to the hits contributing to the beam track. The trajectory can be described by

$$\theta_i = (z + z'(x_i - x_0)) \sin \alpha_i + (y + y'(x_i - x_0)) \cos \alpha_i \quad (3.6)$$

before the bending magnet and

$$\theta_i = (z + z'(x_i - x_0)) \sin \alpha_i + (y + y'(x_i - x_0)) \cos \alpha_i + ca(x_i - x_{mid}) \cos \alpha_i \quad (3.7)$$

after the bending magnet, where θ_i is the track coordinate in the plane at x_i with wire orientation α_i , c is a constant related to the magnetic field strength and x_{mid} is the middle point of the field where the track is idealized to bend. The parameters y, y', z, z' are fitted at x_0 . The parameter a , also a result of the fit, is the measure of the momentum of track.

The edge effect of the magnetic field of the dipole magnet are not taken into account in this fit. The effect of multiple scattering on the track parameters are small for 500 GeV muons and are neglected.

3.3.2 Forward Spectrometer Tracks

The track fitting in the forward spectrometer is done in two steps described below. After the fitting, the tracks with very low $P(\chi^2)$ are rescued by removing the bad hits from the tracks.

1. **The Local Fits** The forward spectrometer is divided into 10 stations PCV, PCN, PCF1, PCF2, PCF3, PCF4, PCF5, DCA, DCB and PSA. In each station the local fit is done using the hits associated with the track in that

station. In PCN, DCA and DCB the straight line fit is done giving y, z, y', z' at each station. For PCF stations, a point fit is done because there are only three planes at each station. A correction to the resulting space points (y, z) is made depending on the slope of the track (after the first spline iteration, see below) to take into account the fact that the PCF planes in a station are separated by 6.7 cm. For the PSA chambers a point fit is done because the planes are too close in x direction to give any meaningful slope information about the track. For PCV chambers a line fit is done if the number of hits contributing to the tracks are more than 4, otherwise a point fit is done. In the best case one has 18 y, z measurements to extract 5 track parameters if the track goes through drift chambers and only 16 measurements if the track passes through the PSA chambers.

2. **Spline Fit** Given the local y, z points in space (in some cases y, z, y', z') the track in space can be fitted to extract the curvature of the track. An exponential quintic spline fit [86] is used if the reconstructed part of the track passes through the CCM magnetic field and a straight line fit is used for the tracks which do not go through the magnetic field. The quintic spline fit is a cubic spline in the second derivative (y'', z'') of the track. The second derivative of track at the two boundary points is assumed to vanish. The magnetic field near the edge of two magnets is changing rapidly and there are not enough measurements (y, z points on track) to take this variation into account in the fit. Extra dummy points are introduced in these regions using the approximate path of the particle and the fit is repeated with the dummy points having no weight in the fit. During this fitting procedure the multiple coulomb scattering is taken into account by adding the smearing due to multiple scattering to the intrinsic resolution of each chamber plane on the track. Special slope corrections are made for the the PCV hits to take into account the fringe field of the CVM magnet. After the track parameters are determined, the intersection point of the track with each plane is calculated and stored for further analysis.

3.3.3 Rescue Procedure

If the $P(\chi^2)$ of the fit is less than 0.05, the plane with the largest χ^2 is removed from the track and the fitting procedure repeated. This iteration is stopped if either $P(\chi^2)$ of the track is greater than 0.05 or a maximum of six planes have been dropped. This procedure is called the **rescue procedure** and the track is flagged if it is rescued.

3.3.4 PCV Hunt Procedure

If the track, reconstructed by pattern recognition, starts at the PCN chambers, it is projected to the PCV chambers and the PCV hits are picked up if they lie within a very narrow window ~ 2 mm. The size of the window is calculated using the momentum of the track and the $\int \bar{B} \cdot d\bar{l}$ where the exact fringe field is used. If the track can be extended to the PCV chambers, the spline fit is repeated to evaluate new track parameters.

3.3.5 The Resolutions and Performance

The track fitting program was tuned using Monte Carlo data. Fig. (3.2) shows the χ^2 probability has a flat distribution for beam, scattered muon and forward hadrons tracks from SAT Monte Carlo. Note that there are no FS tracks at very low $P(\chi^2)$ because they have been removed by the rescue procedure. Fig. (3.3) shows the difference of the fitted track parameters from the generated tracks for scattered muon. All the distributions are gaussian and centered at zero. The width of the distributions are consistent with the calculated resolution bases on the resolution of the MWPC's [86] as indicated by the flat $P(\chi^2)$. The distribution for the beam tracks (not shown) are equally good. The difference between the generated and reconstructed momenta for incident and reconstructed muons is shown in Fig. (3.4). Both distributions are centered at zero.

From these distributions one can conclude that no systematic errors are introduced by the performance of track fitting program in E665 and the quantic spline fit is a good representation of the trajectories of particles through the E665 forward spectrometer.

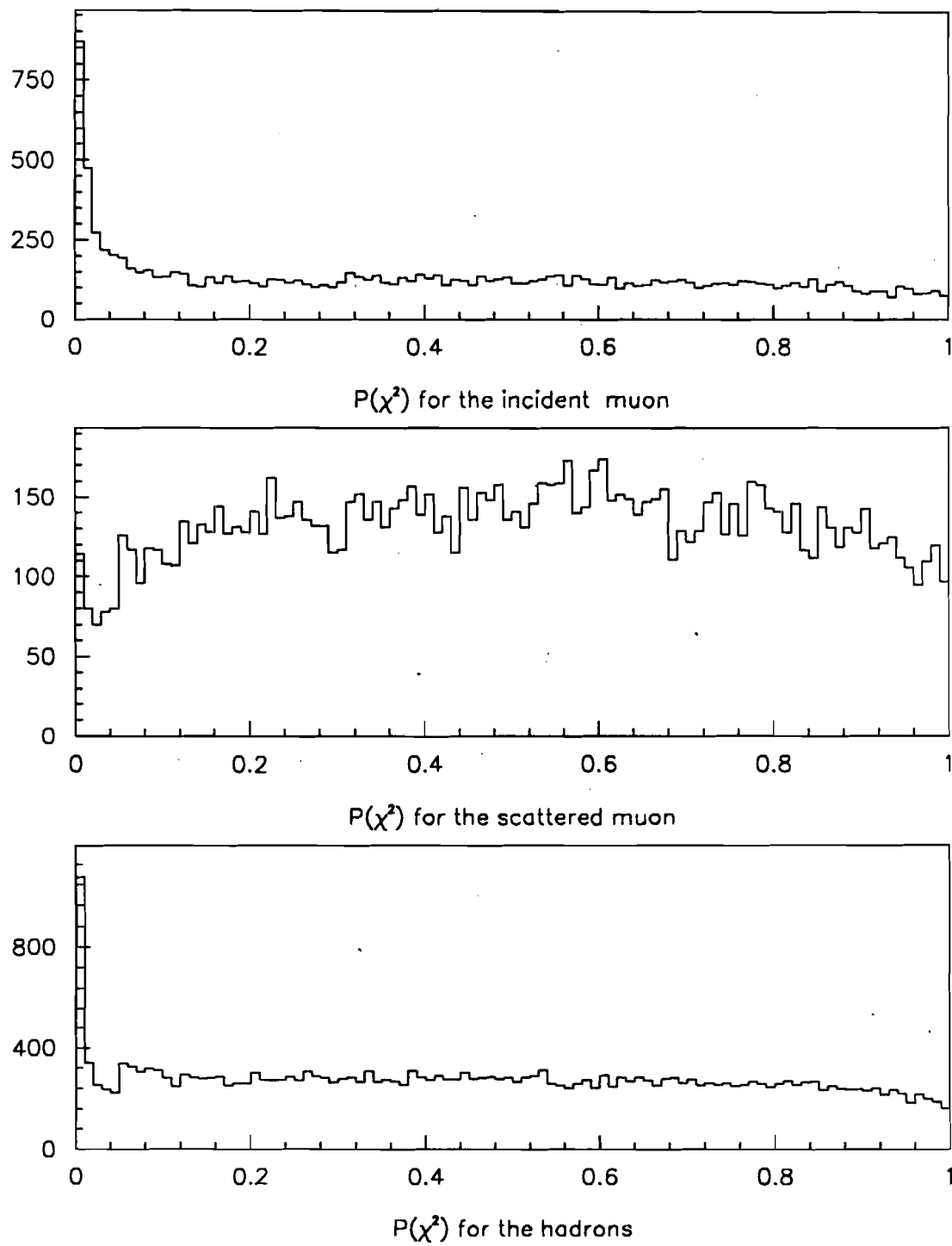


Figure 3.2: The $P(\chi^2)$ probability of the fitted tracks Monte Carlo

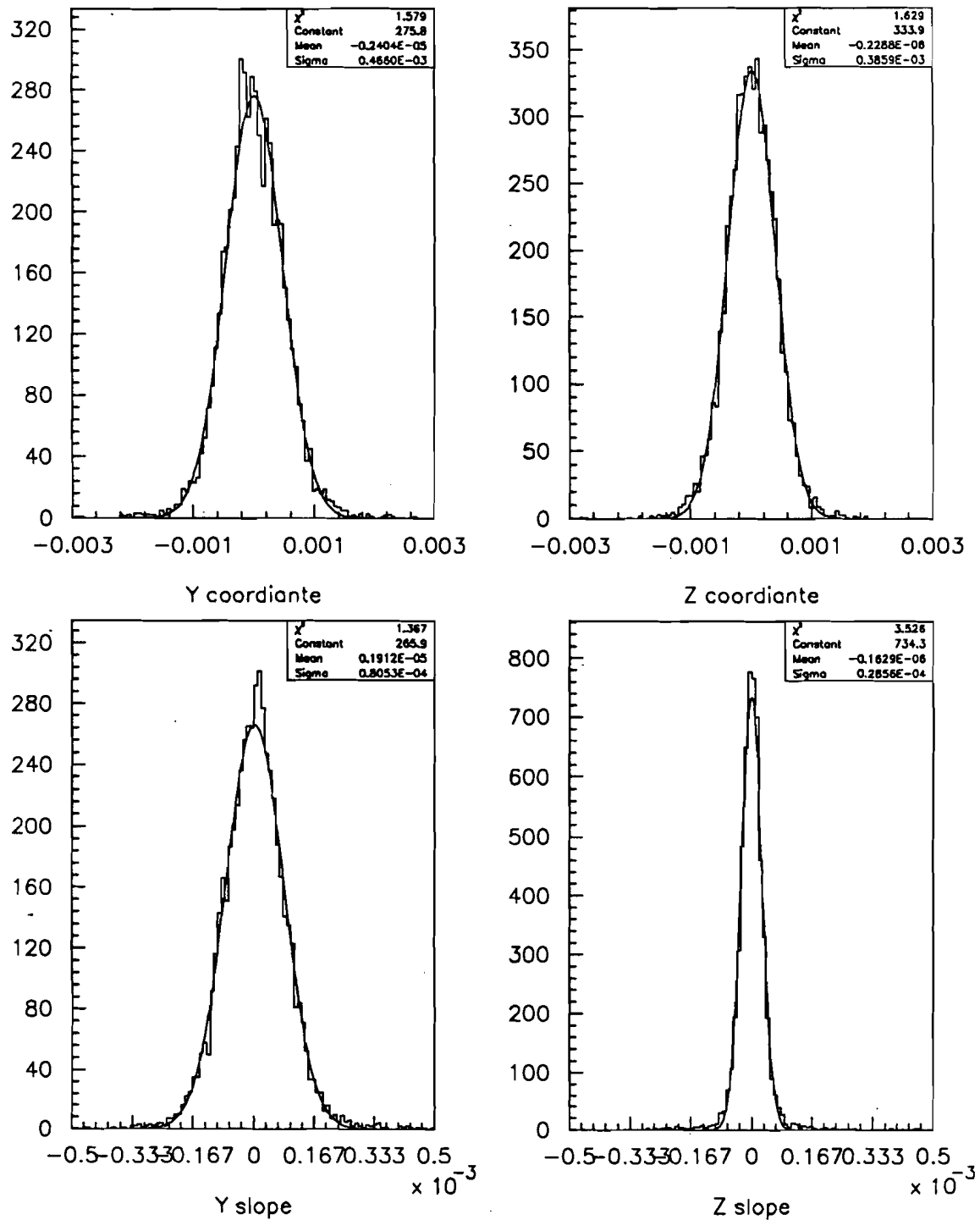


Figure 3.3: The difference between the generated and reconstructed track parameters of scattered muon tracks (SAT Monte Carlo)

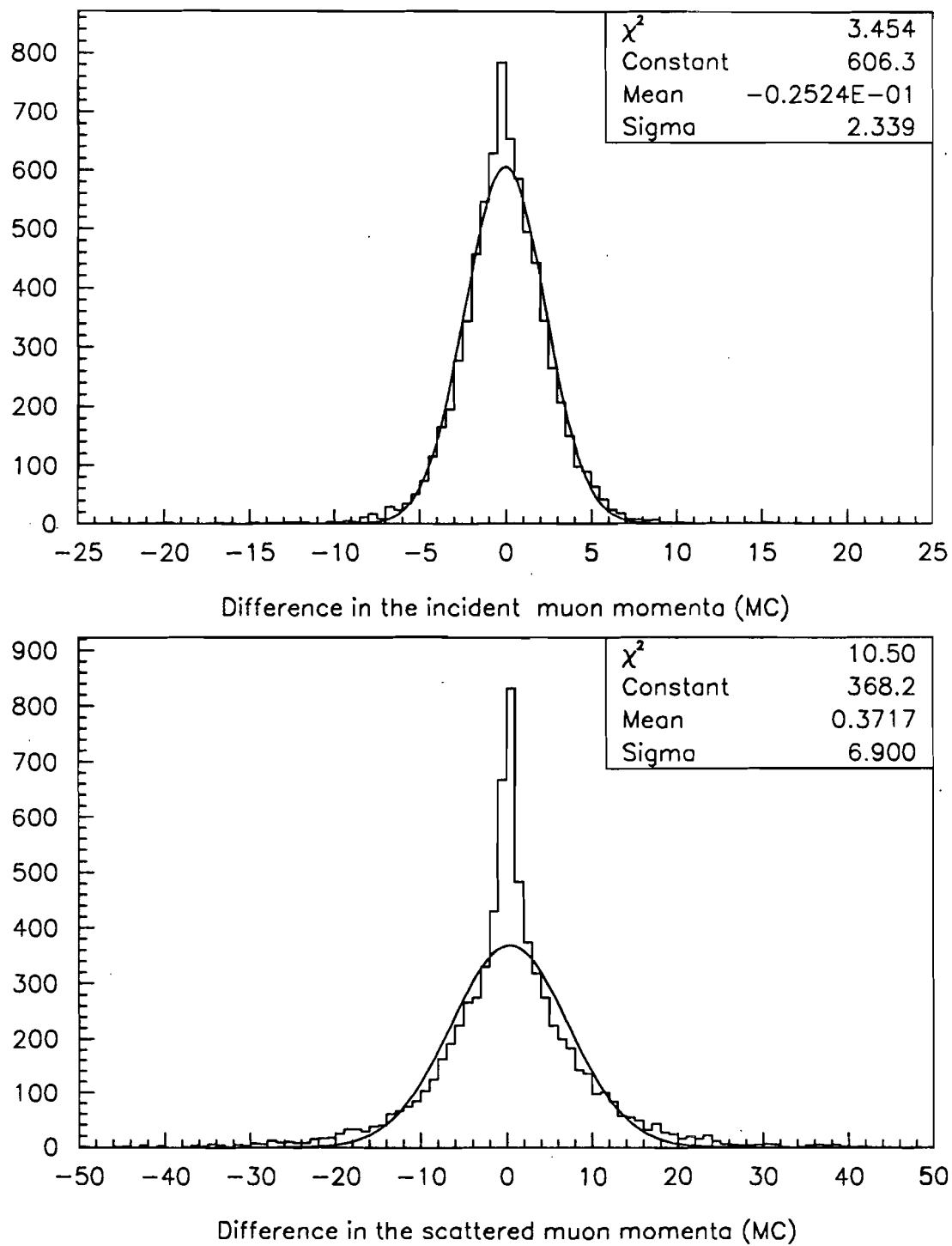


Figure 3.4: The difference between the generated and reconstructed momenta for beam and scattered muon (SAT Monte Carlo)

3.4 Muon Match

The Muon Matching program (MM) in E665 is used to select the forward tracks which are associated with the muon projections downstream of the hadron absorber. As only muons can penetrate the absorber, the tracks are muon tracks.

For a successful match at least two projections, one each in the Y and Z view are required. The track upstream of the absorber is required to have the hits either in DC or PSA chambers. Track ending inside or upstream of the CCM magnet have large error associated with extrapolation to the PTM planes and thus cannot be used.

The muon undergoes multiple scattering in the hadron absorber and EM calorimeter. The muon exiting the absorber will have different track parameters than those measured upstream of the absorber. This change in trajectory of the muon can be taken into account only on a statistical bases. The dispersion in the angle of the track due to multiple scattering is assumed to be gaussian with a width

$$\sigma_{\theta_y} = \frac{0.0141}{p} \sqrt{R_{cal} + R_{abs}} (1 + \log(R_{cal} + R_{abs})/9) \quad (3.8)$$

and the dispersion in position of the track is given by

$$\sigma_y = \frac{1}{\sqrt{3}} L \sigma_{\theta_y} \quad (3.9)$$

$$(3.10)$$

where p is the momentum of track in GeV, R_{cal} and R_{abs} are lengths of calorimeter and absorber in units of radiation length and L is the combined length of the calorimeter and absorber in meters. Using the numerical values one can write

$$\sigma_{\theta_y} = \frac{0.243}{p} \quad \sigma_y = \frac{0.612}{p} \quad (3.11)$$

The dispersion in z view are the same and assumed to be independent of the y view. For a 250 GeV muon the rms due to multiple scattering is about 0.97 mr in angle and 2.5 mm in the coordinate. The typical resolution for the forward track is 0.12 mr for the y slope and 0.3 mm for the y coordinate. The errors for the PTM projections are ~ 1.0 mr in the y or z slope and ~ 4 mm for y or z

coordinate. The typical errors associated with forward track are smaller than the those due to multiple scattering and thus are ignored in the muon match program. A straight-line least-squares fit was used to calculate the parameters of the muon projections and associated error matrix.

The Muon Match procedure consists of two independent methods.

3.4.1 Multiple Scattering Match

For y projection matching, the difference in the y coordinate of the forward spectrometer track and the PTM projection is calculated and χ^2 calculated as defined below.

$$\chi_y^2 = \frac{(y_{FS} - y_{PTM})^2}{\sigma_{PTM}^2 + \sigma_{MCS}^2}, \quad (3.12)$$

where σ_{MCS} is the dispersion due to multiple scattering as described above. A similar χ^2 contribution is defined for the y slope. All the pairs with χ^2 contribution in y and y' less than 40 are accepted as candidate matches. These pairs are ordered according to χ^2 and only the best match for a given forward track is accepted. A similar procedure is repeated for the Z view.

For a successful match, both y and z view projections are required to match with the FS track. In other words the χ^2 in y, y', z, z' was required to be less than 40. In case of a successful match, the tracks are assigned type 3 indicating that these tracks are identified as muon tracks.

3.4.2 Intersection Match

Sometimes the muon in the absorber scatters through a very large angle in a single interaction and the bend introduced may be an order of magnitude bigger than calculated using the above formulae. In such cases the intersection point of the PTM projection and the FS track was calculated. If the intersection point lies between $x_{cal} - 0.50$ m and $x_{abs} + 0.1$ m forward track is matched to the projection. In case of multiple matches, the match with smaller bending angle is kept.

Table 3.3: Reasons for Muon Match Failure in PTMV D LAT

Kink in the steal absorber	30%
Close Halo	20%
Wide Halo	9%
Shower in the Steal absorber	11%
Shower Upstream of absorber	7%
Clean single tracks(beam)	11%
Bremsstrahlung events	2%
Remaining (not categorized)	10%
Total number of input events	100%

3.4.3 Muon Match Performance

The performance of muon match program was most difficult to evaluate because the scattering of muon in three meters of absorber could not be simulated in Monte Carlo program completely. This problem is compounded with the fact that a large fraction of the events in 1987-88 data were triggered by large angle scattering in absorber where the gaussian approximation of multiple coulomb scattering is not valid. In 27% of the filtered LAT events, a match between the PTM projections and a forward track could not be found. A small sample of these events were eye-scanned. The different reasons for failure are described in table (3.3). The effect of these failures can not be gauged directly because it is very hard to determine that a given event (without x_b , and Q^2 information) could belong to the final data set. Given the fact that the failure rate for both H and D is the same, the effect on the ratio of structure functions is negligible. The typical *mismatch* between the forward track and matched PTM projections is shown in figure (3.5). The distributions have nice gaussian shapes centered at zero as expected. This is a good indication that the muon chambers and the forward spectrometer was properly aligned. The absence of the long tails in the distribution implies that all the matched tracks were genuine muons. The χ^2 distribution for the accepted events is shown in figure (3.6). The χ^2 value for all four variables is much smaller than the allowed maximum of 40. The final data sample includes less than 0.01% events which are matched by the interaction point method as expected because the probability of muon scattering in the target and in the steel absorber by a

large angle in the same event is very small.

3.5 Vertex Program

The interaction point where the incoming muon scatters is called vertex point. The purpose of vertex program is to determine this point using the beam, scattered muon and hadron tracks.

Technically the vertex fitting program (VX) in the E665 is used to find the point of the closest approach for a set of *candidate* tracks. This point is called the vertex. The output of the vertex program is the location of the vertex point and the kinematics of the interaction.

In the VX program the track parameters are not modified. In other words the tracks are not forced to go through a common point. The various steps of the program are described in this section. The special features of vertex program relating to streamer chamber tracks are not described here.

Following type of tracks were not used for the reasons described below.

- Some of reconstructed tracks start at PCV chambers and end at PCN or PTA chambers. The reconstructed part of these tracks do not go through the magnetic field and thus their momenta cannot be determined. These tracks are not used in vertex fit.
- Some of the reconstructed tracks starts inside the magnetic field of CCM. These tracks cannot be swum using VTRACK, the track propagation routine. Due to internal requirement in pattern recognition program (PR), none of the reconstructed tracks started at an x position greater than -3.5 m . However, in “rescue phase” of track fitting, some of the hits may be removed from the tracks if they distort the fit. Sometimes the dropped hit is the first point on the track. This changes the starting position of the track, making the track shorter. These tracks were not used in the vertex fit.

3.5.1 Fitting Procedure

The core of the VX is a fitting routine called CVX [89]. In CVX the input tracks are propagated by VTRACK to a point \bar{X}_n on the trajectory. The track can be

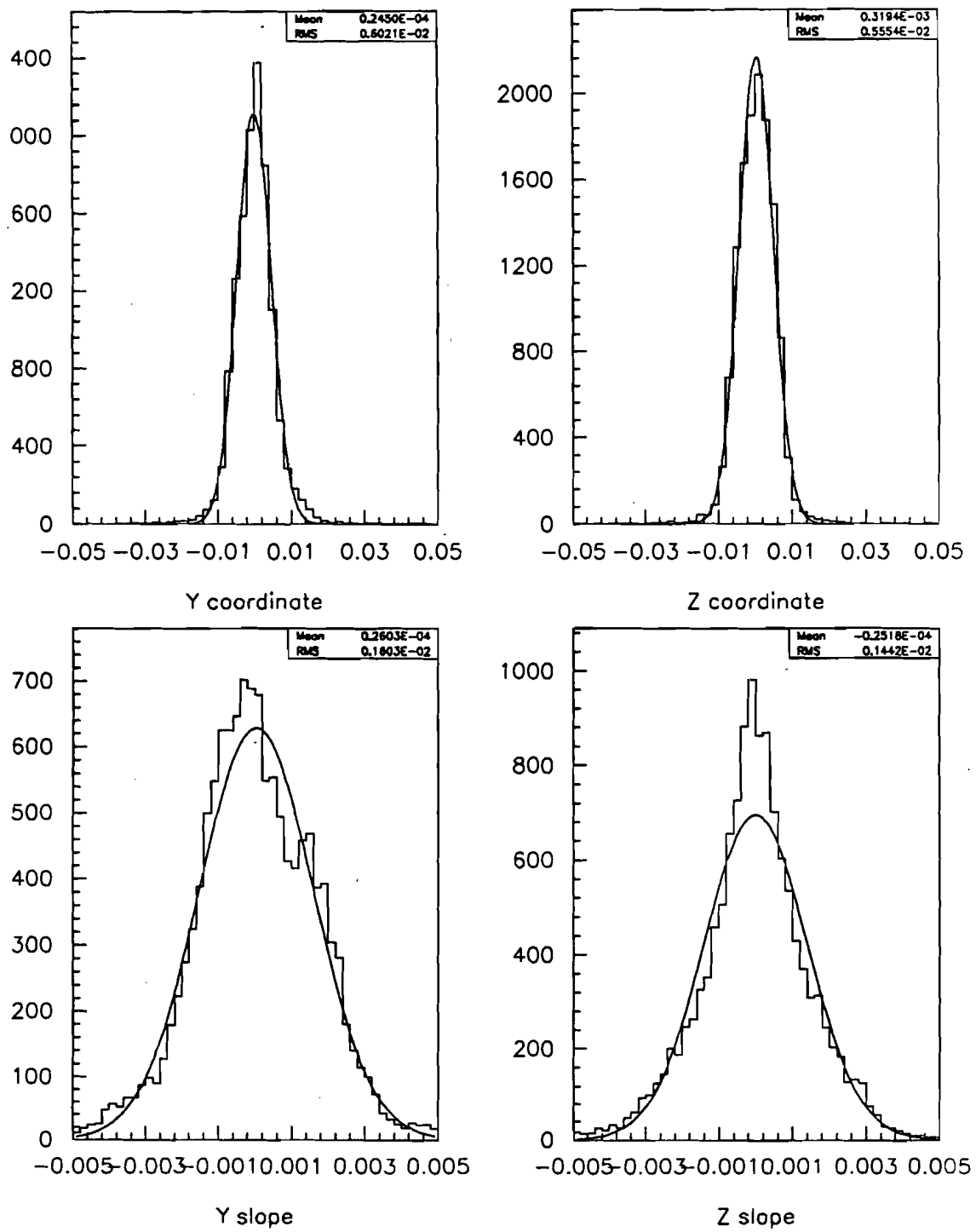


Figure 3.5: The mismatch between Forward track and PTM projections

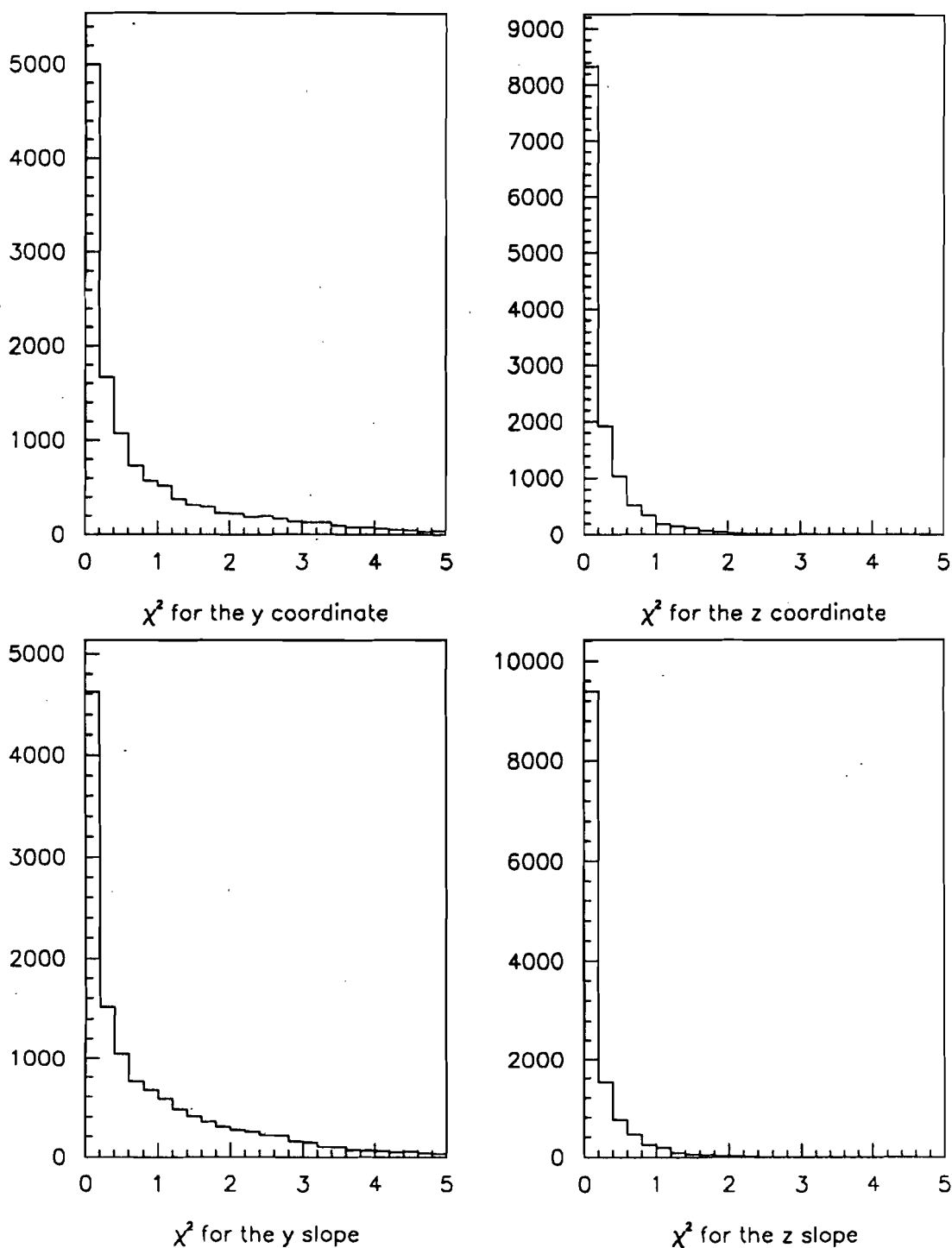


Figure 3.6: χ^2 of the match between PTM projection and forward tracks

approximated locally by its tangent at that point. Thus a point \bar{X} on the track is given by

$$\bar{X} = \bar{X}_n + s_n \bar{T}_n \quad (n = 1, N) \quad (3.13)$$

\bar{T}_n is the unit vector in the direction of the momentum of the particle n at the point \bar{X}_n and s_n is the path length along the direction of motion between the points \bar{X} and \bar{X}_n . The determination of the point of closest approach of N straight lines is mathematically equivalent to computing the weighted average of the points \bar{X}_n where each point \bar{X}_n has an infinite error along the direction of tangent \bar{T}_n . The point of closest approach is \bar{X} such that

$$\chi^2(\bar{X}) = \sum_{n=1}^N (\bar{X} - \bar{X}_n)^T G_n (\bar{X} - \bar{X}_n) \quad (3.14)$$

is minimized. G_n are the weight matrices of the tracks \bar{X}_n . In other words the χ^2 is defined as

$$\chi^2 = \sum_{\text{tracks}} \frac{(\Delta x)^2}{\sigma_{xx}^2} + \frac{(\Delta y)^2}{\sigma_{yy}^2} + \frac{(\Delta z)^2}{\sigma_{zz}^2} + 2 \frac{\Delta x \Delta y}{\sigma_{xy}^2} + 2 \frac{\Delta x \Delta x}{\sigma_{xz}^2} + 2 \frac{\Delta y \Delta z}{\sigma_{yz}^2} \quad (3.15)$$

where

$$\left. \begin{array}{l} \Delta x = x_{\text{vertex}} - x \\ \Delta y = y_{\text{vertex}} - y \\ \Delta z = z_{\text{vertex}} - z \end{array} \right\} \quad (3.16)$$

The point (x, y, z) on the track is the point where the track has minimum distance from the vertex point. The error matrix σ is associated with track coordinates x, y, z .

After the vertex fit the track is swum to the position where the distance from the track to the vertex point is minimum.

In next step the tracks are propagated by VTRACK to new vertex position (\bar{X}) and the fit is repeated using new track parameters. This procedure is iterated until

- The fit has converged *i.e.* the distance to the the new vertex position is less than 0.5 mm from the last iteration for all the tracks included in the fit.

- The number of iterations has exceeded 15. In which case the fit with best $P(\chi^2)$ is reported.
- If in two consecutive iterations the new vertex point is outside the a vertex region along x axis, no vertex point is reported. In 1987-1988 analysis the region was limited from -20.0 m to -4.0 m.

There are three main requirement in vertex program. The first requirement is on the overall quality of the fit. The $P(\chi^2)$ of fit is required to be greater than 0.001. If the $P(\chi^2)$ of the fit is less than 0.001, no vertex is reported. The other requirements are on individual tracks. A track has to be less than 5 cm from the vertex point. Another measure to check the compatibility of the track with the primary vertex point was the distance of the track from the vertex point divided by the associated error. The maximum distance/error allowed was set to 100. Tracks not satisfying these requirements are detached from the vertex and the vertex parameters are evaluated again.

In case the vertex point is determined, the error associated with the vertex position, distance of each track from the vertex point and the distance/error for each track are calculated. All the tracks are reported at the point (x, y, z) on the trajectory of that track which is the closest to the vertex point.

The vertex program has three phases as described below.

3.5.2 Muon-Muon Phase

In the first phase of the VX, a vertex is determined using each pair of beam and muon tracks. This type of vertex is called a $\mu\mu$ vertex and is assigned the vertex type -1. The middle of the target (-11.5) is used as the first approximation for vertex position in the fitting routine CVX described above. In case the $\mu\mu$ vertex cannot be determined, the vertex program stops further processing. The $\mu\mu$ vertex is useful to estimate the biases introduced by including the hadron tracks in the vertex fitting. In principle, for cross section studies where only the incoming muon and outgoing muon tracks are relevant, the $\mu\mu$ vertex should be used but unfortunately resolution in Q^2 and x_{bj} is not very good for $\mu\mu$ vertex.

3.5.3 Hadron Phase

In the second phase, the $\mu\mu$ vertex is used as a seed vertex and a combined fit of the beam, scattered muon and candidate hadrons is performed. The position of $\mu\mu$ vertex is used as first approximation in the fitting routine CVX. If the $P(\chi^2)$ of the fit is less than 0.001, then the track with the biggest χ^2 contribution to the vertex fit is removed from the list of tracks and the vertex is refitted. The procedure is repeated until the $P(\chi^2)$ is greater than 0.001. The original (beam and scattered muon) tracks which define the $\mu\mu$ vertex are considered *safe* tracks and are not removed from the fit.

3.5.4 Secondary Vertices

In this phase the decay and secondary interaction vertices are determined by combining the hadron tracks. If a track belongs to two different vertices, it is dissociated from one of the vertices unless it is a connecting track (joining two vertices). If a track is removed from the primary vertex, the fit is repeated to determine the new primary vertex parameters. For neutral secondary decay vertices the mass of the decay particle is calculated and a particle type is assigned internally. Only the known particles are accepted. This information is not reported.

3.5.5 Vertex Output

After all the vertices have been determined and all the inconsistencies (e.g. tracks belonging to two vertices) removed the output banks LVTX and LTKV are filled. The vertex parameters and associated errors are stored in the LVTX bank. The LTKV banks are the *linked banks* to LVTX. For each track in an event there is one LTKV bank for each LVTX bank. All the tracks which are not fitted to a vertex are called *close* track. A track *fitted* to one vertex will be a *close* track to all other vertices in the event unless it is a connecting track. The track parameters are reported at the point of closest approach to the vertex point.

3.5.6 Selection of Scattered Muon

If more than one FS track fitted to the primary vertex is identified as a muon by the muon match program(MM), vertex program selects the highest momentum

muon as the scattered muon. A Monte Carlo study shows that this procedure picks up wrong muon track less than 1.0% of the time. After identifying the muon, the event kinematics e.g. Q^2 , x_{bj} , ν are calculated and reported in LEVF bank. The LEVF bank also contains the errors associated with the kinematic values.

3.5.7 Vertex Parameters

- The resolution of different vertex parameters and event variables shown in Figure (3.7) is determined from Monte Carlo data in the kinematic region of small angle trigger. The smearing of the kinematics due to reconstruction is small except at very low Q^2 . Even at small Q^2 , the mean difference of less than 0.1 GeV does not effect the results as we are averaging over Q^2 in this analysis.

The Fig (3.8) shows the mean difference between the “true” kinematic quantities and the reconstructed as function of the variable. Again the difference is consistent with zero for x_{bj} , y_{bj} and Q^2 greater than 0.5 GeV².

The calculated error for x_{bj} , y_{bj} and Q^2 for real data events is shown in Figure (3.9). Only the deep inelastic events which pass the event selection requirements (5.1) are included in this set of plots. The fraction resolution in x_{bj} is 12% and is independent of x_{bj} at low x_{bj} . It varies from 12% to 2% for Q^2 from 0.2 to 10.0 GeV. The resolution in y_{bj} is very rapidly decreasing function of y_{bj} .

- The error on the vertex position depend on the errors on the track parameters included in the vertex fit. If a large number of track are included (high multiplicity event), the vertex is determined more accurately and thus the errors on the vertex parameters (x, y, z) are small. The accuracy in position is reflected in the kinematics of the events. For cross section measurements, specially at small angles, the small biases in calculation of the kinematic quantities may be important. The difference in the position of the primary vertex and $\mu\mu$ vertex is shown in Fig. (3.10). Given the $\mu\mu$ vertex the event kinematics can be calculated. Figure (3.12 a) shows the difference in Q^2 calculated using primary vertex Q^2 using $\mu\mu$ vertex parameters. Figure (3.12 b)

shows the same for x_{bj} . It is clear that the event kinematics are not biased by including hadrons in the vertex fit. Here only those events are included where at least one hadron is attached to the primary vertex.

3.6 Detector Simulation

The Monte Carlo programs in the E665 are used to

- design the experiment and develop software using simulated data
- estimate the hardware acceptance and performance of detector and use the estimate efficiency to correct the data
- extract the physics signal given a model for the process study being signal

The exact modelling of the physics processes under study is not crucial for software development, estimation of the geometric acceptance and calculation of correction factors. In E665 the Monte Carlo program is divided into two stages. In stage I (MC1), the physics processes, deep inelastic scattering and hadronization, are simulated. The generated particles are tracked through the spectrometer and track parameters calculated at different x positions along the beam direction.

In stage II Monte Carlo (MC2) the track information is translated to the detector response in the real data format *e.g.* the wire addresses in the MWPC's.

3.6.1 Monte Carlo Stage I

The stage I monte carlo is a modular program, with many different exit points where the event generation can be stopped. The different stages of MC1 are described below.

Table 3.4: Reasons for failure of the vertex fitting program for deuterium LAT data

Multi beam beam tracks	55%
Electromagnetic Showers	19%
Large energy loss down stream of CVM	14%
Remaining (not categorized)	12%
Total number of input events	100%

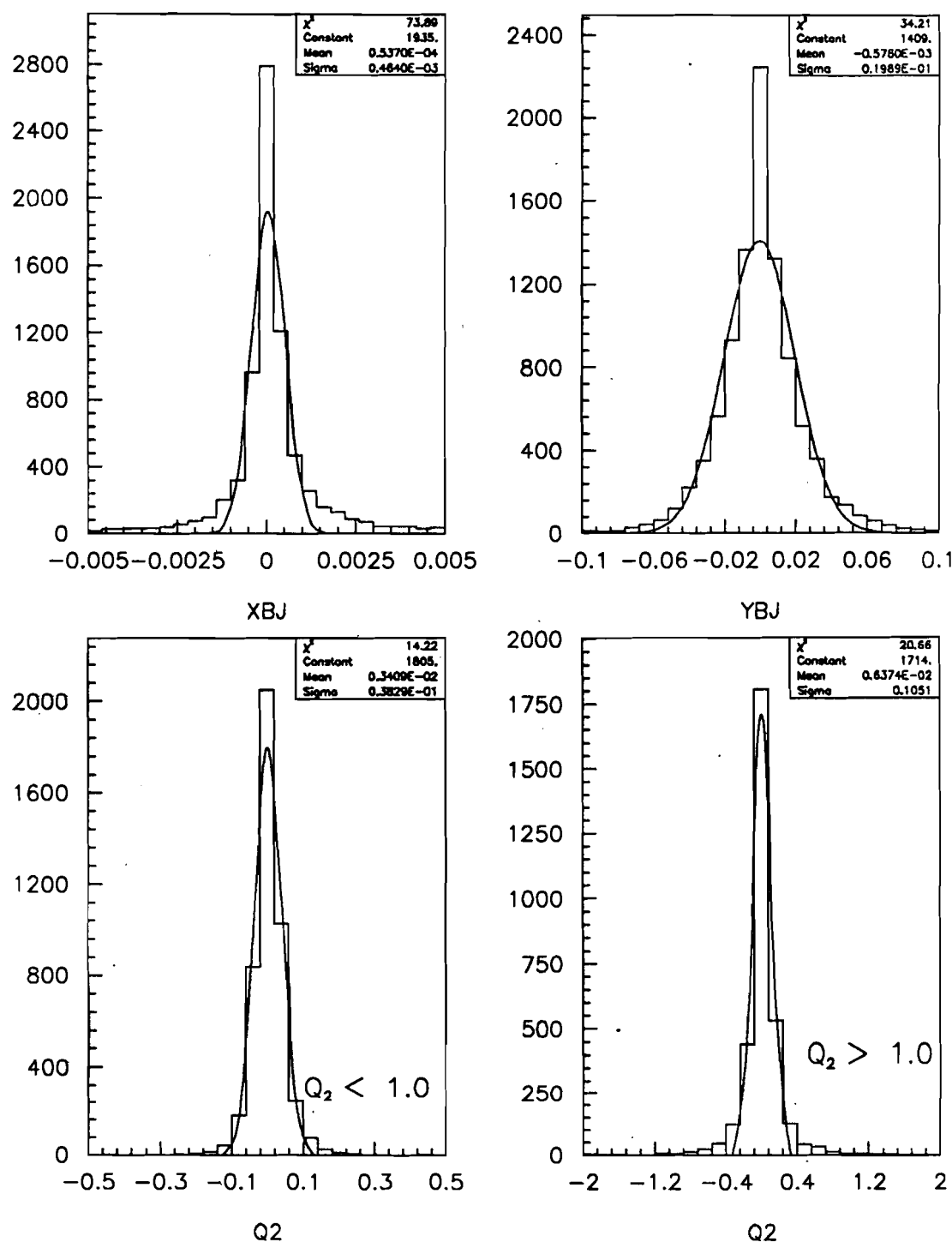


Figure 3.7: The difference between the generated and reconstructed kinematics of the SAT Monte Carlo events

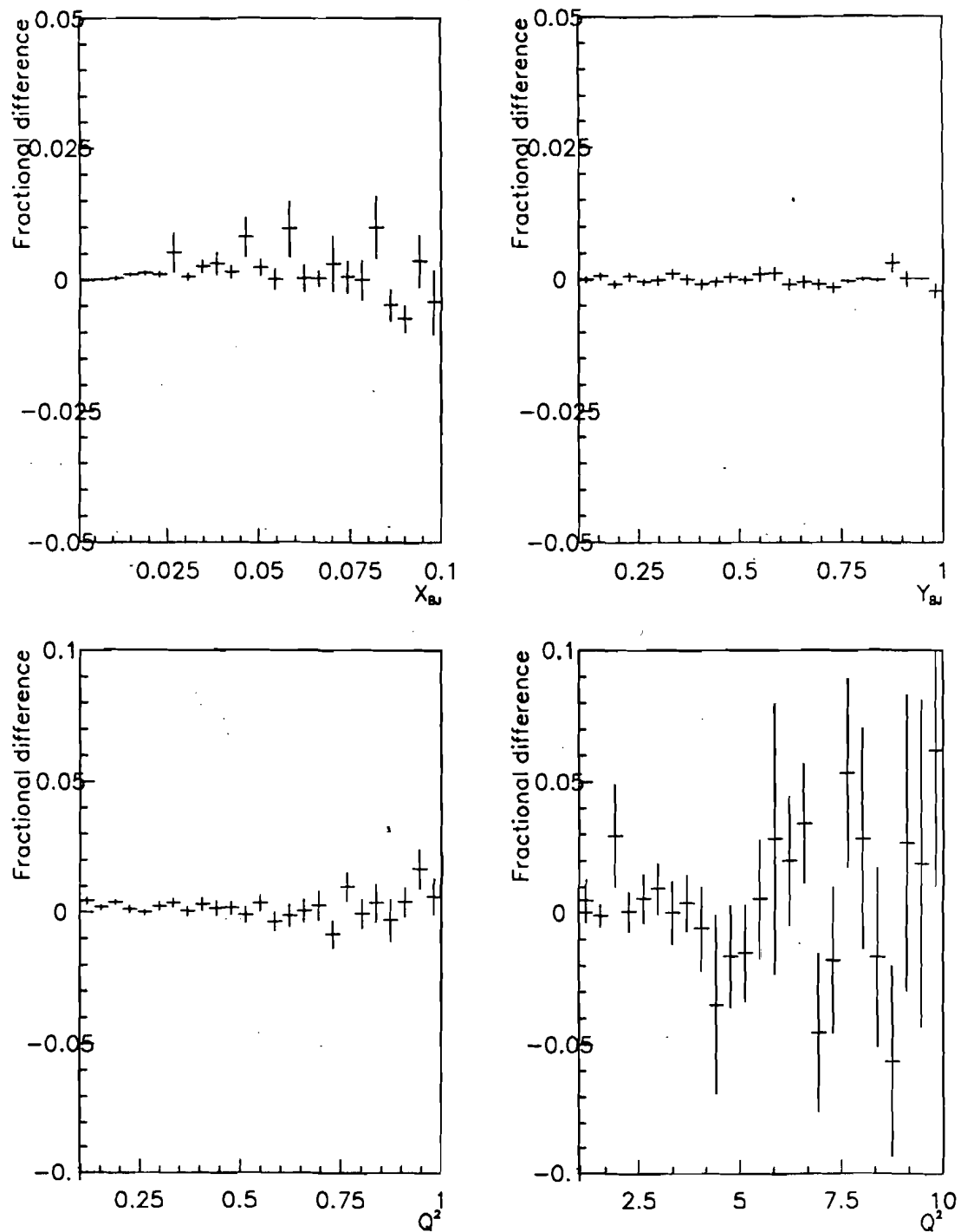


Figure 3.8: The mean difference between the generated and reconstructed kinematics as function of kinematic variable

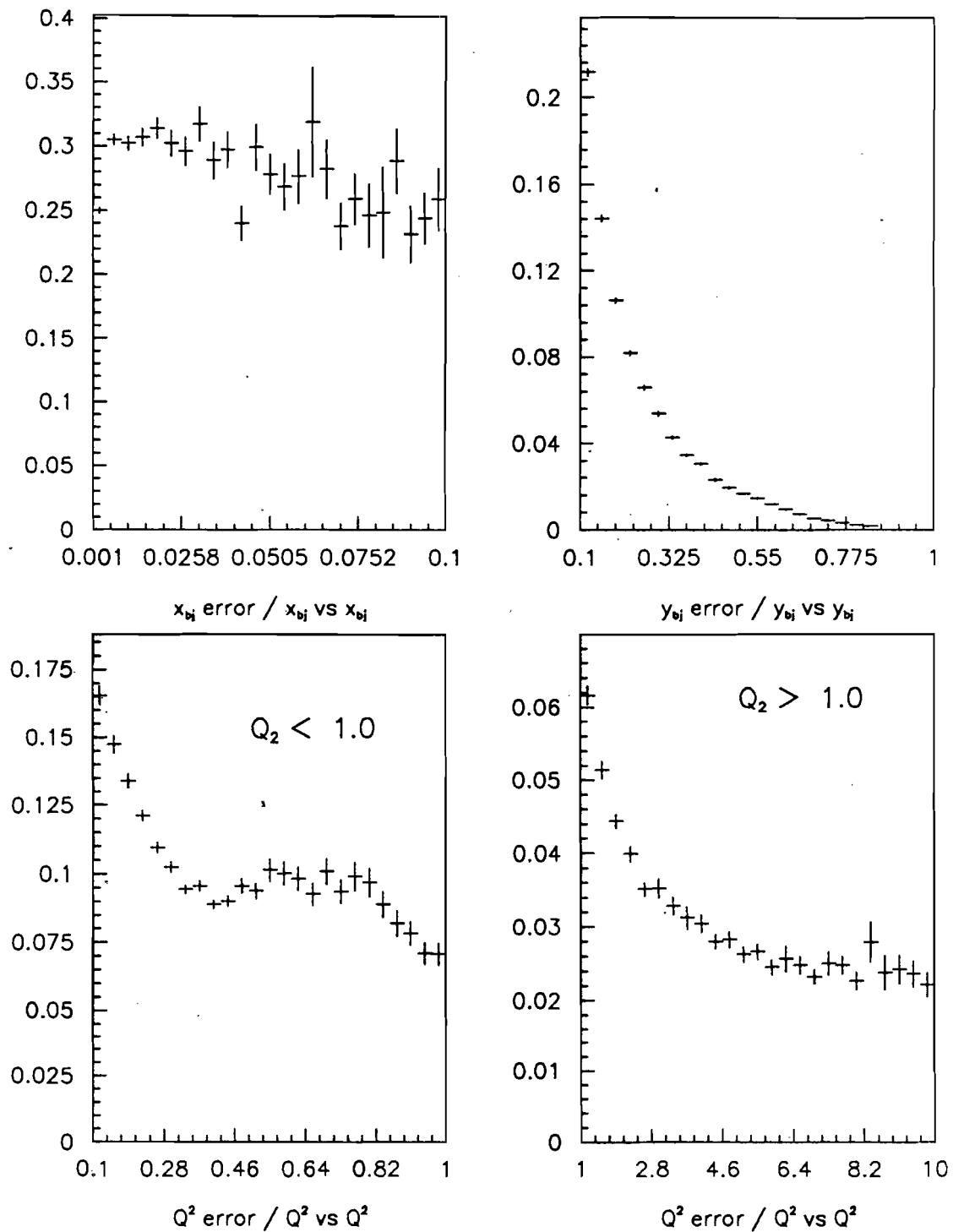


Figure 3.9: The fractional resolution in x_{bj} , y_{bj} and Q^2 as function of x_{bj} , y_{bj} and Q^2

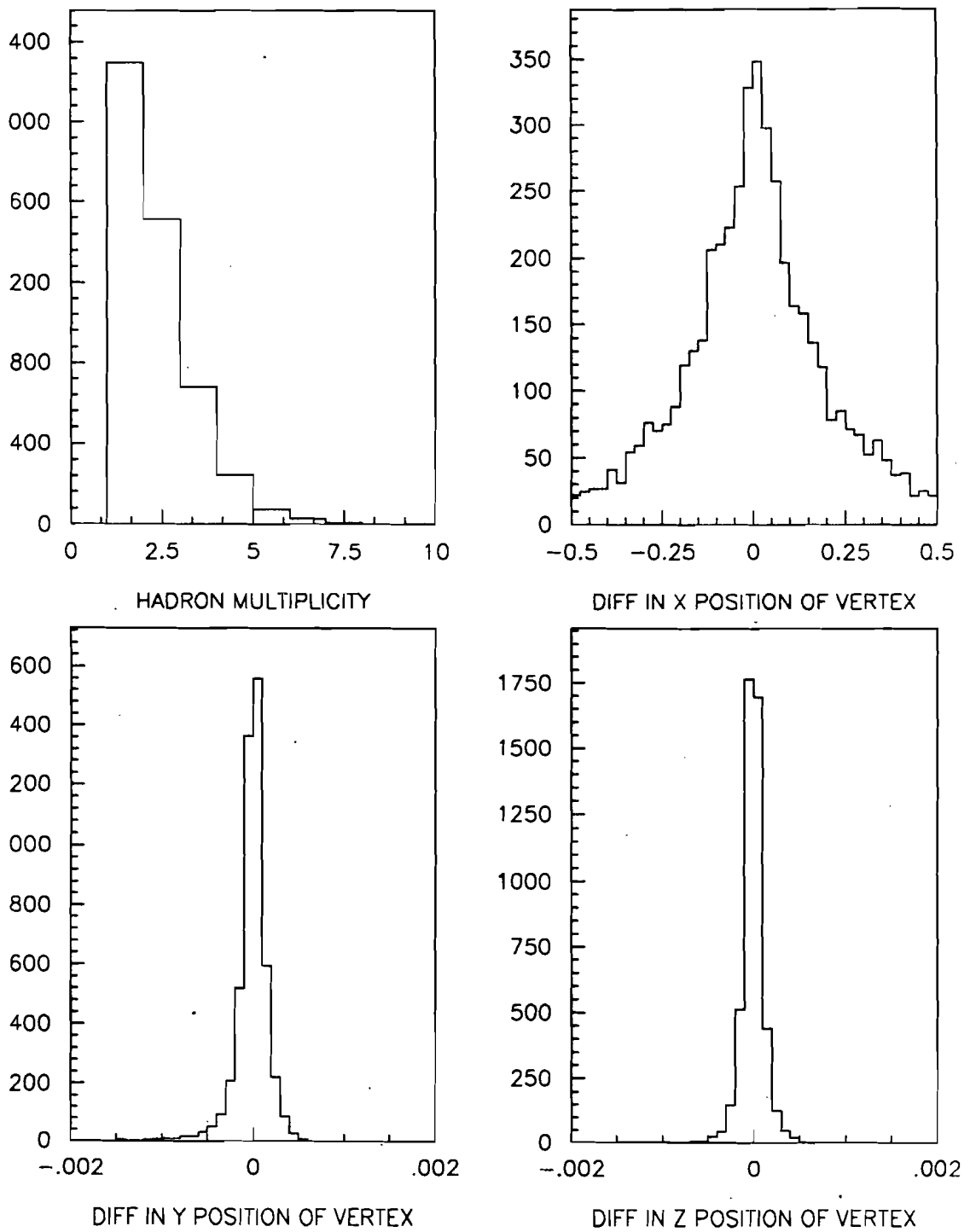


Figure 3.10: The difference in position of primary and $\mu\mu$ vertices
 The events having at least one hadron tracks are included only. The hadron multiplicity is also shown.

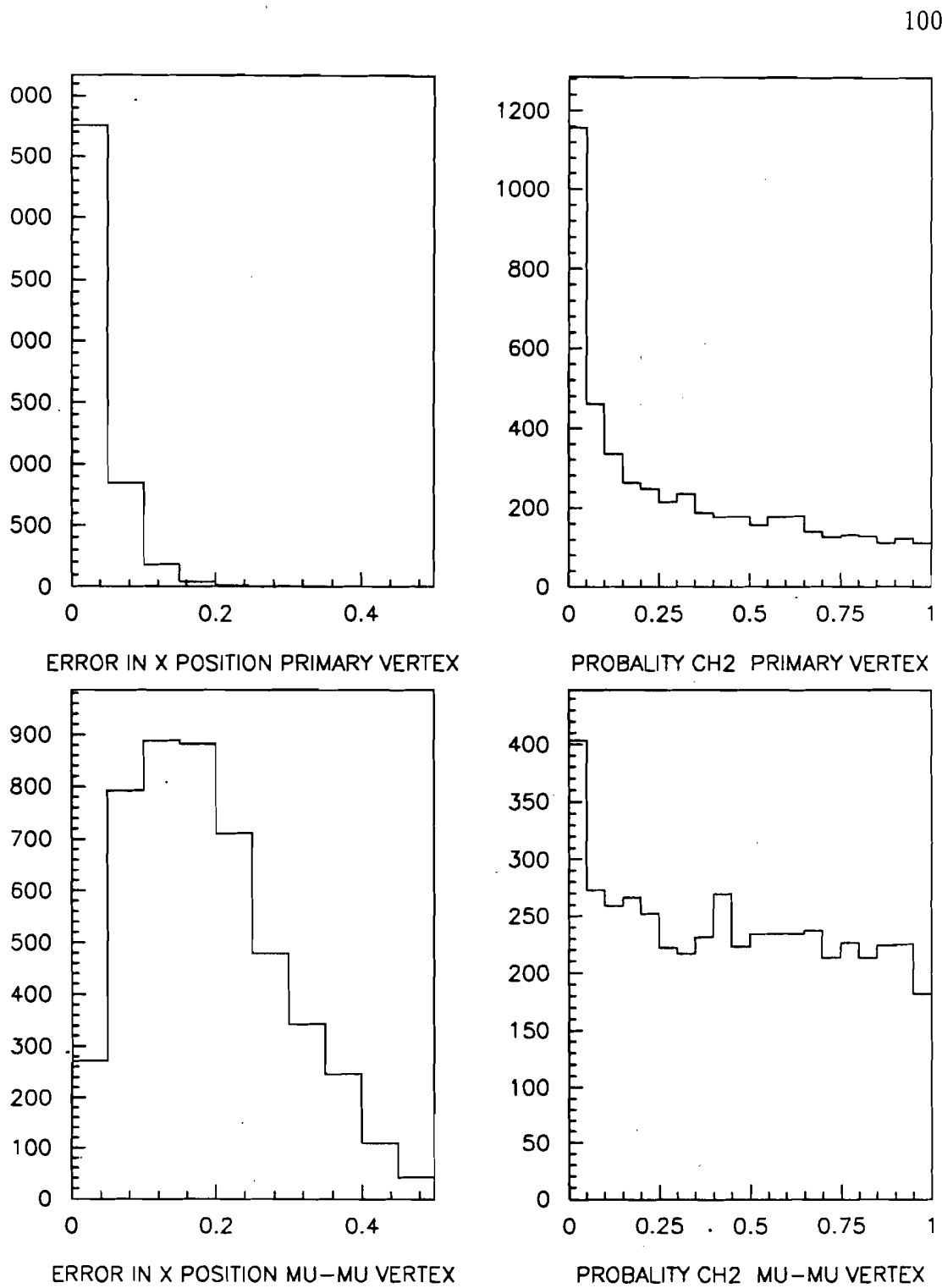


Figure 3.11: The quality of the vertex parameter for $\mu\mu$ and the primary vertex

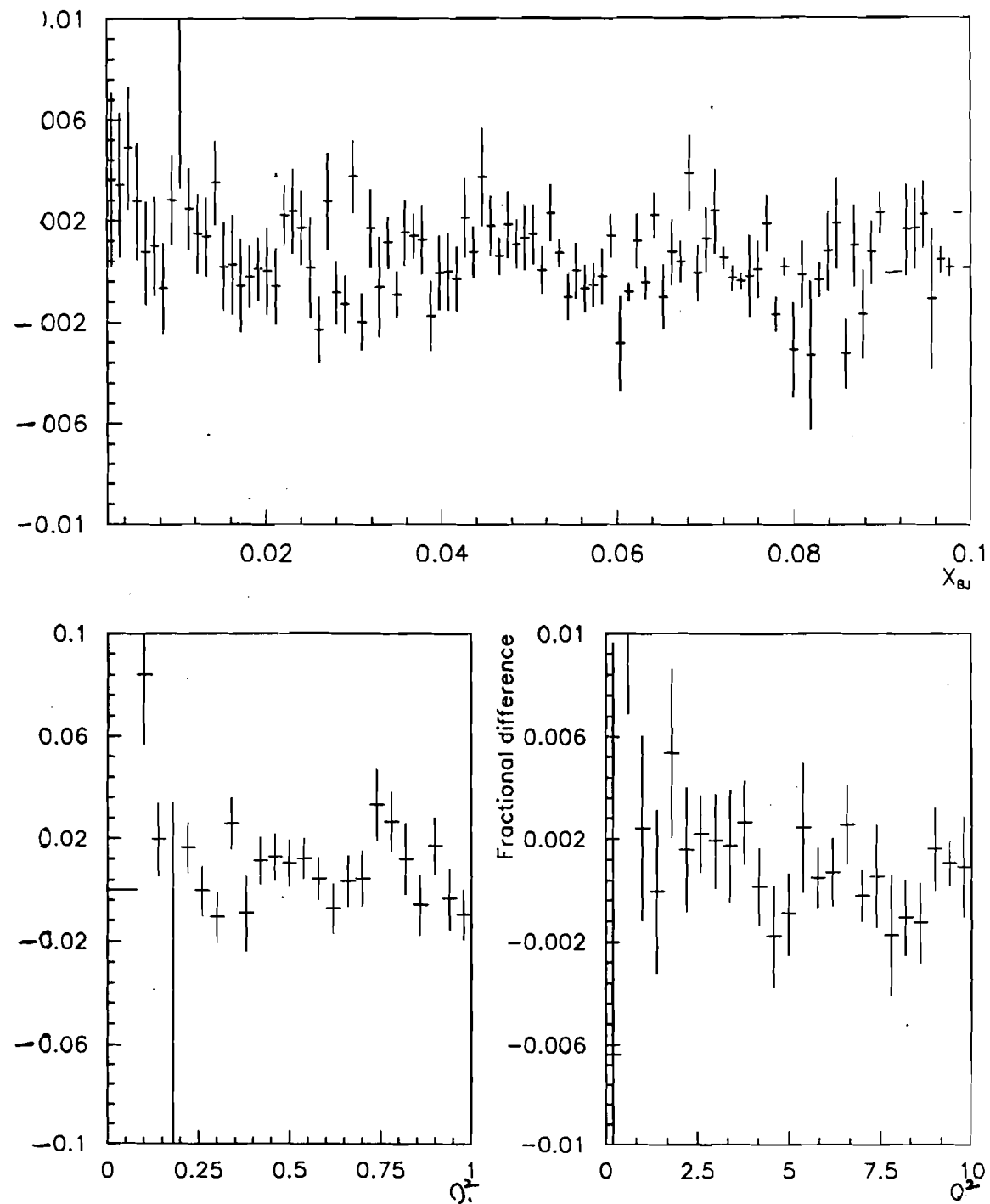


Figure 3.12: The difference in event variables between Primary vertex and $\mu\mu$ vertex

- **Beam** The muon beam track parameters are read from an input files generated from the RBEAM/RSAT data. Therefore the beam phase space for simulated data is exactly same as the real data. Optionally one can generate a gaussian beam with a given mean and width of momentum distribution. Different beam distribution corresponding to different running periods extracted from the data are used.
- **Q^2 and ν Generation** Q^2 and ν can be generated based on the DIS cross section and a particular parameterization of parton distributions (structure functions). To get the events in the phase space region where the cross section is small (e.g. high Q^2 events), one has possibility to use different distribution (e.g. flat in Q^2). Different sets of partons distributions are available and one can switch between them. The determination of the geometric acceptance is not very sensitive to parton distributions. In the final Monte Carlo data set, Morfin-Tung representation of the parton distributions was used [61]. These distributions are determined by doing a global fit to the neutrino data from CDHSW, deep muon inelastic data from EMC and BCDMS and Drell-Yan data from E605. The fit is done to leading order in QCD using DIS normalization scheme. The fit also included the higher twist effect. The parameterization is valid down to $Q^2=1.4$ GeV 2 . The fit is done at $Q^2 = 4.0$ assuming SU(3) invariant sea quark distributions. The functional form of the parton distributions is

$$f^a(x, Q^2) = e^{A_1^a} x^{A_1^a} (1-x)^{A_2^a} \ln^{A_3^a} \left(1 + \frac{1}{x}\right) \quad (3.17)$$

where the A_i^a are given by

$$A_i^a(Q) = C_i^{a,0} + C_i^{a,1} T(Q) + C_i^{a,2} T(Q)^2 \quad (3.18)$$

with $i=0-3$, and

$$T(Q) = \ln \frac{\ln \frac{Q}{\Lambda}}{\ln \frac{Q_0}{\Lambda}} \quad (3.19)$$

The higher twist term is a multiplicative term given by

$$F_2^{HT} = 1. + (-0.294 - 0.732 * x + 4.0 * x^2) / Q^2 \quad (3.20)$$

The higher twist term was not used in the monte carlo generation.

- **Hadronization Model** The Lund Monte Carlo based on the string fragmentation model (JETSET 4.3) is used as the hadronization model. In this model the $q\bar{q}$ pair is connected by a flux tube, a string with a string constant κ . The typical value of κ is 1 GeV/fm. As the $q\bar{q}$ pair moves apart, the string tension increases and eventually the string breaks into two pieces, each piece carrying a $q\bar{q}$ pair on its two end points. in this manner the scattered quark fragments into other $q\bar{q}$ pairs. If the energy of the $q\bar{q}$ pair is less than a preset invariant mass, the pair hadronizes into meson. The production rate of different flavours of quarks and mesons is controlled by ad-hoc parameters extracted from previously measured data.

The Lund Model includes first order QCD corrections to basic $\gamma - q$ interaction. The first order corrections include gluon bremsstrahlung and photon-gluon fusion processes.

- **Tracking through the E665 detector** For the tracking of the scattered muon and the produced hadron the CERN tracking package GEANT was used. This package includes the various physics processes like secondary interactions, gamma conversion and multiple coulomb scattering. Inclusion of these physics effects is necessary to simulate the detector response accurately. The tracks produced in these processes only effect the physics distributions like charge multiplicity and momentum distribution of particles but it can also effect the software reconstruction efficiency.

3.6.2 Monte Carlo Stage II

The stage II Monte Carlo (MC2) in E665 is used to digitize the simulated data. At this stage the track information at each physical plane is translated to the actual response of the detector. For wire chambers and scintillator hodoscope planes the physical address of the wires or fingers is calculated. For drift chambers the drift time, smeared by TDC resolution, is reported. At this stage various physical processes like delta rays and electronic noise in the chambers are simulated. Moreover the dead channels and hot wires are also taken into account. The output format

of MC2 is same as the raw decoded data, so that the reconstruction programs can be used for real and simulated data without a single change in the code.

The real efficiencies of various chambers extracted from Halo and DIS data were used as input to MC2 to simulate the detector performance. The method of extraction and the values are described in section (4.6). The number of extra hits (noise) which accompany the real track were also estimated from the real data. The noise in the detector effects the performance of the reconstruction programs and therefore it is very important to use the correct distribution of such extra hits.

Chapter 4

DATA PROCESSING AND PERFORMANCE

In 1987-88 run the E665 Collaboration recorded ~ 10 million events using three different targets and with 8 different triggers. These data were split into different tapes based on the type of the trigger. The split data were passed through analysis software as described in Chapter 3. They were processed in two parallel streams one each for SAT and LAT data set, using almost the same analysis software. In this chapter data processing, beam normalization and various corrections to be made to the measured events rate are discussed. The corrections include geometric acceptance of trigger system, trigger efficiency, reconstruction efficiency and the radiative corrections. The empty target correction is discussed in Chapter 5.

4.1 Data Processing

4.1.1 The SPLIT Program

During run 1987-88 data from all triggers were written to same tape. In the split program, the data from different triggers were separated because different software was needed to process them. The data were split into separate output tapes based on the Bison Box trigger bits. These trigger bits were set by the hardware trigger processors. The events tagged by more than one trigger were written to all corresponding data streams. For example an event, in which both LAT and SAT trigger bits were set, was written to both output streams. This implies that the SAT and LAT data sets are not completely independent and can not be trivially combined. In the SPLIT program the number of live muons corresponding to each trigger was calculated for normalization purposes.

Table 4.1: The LAT Filter Program cuts.

Difference in Y coordinate	1.0	mm.
Difference in Z coordinate	1.0	mm.
Difference in Y slope	0.39	mr.
Difference in Z slope	0.09	mr.
Difference in the angle between the tracks	0.29	mr.
Difference in the momentum between the tracks	50.0	GeV/c.

4.1.2 The LAT Filter Program

The SPLIT data were passed through a filter program which was designed to reject those events which could be positively identified as background events. All other events were kept for further analysis. The technical details of LAT filter program are desctried in [79]. The LAT filter program consisted of following steps.

The incoming beam tracks were reconstructed in the beam chambers. If no beam track could be reconstructed, the event was rejected. If there were more than one beam track, the event was also rejected to simplify further analysis at a small cost to luminosity. For single beam track events, the event was rejected if it was out of time. An event was declared in time only if at least 6 of the 7 SBT hodoscopes were latched. The hardware requirement of LAT trigger was that all 7 SBT hodoscopes had hits.

For the events having single in-time track in the beam chambers, tracks in the forward spectrometer (FS) were reconstructed only in the central region. If none or more than one track was reconstructed in FS, the event was accepted. For events with a single beam and a single FS track, the parameters of the beam track and the FS track were compared. An event was rejected if the track parameters matched within quite conservative limits. The limits used, based on an RBEAM study, are given in Table 4.1. They are approximately three times the RMS of the distributions for RBEAM events. An RBEAM event consists of a non-interacting beam track. The distributions of RBEAM track parameters are given in reference [79].

The cuts used in the filter program (Table 4.1) are quite conservative and do not effect the final deep inelastic sample. ν of 50 GeV and θ equal to 0.3 mr correspond to Q^2 of 0.02 GeV 2 and x_b of 0.2×10^{-3} for 500 GeV incoming beam

Table 4.2: The LAT Filter Statistics for D2

Not enough SBT hits	27.87%
Less than 1 Beam Tracks	4.70%
Out of Time Beam/More than 1 beam track	16.28%
Momentum of Beam \leq 300.0 GeV	1.75%
Beam Matching	19.05%
Total fraction of events rejected	69.65%
Fraction of events accepted	30.32%
Fraction of events lost	0.03%

muon. Both these values are at least an order of magnitude lower than the lower limits used even in the SAT analysis. Therefore the filter program did not reject good deep inelastic events.

A secondary filter based on an opposite philosophy, the positive identification of a scattered muon in muon chambers, was used to monitor the performance of primary filter. Only 50% of the events (randomly selected) were passed through the secondary filter to keep the output small. Approximately 13.9% of the events on the filter output tapes were selected only by the secondary filter and 23.02% by both filters.

Moreover all the events in which the incoming beam momentum was less than 300 GeV were also rejected. The fraction of events rejected at each stage of the LAT filter program are given in Table 4.2 and Table 4.3. Table 4.2 was compiled using part of the LAT deuterium data (1.66 million triggers). For LAT hydrogen data a small sample of 135 K events was used to compile the table. The fraction of rejected events and their break down into various categories is almost identical for the two targets indicating the trigger configuration did not change during the run. The higher fraction of good events in the deuterium sample is expected because deuterium should have twice the number of DIS events for same incoming beam flux.

4.1.3 The SAT Filter Program

The filter program for the SAT data set followed the same logic as the one used for LAT data except for a few minor differences. The events were required to

Table 4.3: The LAT Filter Statistics for H2

Not enough SBT hits	29.2%
Less than 1 Beam Tracks	5.7%
Out of Time Beam/More than 1 beam track	16.5%
Momentum of Beam \leq 300.0 GeV	1.7%
Beam Matching	20.2%
Total fraction of events rejected	73.3%
Fraction of events accepted	26.7%

Table 4.4: The SAT Filter Statistics for D2

Less than 1 Beam Tracks	6.84%
No In-Time Beam Track	9.49%
SAT trigger requirements	23.36%
Beam Matching	33.84%
Total fraction of events rejected	73.53%
Fraction of events accepted	26.47%

Table 4.5: The SAT Filter Statistics for H2

Less than 1 Beam Tracks	6.84%
No In-Time Beam Track	8.24%
SAT trigger requirements	24.62%
Beam Matching	31.46%
Total fraction of events rejected	73.17%
Fraction of events accepted	26.83%

satisfy the hardware trigger matrices in software. This requirement removed all of the extraneous triggers caused by the noise in the hodoscopes or other hardware problems in the trigger system. Moreover the events having one in-time beam and any number of out-of-time beams were kept for further analysis. The events with low momenta were also not rejected at this stage. Table 4.4 and Table 4.5 describe the fraction of events rejected at each stage of the SAT filter program for deuterium and hydrogen data sets respectively.

The table for deuterium data was compiled using part of the SAT deuterium data (1.513 million triggers) and the table for hydrogen data was compiled using 1.4 million triggers for SAT hydrogen data.

Note that for the SAT data, a larger fraction of events is rejected by "Beam Matching" which is expected because a muon which scatters in the hadron absorber is more likely to satisfy SAT trigger requirements. The fraction of events rejected in the deuterium and hydrogen data sets are similar, confirming that the SAT trigger performance did not change much from deuterium data taking period to hydrogen data taking period (for final numbers see section 4.5.2). The almost negligible difference between the fraction of accepted events in the deuterium and hydrogen samples is an indication that the selected SAT data are still dominated by the background events like muon-electron scattering and bremsstrahlung events.

4.1.4 The PTMV Program

Events selected by Filter program were passed through the full reconstruction program (PTMV). It reconstructs the trajectories of charged particles (PR), determines their momentum (TF), identifies the muon tracks (MM) and calculates the event kinematics if a vertex point can be determined (VX). The technical details of the software flow of PTMV program are described in [80]. The main features of these subprograms are described in Chapter 3. The event processing was stopped at intermediate stages if it could be determined that the vertex would not be reconstructed in an event. At the end of PTMV program, having a reconstructed vertex implied that in that event there was

1. one and only one beam track which was in-time
2. at least one muon projection in each of view (y, z) behind the absorber

3. at least one track in the forward spectrometer which had hits either in the DC or PSA chambers and was linked to the muon projections

The RBEAM, RSAT and empty target data sets were also processed through PTMV. Minor modifications were made to the PTMV program to process the RSAT and RBEAM events.

4.1.5 The Data Reduction Program

The events which satisfied kinematic requirements and had the vertex point close to the target vessel were selected by a Data Reduction program (DR). The technical details of DR are described in [81]. The LAT events with x_b ; less than 0.003 were rejected to reduce the electromagnetic background in the final sample. The geometrical acceptance of the LAT trigger is such that the events at small x_b ; are the events at very high ν and therefore need a large radiative correction to extract the one photon cross section.

The kinematics of electron-muon scattering events overlap with SAT deep inelastic kinematics. Therefore no simple kinematic cut could be devised to reject the background events. Only the events originating far away from the target vessel were rejected. In DR program the data from the electromagnetic calorimeter were processed for the accepted events.

A summary of the number of events rejected by the DR program is given in Table 4.6 and Table 4.7. The 33% of the events rejected because of no beam or no muon projection were selected by secondary filter only. Remaining 67% were selected by primary filter and did have one in-time beam track. Of the events selected by primary filter, 28.8% were rejected by the DR program because muon projections could not be reconstructed and 71.2% were rejected because the χ^2 probability of the beam track was less than 0.1%.

A visual scan of events rejected due to no track in the forward spectrometer indicated that most of the event (greater than 99%) did not have enough hits in the chambers to reconstruct the track. In 56% of these events the track could be reconstructed only up to the PCF chambers. Remember that the scattered muon track was required to have hits either in the DC or PSA chambers.

A small sample of events where the muon match processor could not connect the muon projections with forward tracks were scanned. The reasons of the failures

Table 4.6: Data Reduction statistics for the LAT deuterium sample.

Total number of input events	403464	100.00%
Number of events with no vertex	279374	69.24%
Number of rejected events by DR cuts	92544	22.94%
Number of selected events	31546	7.82%
Number of events with no beam or muon projection	48346	11.98%
Number of events with no Forward Spectrometer track	92145	22.84%
Number of events with no matched muon	111801	27.71%
Number of events with no reconstructed vertex	27082	6.71%
Total number of events with no vertex	279374	69.24%

in the muon match processor are given in Table 3.3.

A visual scan was done for the events where the vertex could not be reconstructed even though the beam and muon tracks were reconstructed. The details of vertex program failures are given in Table 3.4. The events in these tables include the events selected by the monitoring filter program which explains the presence of events with zero or more than one beam.

As it is clear from Tables 3.3 and 3.4, most of the events not reconstructed by software are background to the deep inelastic sample. The visual scan is very subjective and hence the conclusions are not very rigorous. In any case the software failures, if any, should cancel out in the ratio. Moreover data were corrected for the hardware and reconstruction inefficiencies using Monte Carlo. The total number of events selected by the Data Reduction for the physics analysis are given in Table 4.8. The "input" column is the number of events selected by the corresponding filter program. The false triggers which dominated the raw data sample can result from a variety of reasons e.g. close halo or scattering in the absorber.

The triggers caused by close halo and muons in adjacent RF buckets were removed by the filter program. The filter program also removed the events triggered by muons which scattered either in the steel absorber or in the calorimeter.

The events triggered by muon scattering in detectors upstream of the CCM magnet but far away from the target region were removed by the DR program after the interaction point was known. In these events the muon scattered either

Table 4.7: Data Reduction statistics for the SAT Hydrogen sample.

Total number of input events	604064	100.00%
Number of events with no vertex	417077	69.04%
Number of rejected events by DR cuts	77865	12.89%
Number of selected events	109122	18.07%
Number of events with no beam or muon projection	175871	29.11%
Number of events with no Forward Spectrometer track	108954	18.04%
Number of events with no matched muon	96318	15.94%
Number of events with no reconstructed vertex	35934	5.95%
Total number of events with no vertex	417077	69.04%

Table 4.8: The event sample after the Data Reduction Program

Data Set	Input	Output	%
LAT Deuterium Target (post Dec 1987)	403464	31546	7.82
LAT Hydrogen Target	715066	31239	4.37
SAT Deuterium Target	308779	72652	23.53
SAT Hydrogen Target	604064	109122	18.06

in the PBT or PCV chambers.

The physics background events such as muon interacting with the electron in the target or bremsstrahlung in the target could not be separated and were part of the final samples given in Table 4.8. For LAT events some of the electromagnetic background events were eliminated by the x_{bj} cut in DR program. Further kinematics selection was made to restrict the final analysis in well understood kinematic region as will be described in section 5.1.

4.2 Beam Normalization

One of the important and difficult task in a cross section measurements experiment is the calculation of incoming beam flux but it is relatively easy to measure the incoming beam flux in a muon scattering experiment. Because the muon beam has very low intensity ($\sim 10^6/\text{sec}$), each incoming muon can be individually detected and counted. Because of the RF structure of the Fermilab beam, possible time of arrival of each muon is precisely known. The muon experiments have this advantage over neutrino experiments where the flux is measured in an indirect way.

In this section the issues related to the measurement of the muon flux are discussed.

4.2.1 LAT Normalization

- **Scaler data :** The various elements of the Large Angle Trigger (LAT) are described in 2.8.1. The raw beam, ungated $B \cdot \bar{V}$ and gated $B \cdot \bar{V}$ were scaled every spill by end-of-spill scalers. The gated $B \cdot \bar{V}$ (LATB) is the flux of incoming useful beam for LAT data set. The LATB was scaled also for every event by event-scalers. The LATB measured by end-of-spill (EOS) scalers was compared with event-scalers (EVE) for a part of the hydrogen data. The result is shown in Fig. 4.1. The agreement is very good which is not surprising because it is the same signal being fed into two different scalers. The spread in the distribution is caused by the edge effects. The EOS scalers measured the beam during the live period of the n th spill whereas the EVE scalers measured the beam since the last event in the $n-1$ th spill to the last

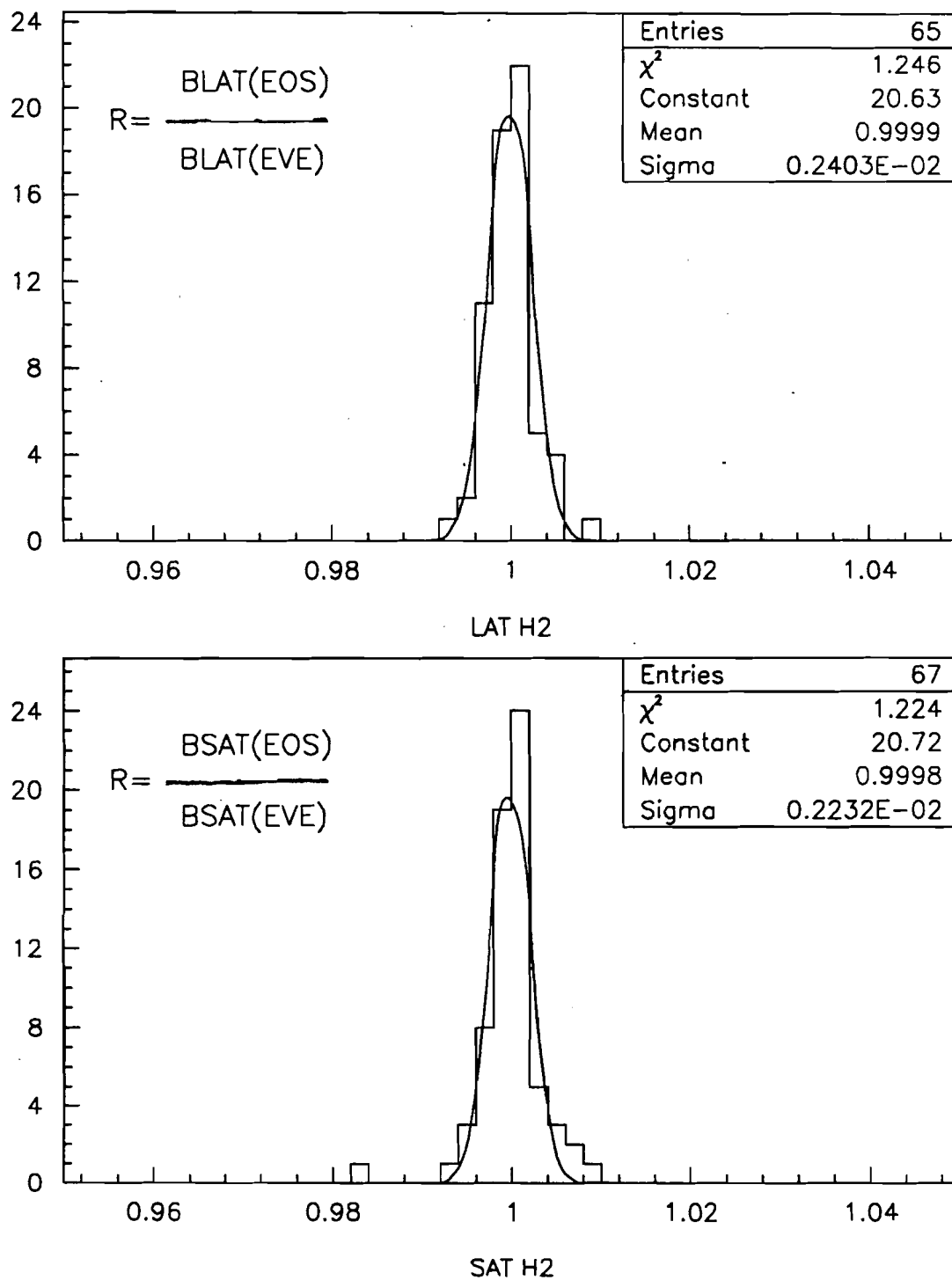


Figure 4.1: Comparison between End-Of-Spill scalers and EVEnt Scalers

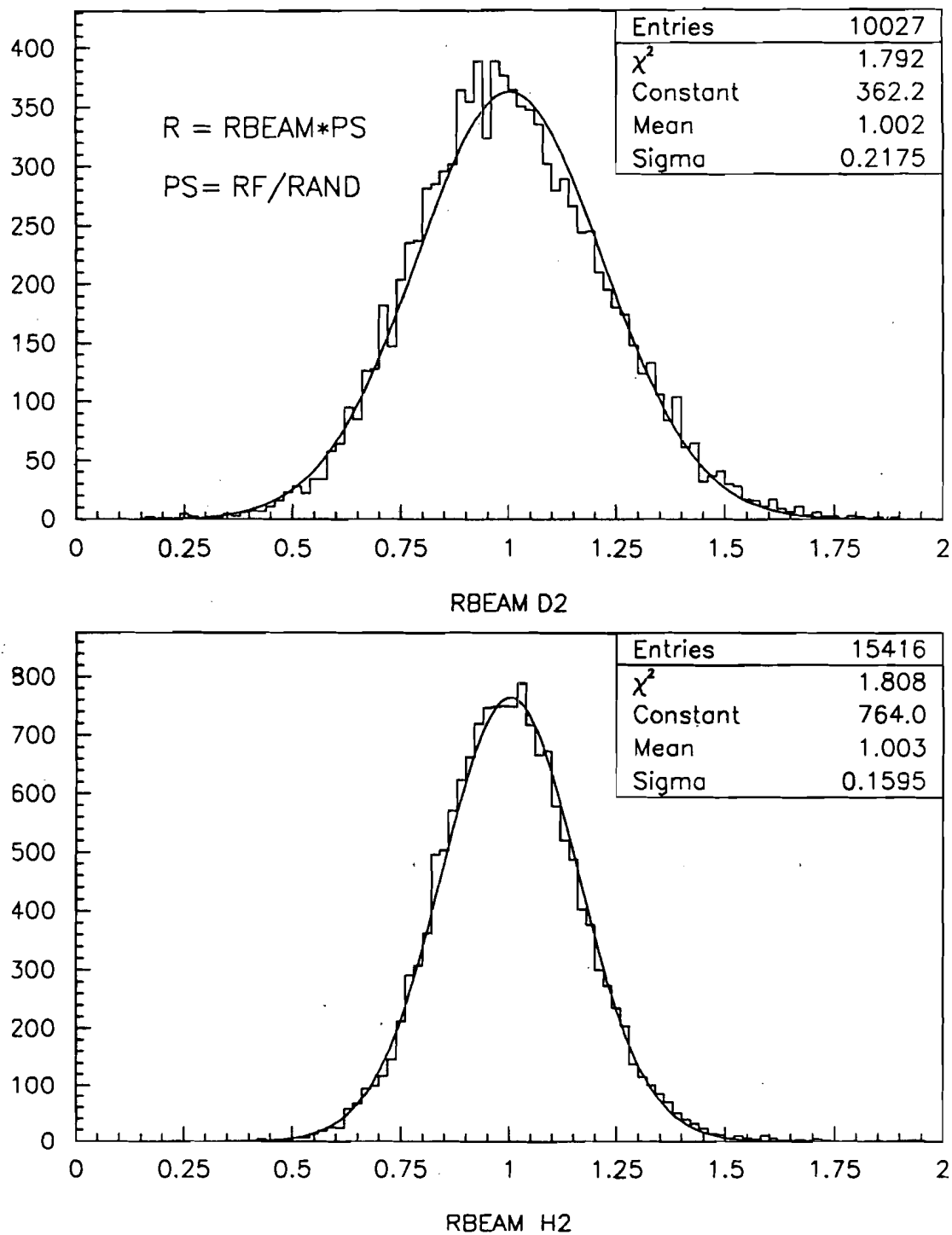


Figure 4.2: Pre Scale Factor for RBEAM data

event in the n th spill which leads to a very small difference in counting. As the two scalers are operated independently, the agreement between them is a proof that the system gating was working properly.

The reconstruction efficiency for the beam tracks is not 100% and the scaled LATB should be corrected for inefficiency. However for the measurement of the ratio of the structure functions such effects cancel out and one can use LATB for normalization. This is true only if the reconstruction efficiency did not change with time. The RBEAM data (see below) have complete information about the event and it can be used to correct the incoming beam flux for any inefficiency in reconstruction.

The trigger bits used in the analysis are the Bison Box trigger bits. The trigger bits were also latched. The total number of triggers in a spill was also scaled. These three different ways of counting the triggers were compared and found consistent. The number of LAT Level I triggers did not agree with the corresponding Level II triggers for a negligible number of spills. The hardware cause of the disagreement was known. This minor discrepancy has no effect on the final results because the Level II trigger is in complete agreement with the Bison box bits. The Level I trigger bits are not used in analysis. The consistency between the different methods confirms that an event tagged as LAT (RBEAM) trigger was actually caused by an LAT (RBEAM) hardware trigger. This is important especially for RBEAM events because no kinematic cuts can be made to select the RBEAM events.

- **RBEAM :** As described in section 2.8.3, The LATB was prescaled by a random prescaler and the events were written to the tape. The software requirements applied to the beam for LAT data can be made for RBEAM trigger. From the number of accepted RBEAM events and the prescale factor, the beam flux can be calculated. This method of normalization can be used independent of the scalers data described above. Histograms of the ratio

$$R = RBEAM \times \text{Prescaled factor} / LATB(\text{EOS})$$

for hydrogen and deuterium data are shown Fig. 4.2. If the prescale factor is

correct, the ratio R should be one. The expected width is $1/\sqrt{N}$ where N , around 25, is the number of RBEAM events in a spill. The width of 0.21 is in agreement with the expected value (0.2). The spills with too few beams or the wrong RF counts have been removed from the distribution shown. They are also removed from the further analysis.

The RBEAM data were passed through the same filter and reconstruction reconstruction program as the LAT data. The final muon flux can be obtained in two different ways.

- calculate the fraction of accepted RBEAM events after reconstruction and use it to correct the event scaler data
- count the number of RBEAM events accepted after the filter program and $P(\chi^2)$ cuts and multiply it by the prescale factor to get the muon flux.

Because the prescale factor is correct for the RBEAM trigger, two methods are completely equivalent. For convenience in book keeping, the first method was used. The correction factor was calculated for each run block separately.

Tables 4.9 and 4.10 show the luminosity lost due to different quality requirements imposed in the software. The difference in the fraction of good live beam between the two targets is $\approx 2.55\%$ which is a measure of the changes in hardware efficiency in the PBT chambers and the beam phase space (where the beam passes through the PBT chambers). Note almost all the difference comes from the requirement that the $P(\chi^2)$ should be greater than 0.001. The same $P(\chi^2)$ cut is used for deep inelastic data and hence this difference does not effect the normalization. This is the advantage of using RBEAM for normalization.

4.2.2 SAT Normalization

- **Scaler data :** The SAT beam (SATB), as defined by SAT trigger matrices was scaled by end-of-spill scalers and event-scalers. The comparison between the SATB as scaled by EVE scalers and the EOS scalers is shown in Fig. 4.1. The agreement is very good. The width of the distribution agrees with the expected value based on edge effects.

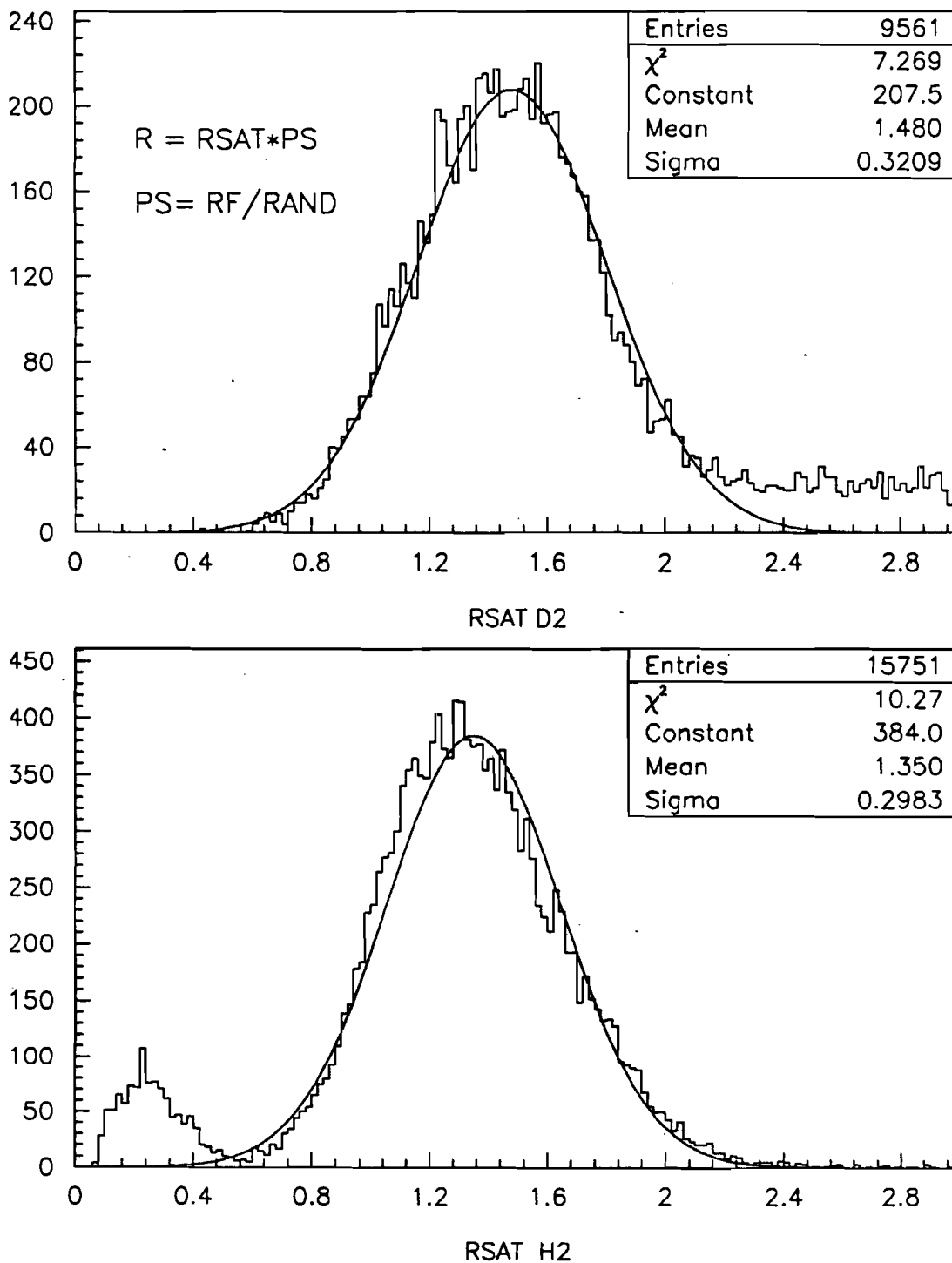


Figure 4.3: Pre Scale Factor for RSAT data before correction

Table 4.9: The number of live muons deuterium for LAT sample

Events RBEAM	219983	
Events RBEAM good run block	191595	1.000
RBEAM passing the filter	156242	0.815
RBEAM passing momentum > 300.0	155880	0.814
RBEAM passing $P(\chi^2) > 0.001$	139596	0.729

Table 4.10: The number of live muons hydrogen for LAT sample

No. of RBEAM events	168362	
No. of RBEAM events in good run blocks	139195	1.000
No. of RBEAM events selected by the filter	113415	0.815
No. of RBEAM events with > 300.0	113224	0.813
No. of RBEAM events with $P(\chi^2) > 0.001$	98825	0.710

- **RSAT** : The RSAT, the prescaled SATB, trigger had a problem in the electronics. The detail of the problem is described in [82]. Due to double pulse produced in an electronic module, some extra triggers were generated. These trigger were out of time from the RF buckets containing the beam muon. The ratio

$$R = RSAT * 2^{16} / SATB (EOS)$$

is plotted in Fig. 4.3. The distribution has the expected gaussian shape but the mean is shifted from 1.0. The width of distribution is consistent with the $1/\sqrt{RSAT}$ where RSAT is number of RSAT triggers per spill. For a small time during the hydrogen running period the prescale factor was raised by a factor of 4 which explains the smaller peak in the distribution.

Using the SBT hodoscope information, the out of time triggers were identified. The RSAT events in which all 7 SBT hodoscopes were not latched were rejected as fake triggers. After these events have been removed, the ratio R defined above was consistent with 1.0

After the correction to number of RSAT triggers is made (and the prescale

Table 4.11: The number of live muons deuterium

Events RSAT	140111	
Events RSAT	140111	1.000
Events RSAT 7/7 SBT	94624	0.675
Events RSAT 7/7 SBT 2/4 SMSZ 2/4 SMSY	91220	0.651
Events RSAT 7/7 SBT 2/4 SMSZ 2/4 SMSY	91220	1.000
RSAT passing filter	84427	0.926
RSAT passing momentum >400.0	80659	0.884
RSAT passing $P(\chi^2) > 0.001$	71336	0.782

Table 4.12: The number of live muons hydrogen

Events RSAT	281609	
Events RSAT	281609	1.000
Events RSAT 7/7 SBT	198436	0.705
Events RSAT 7/7 SBT 2/4 SMSZ 2/4SMSY	193400	0.687
Events RSAT 7/7 SBT 2/4 SMSZ 2/4SMSY	193400	1.000
RSAT passing filter	174798	0.904
RSAT passing momentum > 400.0	167475	0.866
RSAT passing $P(\chi^2) > 0.001$	147672	0.764

factor established), the use of scaler data and RSAT data is equivalent. The scaler data were used because of ease in book keeping.

4.2.3 Estimate of Errors in Normalization

The muon flux being scaled is generated by the same hardware as the one used to generate the beam signal for physics trigger. Any inefficiencies in the hardware are common and do not effect the normalization. The results from different scalers are consistent and give us confidence that the scalers were working properly. The agreement between prescale factor calculated from the number of RBEAM triggers and the scaled LATB with the design value is also impressive.

A potential source of errors is associated with the filtering program for SAT and LAT data. Any errors in the filtering are in principle same for the LAT and RBEAM triggers and the SAT and RSAT triggers. As the filtered reconstructed LAT events are being normalized with the filtered, reconstructed RBEAM events (using the same programs and cuts) all the errors must cancel out.

Another problem is associated with the edge effects. The tape logging was not synchronized to the begin of the spill. For the first spill on the tape end-of-spill scalers counted the beam for full spill but a fraction of the events were written to tape. The EOS information for the last spill is missing from the tape. This is a potential problem only if end-of-spill scalers are used to normalize.

The event scaler (EVE) were not **reset** every event. They measured the cumulative beam since the start of data taking. This implied that the beam for first event on a tape could not be calculated. Therefore it was decided to set the beam for first event of raw data tape to zero. There are ~ 15000 events on a raw data tape. Therefore the error in normalization is $(1/15000)$ or $\sim 6.6 \times 10^{-3}\%$. In the filter program, in which only $\sim 20\%$ of data were written to output tape, a special event at the end of the tape was used to keep count of beam associated with the rejected events after the last good event.

One of the potential problem in the absolute normalization is the fact that the beam pattern recognition efficiency depends on topology of the events. For the events with two or more tracks in the beam chambers, the efficiency drops below 80%. For this reason, multi beam events were rejected in the filter program and the luminosity was corrected using the RBEAM (RSAT) data. The underlying

assumption is that the software losses are same for LAT (SAT) and RBEAM (RSAT) data, and there is no reason to expect otherwise.

One of the convincing ways to set the absolute rate of interaction is to normalize it to some known, understood and calculable physics process. In E665 the natural choice is the muon-electron (μe) scattering process. Given a very segmented electromagnetic calorimeter, the identification of μe events is not difficult in E665. Unfortunately, during 1987-88 run the EM calorimeter performance was not uniform over time and therefore this method does not lead to more precise results (see section 5.1.1).

4.3 Momentum Calibration

To calculate the differential cross section, one of the important quantities to measure is the absolute energy scale of the interaction. The momentum of the incoming beam muon is given by the NMRE field strength and momentum of the scattered muon is given by CCM magnet. Using unscattered muon tracks, the two spectrometers can be cross calibrated.

Fig. 3.4 shows that reconstructed momentum of forward going muon is in good agreement with the generated momentum, indicating that the track fitting program does not introduce any biases. The reconstructed momenta of beam track also agree with the generated value.

The difference in the momenta of an un-scattered muon track (RBEAM) as measure by the beam spectrometer and the forward spectrometer is shown in Fig. 4.4. A comparable difference is also observed for RSAT data. The difference between the two measurements is $\sim 1.5\%$. This would imply that the magnetic field map of the CCM magnet is wrong to 1.5% assuming all the difference comes from the field measurements. The CCM field map is accurate to better than 0.1%. The central value of the magnetic field was measured NMR probe and known to better than .1%. On the other hand one can assume that the source of error is measurement of the track curvature. This translates into a 0.4 mm shift in the y position of the PSA chambers. The residue plots for the PSA chambers show that each PSA chamber is aligned to better than 0.1 mm. The other possibility is that the momentum of incoming beam track is not measured correctly. This would imply that either the field strength of NMRE magnet or the position of the

PBT chambers is wrong.

The cause of the momentum difference could not be traced. In any case the error introduced by this systematic mismatch in ν , Q^2 and x_{bj} is less than few percent which is much less than the corresponding resolutions.

A better method for momentum calibration is to measure the mass of a particle and compare with known value. In E665 K^0 mass is measured to be 0.4954 ± 0.0008 GeV[88]. The particle data book value is 0.497671 ± 0.000030 GeV. The error on the mass measurement is only 0.18% which is very small. This would imply that the forward spectrometer momentum measurement is correct and difference in the momentum measurement comes from the beam spectrometer.

4.4 Geometrical Acceptance of the Trigger

The geometrical acceptance of the trigger was evaluated using the E665 Standard Monte Carlo described in section 3.6.1. The LAT and SAT beam and scattered muon requirements for the trigger were simulated and the acceptance for each $Q^2 - x_{bj}$ bin calculated. The hardware for the trigger system is described in section 2.8. The acceptance at low scattering angles is dictated by the size of the beam veto used for both triggers. The acceptance at high Q^2 or large scattering angle is determined by the SPM aperture. As described in section 2.8.2, presence of the scattered muon was not required in SAT hardware trigger but it was required in software analysis. Therefore the final acceptance at high Q^2 is same for both triggers. Even though the acceptance at high Q^2 is very close to 1.0, the event yield, which is given by rapidly falling $1/Q^4$ cross section, is very small. In 1987-88 data, the event yield for $Q^2 > 150$ GeV 2 is essentially zero.

The acceptance was defined as the ratio

$$ACC = \frac{(\text{number of events accepted})_{\Delta Q^2, \Delta x_{bj}}}{(\text{number of events generated})_{\Delta Q^2, \Delta x_{bj}}}$$

where the accepted events were required to satisfy only the hardware trigger

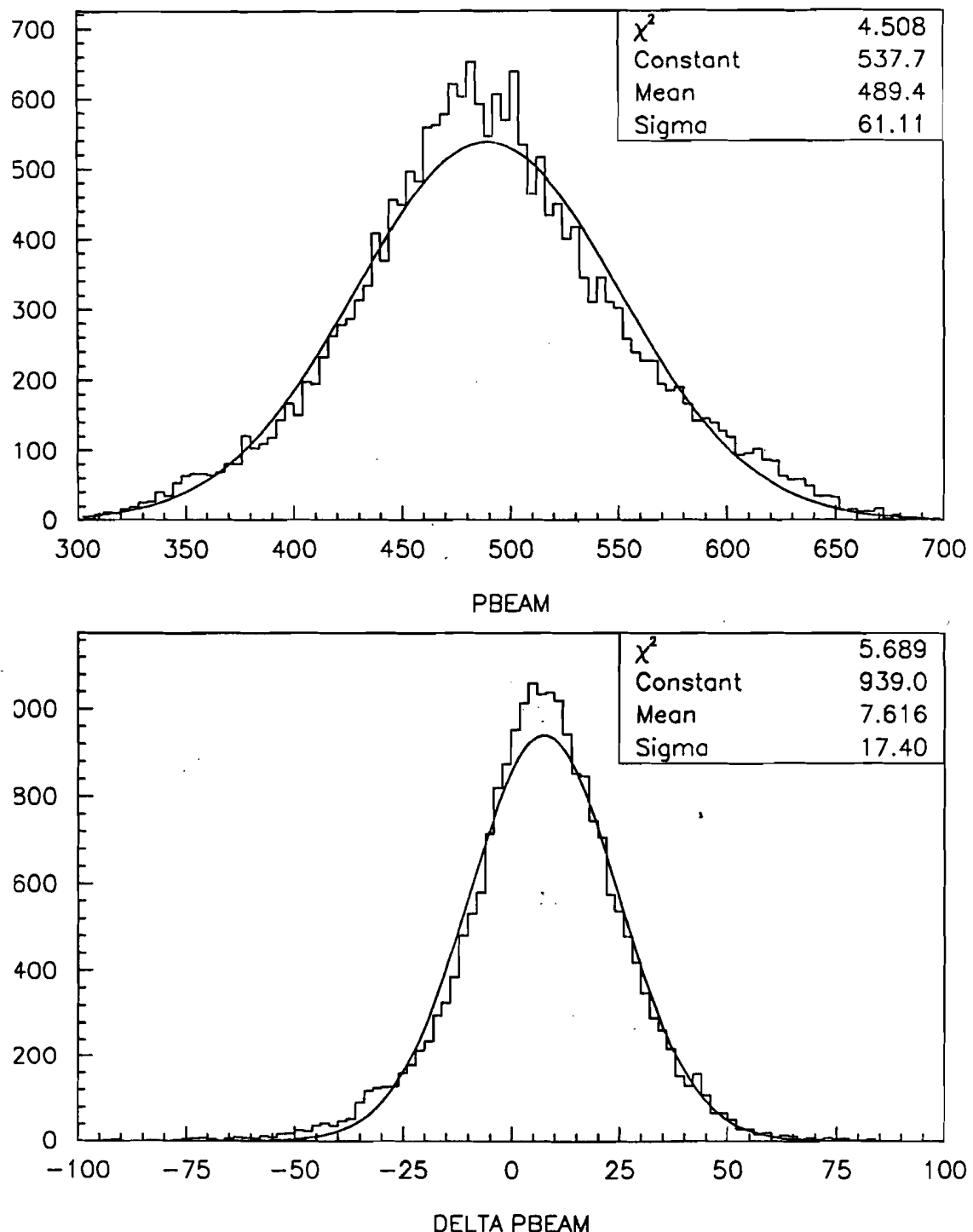


Figure 4.4: The comparison of RBEAM momenta as measured by Beam and Forward spectrometer

requirement as described in section 2.8.

The events were generated according to deep inelastic cross section. For event generation, the Morfin-Tung parton distributions were used. Given fine enough bins (i.e. if the variation of acceptance within a bin is small) the acceptance is independent of the underlying distribution. Therefore the acceptance was calculated using only one set of parton distributions.

The geometric acceptance depends only on the trajectory of the scattered muon through the detector and not on the flavour of the quark (target) it scatters from. The trajectory of the scattered muon depend on the vertex point, the scattering angle and the energy of the scattered muon. The location and the size of the target vessel used for the deuterium and hydrogen was same. The beam phase space for the two running periods was also found to be same. Therefore for given Q^2 and ν the geometric acceptance for two targets is same and cancels out in the ratio σ_d/σ_p .

The effects of the scattered muon going through the dead regions in the tracking chambers or outside the active area of chambers were assumed to factorize from the geometric acceptance of the trigger and was treated separately. The evaluation of the effects of dead regions, finite active areas of forward chambers and any hardware or software inefficiencies require a more detailed monte carlo and are described in section 4.6.

The trigger acceptance depends on the geometry of the detector. The accuracy of information about the location of various elements used in the trigger determines the systematic uncertainty of the acceptance function. As described in section 3.1, the location of various elements in the SMS hodoscopes are known to better than 1 millimeter as compared to veto size of 66 mm and therefore the systematic error due to misalignment can be neglected.

The acceptance function is a rapidly varying function of Q^2 and x_{bj} , specially at low values of Q^2 and x_{bj} . The resolution in the determination of the kinematic variables is described in section 3.5.7. The typical resolution in x_{bj} is $\sim 15\%$ and is independently of x_{bj} . In Q^2 the resolution varies from 12% at 0.2 GeV to $\approx 2\%$ at Q^2 equal to 10 GeV. Therefore the smearing in the measurement of kinematic quantities effects the acceptance by less. few percent. This effect is taken into account while making the detector efficiency corrections.

Another problem related with geometric trigger acceptance is the so-called suicide events. A muon which scattered in the target can also interact in the absorber and produce more particles. These particles might go through SMS counters and generate a veto signal. Thus a good DIS event might be lost. Similar effect is seen if the scattered muon changes its direction while passing through the absorber. Both these effects are important only when the scattered muon is very close to the veto counters. The effect of suicide events is not taken into account in the geometric acceptance described below. This effect can be measured from the data only.

4.4.1 LAT Acceptance

For the LAT acceptance calculations the beam distribution extracted from the RBEAM data was used. The beam momentum was required to be greater than 300.0 GeV. The acceptance grid was made fine enough that the variation in acceptance from neighbouring bins was not more than 5%. A total of 150 K events were generated according to deep inelastic cross section. The LAT acceptance study was restricted to following kinematic regions.

$$\begin{aligned}
 0.003 &\leq x_{bj} \\
 0.1 &\leq y_{bj} \leq 0.7 \\
 1.0 &\leq Q^2
 \end{aligned} \tag{4.1}$$

The LAT acceptance is independent of the vertex position as shown in 4.5 (a) as expected by the approximate focussing arrangement of the dipole magnets. The LAT trigger has non-zero acceptance for a minimum scattering (~ 3 mr) angle dictated by the size of SMS counters and for a maximum scattering angle given by the SPM active area. The SPM planes subtend half angle approximately equal to 50 mr at the center of target (± 1.5 m at a distance of 30 meter). This governs the hardware LAT trigger acceptance at high Q^2 . In reality the LAT acceptance turns on gradually with scattering angle as shown in Fig. 4.5(b). It is because the trajectory of the muon depends not only on its scattering angle but also on its energy.

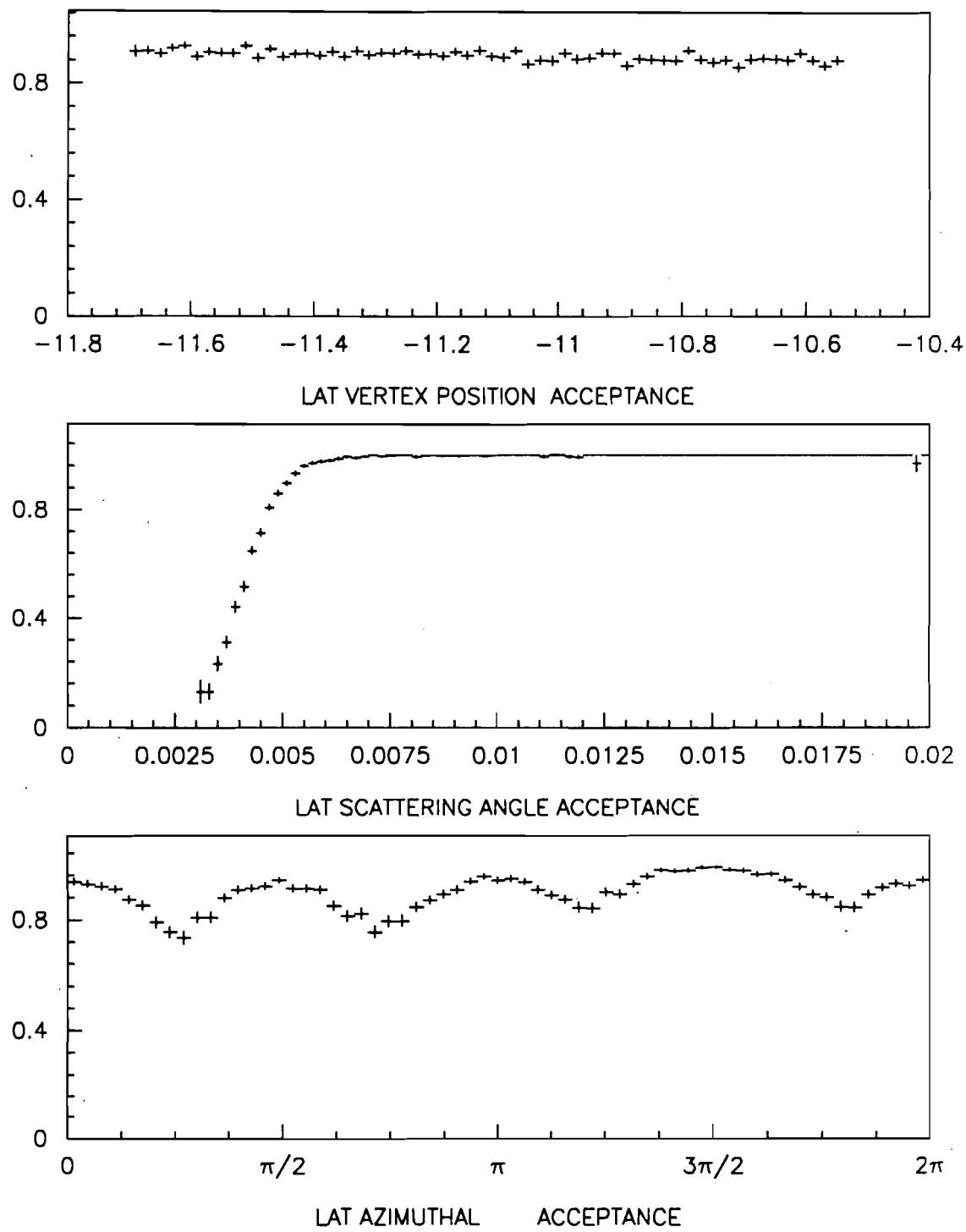


Figure 4.5: LAT acceptance as function of vertex position, θ and ϕ

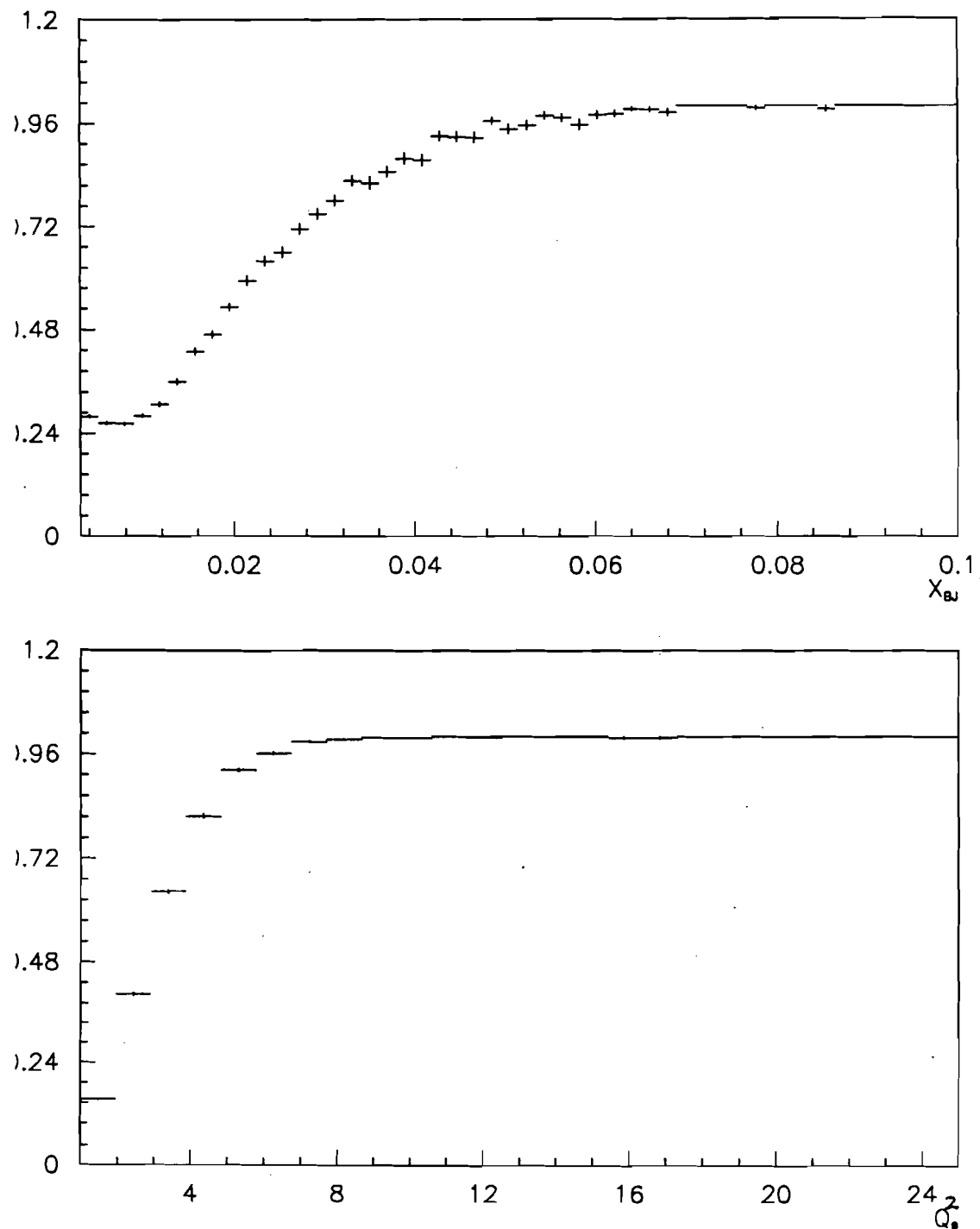


Figure 4.6: LAT acceptance as function of x_{bj} and Q^2

The shape of acceptance curve verses the azimuthal angle shown in 4.5 agrees with what is expected from the square shape of SMS veto. For the pencil beam incident at the center of veto region, one would expect equal acceptance at $0, \pi/2, \pi, 3\pi/2$ and 2π radians. The acceptance at the corners of the square ($\pi/4, 3\pi/4, 5\pi/4$ and $7\pi/4$) is also equal but lower. The bending of the scattered muon by magnetic field toward east increases the acceptance for ϕ in between $\pi/2$ and $3\pi/2$. As the real beam is low in vertical direction, the acceptance for ϕ greater than π is higher.

The agreement between the expected geometric dependence of the acceptance and simulated results imply that the simulation is correct and therefore we can trust the variation of acceptance with the kinematic variable.

The average acceptance verses x_{bj} and Q^2 is shown in Fig. 4.6. The kinematic cuts described above have been used. The acceptance is almost 100% for Q^2 greater than 7.0 GeV^2 . It is close to unity for x_{bj} above 0.05.

4.4.2 SAT Acceptance

For SAT acceptance studies, the beam phase space extracted from RSAT data was used. The generated beam track was required to satisfy the SAT beam requirement. The momentum was required to be more than 400.0 GeV . A total of 100 K events were generated. The two dimensional grid in x_{bj} and Q^2 had 25×11 points. The typical statistical (binomial) error at each grid point was less than 1%. Each grid point had at least 100 events in it.

The acceptance as function of three geometrical variables, vertex position, scattering angle and the azimuthal angle, is shown in Fig. 4.7. As described in section 2.8.2, the SMS veto was used only in the y view. The SAT azimuthal (ϕ) acceptance is reflection of that choice. The acceptance at ϕ equal to $\pi/2$ and $3\pi/2$ is low. The east-west difference (difference between ϕ at 0 and π) is caused by the bending of the muon by the magnetic field. For Q^2 greater than 4.0 GeV^2 , the acceptance at ϕ at π and $3\pi/2$ is same and equal to 1.0. The data taken during the run also exhibit the same ϕ distribution, indicating the monte carlo simulation of trigger is a reasonable reflection of the hardware trigger.

The SAT trigger matrices were calculated under the assumption that the two dipole magnets are arranged in focussing condition. In reality the focussing con-

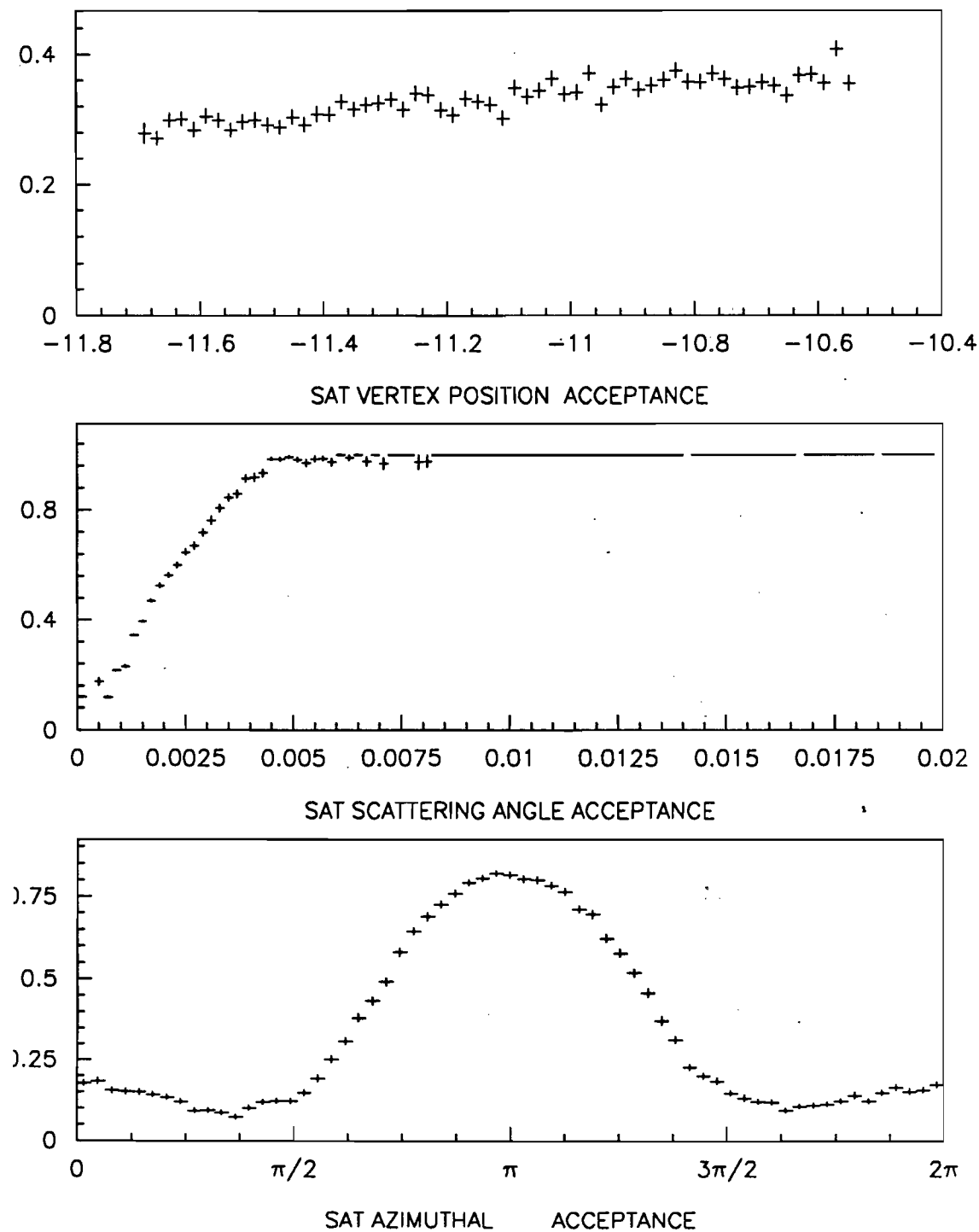


Figure 4.7: SAT acceptance as function of vertex position, θ and ϕ

dition is only approximately satisfied. In particular the muons with vertex point upstream of the center of the CVM field get a different P_t kick than the one downstream at same energy transfer ν . Bending of the muon and therefore the acceptance depends on the location of the interaction point.

Fig. 4.8 shows the mean acceptance for SAT data verses the kinematic variables x_{bj} and Q^2 . The Monte Carlo data with $Q^2 > 0.1 \text{ GeV}^2$ and $x_{bj} > 0.002$ were used. Moreover data were limited to y_{bj} range between 0.1–0.7.

4.5 Trigger Efficiency

The trigger efficiency is a measure of how well the trigger hardware worked. It can be only extracted from the real data. E665 used two independent physics triggers (LAT, SAT) in 1987-88 run and thus one can measure the efficiency of one trigger from other. To measure the efficiency of the LAT, the SAT trigger may not be 100% efficient. Same is true for measuring the SAT efficiency using the LAT trigger. Of course, one can not measure efficiency of the class of events which are missing from both data sets. Geometrical properties of the events which are independent of kinematics of the interaction are good indicator of any problems in the hardware.

4.5.1 LAT Trigger Efficiency

The ϕ distribution shown in Fig. 4.9 of LAT events clearly shows that the LAT trigger was not fully efficient for ϕ greater than π radians. The cause of the inefficiency was traced to the delay in the time of arrival of the SPM signal to the LAT trigger logic electronics [85]. The other possible reason i.e. the lower SPM counters are inefficient is ruled out by the fact that the same signal latched by a wider gate is not inefficient. The SPM efficiency measured using Halo or SAT data sets is also close to 100%. The SAT trigger logic did not require the SPM signal and thus is a good candidate to measure the SPM inefficiency.

The LAT trigger inefficiency was measured using the SAT data using the LAT hardware requirements in software. Only the events selected by SAT filter were used. The beam momentum was required to be greater than 400.0 The SAT data

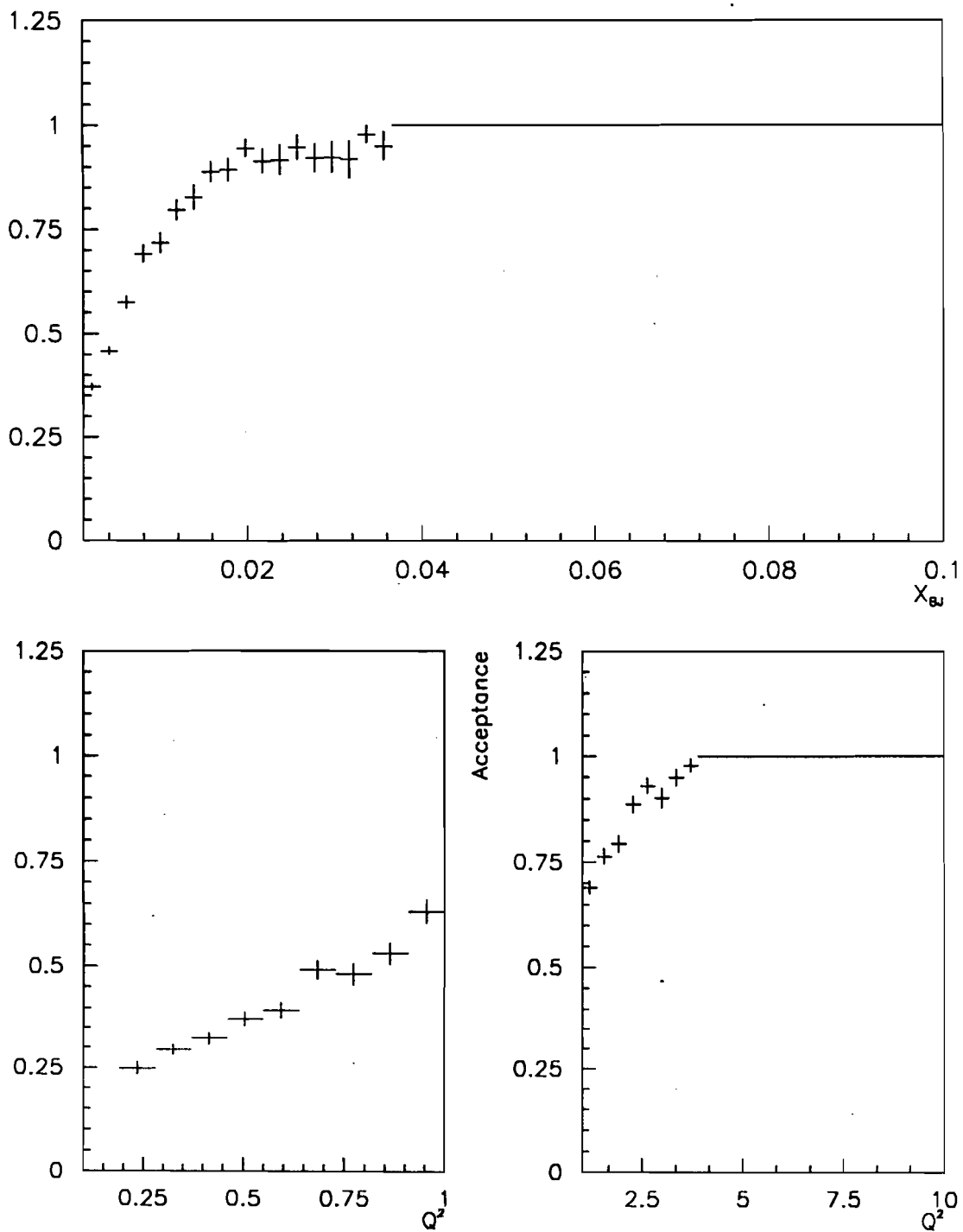


Figure 4.8: SAT acceptance as function of x_{bj} and Q^2

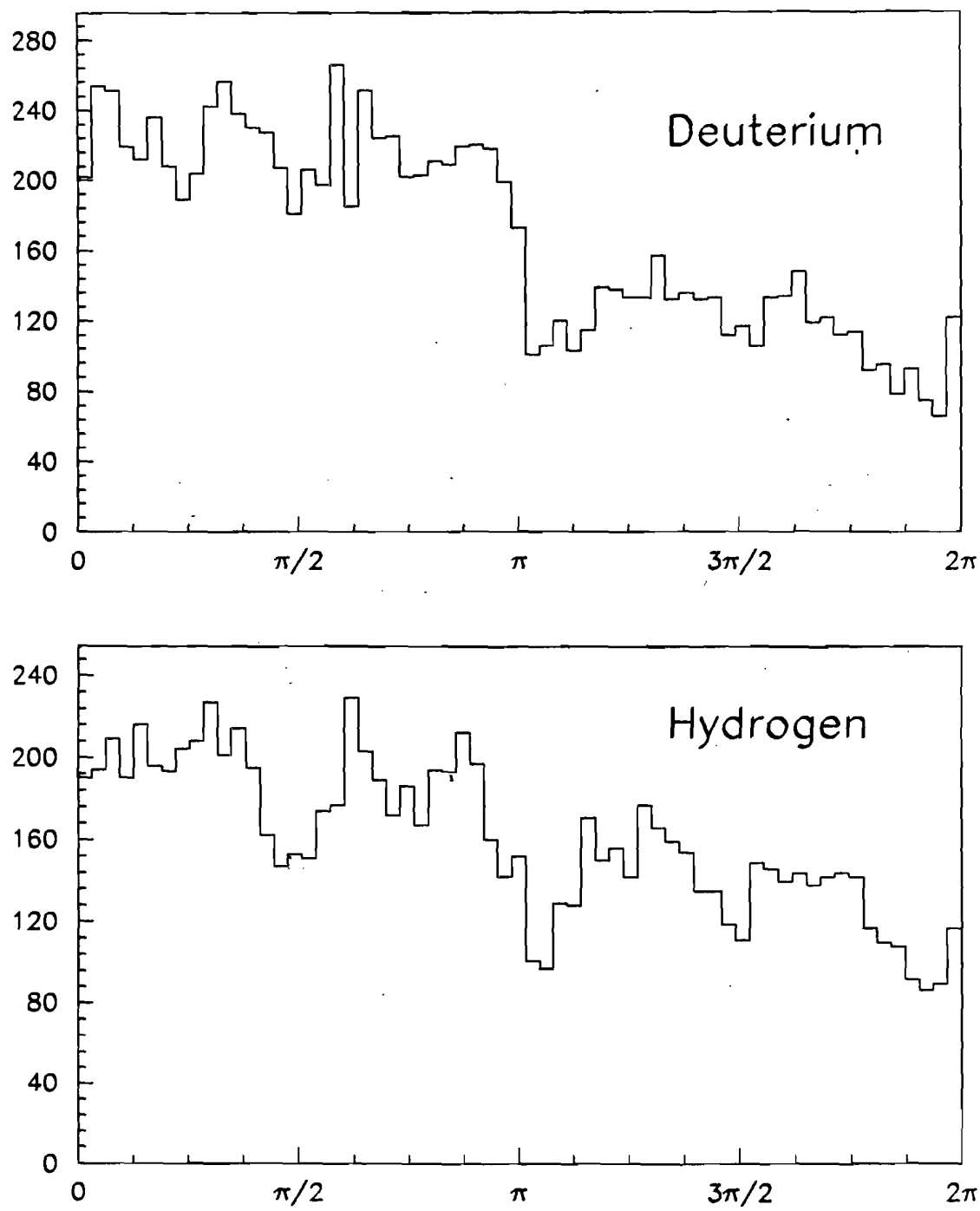


Figure 4.9: ϕ distribution of LAT events sample

Table 4.13: LAT trigger efficiency D2

Number of SAT Events	$\phi < \pi$			$\phi > \pi$		
	Total	LAT	%	Total	LAT	%
No hits in the BEAM Veto System	6362	1321		6024	603	
No hits in the SMS Veto counters	1209	1092	98.59	1237	603	48.70
No hits around the SMS Veto counters	1209	1186	98.10	1237	603	48.70
Muon track associated with SPM hits	1206	1186	98.34	1235	602	48.74

Table 4.14: LAT trigger efficiency H2

Number of SAT Events	$\phi < \pi$			$\phi > \pi$		
	Total	LAT	%	Total	LAT	%
No hits in BEAM Veto System	7388	1349	-	7352	887	
No hits in SMS Veto	1372	1347	98.18	1407	885	62.90
No hits around SMS Veto	1372	1347	98.18	1407	885	62.90
Muon track associated with SPM hits	1367	1347	98.64	1399	884	63.19

was also required to pass following cuts.

$$x_{bj} > 0.001 \quad 0.05 < y_{bj} < 0.85 \quad Q_2 > 0.1 \text{ GeV}^2$$

The inefficiency of LAT trigger is tabulated in Table 4.13 and Table 4.14. The requirements imposed are successive. The LAT trigger efficiency for deuterium is lower than one for hydrogen. Therefore it was decided to use only the events with azimuthal angle (ϕ) less than π where the trigger performance is relatively stable with time.

4.5.2 SAT Trigger Efficiency

The SAT trigger efficiency was determined using the LAT data set. As mentioned before, the SAT trigger used a subset of incoming beam and a smaller veto behind the absorber. Events from the LAT sample which satisfied the SAT beam

Table 4.15: SAT trigger efficiency D2 using LAT data

	Total	SAT	Efficiency
Events in LAT sample	12594		
Events satisfying BSAT	1971	1372	69.6%
Events with no hits in SMS's	1827	1292	70.7%
Events no extra hits in SBT's	1102	867	78.7%
Events no extra hits in PBT's	714	559	78.3%

requirements and the final kinematic and vertex position cuts were selected. Table 4.15 shows the SAT efficiency for deuterium sample. The requirements are successive. The SMS veto was part of the LAT trigger and therefore does not effect the results. The extra hits in SBT hodoscopes are the hits leftover after all the hits associated with the beam tracks have been removed. This requirement mimics the SAT hardware requirement of *clean* beam. A beam was defined *clean* if there were no extra hits in the SBT hodoscopes apart from the one used in the trigger. The extra hits in the PBT chambers are the leftover ones after the hits associated with the beam tracks have been eliminated. Because PBT chambers have 200 ns long live time, no extra hits in the PBT chambers implies that there were no beam particles in close by RF buckets, a hardware requirement for the SAT trigger. The results for the hydrogen data set are tabulated in Table. 4.16.

The restriction imposed in this study are very stringent and hence the final numbers may be an overestimate of the real trigger efficiency. The SAT trigger efficiency does not depend on any of the kinematic variables. Therefore any correction is an overall multiplicative factor. The consistency of SAT trigger in two running periods can also be seen by comparing the geometrical properties of events for two targets. In Fig. 4.10 ϕ distribution and position of the vertex along the beam for real data are shown. The distributions for two targets have been normalized to same number of events. The distributions for hydrogen and deuterium are similar.

The difference in the trigger efficiency for two targets is $\approx 2\%$ and this tends to decrease the F_2^n/F_2^p ratio. This correction is not applied to the final answer.

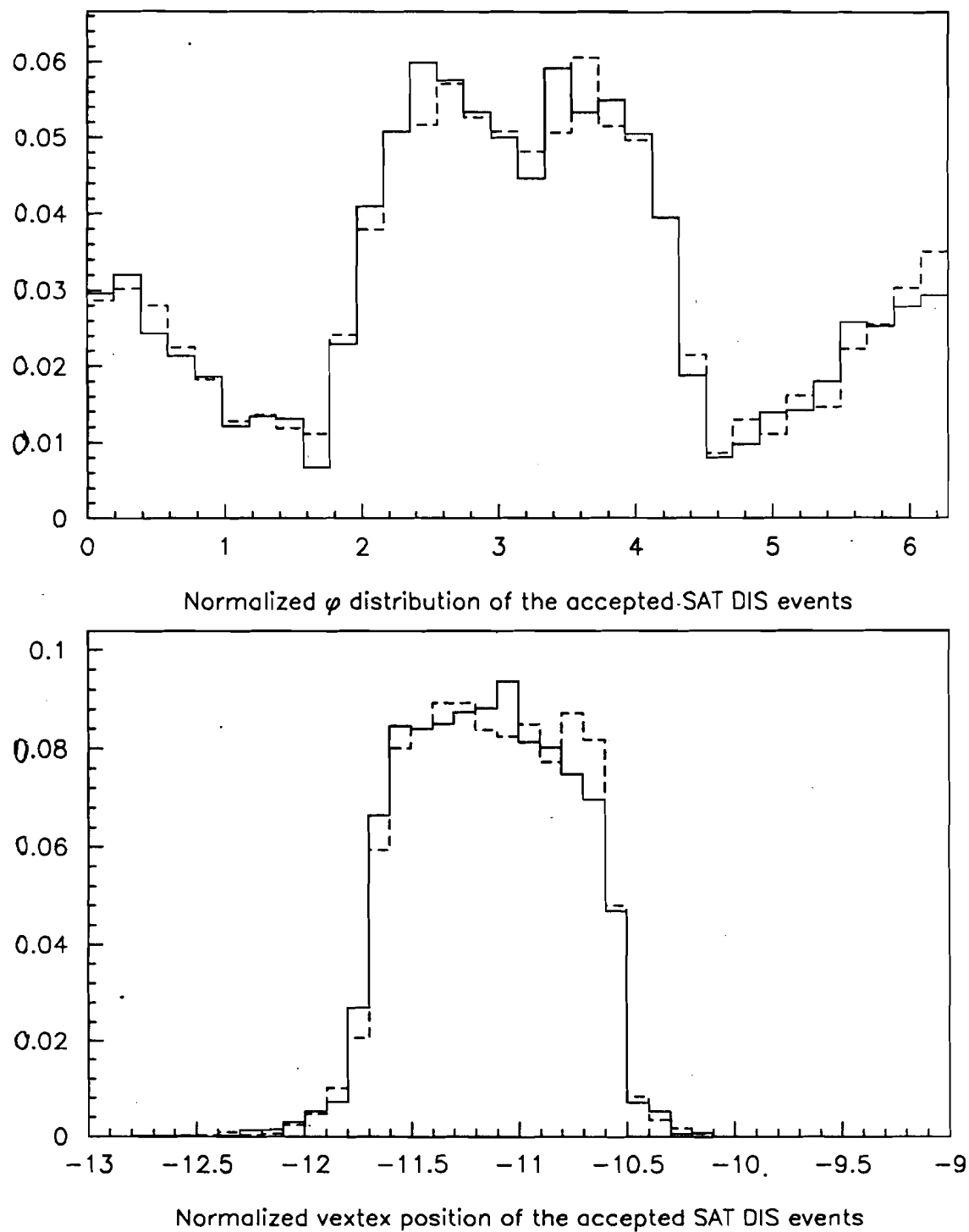


Figure 4.10: Geometric properties of SAT Deep Inelastic Sample
 The solid line is for hydrogen data and dotted line for deuterium data

Table 4.16: SAT trigger efficiency H2

	Total	SAT	Efficiency
Events in LAT sample	11284	—	
Events satisfying BSAT	1795	1237	68.6%
Events with no hits in SMS's	1652	1166	70.6%
Events no extra hits in SBT's	1304	965	74.0%
Events no extra hits in PBT's	898	683	76.1%

4.6 Detector Hardware Efficiency

The efficiency of the detector includes the effect of finite aperture of the chambers, any dead regions and the actual efficiency of the chambers during data taking. The efficiency of the chambers can be estimated from the data. The consequences of the finite aperture and dead region can be only estimated using a detail Monte Carlo. The procedure which was used to evaluate the chamber efficiency from data was as follows.

- Reconstruct the track and calculate the track parameters
- Project the track to the plane under study
- Look for the hit in the plane in the vicinity of the projected position. If the χ^2 for the hit in the plane defined as

$$\chi^2 = \frac{(\theta - \theta^P)^2}{\sigma_{plane}^2 + \sigma_{track}^2}$$

was less than 5.0 then the plane was assumed to contribute to the track. θ^P is the projected coordinate.

The deep inelastic data after the DR program was used to calculate the efficiency of the planes. All the events in this data set were good events. For the PCN, PCF, PCV and DC chambers, the LAT data were used. The SAT data were used to measure the efficiency of PSA chambers. The details of the final efficiency distributions are given in [77]. The location of support wires in PCF chambers and dead regions in DC chambers were determined and parameterized. Hardware problems with some of the chambers were discovered during these studies and were properly represented in Monte Carlo. They include the annular dead

region in the PCN chambers and few dead planes in the PSA chambers. The chamber efficiencies changed appreciably from first half of the deuterium data taking period to the second half. Therefore the deuterium data taking period was divided into two section. Similarly the hydrogen data taking period was also divided into two periods. As an example, the efficiency maps for the PCF chambers are shown in Appendix A. The efficiency of beam chambers, PTM's and SMS's scintillators was also measured. As the RBEAM (RSAT) data are being used to correct the software losses in the beam chambers, the beam chamber inefficiencies are irrelevant.

The efficiency measured by method described above agreed with an earlier study using Halo tracks [78]. This study used theoretically more rigorous formalism but was limited by statistics.

The hardware efficiency can be gauged from the number of different planes contributing to a track. If the number of planes contributing to the Monte Carlo tracks is same as the number of planes contributing to the real data tracks then one can conclude that the hardware efficiencies are represented accurately in the Monte Carlo. The numbers of planes contributing to the incident beam and scattered muon from each detector subsystem are shown in Fig. 4.11. The superimposed points are from SAT hydrogen data set. The agreement is quite good, indicating that hardware efficiencies of different planes were represented accurately in the Monte Carlo.

The Monte Carlo event sample with $x_{bj} > 0.001$ and $Q^2 > 0.1$ was generated. The final reconstruction efficiency for SAT data sample is shown in Fig. 4.12. Only those events where the reconstructed beam track had $P(\chi^2) > 0.001$ were used. The overall reconstruction efficiency is 77.66% for deuterium and 77.09% for hydrogen SAT data set.

4.7 Radiative Corrections

The two independent numerical algorithms have been used to correct for the radiative effects in deep inelastic experiments. The Mo and Tsai formulation [94] has been used by the EMC group and SLAC-MIT group. The BCDMS Collaboration has used the Bardin formulation [30]. Recently the EMC and SLAC data have been re-analysed using the Bardin formulation. The re-analysed EMC data

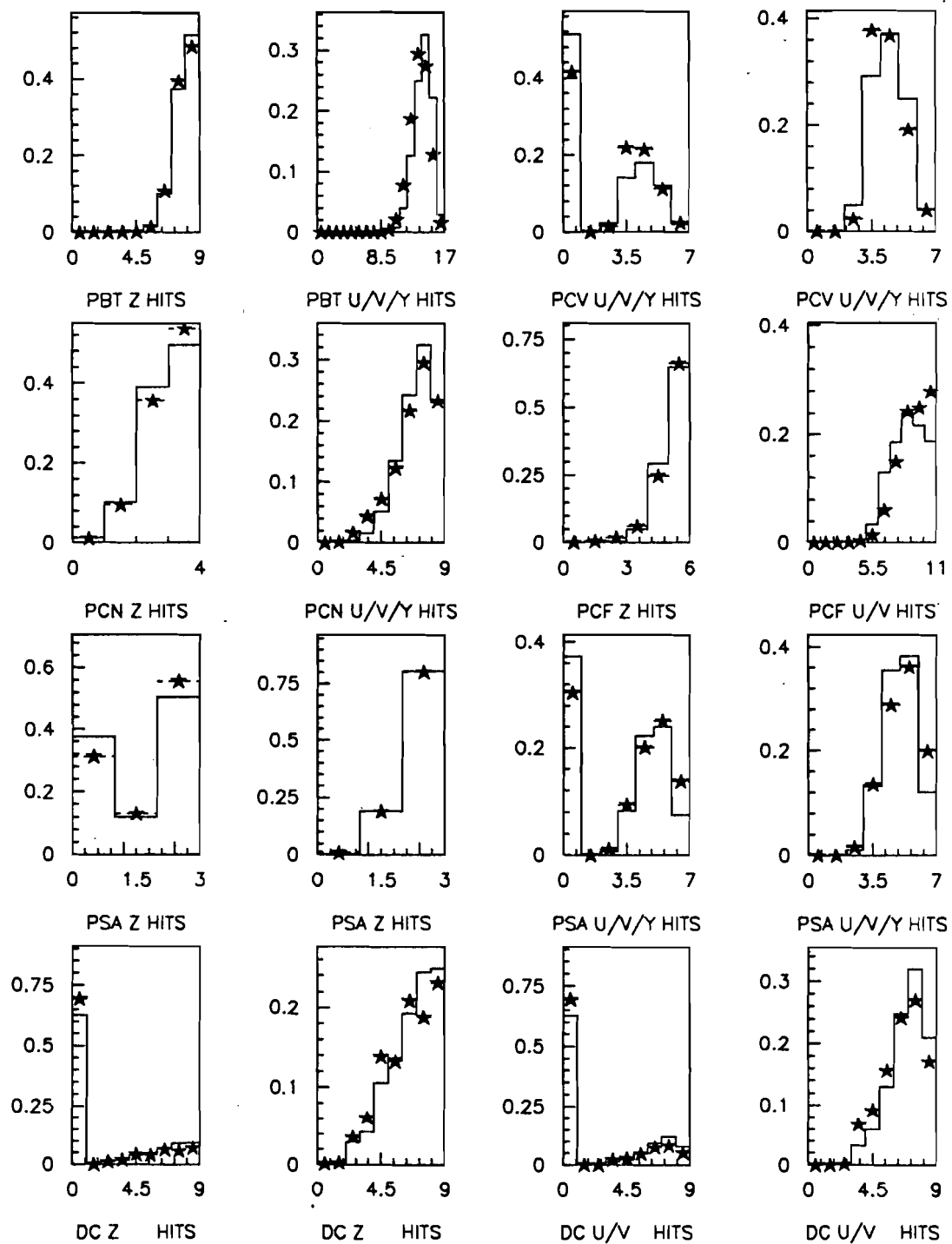


Figure 4.11: The number of planes contributing to incident beam and scattered muon track.

The solid curve is for Monte Carlo and the stars are from hydrogen SAT data

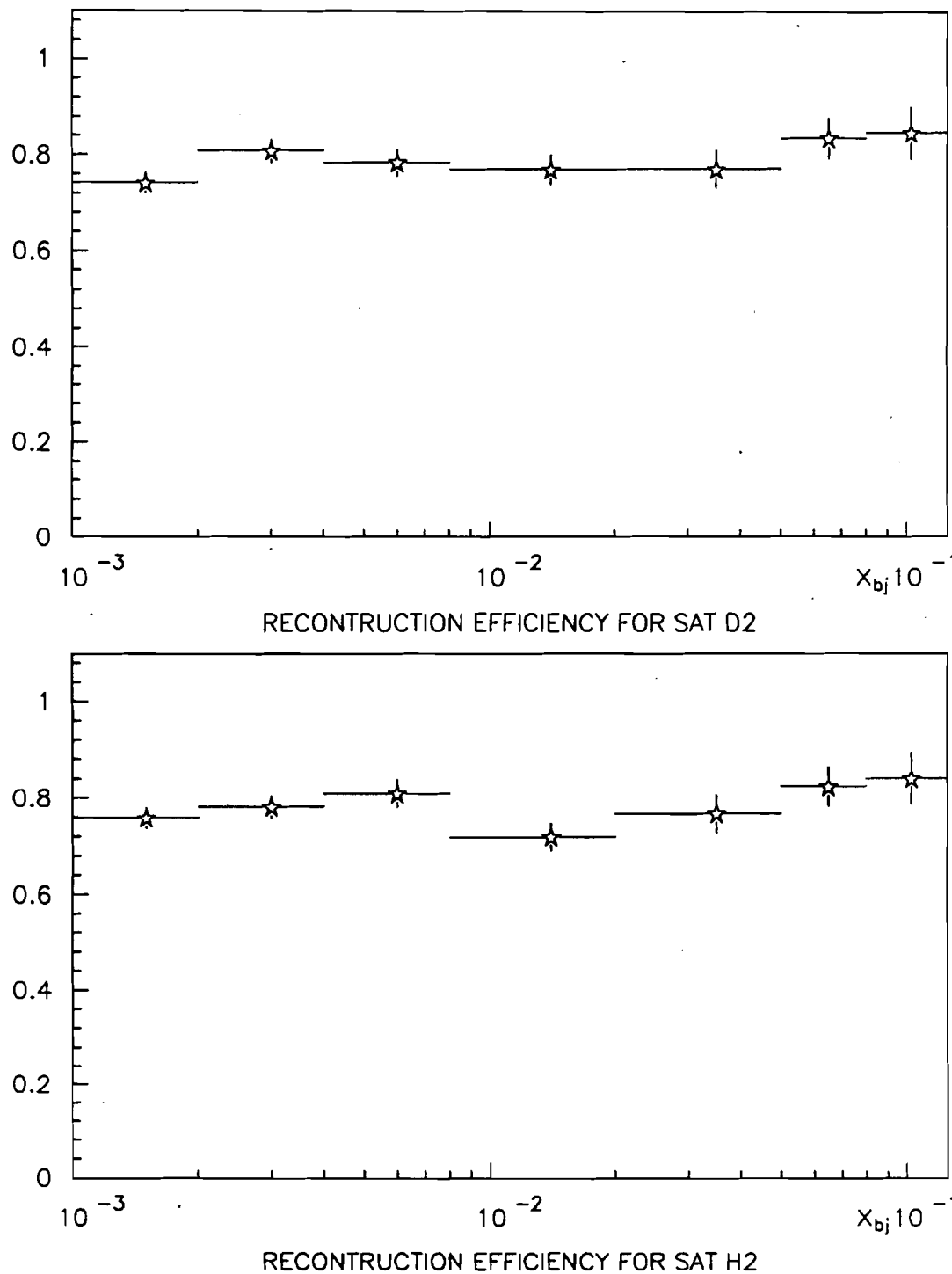


Figure 4.12: The reconstruction efficiency for SAT deuterium and hydrogen data calculated using full monte carlo simulation

are in better agreement with the BCDMS results.

The Mo-Tsai formulation is based on the so called peaking approximation. In the radiative process, the emitted photon is predominantly along the direction of either incoming muon (s peak) or the outgoing muon (p peak). The width of the peaks are approximately $(m/E_\mu)^{1/2}$ and $(m/E'_\mu)^{1/2}$ for s and p peaks respectively [94]. For high y_{bj} events there is a third peak (t peak) along the direction of apparent virtual photon. In Mo-Tsai calculations, the integral is approximated to contribute only along s and p directions. This approximation is good to few percent in most of the kinematic regions. The disagreement for high y_{bj} events is more than 30% because the t-peak is completely neglected in this approximation.

The Bardin formulation is based on the Lorentz-invariant QED calculation for two spin-1/2 particles [90]. As opposed to Mo-Tsai, this method does not have an arbitrary cutoff called Δ . The calculation of radiative contributions require prior knowledge of structure functions. For the calculation of the inelastic continuum contribution at the lepton vertex the Morfin-Tung parameterization of the parton distribution is used except at low Q^2 . At small Q^2 and W^2 values ($Q^2 < 10.0 \times (1 - W^2/15.0)$) the structure functions from SLAC data are used. In threshold region ($W^2 < 3.0$ and $x_{bj} > 0.75$) the SLAC fits [92] are used. Note the the minimum W^2 for E665 data is about 80 GeV 2 and maximum x_{bj} is about 0.3.

However the hadronic and weak contributions are model dependent. The distribution of quarks inside nucleon and quark masses must be known for this calculation. For calculation the quark distribution given in [91] are used. The quark mass is set to 0.33 GeV. The results are found to be insensitive to the small variation in the quark masses [30]. The hadron, weak and higher order corrections are small in magnitude and therefore the choice of quark distribution does not effect the results by more than one percent. This also, *a posteriori*, is a justification to overlook the inconsistency in use of quark distribution in calculation of radiative correction associated with lepton vertex and hadron vertex.

In Bardin code, the radiative contributions from elastic and quasi elastic scattering from the proton, neutron and deuterium targets are calculated using the form factors described in [92]. In code based on Mo-Tsai method, the elastic form factor of proton is taken from Atwood et. al.[93]. In Mo and Tsai code the elastic contribution from the deuterium nucleus scattering is not included in the total

corrections.

The results of using different structure functions from EMC, BCDMS and M-T were compared. The difference was found to be less than 4% of the one-photon cross section over most of the kinematic region. The correction factor normalized to Born cross section using different structure function are shown in Fig. 4.13. This comparison is done at fixed x_b ; equal to 0.005. For the final corrections the M-T parton distributions were used. These parton distributions are valid down to $Q^2 = 1.4$ and include the higher twist corrections which are important at low Q^2 . In the absence of structure functions measured at the kinematic regions of this analysis (low x_b ; and low Q^2), this choice is a bit arbitrary. The systematic error introduced by choice is less than 4% to the absolute cross section measurement.

In this analysis the code based on the Bardin algorithm was used. The results were compared to the corrections using Mo-Tsai formulation and the difference, in the kinematic regions of this analysis were found very small except at very low x_b ; for hydrogen target only. This difference was traced to the difference in contribution of inelastic continuum in two methods. The correction factors due to radiative effects as a percentage of the one photon cross section are given in Table 4.17 for Bardin code and in Table 4.18 for Mo-Tsai code. The corrections given are for hydrogen target. **total** is the total corrections to addition to the Born cross section. The correction factor can be calculated as

$$\text{RADCOR} = \frac{100}{100 + \text{total}}$$

The **ONEL** is the total correction at one loop level. Other symbols are self evident.

For Mo-Tsai formalism, the elastic, quasi elastic and inelastic contributions are listed. The **RADCOR** is defined above. The total correction also include the vacuum polarization, vertex correction and the "exponentiation". The **SIGEXP** is the total measured cross section $d\sigma/(dE'd\Omega)$ in $\mu\text{barn}/\text{GeV}/\text{sr}$.

Most recently the NMC collaboration has used the Mo-Tsai code to correct the measure F_2^n/F_2^p and report about 10% correction in the low x_b ; values. The total correction using Bardin code are of order of 1%.

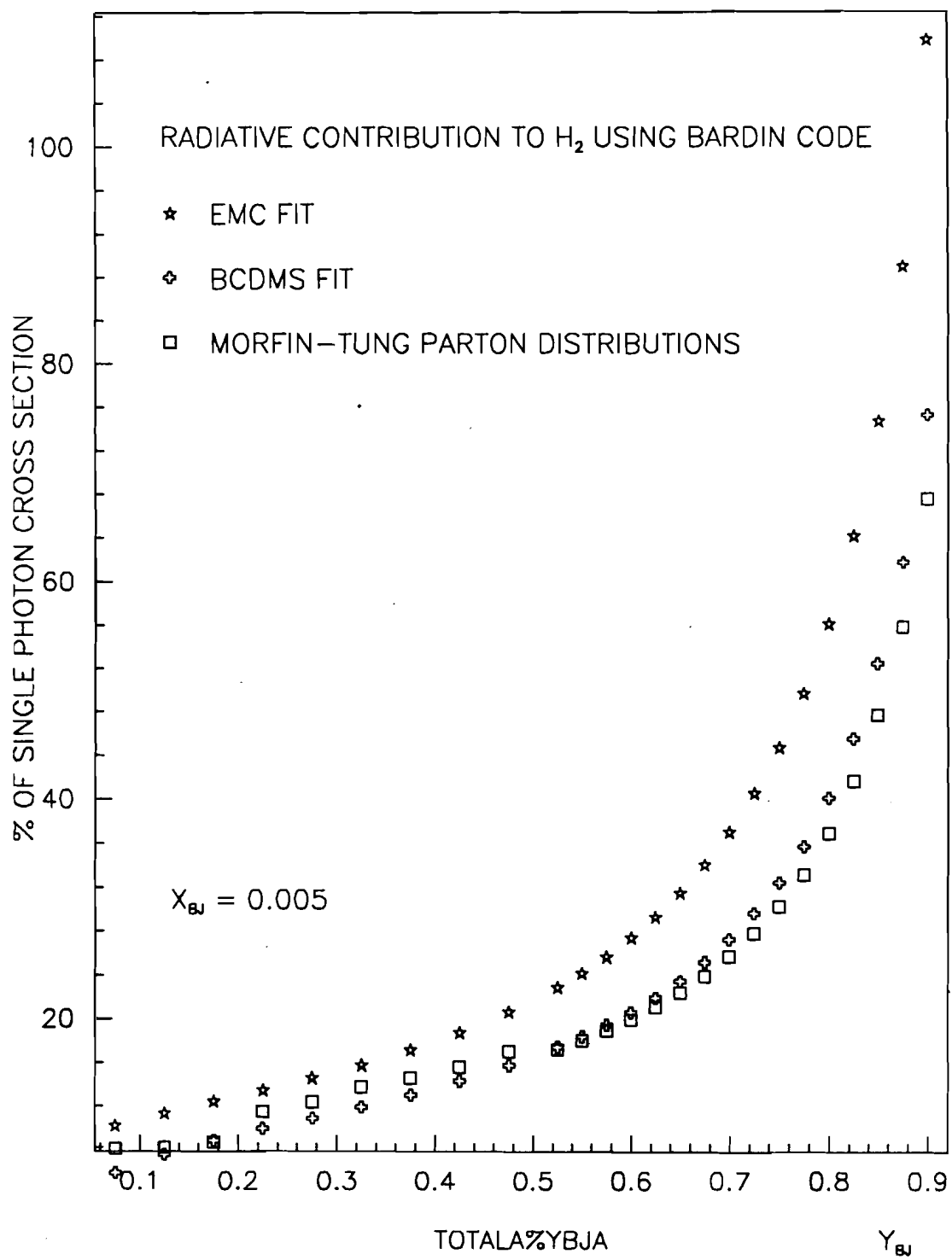


Figure 4.13: Radiative Corrections for different choice of Structure Functions

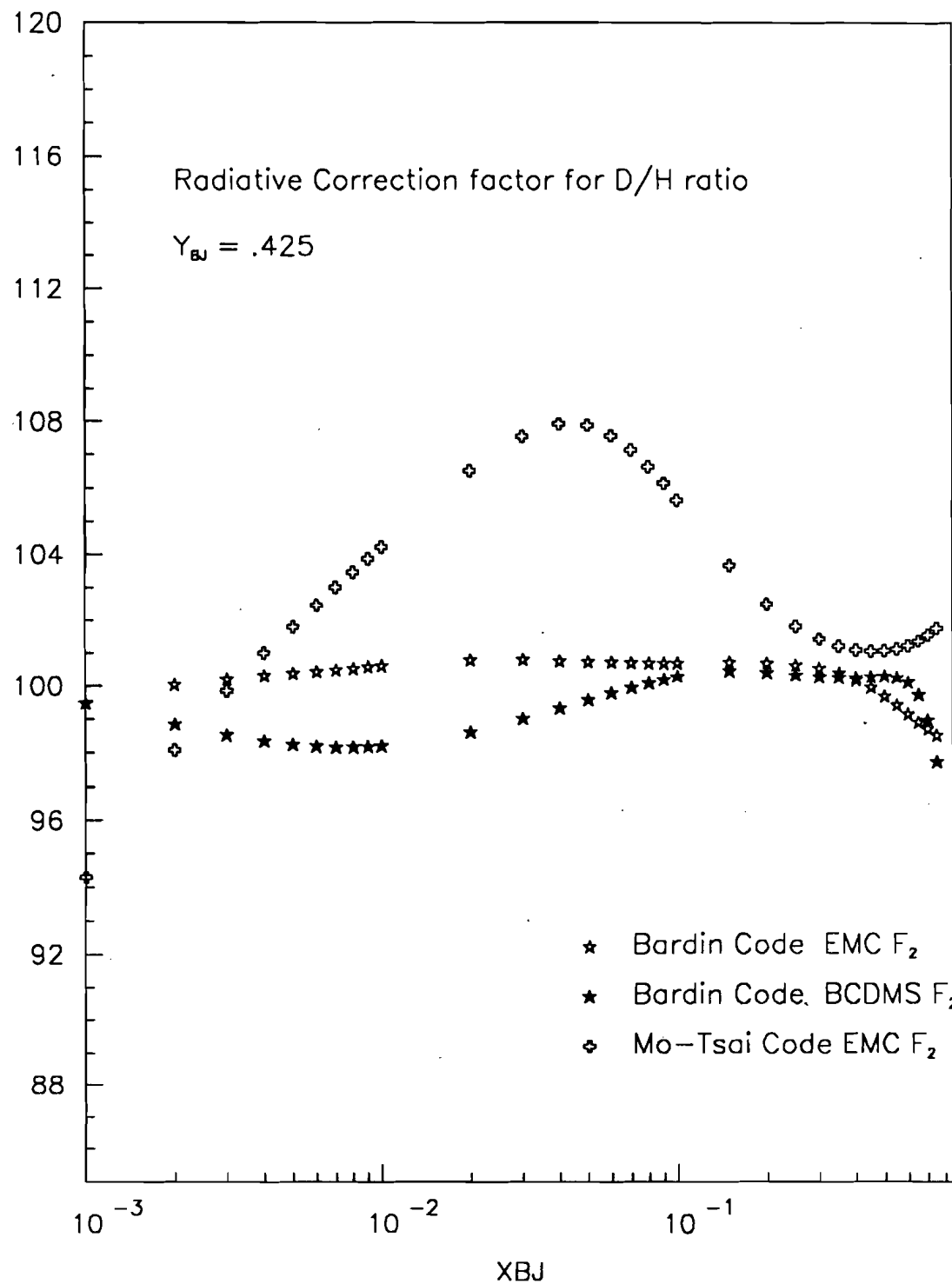


Figure 4.14: Radiative Corrections to the D/H ration

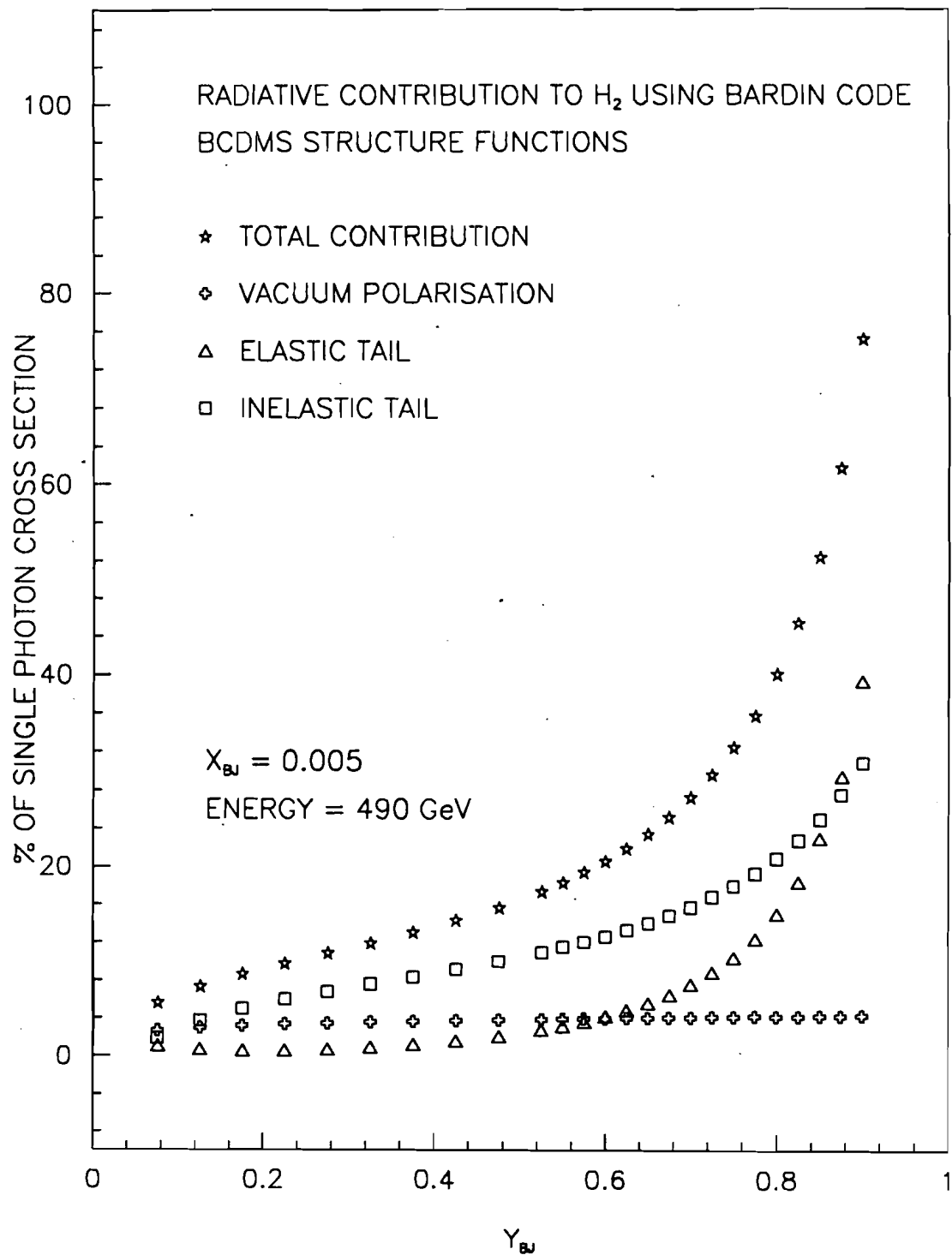


Figure 4.15: Different Contributions of Radiative Corrections

Table 4.17: The magnitude of radiative corrections using Bardin

Y	DVAC	ALFASQ	TAILS	CONTIN	WEAK	HADRON	LEPT	ONEL	TOTAL
0.075	2.63	-0.06	2.40	5.114	0.00	-0.01	7.51	10.14	10.11
0.125	2.93	-0.05	1.32	7.100	-0.00	-0.01	8.42	11.35	11.34
0.175	3.15	-0.04	0.99	8.313	-0.00	-0.02	9.30	12.43	12.43
0.225	3.32	-0.04	1.00	9.216	-0.00	-0.05	10.22	13.49	13.50
0.275	3.44	-0.05	1.22	10.036	-0.00	-0.08	11.25	14.62	14.63
0.325	3.56	-0.05	1.57	10.818	-0.00	-0.11	12.39	15.83	15.84
0.375	3.65	-0.04	2.05	11.625	-0.01	-0.15	13.68	17.18	17.20
0.425	3.74	-0.02	2.71	12.513	-0.01	-0.20	15.22	18.76	18.81
0.475	3.82	0.00	3.55	13.481	-0.01	-0.25	17.03	20.60	20.67
0.525	3.90	0.04	4.63	14.620	-0.02	-0.30	19.25	22.84	22.96
0.550	3.93	0.06	5.31	15.242	-0.02	-0.33	20.56	24.15	24.29
0.575	3.97	0.09	6.09	15.936	-0.02	-0.35	22.02	25.62	25.79
0.600	4.00	0.12	6.98	16.693	-0.02	-0.38	23.68	27.27	27.48
0.625	4.03	0.16	8.02	17.524	-0.03	-0.42	25.54	29.13	29.38
0.650	4.06	0.20	9.25	18.450	-0.03	-0.45	27.70	31.28	31.58
0.675	4.09	0.26	10.70	19.494	-0.03	-0.48	30.20	33.78	34.13
0.700	4.12	0.33	12.43	20.672	-0.03	-0.51	33.10	36.68	37.09
0.725	4.15	0.41	14.54	22.008	-0.04	-0.55	36.55	40.11	40.61
0.750	4.17	0.51	17.11	23.538	-0.04	-0.58	40.65	44.20	44.80
0.775	4.20	0.63	20.22	25.303	-0.04	-0.62	45.52	49.06	49.78
0.800	4.22	0.80	24.46	27.364	-0.04	-0.67	51.83	55.34	56.24
0.825	4.25	1.01	29.89	29.793	-0.05	-0.71	59.69	63.18	64.29
0.850	4.27	1.31	37.27	32.686	-0.05	-0.76	69.96	73.42	74.83
0.875	4.30	1.72	47.70	36.160	-0.05	-0.81	83.86	87.29	89.12
0.900	4.32	2.35	63.57	40.384	-0.05	-0.88	103.96	107.34	109.80

Table 4.18: The magnitude of radiative corrections using Mo-Tsai

YBJ	TAIL(ALL)	COHERENT	QELASTIC	INELASTIC	RADCOR
0.075	0.101566	0.000000	0.007793	0.093773	0.948359
0.125	0.127345	0.000000	0.006869	0.120476	0.933983
0.175	0.145776	0.000000	0.006597	0.139179	0.922423
0.225	0.161139	0.000000	0.007227	0.153913	0.911692
0.275	0.175262	0.000000	0.008779	0.166482	0.900809
0.325	0.189163	0.000000	0.011296	0.177867	0.889147
0.375	0.203617	0.000000	0.014886	0.188730	0.876126
0.425	0.219260	0.000000	0.019736	0.199524	0.861205
0.475	0.236753	0.000000	0.026119	0.210635	0.843758
0.525	0.256845	0.000000	0.034412	0.222433	0.823025
0.550	0.268133	0.000000	0.039431	0.228702	0.811141
0.575	0.280415	0.000000	0.045137	0.235278	0.798068
0.600	0.293837	0.000000	0.051626	0.242211	0.783648
0.625	0.308563	0.000000	0.059015	0.249548	0.767700
0.650	0.324780	0.000000	0.067440	0.257340	0.750018
0.675	0.342702	0.000000	0.077067	0.265635	0.730366
0.700	0.362578	0.000000	0.088099	0.274479	0.708469
0.725	0.384696	0.000000	0.100785	0.283912	0.684007
0.750	0.409394	0.000000	0.115435	0.293959	0.656608
0.775	0.437067	0.000000	0.132447	0.304620	0.625834
0.800	0.468186	0.000000	0.152334	0.315852	0.591164
0.825	0.503325	0.000000	0.175784	0.327541	0.551967
0.850	0.543179	0.000000	0.203750	0.339429	0.507474
0.875	0.588627	0.000000	0.237630	0.350998	0.456725
0.900	0.640842	0.000000	0.279614	0.361228	0.398437

Chapter 5

RESULTS AND CONCLUSIONS

In this chapter the analysis after the Data Reduction program (section 4.1.5) is described and the final results are presented.

In section 5.1 various kinematic requirement used in this analysis are described. In section 5.2 the method of subtracting the events in which the muon scattered from the target walls is described. In Chapter 4, the geometric acceptance of the trigger, the reconstruction efficiency and the radiative corrections were described. One has to apply these corrections to evaluate the cross section from the raw data. In this chapter those corrections are used to calculate the muon-proton and muon-deuteron cross section. From these cross sections, the ratio of F_2^n/F_2^p is calculated. Using the measured F_2^n/F_2^p ratio and the Morfin-Tung partons distributions the Gottfried sum is evaluated in x_{bj} range from 0.001 to 0.125.

5.1 The kinematic Region E665 SAT data

The kinematics of the SAT data sample remaining after the data reduction (section 4.1.5) are shown in Fig. 5.1. This plot includes only those events in which interaction took place in the region between -9.4 and -12.4 meters. The target vessel is located in between -10.54 and -11.69 meters. The main background to the small angle muon-nucleon interaction data is the muon-electron scattering (μe) events. The other major background is the Bremsstrahlung events in which muon radiates a photon before or after the interaction with nucleon. These events can not be separated from the single-photon-exchange events except over a limited region in phase space where the radiated photon can be identified in the detector. However the leading Bremsstrahlung contributions can be calculated as described in section 4.7. The magnitude of radiative corrections is more than 30% of the Born cross section for $y_{bj} > 0.75$ and therefore the theoretical uncertainty in the estimated corrections is large. An upper limit of $y_{bj} = 0.75$ was imposed as an

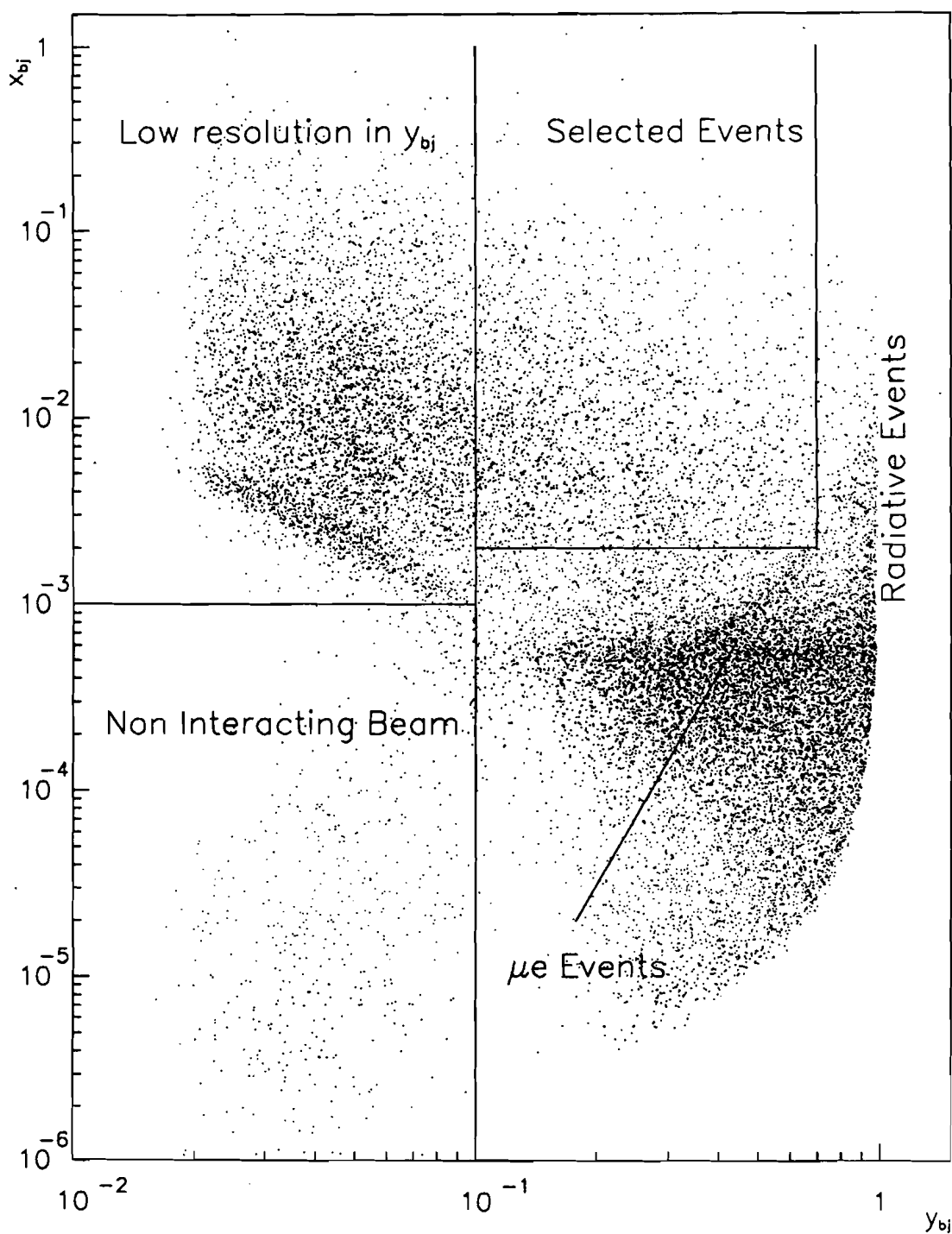


Figure 5.1: Kinematic distribution of the SAT deuterium events

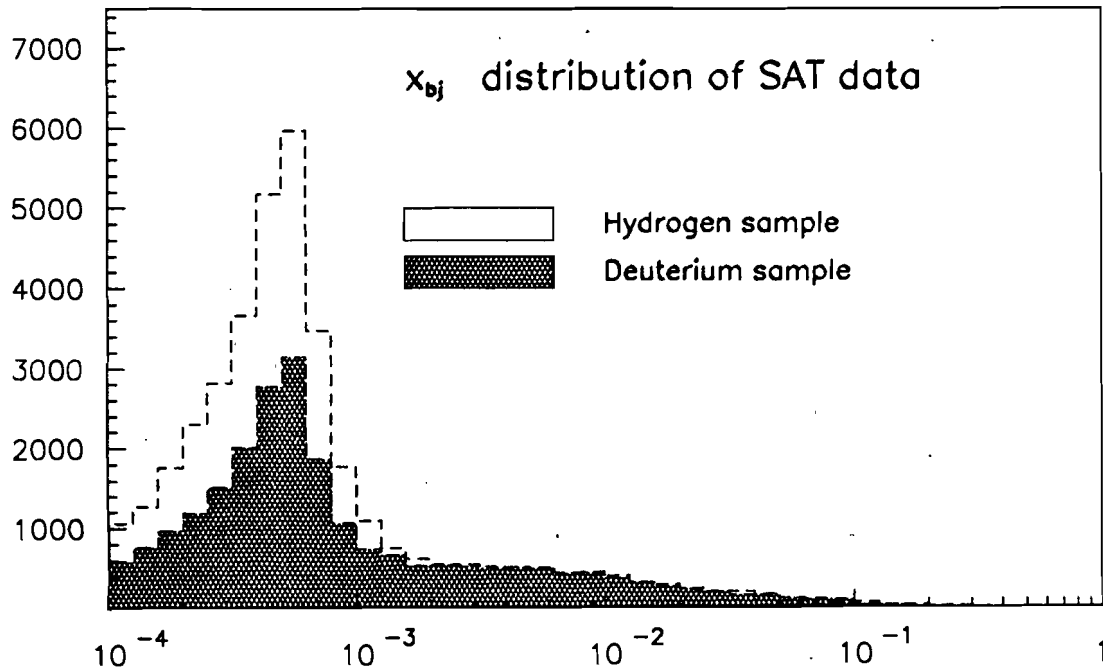


Figure 5.2: The x_{bj} distribution of SAT events after DR selection

event selection criterion to exclude the region where the radiative events dominate the event sample.

5.1.1 Muon-Electron Scattering background

The elastic muon-electron (μe) scattering events ($x_{bj}^{\mu e} = 1$) correspond to the deep inelastic Bjorken x

$$x_{bj}^{DIS} = \frac{Q^2}{2m_p\nu} \frac{m_e}{m_e} = x_{bj}^{\mu e} \times \frac{m_e}{m_p} \simeq 1/1836 = 0.000544$$

where x_{bj}^{DIS} is defined as $Q^2/(2m_p\nu)$ for muon-nucleon (DIS) scattering. Therefore the μe scattering events should be concentrated at $x_{bj} = 0.00054$.

For a given number of nucleons, the hydrogen has twice the number of electrons as the deuterium. Therefore the μe scattering events (normalized to the deep inelastic luminosity) in the hydrogen sample are twice in number than those in the deuterium sample as can be inferred from Fig. 5.2.

The comparison between μe scattering event rates from the deuterium and

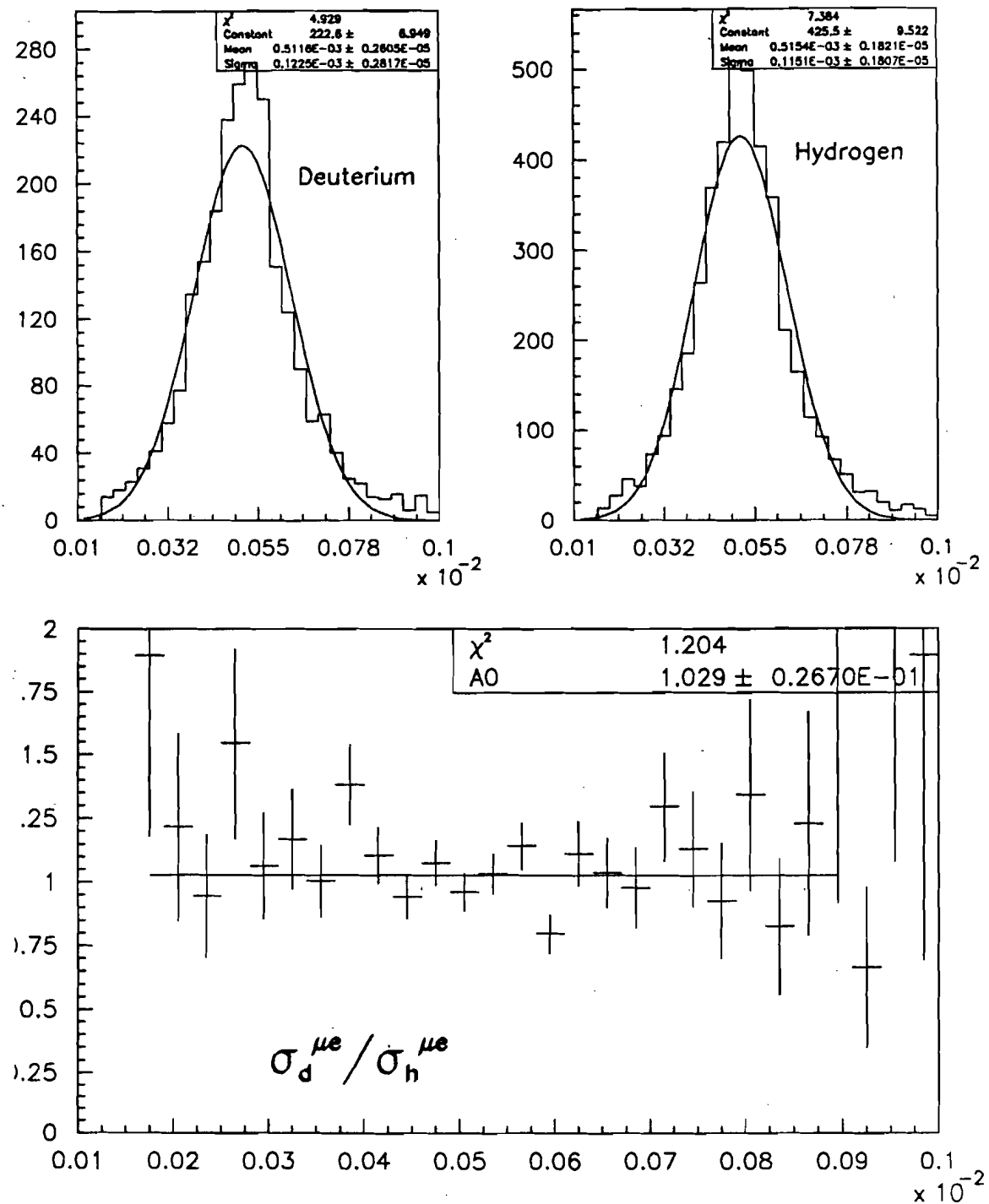


Figure 5.3: The ratio of muon-electron scattering events from deuterium and hydrogen data sets

Table 5.1: The kinematic and geometrical requirements used for SAT data sample

x_{bj}	>	0.001
y_{bj}	>	0.1
y_{bj}	<	0.75
Q^2	>	0.2
x_{vertex}	>	-12.0
x_{vertex}	<	-10.2

hydrogen targets can be used to estimate the change in the detector performance between two running periods. The ratio $\sigma_d^{\mu e}/\sigma_p^{\mu e}$ should be 1.0 where $\sigma_d^{\mu e}$ is the cross section for μe scattering measured using the deuterium data and $\sigma_p^{\mu e}$ is the cross section measured using hydrogen data. The cross section is normalized to the incident muon flux and the number of electrons in the respective targets.

The μe scattering events have unique topology. These events have two forward going tracks with opposite charges. The electrons deposit almost all of their energy in the electromagnetic calorimeter. The events which had only two tracks going through the forward spectrometer were selected. It was required that at least 75.0 GeV energy was deposited in the EM calorimeter. Further more it was required that at least half of the energy lost by muon (hence gained by electron) was deposited in the EM calorimeter. The charge of the electron track was not checked. Moreover no association was made between the impact point of the track at calorimeter and the position of the energy deposited. The x_{bj} distributions of selected μe scattering events from deuterium and hydrogen data sets are shown in Fig. 5.3 (a, b). The ratio of normalized cross sections is shown in Fig. 5.3 (c). The ratio is 1.029 ± 0.026 consistent with the expected value of 1. This implies that even with the crude selection criteria used to select the μe scattering events, the ratio is consistent with the expected value. Therefore one can conclude that the change in the detector performance with time is small.

A minimum x_{bj} cut of the 0.001 was used to minimize μe scattering background in the SAT sample. The minimum Q^2 requirement for SAT was 0.2 GeV².

Table 5.2: The uncorrected beam flux used in 1987-88 running period

Trigger	Beam flux		
	D	H	MT
LAT	0.5826E+11	1.087E+11	.1140E+11
SAT	0.5722E+10	1.339E+10	.1370E+10

5.1.2 Resolution

The momentum of a very high energy scattered muon can not be measured very accurately in the forward spectrometer. As shown in Fig. 3.9 the fractional uncertainty in y_{bj} increases with decreasing y_{bj} reaching to $\approx 30\%$ at $y_{bj} = 0.1$. Therefore the events with $y_{bj} < 0.1$ were not used in the analysis.

5.2 Empty Target Corrections

The target vessel is made of different material than hydrogen or deuterium. The events in which muon scatters from the walls of the target must be excluded from the final sample. Given the experimental resolution in the x position of the vertex point, these events can not be identified individually. Such events can be subtracted only on the statistical basis. The data were taken using the target vessel filled with gaseous hydrogen (MT target) using the same trigger configuration as the one used during the deep inelastic data taking period. Both the MT target data and DIS data were processed by the same software programs. The beam flux used for various targets is given in Table 5.2. The events from the MT target were normalized to the beam flux used for the deep inelastic data and were subtracted from the deep inelastic event sample. The subtraction was done for each x_{bj} bin separately.

5.2.1 Empty target correction for SAT data

The vertex distribution of the empty target SAT data, normalized to the beam used for the hydrogen data, is shown in 5.4 (a), superimposed on the deep inelastic sample for hydrogen data. As expected the MT target events originate from the target walls. Some of the MT target events upstream of the target are caused by

Table 5.3: Kinematic cuts for the x_{bj} bins for SAT analysis

The mean values of Q^2 and x_{bj} for each bin for hydrogen and deuterium are given.

Bin No.	x_{bj}^{min}	x_{bj}^{max}	x_{bj}^{mean}		Q^2_{min}	Q^2_{max}	Q^2_{mean}	
			D	H			D	H
1	0.001	0.002	0.0014	0.0018	0.2	2.0	0.52	0.54
2	0.002	0.004	0.0028	0.0029	0.2	2.0	0.76	0.73
3	0.004	0.008	0.0057	0.0057	0.4	5.0	1.40	1.45
4	0.008	0.020	0.0126	0.0127	1.0	8.0	2.86	2.79
5	0.020	0.050	0.0309	0.0309	2.0	14.0	5.67	5.64
6	0.050	0.080	0.0628	0.0638	5.0	20.0	10.11	10.1
7	0.080	0.125	0.0954	0.1009	8.0	38.0	14.57	17.8

extra material close to the upstream end of the target.

Due to limited empty target data, only 96 events survived the deep inelastic requirements for SAT data which are equivalent to 936 events when normalized to the flux for SAT hydrogen data. Out of these 96 events 74 were in the first x_{bj} bin (0.001-0.002). Fig. 5.4(b) shows the x_{bj} distribution of MT target events superimposed on the hydrogen target events. The equivalent MT target events were subtracted from the SAT sample for each x_{bj} bin. The error was calculated using

$$[\delta(N_{DIS})]^2 = [\delta(N_{FLD})]^2 + C \times [\delta(N_{MT})]^2 \quad (5.1)$$

where the N_{FLD} is the number of events from the target filled with either deuterium or hydrogen, N_{MT} is the number of empty target events and C is the ratio of the number of muons used for filled target data to the number of muons used for MT target data.

5.3 The μ Proton and μ Deuteron Scattering Cross Sections

Lower and upper Q^2 cuts given in Table 5.3 were used for the x_{bj} bins in the SAT analysis. The raw and corrected distributions of double differential cross section $\Delta\sigma/(\Delta x \Delta Q^2)$ for D and H samples are shown Fig. 5.5 and Fig. 5.6 after

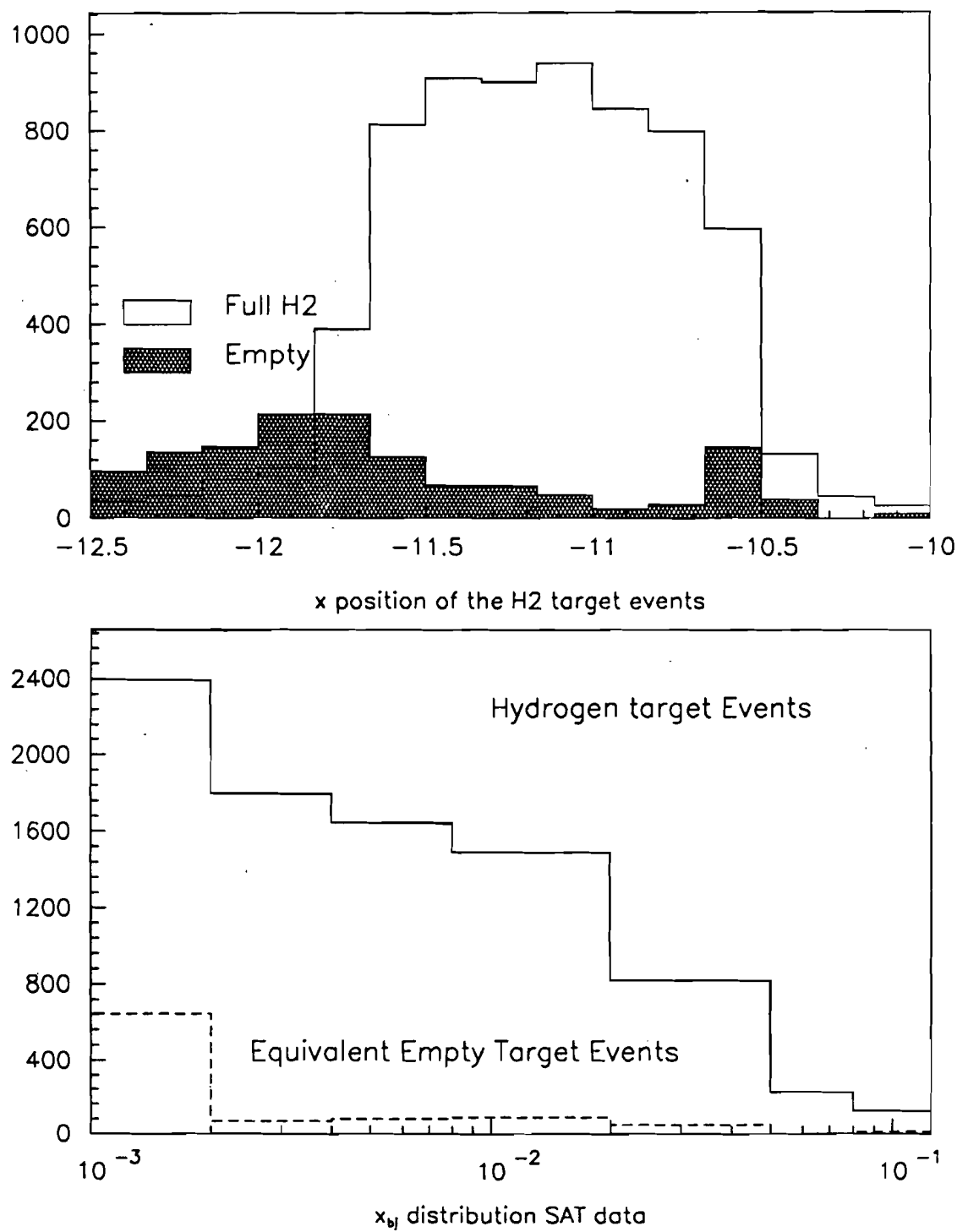


Figure 5.4: Comparison of empty target data with SAT hydrogen data

Table 5.4: Raw Event Yield for SAT Deuterium data set

Number of Raw Events	Number of MT Events	Reconstruction Efficiency	Radiative Corrections	Geometric Acceptance
1829	276	0.742 ± 0.021	1.172	0.455
1677	29	0.808 ± 0.024	1.129	0.499
1572	33	0.783 ± 0.028	1.116	0.645
1409	38	0.769 ± 0.031	1.104	0.819
781	20	0.770 ± 0.039	1.079	0.957
218	0	0.834 ± 0.043	1.056	1.000
131	4	0.846 ± 0.054	1.042	1.000

Table 5.5: Raw Event Yield for SAT Hydrogen data set

Number of Raw Events	Number of MT Events	Reconstruction Efficiency	Radiative Corrections	Geometric Acceptance
2393	644	0.758 ± 0.022	1.160	0.469
1797	68	0.781 ± 0.024	1.120	0.485
1646	78	0.809 ± 0.029	1.114	0.654
1490	88	0.718 ± 0.029	1.103	0.815
818	49	0.766 ± 0.040	1.082	0.955
223	0	0.823 ± 0.041	1.059	1.000
122	10	0.839 ± 0.053	1.051	1.000

all kinematic and geometrical cuts described above. Note that in these plots the average values of x_{bj} and Q^2 do not coincide with the center of the bin.

As will be discussed later the event rate measured in E665 is consistent with the prediction calculated using Morfin-Tung parton distribution functions. Fig. 5.7 and Fig. 5.8 show the Q^2 distribution for each x_{bj} bin for the SAT data. The Q^2 distributions shown have not been corrected. As expected the mean value of Q^2 increases with the x_{bj} . The Q^2 distributions for deuterium data are similar to the one for hydrogen data.

5.4 Ratio of Neutron and Proton Structure Functions

The ratio of the neutron and proton cross sections is related to deuterium and hydrogen cross sections by

$$\frac{\sigma^n}{\sigma^p} = \frac{\sigma^d - \sigma^p}{\sigma^p} \quad (5.2)$$

where any binding effects in the deuterium have been ignored. In the kinematic regime of SAT data, the Fermi motion corrections are negligible.

The ratio of the neutron and proton cross sections is shown in Fig. 5.9 for E665 SAT data. The σ^n/σ^p is essentially flat between x_{bj} of 0.001 and 0.125 and consistent with 1.0.

The structure function $F_2(x, Q^2)$ is related to the normalized cross section by

$$\frac{d^2\sigma}{dx dQ^2} = C(x, Q^2) \times F_2(x, Q^2) \quad (5.3)$$

where

$$C(x, Q^2) = \frac{4\pi\alpha^2}{Q^4 x} \left\{ 1 - y - \frac{Mxy}{2E} - \frac{y^2(1 + 4M^2 x^2/Q^2)}{2(1 + R(x, Q^2))} \right\} \quad (5.4)$$

The ratio σ^n/σ^p is equal to F_2^n/F_2^p provided the $R(x_{bj}, Q^2)$ is same for hydrogen and deuterium. As described in section 1.13.1 the $R(x_{bj}, Q^2)$ is measured to be same for the neutron and proton. The Q^2 distributions for the x_{bj} bins are also similar for hydrogen and deuterium data sets, therefore the value of the coefficient $C(x_{bj}, Q^2)$ is also equal.

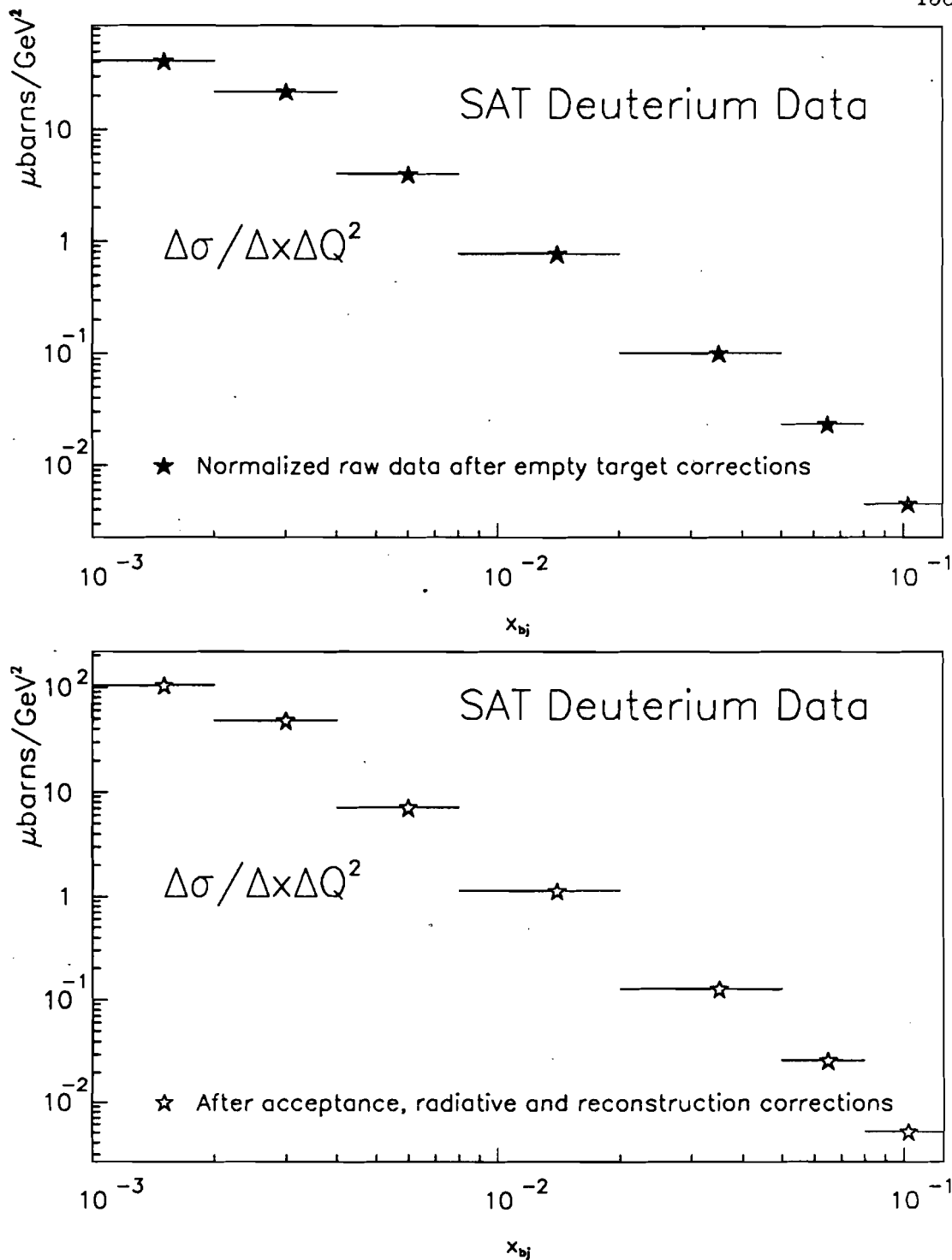


Figure 5.5: The double differential cross section ($\Delta\sigma/\Delta x\Delta Q^2$) for SAT deuterium data as a function of x_{bj}

Note that the mean values of x_{bj} and Q^2 do not correspond to the the center of the bin

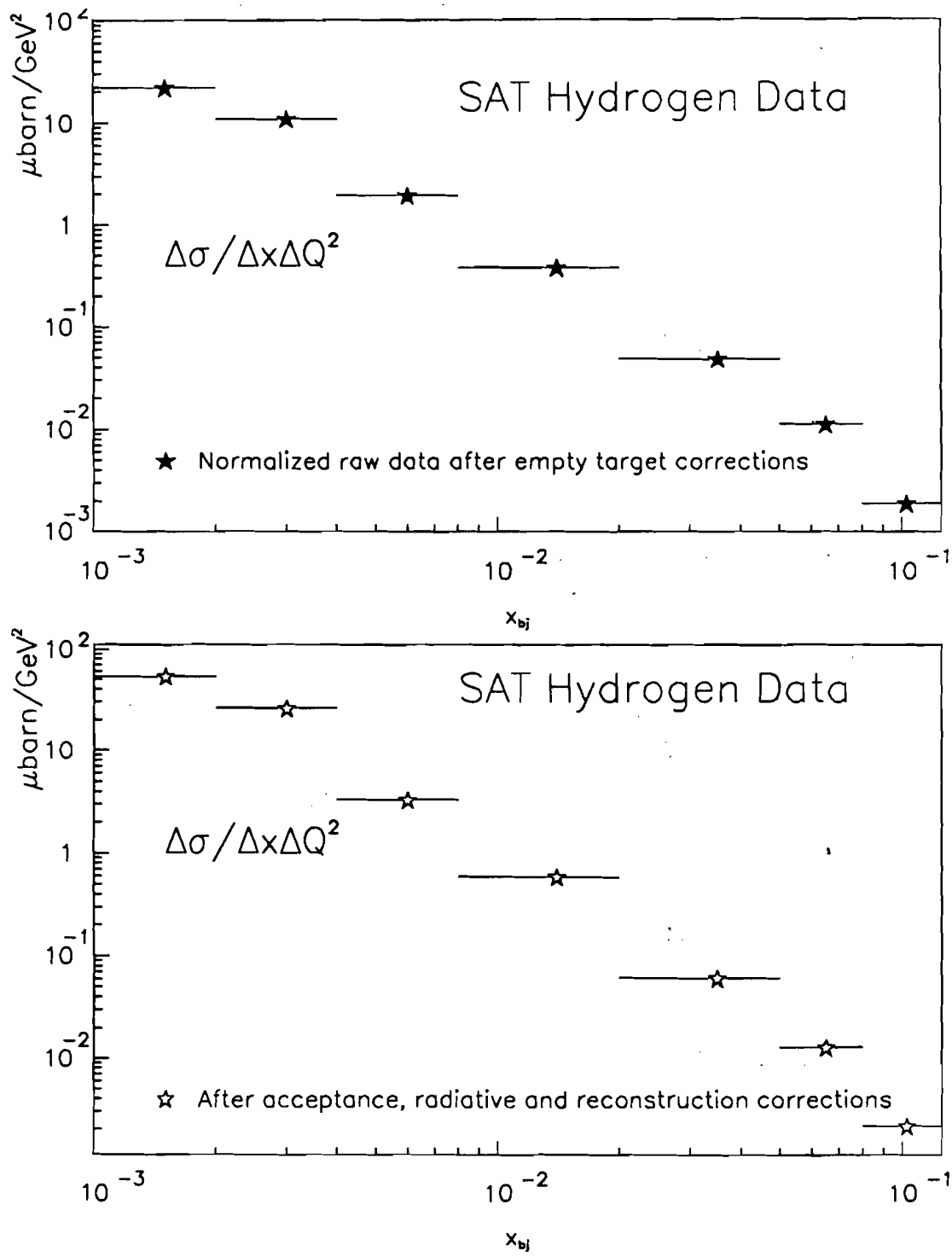


Figure 5.6: The double differential cross section ($\Delta\sigma/\Delta x \Delta Q^2$) for SAT hydrogen data as a function of x_{bj}

Note that the mean values of x_{bj} and Q^2 do not correspond to the center of the bin

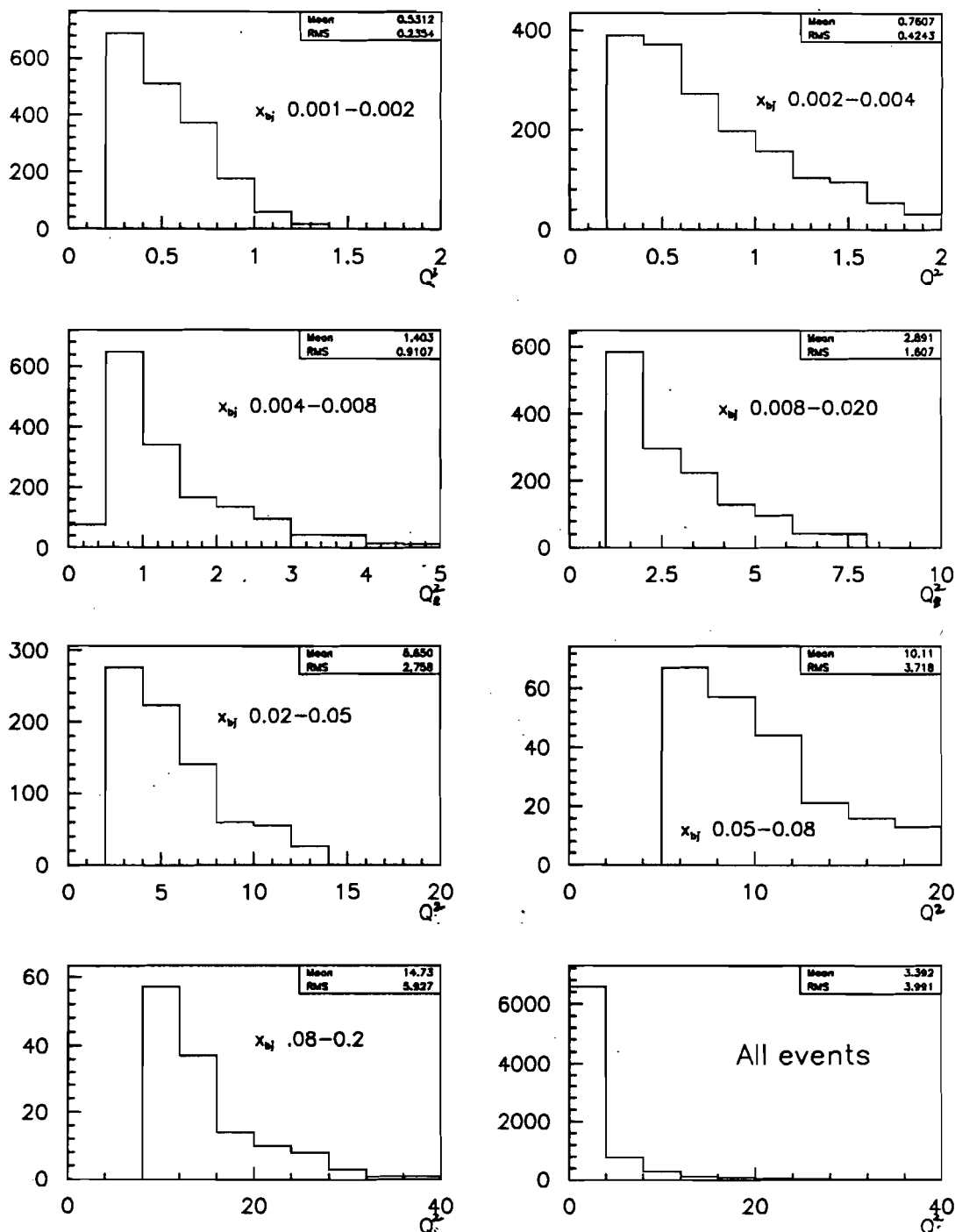


Figure 5.7: The Q_2 distributions of SAT deuterium data for each x_{bj} bin
The distributions have not been corrected.

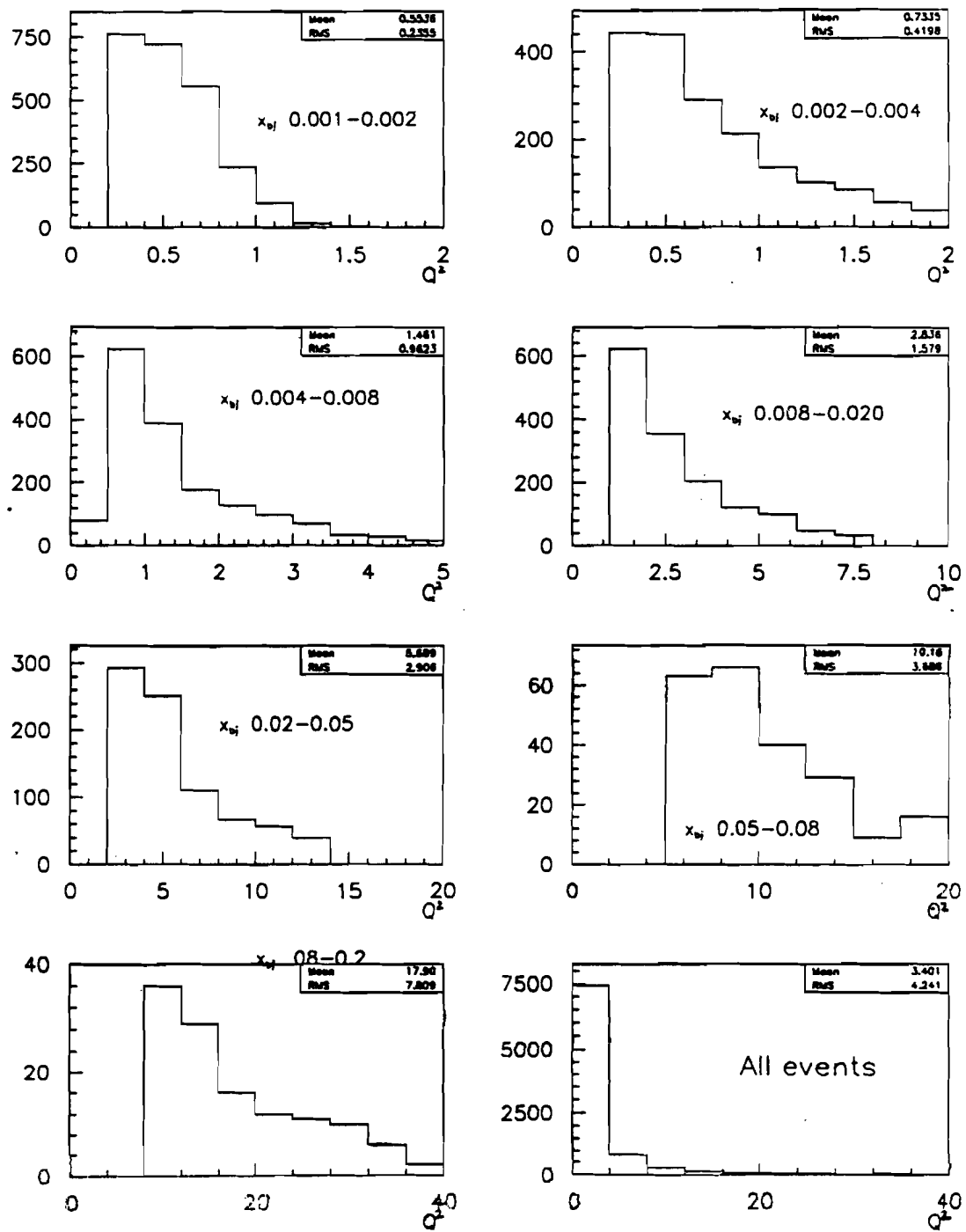


Figure 5.8: The Q^2 distributions of SAT hydrogen data for each x_{bj} bin
The distributions have not been corrected.

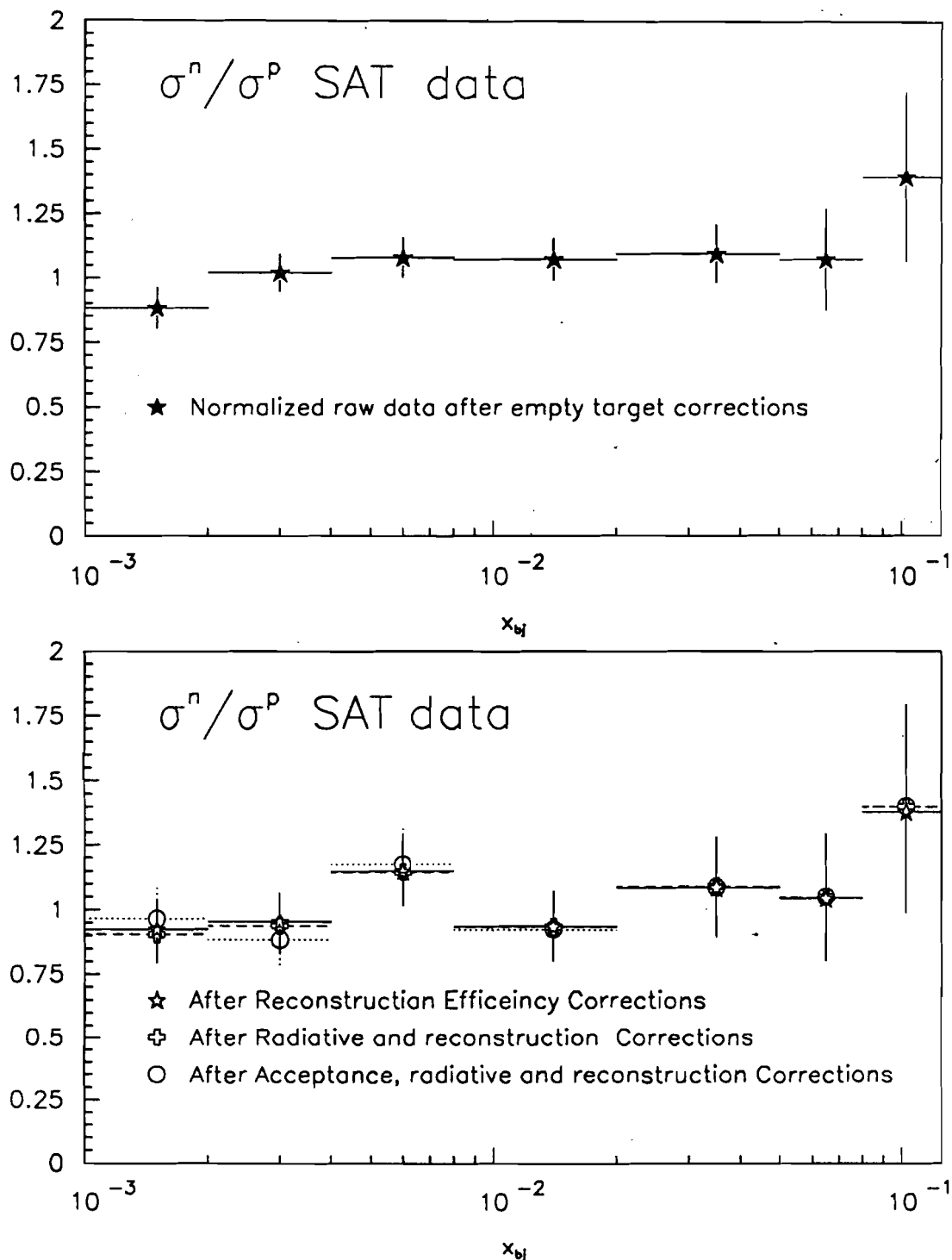


Figure 5.9: The ratio of neutron and proton structure functions for SAT data

5.4.1 Estimate of systematic errors for F_2^n/F_2^p

In this section the major sources of systematic errors to F_2^n/F_2^p are described. The corrections made to the raw data to extract the cross section ratio are described in Chapter 4.

The total systematic error in the DIS cross section ratio can be estimated from the ratio of μe events from hydrogen and deuterium data sets. The measured ratio is 1.029 ± 0.027 which is consistent with the expected value of 1.0. If one assumes that all the discrepancy in the ratio of muon-electron scattering is due to the changes in the detector performance (including flux measurement, trigger performance and reconstruction efficiency) the error on the ratio σ^d/σ^h is $\sim 3\%$. However the calorimeter response did change during 1987-88 run and thus the above estimate is not exactly correct but not far from the actual value. Moreover as the kinematic region of the μe sample do not overlap with the deep inelastic sample, the reconstruction efficiency for two events samples might be different.

- **Beam Normalization :** The estimated error in the book keeping of the raw flux is less than 0.5%. The errors in software requirements (filter) and time dependence of beam spectrometer contribute by another 0.3%. Adding them in quadrature, the total error in normalization is less than 0.6%. Note that the RSAT correction factors to the flux for deuterium and hydrogen sample differ by 0.3% only.
- **Trigger Acceptance :** The same target vessel was used for the hydrogen and the deuterium data set. Therefore at given x_{bj} and Q^2 geometric acceptance of two data sets was equal provided the position of the target and the components used in the trigger logic were same for the two targets. The trigger matrices used to generate trigger signal for two data taking periods were exactly same. The position of the target did not change during the run. The movement in the SMS scintillators was less than 0.5 mm during data taking which is small when compared to the size of the SAT trigger veto region (60-75 mm). Change in the location of the SBT hodoscopes was also negligible. Therefore the change in the acceptance due to movement of the SAT trigger elements is negligible. No systematic error has been assigned to this effect. The acceptance corrections cancel out in calculation of the ratio

of the structure functions, therefore their precise value is not very crucial.

- **Radiative Corrections :** The procedure of extracting the single photon cross section from the measured cross section is described in detail in section 4.7. The magnitude of the corrections depends on the choice of the structure functions. The correction to the μp measured cross section changes by 3% when different structure functions (Morfin-Tung, EMC and BCDMS) are used at $x_{bj} = 0.005$ and $y_{bj} = .475$. The corresponding change in the correction to μd measured cross section is 4%. Therefore the systematic error due to radiative corrections on the final σ^n/σ^p is less than 2.0% since the change in the correction to hydrogen data is correlated to the change in the correction to deuterium data.
- **Trigger Efficiency :** The time dependence in the trigger hardware performance discussed in section 4.5 contribute to a 2% change in the value of the σ^d/σ^p for SAT sample. As no correction has been made to the data for the trigger inefficiency, the estimated systematic error of the ratio is 2% for SAT sample.
- **Detector Efficiency :** This correction includes both the detection efficiency of the hardware and the reconstruction efficiency of the software. The detector efficiency was measured for different time periods as described in section 4.6. The monte carlo events were generated according to deep inelastic cross section using Morfin-Tung parton distributions. For each x_{bj} bin, the detector efficiency is calculated as

$$R_{MC} = \frac{N_{reconst}}{N_{generated}}. \quad (5.5)$$

The corresponding error is calculated as

$$\delta R_{MC}^{stat} = R_{MC} \times \left(\frac{1}{N_{generated}} + \frac{1}{N_{reconst}} \right)^{1/2} \quad (5.6)$$

where the $N_{generated}$ the generated Monte Carlo events and N_{recon} is the number of events reconstructed. The same kinematic cuts are used for the generated and reconstructed events as the one used for the real data

analysis. The statistical errors (δR_{MC}^{stat}) for the monte carlo corrections were calculated using poisson statistics. For a given x_b , bin, the events in the numerator are not a proper subset of the events in the denominator. Due to smearing in the kinematics of the events due to finite detector resolution, the events migrate from bin to bin. Therefore it is more appropriate to use poisson statistics. However the numerator and denominator are still largely correlated and therefore the calculated value of error is an overestimate of the actual error. These errors (δR_{MC}^{stat}) were added in quadrature to the statistical errors of the data while correcting the data distributions.

The detector efficiency for the SAT deuterium and hydrogen sample is shown in Fig. 4.12. For the ratio of structure functions, the change in the efficiency is more important than the absolute value of the efficiency.

The overall detector efficiency for the deuterium data is $77.7 \pm 1.2\%$ and $77.1 \pm 1.2\%$ for the hydrogen data. As discussed before the statistical accuracy of the detection efficiency measurement is better than 1% whereas any systematic error is less than 2%. The reconstruction software used is the same for the two data sets. Any other error which may arise from the misalignment of the detector planes or calibration of drift chambers are also estimated to be negligible. Therefore any systematic errors which might arise from the wrong estimates of the chambers efficiencies or inaccurate representation of detector resolution are less than 2-3%.

Only the normalization, the trigger efficiency and the detector efficiency corrections are important in the calculation of $\sigma_d^{\mu e}/\sigma_p^{\mu e}$. The total systematic error to this ratio from these three contributions is $\sim 2.9\%$ consistent with difference between the measured and the expected ratio of μe event rates. Therefore two methods of estimating systematic errors agree with each other.

5.4.2 Comparison of F_2^n/F_2^p with other Experiments

In Fig. 5.10 the E665 data are compared to the previous muon scattering experiments. Even though the E665 data are systematically higher than data from other experiments, they are consistent with them within statistical errors. The E665

SAT data extend the kinematic range down to x_{bj} equal to 0.001. The previous best measurement, done by the NMC collaboration, goes down to 0.004 only.

The superimposed solid curve, F_2^n/F_2^p , is the prediction from HRMS parton distributions [95]. In reference [95] the data from BCDMS and CDHS collaborations have been used to extract the parton distribution. The input data set also includes the recent high statistics measurement of the ratio F_2^n/F_2^p done by the NMC collaboration. In this fitting procedure, the sea quark distributions for up and down quarks are assumed to be equal. The strange quark distribution is half that of the up quark distribution. The fitted curve is systematically below the NMC data points at low x_{bj} . The E665 data points are higher than NMC points. The HRMS predictions is an underestimate, though consistent within errors, of the ratio F_2^n/F_2^p calculated in this analysis. As described in section 1.12.1, the HRMS parton distributions satisfy the Gottfried sum rule whereas the NMC data alone does not. This point will be discussed further in section 5.6.

5.5 Comparison of Event Yield with Previous Experiments

To extract $F_2(x, Q^2)$ from the cross section, structure function $R(x, Q^2)$ must be known. The distribution of $R(x, Q^2)$ from a global fit [36] of the data from SLAC, EMC, CDHSW and BCDMS collaborations was used. The shape of $R(x, Q^2)$ for three different values of Q^2 is shown in Fig. 1.7.

The event yield in a bin is the integral of the coefficient $C(x, Q^2)$ with $F_2(x, Q^2)$ over the area of the bin. Both $C(x, Q^2)$ and $F_2(x, Q^2)$ change appreciably over the bin range and therefore one can not just use the mean values of x_{bj} and Q^2 . To extract $F_2(x, Q^2)$, one has to use a test function $F_2^{test}(x, Q^2)$. The equation

$$F_2^{new}(x, Q^2) = \left\{ \frac{\Delta\sigma^{measured}}{\int_{bin} C(x', Q'^2) F_2^{test}(x', Q'^2) dx' dQ'^2} \right\} F_2^{test}(x, Q^2) \quad (5.7)$$

can be used to relate the measured $F_2(x, Q^2)$ to the test $F_2(x, Q^2)$. The extracted F_2^{new} can be used as test function in the next iteration to get a consistent picture.

The event yield for $x_{bj} > 0.002$ and $Q^2 > 1.0$ GeV 2 was calculated using the structure functions measured by the EMC collaboration and a combine fit to different SLAC experiments. All other kinematic cuts used are the same as

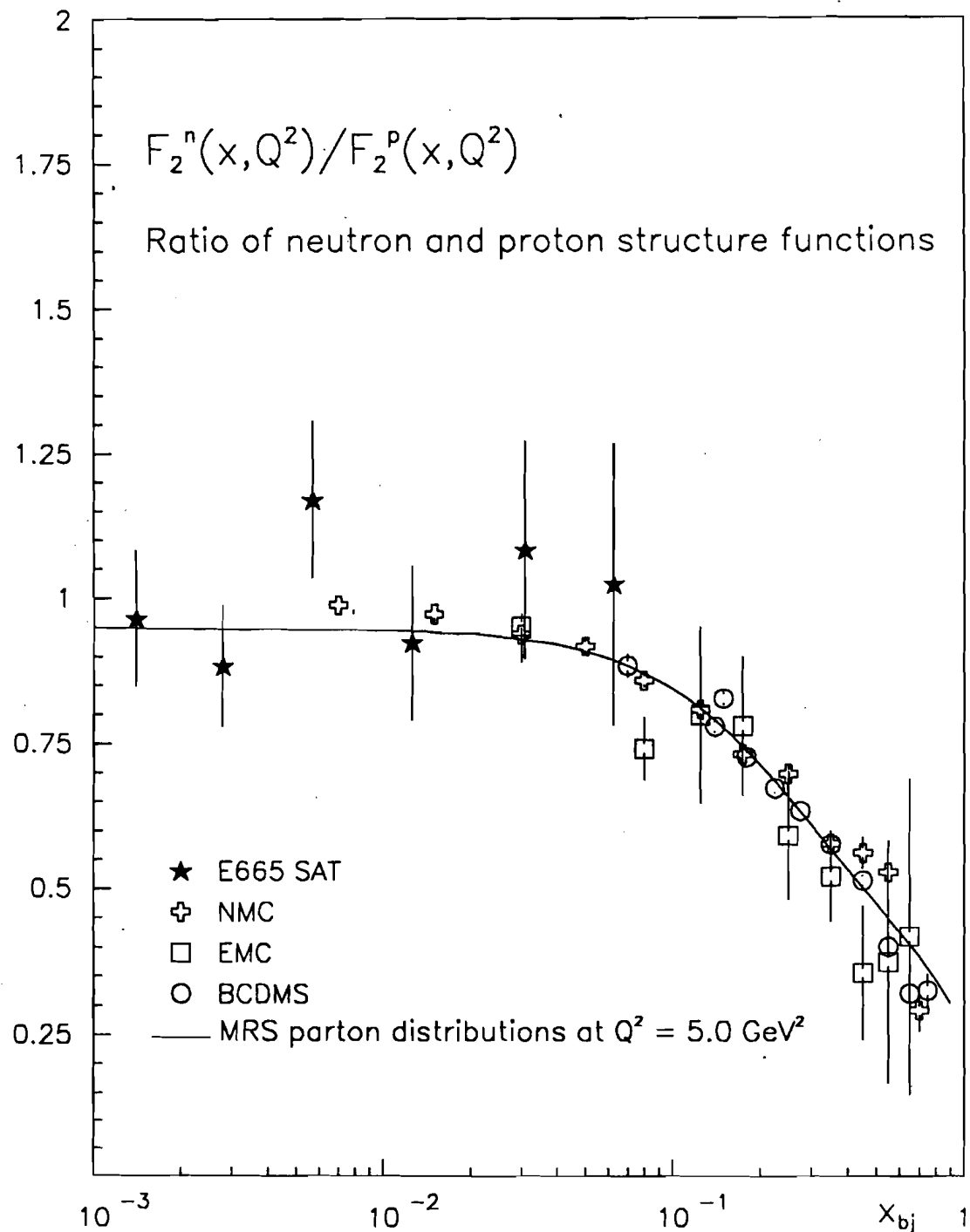


Figure 5.10: Comparison of F_2^n / F_2^p from E665 with the results from other experiments

The highest x_{bj} SAT point has been removed.

Table 5.6: Comparison of event yield from E665 SAT deuterium data with predictions calculated using different structure functions

x_{bj}	Q^2	DATA	EMC		SLAC		HMRS		M-T	
			Yield	F_2	Yield	F_2	Yield	F_2	Yield	F_2
0.0030	1.5	340	249	0.255	325	0.307	219	0.221	307	0.307
0.0060	3.0	572	498	0.269	673	0.404	482	0.248	629	0.404
0.0140	4.5	977	718	0.278	990	0.411	780	0.291	920	0.411
0.0350	8.0	467	323	0.295	447	0.404	385	0.361	434	0.404
0.0650	12.5	121	80	0.317	98	0.383	96	0.379	98	0.383
0.1025	23.0	62	54	0.342	58	0.358	59	0.364	59	0.358

Table 5.7: Comparison of event yield from E665 SAT hydrogen data with predictions calculated using different structure functions

x_{bj}	Q^2	DATA	EMC		SLAC		HMRS		M-T	
			Yield	F_2	Yield	F_2	Yield	F_2	Yield	F_2
0.0030	1.5	651	494	0.244	952	0.4793	475	0.226	662	0.3117
0.0060	3.0	1215	1031	0.284	1950	0.5624	1041	0.253	1361	0.4117
0.0140	4.5	2168	1563	0.307	2801	0.5683	1682	0.296	2004	0.4218
0.0350	8.0	963	759	0.335	1232	0.5319	838	0.371	959	0.4224
0.0650	12.5	218	187	0.347	255	0.4691	214	0.399	222	0.4108
0.1025	23.0	152	120	0.346	143	0.4097	137	0.396	137	0.3943

described in Table 5.1. The event yields using the HRMS and Morfin-Tung parameterization of parton distribution are given in Table 5.6 for deuterium data and in Table 5.7 for hydrogen data. The event yield from E665 data in the same kinematic region is also shown. The E665 data favours the Morfin-Tung parameterization of parton distributions. The $F_2(x, Q^2)$ given in tables is evaluated at x_{bj} and Q^2 given there.

5.6 Evaluation of $F_2^p(x) - F_2^n(x)$ and Gottfried Sum

The difference in the proton and neutron structure functions, $F_2^p(x) - F_2^n(x)$, can be calculated in two different ways.

1) Given the F_2^p and F_2^n , the difference can be calculated explicitly. For a given experiment the measured $F_2(x, Q^2)$ points are not at the same Q^2 . One has to interpolate or extrapolate the measured value to a common Q^2 so that the Gottfried Sum can be calculated which is defined for a fixed Q^2 . Due to limited number of events, the $F_2(x, Q^2)$ evaluated from the E665 1987-88 data set has large statistical errors and therefore this method is not used.

2) The second method is to combine a precise absolute measurement of the F_2 from some other experiment and the ratio F_2^n/F_2^p measured by E665.

The $F_2^p - F_2^n$ is given by

$$\begin{aligned} F_2^p - F_2^n &= \left\{ \frac{F_2^p - F_2^n}{F_2^p + F_2^n} \right\} \times F_2^d \\ &= \left\{ \frac{1 - F_2^n/F_2^p}{1 + F_2^n/F_2^p} \right\} \times F_2^d \end{aligned} \quad (5.8)$$

From equation (5.8), under the assumption that F_2^n/F_2^p is constant over a bin, the Gottfried sum can be written as

$$\int_{x_1}^{x_2} \frac{dx}{x} [F_2^p - F_2^n] = \sum_i \frac{1 - F_2^n/F_2^p}{1 + F_2^n/F_2^p} \int_{x_1^i}^{x_2^i} \frac{dx}{x} F_2^d(x, Q^2) \quad (5.9)$$

In the E665 data, the measured F_2^n/F_2^p points are evaluated at different Q^2 valued. However, as shown in Fig. 1.8 the ratio F_2^n/F_2^p is independent of Q^2 at small x_{bj} values. Therefore, one does not have to extrapolate the E665 F_2^n/F_2^p to a common Q^2 value.

In this ratio some of the correction factors like geometric acceptance of trigger, trigger efficiency and hardware detection efficiency and software reconstruction efficiency cancel out. The only effects remaining are the changes in performance in detector with time and the radiative corrections. Moreover any common problems in beam normalization are also factored out. The ratio F_2^n/F_2^p and therefore the final Gottfried sum has smaller systematic errors as compared to the Gottfried sum evaluated using first method.

As the errors from the E665 measurement dominate the final results, the errors on the fitted F_2^d are ignored.

The $F_2^p - F_2^n$ as a function of x_{bj} is given in Table. 5.8. The F_2^d is taken from Morfin-Tung parameterization. The structure function $F_2^d(x, Q^2)$ and $F_2^p - F_2^n$ are

evaluated at $Q^2 = 5.0$. The Gottfried sum is evaluated according to equation (5.9) for each bin and is given in the last column. The Gottfried sum integrated from $x_{bj} = 0.001$ to $x_{bj} = 0.125$ is

$$\int_{0.001}^{0.125} \frac{dx}{x} [F_2^p - F_2^n] = -0.044 \pm 0.123. \quad (5.10)$$

As described in section 1.12.1, the value of the Gottfried sum of 0.240 ± 0.014 measured by NMC collaboration is below the expected value of $1/3$. Their contribution from the range 0.004 – 0.20 [34] is

$$\int_{0.004}^{0.120} \frac{dx}{x} [F_2^p - F_2^n] = 0.110 \pm 0.006 \quad (5.11)$$

which is consistent with the E665 measurement of -0.106 ± 0.106 in the range 0.004 – 0.125 within two standard deviations. The E665 contribution from the region 0.001 – 0.004 is 0.062 ± 0.062 which can be compared to the NMC extrapolated value of 0.011 ± 0.003 in the x_{bj} range 0.0 – 0.004 . Again the values are consistent within errors.

The Gottfried sum calculated from the HRMS parton distributions [10], is consistent with both the measurement by the NMC collaboration and the quark-parton model calculations. In this calculation one third (~ 0.1) of the sum comes from the unmeasured low x_{bj} region ($x_{bj} < 0.004$). The contribution as measured by experiment E665 from the region 0.001 – 0.004 is 0.062 ± 0.062 . The results are again consistent.

5.7 Conclusion

In this analysis, the cross section for the hydrogen and deuterium data samples was evaluated. The results are consistent with the predictions calculated using the structure functions from previous experiments EMC and SLAC. The results are also consistent with the predictions based on the HRMS and Morfin-Tung parton distribution functions. The E665 measurement prefers the Morfin-Tung distributions. This measurement extends the kinematic region where the cross section is known down to $x_{bj} = 0.001$.

From the normalized event yield, the ratio of the proton and neutron structure functions $F_2^n(x, Q^2)/F_2^p(x, Q^2)$ was evaluated. This measurement also extends the

Table 5.8: The difference in the proton and neutron structure functions and Gottfried Sum

x_{bj}	$F_2^d(x, Q^2)$	F_2^p/F_2^n	$F_2^p - F_2^n$	Gottfried Sum
0.0014	0.756	0.965 ± 0.117	0.0177 ± 0.061	0.0175 ± 0.047
0.0028	0.686	0.883 ± 0.104	0.0618 ± 0.059	0.0440 ± 0.041
0.0057	0.621	1.170 ± 0.136	-0.0800 ± 0.058	-0.0507 ± 0.037
0.0126	0.557	0.923 ± 0.133	0.0398 ± 0.072	0.0311 ± 0.056
0.0309	0.488	1.084 ± 0.188	-0.0406 ± 0.087	-0.0284 ± 0.060
0.0628	0.433	1.024 ± 0.243	-0.0119 ± 0.116	-0.0079 ± 0.039
0.0954	0.396	1.352 ± 0.394	-0.1490 ± 0.137	-0.0497 ± 0.041

kinematic regime to $x_{bj} = 0.001$. The previous best measurement goes down to only $x_{bj} = 0.004$. The measured ratio is flat between the kinematic regime of E665 SAT data set. This implies that the neutron structure function (F_2^n) is equal to the proton structure function (F_2^p). In quark-parton model, it implies that the quark distributions in the proton are the same as in the neutron in the kinematic regime of this analysis.

From the ratio of structure functions, the Gottfried sum is evaluated between $x_{bj} = 0.001$ and 0.125. The numerical value of Gottfried sum in this range is -0.044 ± 0.123 at $Q^2 = 5.0$ GeV.

BIBLIOGRAPHY

- [1] E.D. Bloom, et. al. *Phy. Rev. Lett.* **23**, 930 (1969)
M. Breidenbach, et. al. *Phy. Reb. Lett.* **23**, 935 (1969)
- [2] J.D. Bjorken, *Phy. Rev.* **179** 1547 (1969)
J.D. Bjorken, E.A. Paschos *Phy. Rev.* **179** 1547 (1969)
- [3] R.P. Feynman, *Photon-Hadron Interactions* (1972)
- [4] Hazlen and Martin, *Quarks & Leptons* (1984)
- [5] D.H. Perkins, *Introductions to High Energy Physics*
- [6] Predazzi and Leader, *Gauge Theories and the New Physics* (1982)
- [7] W. Weise, *Quarks and Nuclei* (1984)
- [8] WA21, Jones et. al. *Z. Phy. C Particles and Fields* **44** (1989) 379
- [9] K. Gottfreid, *Phys. Rev. Lett.* **18** 1154(1967)
- [10] A.D. Martin, W.J. Stirling and R.G. Roberts Parton Distributions, The Gottfried Sum Rule and the W Charge Asymmetry *Phys.Lett.* **B252**:653-656 (1990).
- [11] A.D. Adler, *Phys. Rev.* **143** 1144(1966)
- [12] G. Altarelli, R.K. Ellis, G. Martinelli *Nucl. Phy.* **B143** (1978) 521
- [13] D. Allasia et. al. *Z. Phys. C Particles and fields* **28**, 321-333 (1985)
- [14] M.A.B. Beg, *Phys. Rev.* **D11** 1165 (1975)
- [15] S.L. Adler, Wu-Ki Tung, *Phy. Rev. Lett.* **22** (1969) 978
- [16] S.R. Mishra, Probing Nucleon Structure with ν -N Experiments in Hadron Structure Functions and Parton Distributions ed. Geesaman et. al.
- [17] R.K. Ellis and W.J. Stirling, *QCD and Collider Physics*, Fermilab-Conf-90/164-T (1990)

- [18] H.D. Abarbanel, M.L. Goldberger and S.B. Treiman *Phy. Rev. Lett.* **22** (1969) 500
- [19] H. Harari, *Phy. Rev. Lett.* **22** (1969) 1078
- [20] F.E. Close, *An introduction to Quarks and Partons* (1979)
- [21] S.J. Broadsky and G.R. Farrar *Phy. Rev. Lett.* **31** (1973) 1153
G.R. Farrar *Nucl. Phys.* **B77** (1974) 429
- [22] P.D.B. Collins & A.D. Martin, *Hadron Interactions* (1984)
- [23] NMC, P. Amaudruz *et. al.* CERN-PPE/91-52 (1991)
- [24] E. Berger and J. Qui *Phy. Lett.* **B206** (1988) 141
F.E. Close, J. Qiu, R.G. Roberts, *Phys. Rev.* **D40** (1989) 2820
- [25] L. Frankfurt, and M. Strickman, *Phys. Rep.* **160** (1988) 235
- [26] J.P. Rutherford, in *Hadron structure functions and Parton distributions* ed. Geesaman *et. el.*
- [27] F. Halzen, *Proton Structure from $p\bar{p}$ colliders in Hadron structure functions and Parton distributions* ed. Geesaman *et. el.*
- [28] P. Aurenche, *et. al.*, *Gluon content of nucleon probed with real and virtual* *Phy. Rev.* **D39** (1989) 3275
- [29] Y.S. Tsai SLAC-PUB-848 (1971)
- [30] A.A. Akhundov, D.Y. Bardin, W. Lohmann *Radiative Corrections to Deep Inelastic Muon Scattering* JINR Communications **E2-86-104** (1986)
- [31] A. Milsztajn, *A Comparison of High Statistics Measurements of Proton and Deuteron Structure Functions* CERN-PPE/90-135 (1990)
- [32] EMC, J.J. Aubert *et. al.* *Nucl. Phys.* **B293** (1987) 740
- [33] BCDMS, A.C. Benvenuti *et. al.* *Phys. Lett.* **B237** (1990) 592
- [34] NMC, Amaudruz *et. al.*, *The Gottfried Sum from the Ratio F_2^n/F_2^p* , *Phy. Rev. Lett.* **66** 2712 (1991)

- [35] R.D. Field, and R.P. Feynman, Phys. Rev. **D15** (1977) 2590
- [36] L. W. Whitlow, Ph.D. Thesis Standford University, (1990), SLAC-Reports-357 (1990)
- [37] L. Frankfurt and M. Strickman, Phys. Lett. **B76** (1978) 333 Nucl. Phys. Rev. **B121** (1981) 22
- [38] A. Bodek and J.L. Richie, Phys. Rev. **D23** (1981) 1070
- [39] G. Altarelli, G. Parisi, Nucl. Phys, **B126**, 278 (1977)
- [40] G. Altarelli, Phys. Reports **81** (1982) 1
- [41] J. Bartels, Structure Functions at Small-x: New Physics at HERA DESY 90-153 (1990)
- [42] E. Reya, Phy. Report **69** (1981) 195
- [43] R. D. Field, Applications of Perturbative QCD Addison-Wesley (1989)
- [44] P. Collins, A. Martin and E. Squires, Particle Physics and Cosmology, Wiley-Interscience(1989)
- [45] H. Georgi, and H.D. Politzer, Phy. Rev. **D14** (1976) 1829
- [46] O. Nachtmann, Nucl. Phys. **B63** (1973) 237
- [47] R.K. Ellis et. el. Nucl. Phy. **B212** (1983) 29
- [48] A. Bodek, and A. Simon, Z. Phys.C Particles and Fields **29**, (1985) 231-234
- [49] A. Bodek et. el. Phy. Rev **D20** (1979) 1471
- [50] D. L. Fancher et. al., "Precision Comparison of Inelastic Electron and Positron Scattering from Hydrogen", Phys. Rev. Lett., Volume 37, Number 20, (1976) 231
- [51] D.O. Caldwell et. el. Phy. Rev **D7**(1973) 1362
- [52] T. Sloan et. al., The quark structure of the nucleon from the CERN muon experiments Phy. Reports **162** Nos. 2 & 3 (1988) 45-167

- [53] S.R. Mishra and F. Sciulli, Nevis R#1409, (April 1989)
- [54] D.J. Gross and C.H. Llewellyn Smith, Nucl. Phys. **B14** (1969) 337
- [55] Particle Data Group, Phy. Lett. **B239** (1990)
- [56] EMC, J.J. Aubert et. al. Nucl. Phys. **B259** (1985) 189
- [57] BCDMS, A.C. Benvenuti et. al. Phys. Lett. **B223** (1989) 485
- [58] CHIO, B. A. Gordon et. al. Phys. Rev. **D20** (1979) 2645
- [59] EMC-NA28, M. Arnedo et. al. Nucl. Phys. **B333** (1990) 1
- [60] NMC, D. Allasia et. el., Phy. Lett. **B249** (1990) 366
- [61] J. Morfin, and Wu-Ki Tung, Parton Distributions from a Global QCD analysis of Deep Inelastic and Lepton-Pair Production FERMILAB-Pub-90/74 (1990)
- [62] E665 Collaboration, Nucl. Instr. and Meth. **A291** (1990) 533
- [63] EMC, O.C. Allkofer et. al., Nucl. Instr. and Methods **179** (1981) 445
- [64] EMC EMC, J.P. Albanese et el., Nucl. Instr. and Meth. **212** (1983) 111
- [65] F.L. Navaria, C. Zupancic, J. Feltesse, Nucl. Instr. and Meth. **212** (1983) 125
- [66] The Tevatron Muon Beam: A High Intensity Beam with Well Defined Polarization A. Malensek and J.G. Morfin, July 1983.
- [67] Jorge Morfin, Private Communication
- [68] Tim Carrol, Private Communication
- [69] Uwe Ecker, Determination of the liquid target densities in E665 Run 1987/88 E665 Internal Report
- [70] V. Eckhardt, The PCV proportional chamber, E665 Internal Report
- [71] $2 \times 2 \text{ M}^2$ Proportional Chamber, [PC 1-3], E665 Internal Report VS0131
- [72] T. Kirk, H. Melanson, S. Wolbers, E665 Internal Report FL027 (1985)

- [73] H. Melanson, S. Wolbers, Drift Chamber Calibration E665 Internal Report (1988)
- [74] M. Schmitt, private communication (1990)
- [75] S. Wolbers, Drift Chambers Dead Regions E665 Internal Report (1989)
- [76] D.F. Geesaman, et. al Data Acquisition for FNAL E665 (1990)
- [77] J.J. Ryan, A. A. Bhatti, M. Schmitt E665 Internal Report (1990)
- [78] D.M. Jansen, PC Efficiency E665 Internal Report (1989)
- [79] A. Bhatti, Some recent results from LAT Filter program E665 Internal Note (1989)
- [80] S. Wolbers, The PTMV program E665 Internal Note (1989)
- [81] A. Bhatti et. al., The Data Reduction Program E665 Internal Note (1989)
- [82] M. Adams and S. Magill, E665 Internal Report (SF) (1989)
- [83] S. Magill, Ph.D. Thesis University of Illinois (1990)
- [84] D.M. Jansen, Ph.D. Thesis University of Washington (1991)
- [85] S. Aid, Ph.D. Thesis University of Maryland (1991)
- [86] A. Salvarani, Ph.D. Thesis University of San Diego (1991)
- [87] M. Schmitt, Ph.D. Thesis Harvard University (1991)
- [88] M. Schmitt, A Study of the Momentum Discrepancy between the Beam and Forward Spectrometers, E665 Internal Note (1991)
S. Wolbers K0 production in E665 (1990)
- [89] W. Wittek EMC Internal Report EMCSW/81/14 (1981)
- [90] D.Y. Bardin, D.Y. Shumeiko, Nuc. Phys. **B127** (1977) 242
- [91] V. Barger, R.J.N. Phillip, Nucl. Phys. **B73** (1974) 269
- [92] S. Stein et. al. Phy. Rev. **D12** (1975) 1884
- [93] W.B. Atwood, SLAC-185(1975)

- [94] L.W. Mo and Y.S. Tsai Rev. Mod. Phys., **41**, (1969) 205
- [95] J. Stirling, Private communication (1990) J. Kwiecinski, A.D. Martin, W.J. Stirling, R.G. Roberts Phys.Rev.D42:3645 (1990). P.N. Harriman, A.D. Martin, W.J. Stirling, R.G. Roberts, Phys.Rev.D42:798 (1990).
- [96] E. Sauli, Principles of Multiwire Proportional Chambers CERN Report 77-09 (1977)
- [97] Nanometrics, Inc.
- [98] S. Krzywdzinski Progress Report with PCF Chambers E665 Internal Note (1986)
- [99] A. Bhatti et. el., E665 Internal Report, UW016 (1985)

Appendix A

PCF CHAMBERS

University of Washington is responsible for construction and maintenance of PCF chambers. The design, construction, operation and role of these chambers in E665 spectrometer are described in this appendix. The chambers and the readout electronics was designed and fabricated by Nanometrics Systems Inc.[97].

The PCF chambers are located in the CCM magnet to reconstruct and momentum analyse the forward going charged tracks. The PCF chambers have $2 \times 1 \text{ m}^2$ area and are arranged in 5 stations. Each station has three chambers (U,V,Z) measuring particle position in U,V and Z directions. The angles of orientation of the wires are 105° (U), 75° (V) and 180° (Z) with respect to $-Z$ axis in E665 coordinate system. The nominal wire spacing in PCF chambers is 2 mm. The ideal intrinsic resolution of the PCF chambers is 0.58 mm.

A.1 Principle of Operation

A multiwire proportional chamber (MWPC) consists of a cathode plane and a anode plane consisting of sense of wires held in a strong electric field in a special gas mixture. In this section the principle of operation of MWPCs is described briefly. Details of the principle of operation, design and construction of MWPCs can be found in classic paper by Sauli [96].

When a charge particle passes through a gas, it ionises the gas provided the incident particle has energy greater than the ionization energy of the gas. The generated electron-ions pairs are accelerated in the electric field in opposite direction before they have enough time to recombine. The electrons are collected at the anode wire and the ions neutralize at the cathode plane by extracting the electrons from the surface. The electrons gain energy in the electric field and collide with other molecules producing more electron-ions pairs. The number of electron-ion pairs produced depend on the strength of electric field, nature of gas mixture and the geometry of the chamber. At low electric fields, the secondary

ionization (gas gain) is proportional to the field strength and the primary ionization caused by passage of the incident particle. As the electric field strength is increased this proportionality is gradually lost. At very high electric field strength a discharge or spark break down occurs. In a breakdown the electric field around the wire is modified due to accumulation of electrons all along the wire. It takes several hundred micro seconds for this space charge to neutralize, prohibiting any further detection of the particles during this time. The proportional chambers are normally operated at an electric field strength at which gas gain begins to deviate from proportional mode to get maximum gain without large dead time associated with the gas break down.

The electrons reaching the anode wire are detected by external electronics. Thus the detection of the signal by electronics indicates that a charged particle passed close to the corresponding wire. From the location of wire in space, a coordinate on the trajectory of charged particle can be inferred.

A.1.1 Gas Mixture

A desirable feature of a gas mixture to be used in MWPC is that it should have large gas gain at low enough working voltage. The gas gain and hence the detection efficiency should be insensitive to small variation in the high voltage. The gas should also be able to neutralize quickly after ion-electron pairs are created by the passage of charged particle. In other words, the gas should have small recovery time. Noble gases have low operating voltage because of the absence of any vibrational modes in mono-atomic molecules. The small quantities of polyatomic gases are added to increase the gas gain and the stability of operation. The argon is the natural choice among noble gases because of economic reasons.

In pure argon gas, the ions can return to ground state only by emitting a photon of energy 11.6 eV (ionization potential of argon). Usually, the work function of the metal used for the cathode is smaller than 11.6 eV. Therefore the emitted photons can extract electrons from the cathode which may initiate a second avalanche prolonging the recovery time. The argon ions neutralize by extracting the electrons from cathode. In this process either photons or secondary electrons are emitted which may initiate a secondary avalanche. Polyatomic gases (like CO₂, Freon, isobutane, Ethanol) are added in small quantities to suppress

the secondary avalanche. During the collisions between the argon ions and polyatomic molecules, the electrons move from polyatomic molecules to argon. This charge-exchange process reduces the number of argon ions neutralizing at cathode plane and therefore the probability of secondary discharge is decreased. The polyatomic gases (with many vibrational and rotational degrees of freedom) have very good photons absorption properties also. The excited polyatomic molecules reach ground state via a cascade of transitions releasing the energy in large number of photons each carrying small amount of energy. The electronegative gases like Freon absorb free electrons and thus reduce the probability of secondary discharge. In pure argon the gas gain is limited to $10^2 - 10^3$ but addition of polyatomic gas can increase it to 10^6 with a very stable operation.

A.2 Need for the PCF Chambers

The main role of PCF chambers in E665 reconstruction software is to link the track segments upstream of the CCM magnet with the segments downstream. Their good spacial resolution (2 mm wire spacing) improves the accuracy in the momenta of the tracks also.

The medium momentum particles are spread out in the magnetic fields of CVM and CCM such that some of these particles do not enter the chambers downstream of CCM (DC, PSA). The PCF chambers are used to determined the momenta of these tracks exclusively.

In E665 software many different algorithm are used to pattern recognize the tracks. The PCF chambers play a very important role in all the algorithms used to reconstruct the forward spectrometer tracks. In one of the algorithms, the track segments in the PCF are used as seeds to find the tracks upstream and downstream of the CCM magnet.

A.3 Acceptance

The physical aperture of first PCF plane subtends angles $\sim \pm 60$ mr in vertical direction and $\sim \pm 120$ mr in horizontal direction at the center of the target. These angles define the angular acceptance of charged track in the absence of the magnetic fields of CVM and CCM. As the downstream chambers (DC, PSA, PTM)

completely cover the CCM gap, the acceptance for forward tracks is determined by size of PCF chambers, given the present pattern recognition software. Very low momenta tracks which bend through large angles can not be reconstructed. This means that a high y_b event which has very small momentum scattered muon can not be reconstructed. The actual acceptance of the tracks depends on the momenta of the tracks and can only be determined using full simulation of detector.

A.4 Physical Construction

Each PCF chamber is a separate unit and can be operated independently. These cathode plane is made of Aluminized Mylar stripes which are glued to 1.27 cm thick Styrofoam for structural support. The cathode plane was divided into stripes to make the electric field uniform. The outer side of styrofoam is also covered with aluminized mylar to shield the chamber from the external electromagnetic fields. The anode and cathode planes are 0.635 cm apart. They are supported in a G-10 frame. There are 1096, 1096 and 496 wires in U, V and Z chambers respectively. These wires are made of gold plated tungsten and are $20 \mu\text{m}$ in diameter. The anode wires in U/V chambers are supported at the middle by a pair of insulated wires. One wire is glued on each side of anode wire plane. The region around the support wires has low efficiency because anode wires are insulated by glue. The support wires run along horizontal direction approximately at the middle of the chamber for U and V planes. For Z plane, two pairs of vertical support wires are used, located at ~ 0.35 m away from center. The support wires in different stations are staggered and therefore they do not effect the pattern recognition efficiency. Three hour-glass G-10 spacers are used to keep the spacing between cathode planes uniform. The three planes in a station are aligned together by precisely machined aluminum bushings to ensure that the relative positions of anode wires in a station is easily reproducible.

Total radiation length of all the material in a chamber is 0.16 gm/cm^2 . The amount of material in a plane was measured using a radioactive source. The measurement of the attenuation of electrons indicated that the calculated value of radiation length is about the half value measured. The extra material was identified as the epoxy used to glue aluminized mylar on the styrofoam. The

capacitance between the anode wires and the cathode plane was calculated to be 4.36 pF/m. Negative potential was applied to cathode planes and the anode wires were grounded through a diode. The high voltage power supply was connected to cathode strips through a $20\text{ M}\Omega$ resistor. This resistor determined the maximum current which can flow through the chamber.

A.4.1 Location of Chambers

As mentioned above the PCF chambers are arranged in 5 station. The planes in each triplet are 6.7 cm apart. The distance between two consecutive stations is 85 cm. The most upstream station is located almost outside magnetic field of CCM the at -3.25 meter and the last one just down stream of CCM center at 0.28 meter. The stations are arranged in upstream part of magnet to increase the acceptance for the medium energy tracks. The first PCF station is placed outside the magnetic field to facilitate the pattern recognition.

A.4.2 Gas System

A non-explosive gas mixture (80% Argon, 20% CO_2 , 0.3% Freon-13B) was used. The Freon content was adjusted to maximize the efficiency at minimum operating high voltage, dark current and the second peak (see A.6). The gas flow rate was adjusted to $0.3\text{ ft}^3/\text{hour}$. The typical operating high voltage was 3.8 kV. The dark current in between the spills was less than $0.5\text{ }\mu\text{A}$ and during a spill, the chambers drew $2\text{-}5\text{ }\mu\text{A}$ current.

A.5 Readout Electronics

The data from the PCF chambers are readout serially. The serial readout has a major advantage of reducing the number of cables from the chambers to the scanners. Therefore it is easy to install and maintain the system. The main disadvantage is that it introduces a large dead time due to one-shot pulse width, specially if only a single stage one-shot is used.

The readout system for PCF chamber is based on Nanometric card N-810. The N-810 has a comparator, a one-shot and a shift register bit for each wire. Each card can read 8 wires. The signal on the anode wire is amplified by a

comparator used in infinite gain mode. The amplified signal is fed into the one-shot. The width of the one-shot was controlled by an RC circuit and could be changed easily by adjusting the variable resister. The width of the one-shot was set to be 700 ns during 1987-88 run. The one-shot used is non-triggerable and therefore the wire is dead for 700 ns after the one-shot fires. The output of one-shot is differentiated. If the differentiated signal is in coincidence with the load pulse (Level I trigger), the corresponding bit in shift register is set high. If it does not the content of shift register is not changed. The fast OR of all the wires (comparators) is available on the coupler card. The fast OR can be used as a trigger. At the rate of 10^6 muons per second uniformly distributed over 25 wires, a typical rate in the 1987-88 run, each wire in the beam region had less than 3% dead time.

The data from the shift register is transferred serially to the scanner which sits in a CAMAC crate. On arrival on Level II trigger, the scanner generates a 5 Mhz clock signal. The length of clock train can be adjusted using a dip switch in the scanner. The clock transfers the data from shift registers to the scanner and sets the contents of shift registers to low. In the scanner the serial data stream (0s and 1s) is encoded into 16-bit words and stored in the local memory of the scanner. The datum in phase with the first returned clock pulse corresponds to first wire(0). Therefore it is important that the return clock pulse is synchronized with the transferred data. External cable delay was used to adjust the relative timing between returned clock and the data stream. The address of the wire is encoded in 14 most significant bits of the word and the two least significant bits are used to store the cluster size. The maximum possible cluster size is 3. The cluster size of 00 signals the end of the data. At the end of clock train the LAM (Look At Me) in the scanner is set high, signaling the completion of data transfer. The computer checks the LAM after the Level II trigger is generated. If the LAM is set, it initiate reading of the scanner memory. The LAM is reset by the Level II or can be reset by the CAMAC command. The scanner memory can be read word by word or in the Direct Memory Access (DMA) mode. The scanner memory is not erased after the being read by computer. Only the memory pointer is moved to the end of the data. The memory pointer has to be repositioned if the same data are to be read again. This function provides a method of reading the

same data by two different computers in sequence. The scanner has 1024 16-bit word memory. It can be used to read out a maximum of 2048 wires if every other wire fires and 3072 wires if every wire fires. During 1987-88 run 5 scanners, each reading one station (2588 wires), were used.

All the readout electronics is based on TTL logic levels except two coupling cards. The scanner generated and received TTL signals (clock,data). All the electronics on the chambers is also based on TTL logic levels. To avoid ground¹ loops differential ECL signals are used to connect the scanners to the chamber electronics through a level converting and fanout module (orange box). On the chamber mother board the ECL signal are converted back to TTL logic levels.

An important feature of PCF readout electronics is Nano wire. The nano wire is used to feed charge capacitively to the comparator, simulating the signal on the wire. The readout proceeds in the usual manner. This feature can be used to check the data path, the one-shot timing and the broken channels (comparator, one-shot, shift register).

For monitoring purposes first and the last wires in each station are permanently set high. For each event the data integrity can be ensured by checking the presence and the location of the marker wires.

The high voltage is provided by the Droege power supplied sitting in a NIM crate. As the chamber frame is locally grounded, the no return path on high voltage cable is provided. The Droege power supply is locally grounded in the CAMAC crate. The high voltage setting is controlled by a computer using a pair of ADC and DAC modules. The DAC module is used to generate the low voltage control signal for the Droege power supply and the ADC reads back the applied high voltages on the chambers. The ADC module also reads the low voltages.

A.6 Initial Tests and Efficiency

The first three PCF chambers were tested in the muon beam in Old Muon Lab in 1985. All the chambers were tested in Muon Lab using a 3.5 MeV electron source, ²⁰⁶Ru. During these tests the stability of operation and the electronic readout system were checked. The efficiency of the chambers was measured and

¹ The chamber and scanner are both locally grounded.

appropriate changes were made.

The test readout system was based on an IBM PC with a CAMAC interface module. The trigger was generated by coincidence of a pair of small (5.08×5.08 cm 2) scintillating counters, placed on two sides of the triplet. The trigger rate was ≈ 650 counts/minute. The width of the load pulse used during these measurements was 100 ns wide unless otherwise mentioned.

The efficiency as the function of the high voltage is shown in Fig. A.1 (a). The plateau is about 400 volts wide for all three chambers which is very good. In general the Z chambers had a wider plateau by about 100 volts and higher efficiency than U and V chambers. The typical plateau width was 250-350 volts and it varied across the face of the chamber due to, may be, non-uniformity of the cathode planes. These plots were used to select operating voltage in 1987-88 data taking run.

The efficiency as a function of the delay time, time elapsed between passage of the particle through the chambers and the arrival of load pulse (Level I trigger) to the chamber, is shown in Fig. A.1 (b) for a U chamber. The gate width used for this study was 30 ns. The second peak is ascribed to the secondary avalanche caused by electrons extracted from cathode plane by argon ions when they neutralize at the cathode. The secondary signal reaches the wire while the one-shot is high and therefore does not cause a problem. The effect is seen at the neighbouring wires as indicated by the average number of hits/trigger near the second peak[98]. The efficiency of the U chamber is close to 60% at the second peak. The 150 ns time difference between two peaks implies that the electron drift velocity is 4.36 cm/ μ s.

A.7 Computer Interface and Readout System

The PCF chambers are read by five scanners via CAMAC. The E665 Level I trigger is delayed and shaped in the PCF crate and is fanned out to the chambers. The pulse width of the Level I trigger is set to 70 ns. The delay was adjusted to get the maximum efficiency.

The local trigger logic in the PCF crate also includes a pulser trigger, the Nano wire trigger and a system to test the scanner memory. The test setup can be used only when the E665 data acquisition is not active. The crate controller used by the

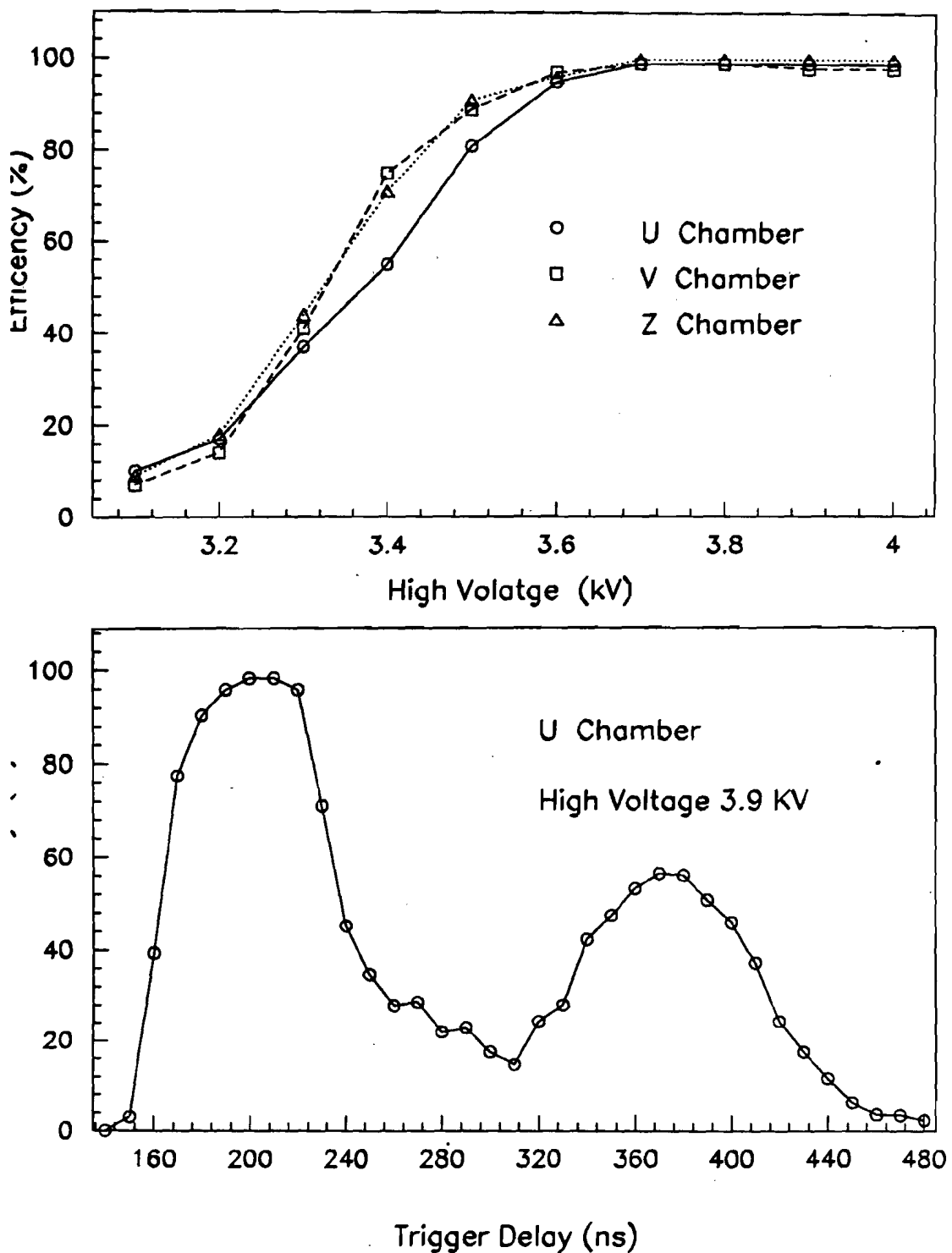


Figure A.1: Efficiency as function of high voltage and trigger delay time.

E665 data acquisition has priority protocol over Transiac, the auxiliary controller used by the IBM PC.

A.7.1 Online Monitoring

The data integrity was checked by the online monitoring program, the PCF consumer[84] written in the VAXONLINE software. In this program the data from the chambers were decoded and wiremaps were made. The number of hits per event and number of planes fired per event were calculated. These numbers are a rough estimate of the plane efficiency. If the data indicated any problem, a message was sent to the shift operator.

The high and low voltages were read by the computer in between spills and compared with the preset values. If a voltage had drifted from the preset value, a error message was sent to operator console.

The PCF electronics was checked regularly using the Nano wire test system and the dead channel were replaced.

A.8 Performance During the 1987-88 Run

The PCF subsystem performed better than any other subsystem during 1987-88 run. The PCF chambers had high efficiency and suffered very few electronics problems during 1987-88 run. The high voltages during the run were adjusted from time to time to get the highest efficiency without a large dark current flowing though the chamber.

The Fig. A.2 and Fig. A.3 show the result of the alignment of each wire in PCF chambers. The four PCF planes (1U,1Z,4U,4Z) were used as the reference planes. The bin width is equal to the wirespacing. The mean of difference between projected track and the position of wire hit is shown. The error bars represent the width of the distribution. The wire spacing of the PCF chambers was adjusted to 1.997. The consistency in wire spacing between different chambers is good except, may be, upper half of the PCF2Z. The orientations of the wires in various chambers was also adjusted. The mean residue as a function of the distance along the wire is shown in Fig. A.3. The maximum slope in the plots is less than 0.2 mr. A slope of 0.2 mr leads to error of 0.2 mm in the position of track which is one

Table A.1: The PCF Efficiency for deuterium using SAT data.

PCF Chamber	Efficiency		
	Total	Beam Region	Outside Beam
PCF1U	0.911±0.002	0.888±0.004	0.939±0.003
PCF1V	0.903±0.003	0.865±0.004	0.950±0.003
PCF1Z	0.910±0.001	0.901±0.002	0.922±0.002
PCF2U	0.873±0.003	0.858±0.004	0.891±0.004
PCF2V	0.837±0.003	0.782±0.005	0.900±0.004
PCF2Z	0.908±0.001	0.896±0.002	0.922±0.002
PCF3U	0.838±0.003	0.816±0.005	0.862±0.004
PCF3V	0.851±0.003	0.821±0.005	0.885±0.004
PCF3Z	0.877±0.002	0.879±0.002	0.873±0.002
PCF4U	0.898±0.003	0.886±0.004	0.912±0.004
PCF4V	0.882±0.003	0.851±0.004	0.914±0.004
PCF4Z	0.848±0.002	0.859±0.002	0.837±0.003
PCF5U	0.903±0.003	0.897±0.004	0.910±0.004
PCF5V	0.901±0.003	0.908±0.003	0.892±0.004
PCF5Z	0.913±0.001	0.909±0.002	0.916±0.002

meter away from center. This difference has no effect on the tracks reconstruction and has a negligible effect on momentum measurement.

The efficiency of the PCF chambers is shown in Fig. A.4. The support wires in the chambers are not visible clearly because the bins are 2 cm wide. The efficiency is almost constant outside the beam region. The efficiency in the beam region was determined separately. The dead regions caused by the support wires are not more than few millimeter wide. The variation in the efficiency with time is less than 2%. The tables A.1, A.2 show the efficiency using the deep inelastic data for the deuterium (post Dec) and hydrogen targets.

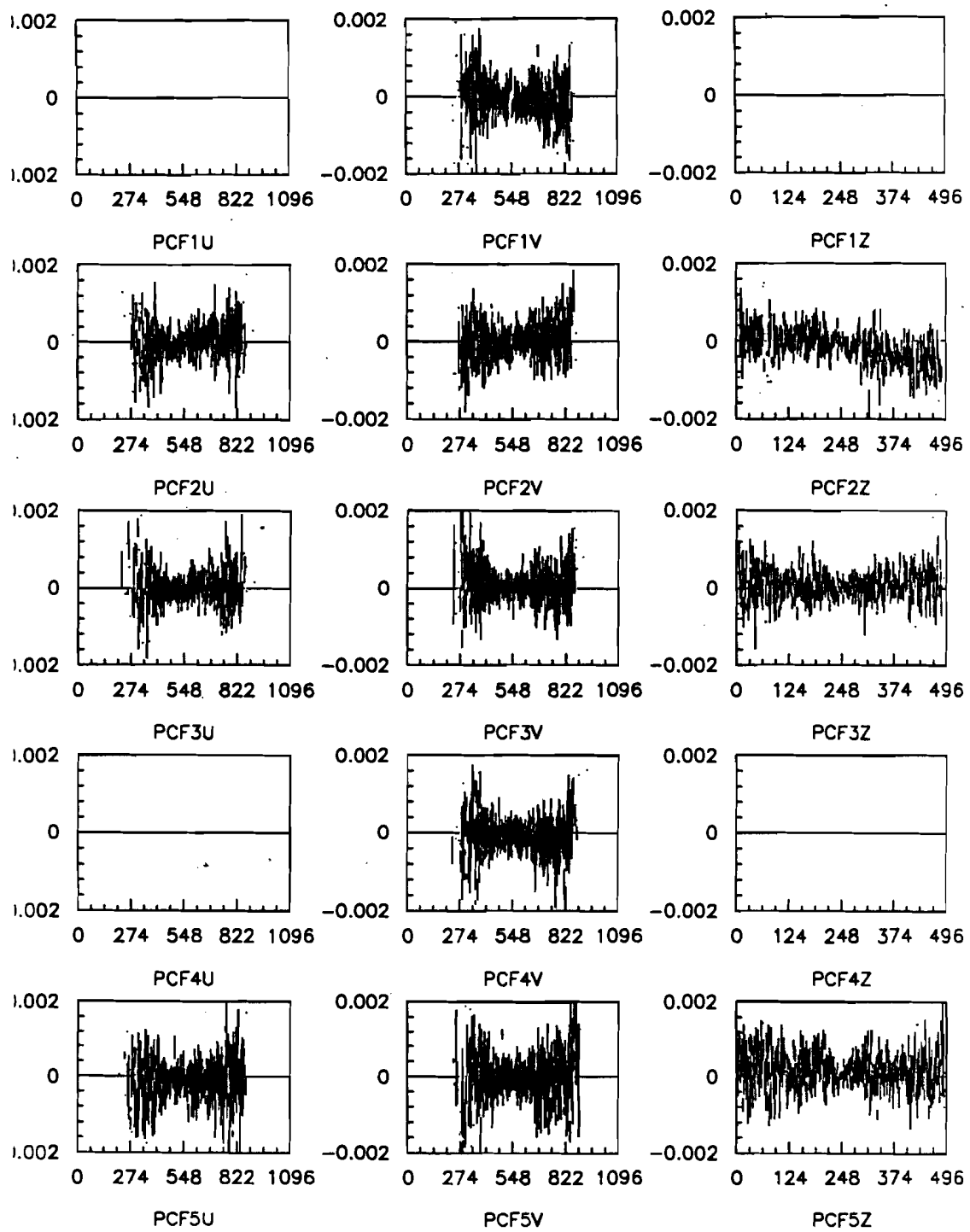


Figure A.2: The wire spacing alignment: The mean residue as a function of distance perpendicular to the wire.

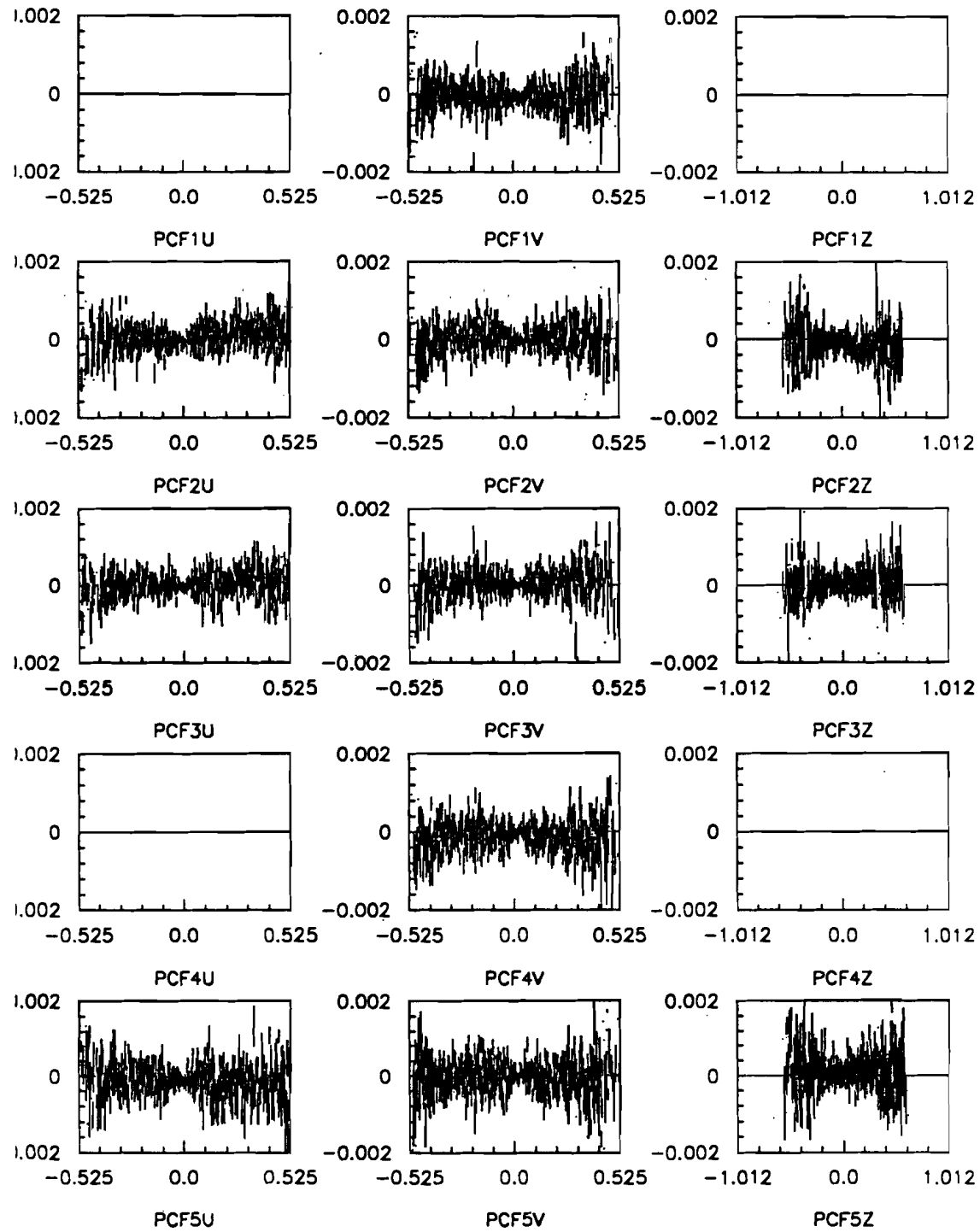


Figure A.3: The α alignment: The mean residue as a function of distance along the wire.

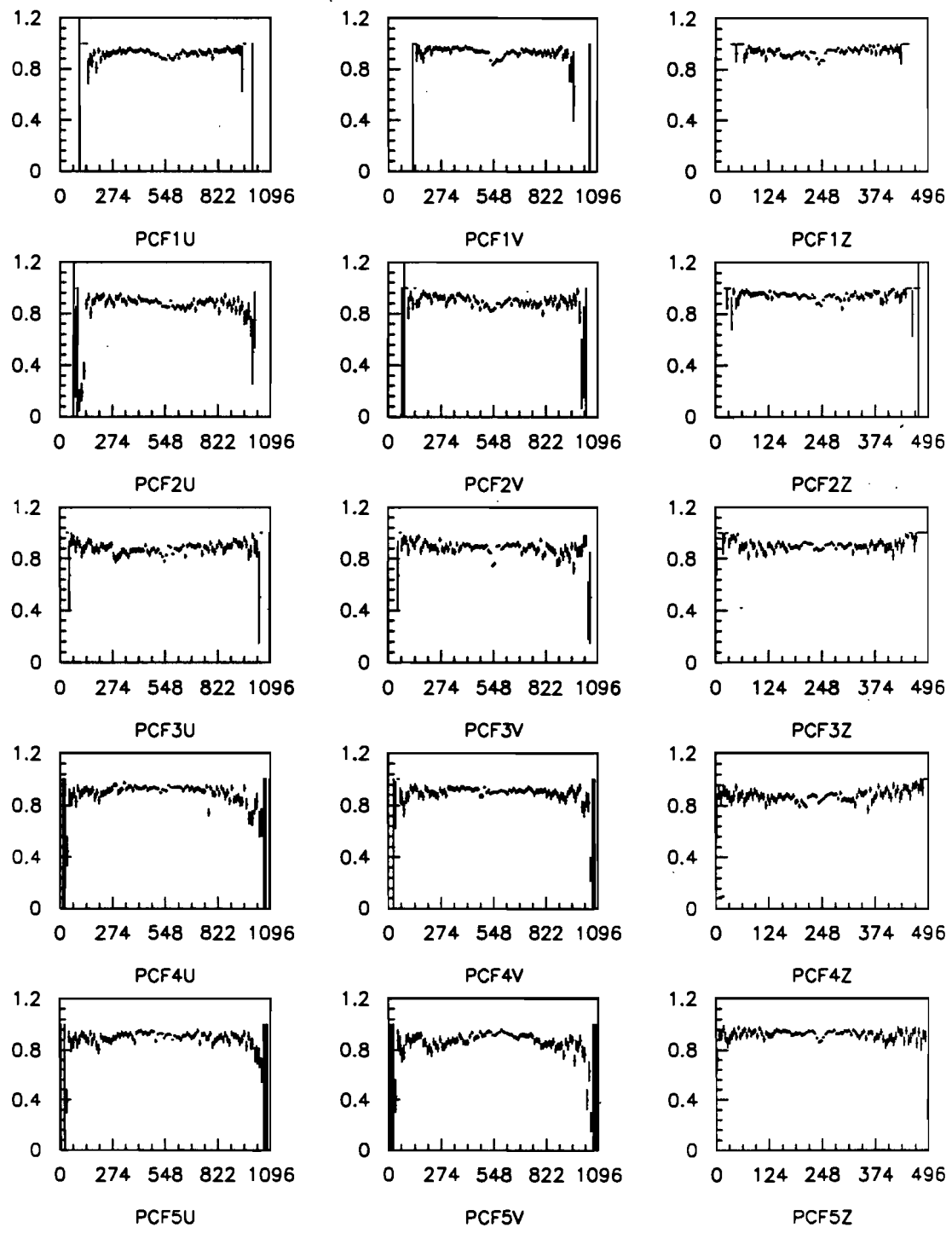


Figure A.4: PCF Efficiency during 1987-88 Deuterium Run.

Table A.2: The PCF Efficiency for hydrogen using SAT.

PCF Chamber	Efficiency		
	Total	Beam Region	Outside Beam
PCF1U	0.905 ± 0.001	0.881 ± 0.002	0.940 ± 0.002
PCF1V	0.900 ± 0.002	0.870 ± 0.002	0.943 ± 0.002
PCF1Z	0.913 ± 0.001	0.911 ± 0.002	0.917 ± 0.002
PCF2U	0.863 ± 0.002	0.842 ± 0.002	0.892 ± 0.002
PCF2V	0.812 ± 0.002	0.748 ± 0.003	0.898 ± 0.002
PCF2Z	0.899 ± 0.002	0.882 ± 0.002	0.922 ± 0.002
PCF3U	0.823 ± 0.002	0.799 ± 0.003	0.853 ± 0.003
PCF3V	0.833 ± 0.002	0.798 ± 0.003	0.877 ± 0.003
PCF3Z	0.885 ± 0.002	0.885 ± 0.002	0.886 ± 0.002
PCF4U	0.879 ± 0.002	0.842 ± 0.002	0.926 ± 0.002
PCF4V	0.846 ± 0.002	0.791 ± 0.003	0.915 ± 0.002
PCF4Z	0.867 ± 0.002	0.871 ± 0.002	0.862 ± 0.003
PCF5U	0.886 ± 0.002	0.867 ± 0.002	0.912 ± 0.002
PCF5V	0.898 ± 0.002	0.890 ± 0.002	0.909 ± 0.002
PCF5Z	0.924 ± 0.001	0.917 ± 0.002	0.932 ± 0.002

Appendix B

TECHNICAL DETAIL OF ANALYSIS

In this appendix the technical details of the analysis is described. After the data reduction program described in the section 4.1.5, the the SAT sample was further reduced using following cuts.

Following run blocks were rejected because of the hardware failures like the CCM, CVM trips, chamber inefficiencies or incorrect pre-scale factor for RBEAM/RSAT. For hydrogen period, the density of target was changing during run blocks 5463-5467. These run blocks were also rejected.

D2 RUN BLOCKS 3106, 3124, 3146, 3150, 3198, 3247, 3355, 3279
H2 RUN BLOCKS 4968, 5463, 5466, 5467, 5076, 5081, 5324-5394

Removal of these run blocks decreased the flux by 12.2% for LAT H sample and 13.1% for D sample. The corresponding decrease in the SAT flux was also 15% and 11.2%.

As explained before the filter program rejected the events which did not satisfy the criteria described in section 4.1.2. The incoming beam needs to be corrected for these offline requirement. The correction factor is defined as:

$$\text{BMCOR} = \left(\frac{\text{Random Beam passing filter}}{\text{Total Random Beam}} \right) \left(\frac{\text{Random Beam with } P(\chi^2) \geq 0.001}{\text{Random Beam passing filter}} \right)$$

Only the events satisfying the 7/7 SBT and 2/4 SMSZ and 2/4 SMSY requirements were included in the Total Random Beam for RSAT. The above correction factor was calculated for each run block separately. Thus the total flux for a given target is given by

$$\text{Flux} = \Sigma \text{Beam} \times \text{BMCOR} \times N_t \quad (\text{B.1})$$

where N_t is the number nuclei in the target as given below.

$$N_t = \frac{\rho [\text{gm}^2/\text{cm}] \times L [\text{cm}]}{m_t [\text{gm}]} \quad (\text{B.2})$$

where ρ is the density of the target and L is length of the target. m_t is the mass of proton (6.67×10^{-27} gm) or deuteron (12.4×10^{-27} gm) for H and D target respectively.

For the run block where the Random Beam (RBEAM/RSAT) information was missing the mean value for that target was used. This information was missing for only few run block in hydrogen data because of a tape read error.

The above procedure treats each run block as a separately entity and thus takes into account any change in the running conditions with time.

The normalize $d\sigma/dx$ for H is defined as

$$\frac{d\sigma}{dx} = \left(\frac{1}{F_p} \frac{dN_p}{dx} - \frac{1}{F_e} \frac{dN_e}{dx} \right) \text{RADCOR} \times \text{ACC} \times \text{EFF} \quad (\text{B.3})$$

where

RADCOR = radiative corrections

F_p = corrected flux factor for Hydrogen

dN_p = the number of Hydrogen events in x_{bj} range dx

F_e = corrected flux for empty target

dN_e = the number of empty target events in x_{bj} range dx

ACC = geometric acceptance (trigger)

EFF = the hardware and reconstruction efficiency

In practice the the each event was weighted by the factor C given by

$$C(x, Q^2) = \text{RADCOR}(x, Q^2) \times \text{ACC}(x, Q^2) \times \langle \text{EFF}(x) \rangle_{Q^2} \quad (\text{B.4})$$

where for efficiency (EFF) the correction factor was averaged over Q^2 in a x_{bj} bin. The calculation of these factors is described in chapter 4. This allows one to use a much finer grid to calculate the correction factors.

If one ignores the empty target correction, the remaining correction factors due to trigger acceptance and hardware/reconstruction efficiency (as long it is independent of time) cancel out and expression for the $d\sigma_d/d\sigma_p$ reduces to

$$\frac{d\sigma_d}{d\sigma_p} = \frac{dN_d}{dx} / \frac{dN_p}{dx} \quad (\text{B.5})$$

Assuming that the correction due to Fermi motion of the nucleons in deuterium target are negligible, the σ^n/σ^p is

$$\frac{d\sigma_n}{d\sigma_p} = \frac{d\sigma_d}{d\sigma_p} - 1 \quad (B.6)$$

$$\left(\frac{dN_d}{dx} / \frac{dN_p}{dx} \right) - 1 \quad (B.7)$$

$$(B.8)$$

The statistical error of the σ^n/σ^p for a given bin was calculated as

$$\delta\left(\frac{d\sigma_n}{d\sigma_p}\right) = \delta\left(\frac{d\sigma_d}{d\sigma_p} - 1\right) \quad (B.9)$$

$$= \delta\left(\frac{N_d}{N_p}\right) \quad (B.10)$$

$$= \left(\frac{N_d}{N_p}\right) \left[\left(\frac{\delta(N_d)}{N_d}\right)^2 + \left(\frac{\delta(N_p)}{N_p}\right)^2 \right]^{\frac{1}{2}} \quad (B.11)$$

$$= \left(\frac{N_d}{N_p}\right) \left[\frac{1}{N_d} + \frac{1}{N_p} \right]^{\frac{1}{2}} \quad (B.12)$$

$$(B.13)$$

where the error in the number of events(N) is assumed to be given by square root of number of events (\sqrt{N}). The statistical errors associated with the corrections are small. The systematic errors are treated separately.

VITA

Anwar Ahmad Bhatti was born on December 17, 1958 in Jhang, Pakistan. He joined Pakistan Air Force College Sargodha, in 1971 and got B.Sc. in 1978. He attended the Quid-i-Azam University Islamabad, Pakistan from 1979 to 1982, getting M.Sc. in Physics. In September 1982 he arrived in Seattle USA, to pursue a Ph.D. degree in Physics at the University of Washington. He obtained a M.S. in Physics from the University of Washington in 1984.